arXiv:nucl-ex/0502004v2 21 Mar 2005

Structure of collective modes in transitional and deformed nuclei

A Dissertation
Presented to the Faculty of the Graduate School
of
Yale University
in Candidacy for the Degree of
Doctor of Philosophy

by
Mark Anthony Caprio

Dissertation Director: Professor Richard F. Casten

May 2003

©2003 by Mark Anthony Caprio
All rights reserved.

Abstract

Structure of collective modes in transitional and deformed nuclei

Mark Anthony Caprio
2003

The collective structure of atomic nuclei intermediate between spherical and quadrupole deformed structure presents challenges to theoretical understanding. However, models have recently been proposed in terms of potentials which are largely independent of the quadrupole deformation β [beta]. These models, E(5) and X(5), describe a transitional nucleus either free to undergo deviations from axial symmetry (γ[gamma]-soft) or confined to axial symmetry, respectively.

To test these models, information is needed on low-spin states of transitional nuclei. The present work involves measurement of electromagnetic decay properties of low-spin states for nuclei in the $A\approx100$ (γ-soft) and $N\approx90$ (axially symmetric) transition regions. Population in β-decay and thermal neutron capture are used, and measurements are carried out using γ-ray coincidence spectroscopy, fast electronic scintillation timing, and γ-ray induced Doppler broadening techniques. Results are obtained for ^{102}Pd, ^{152}Sm, ^{154}Dy, ^{156}Dy, ^{162}Yb, and ^{162}Er, from experiments at the Yale University Wright Nuclear Structure Laboratory, the TRIUMF ISAC radioactive beam facility (Vancouver), and the Institut Laue-Langevin high-flux reactor (Grenoble).

The present data allow detailed comparison of transitional nuclei to model predictions. Many characteristics of the N=90 transitional nuclei (Nd, Sm, Gd, Dy) are found to be reproduced by X(5) and similar β-soft axially symmetric descriptions. The nucleus ^{162}Er, bordering the $N\approx90$ region, appears to support a low-lying β-vibrational excitation, indicating comparatively β-soft structure. And ^{102}Pd is found to match descriptions involving a β-soft, nearly γ-independent, potential.

To facilitate interpretation of these nuclei, a new approach is developed that simplifies the application of the geometric collective model (GCM) by use of scaling properties. Solutions are also obtained for the E(5) Hamiltonian for finite well depths.

These results demonstrate the relevance of β-soft potentials, and in particular the new E(5) and X(5) models, to transitional nuclei. They suggest that such nuclei, historically among the most difficult to describe theoretically, are amenable to descriptions of comparable simplicity to those used for spherical and well-deformed nuclei.

Contents

List of Figures vi

List of Tables ix

Acknowledgements x

Part I Introduction

1 Investigation of collective nuclear structure 2
- 1.1 The nuclear structure problem . . . 2
- 1.2 Collectivity in nuclear structure . . . 3
- 1.3 Transitional phenomena . . . 8
- 1.4 Overview of the present work . . . 13

Part II Experimental techniques

2 Gamma-ray spectroscopy: Aims and methods 18

3 Beta decay and tape collector techniques 21
- 3.1 Beta decay as a population mechanism . . . 21
- 3.2 Beta decay in an accelerator environment: The Yale MTC . . . 23
- 3.3 Beta decay at an ISOL facility: The ISAC GPS . . . 27

4 Gamma-ray spectroscopy with modern high-efficiency arrays 31
- 4.1 Coincidence spectroscopy for transition intensities . . . 31
- 4.2 Angular correlation and polarization measurements . . . 36
  - 4.2.1 Theoretical summary . . . 36
  - 4.2.2 Experimental considerations . . . 39
- 4.3 Fast electronic scintillation timing measurements . . . 44

5 Gamma-ray induced Doppler broadening measurements 51

Part III Experimental results

6 ^{152}Sm **56**
6.1 Experimental motivation . . . 56
6.2 Spectroscopic measurements . . . 57
6.3 Lifetime and polarization measurements . . . 61

7 ^{156}Dy **64**
7.1 Experimental motivation . . . 64
7.2 Spectroscopy experiment overview . . . 65
7.3 Transitions depopulating low-lying levels . . . 67
7.4 Previously reported levels from β decay for which no evidence is found . . . 75

8 ^{162}Yb **78**

9 ^{154}Dy **82**

10 ^{102}Pd **87**

11 ^{162}Er **93**
11.1 Experimental motivation . . . 93
11.2 Spectroscopic measurements . . . 94
11.3 Lifetime and angular correlation measurements . . . 97
11.4 Interpretation . . . 102

Part IV Model analysis

12 The geometric collective model parameter space **108**
12.1 Introduction to the GCM . . . 108
12.1.1 The geometric Hamiltonian . . . 108
12.1.2 Numerical solution of the GCM eigenproblem . . . 110
12.1.3 Application of the GCM . . . 111
12.2 Scaling properties for the GCM . . . 112
12.3 Mapping the GCM parameter space . . . 120

13 Special potentials in the geometric collective model **132**
13.1 The quadratic-quartic potential . . . 132
13.2 X(5)-like structure . . . 137

14 Finite well solution for the E(5) Hamiltonian **141**

15 Phenomenological interpretation **150**
15.1 The $N\approx90$ transitional nuclei . . . 150
15.2 ^{102}Pd . . . 159

Part V Conclusion

16 Conclusion **165**

Appendices

A Collective nuclear structure benchmarks **168**
A.1 Preliminary definitions 168
A.2 Spherical oscillator 169
A.3 Deformed γ-soft structure 170
A.4 Deformed axially symmetric rotor 171
A.5 Square well potentials: E(5) and X(5) 174

B Gamma-ray transition rates and matrix elements **178**

C Rotational $\Delta K = 0$ mixing relations **181**

D Calculation of angular correlation and polarization functions **184**

E Scaling relation for the n-dimensional Schrödinger equation **187**

F Moving tape collector cycle optimization **190**

G Data acquisition and the `cscan` sorting package **193**

H Gamma-ray coincidence intensity spectroscopy **197**
H.1 Coincidence techniques 197
H.2 Array coincidence efficiency 200

I Spectroscopic data for ^{156}Dy **206**

Bibliography **220**

Submitted to the Yale Graduate School April 5, 2003. University Microfilms catalog number 3084266. E-print `arXiv:nucl-ex/0502004`. Dissertation Abstracts International B **64**, 1312 (2003). Dissertation Abstracts Online AAT 3084266.

List of Figures

1.1 Filling of single-particle levels in closed-shell and open-shell nuclei. 4
1.2 Liquid drop shapes with quadrupole and octupole deformation. 5
1.3 Level schemes for quantized liquid drops. 6
1.4 Classical quadrupole modes of a deformed liquid drop. 6
1.5 Symmetry triangle illustrating the parameter space for the IBM. 8
1.6 Schematic view of the evolution from undeformed to deformed structure. . 9
1.7 Illustration of distinction between deformation magnitude and structure. . 10
1.8 Evolution of the 2_1^+ and 0_2^+ states across the transition. 11
1.9 The square well as a transitional potential. 13
1.10 Potential energy surfaces, including the E(5) and X(5) potentials. 14
1.11 Structural investigations discussed in the following chapters. 15
1.12 Recent experimental work in the $A\approx100$ and $N\approx90$ regions. 16

2.1 Population patterns in heavy-ion fusion-evaporation. 19

3.1 Population patterns in a β-decay daughter nucleus. 22
3.2 Population of an even-even daughter by two-step β decay. 24
3.3 Photograph and schematic diagram of the Yale Moving Tape Collector. . . 26
3.4 Kinematic separation of beam and product nuclei in the Yale MTC. 26
3.5 Photograph and schematic diagram of the ISAC GPS. 29

4.1 Schematic illustration of a nuclear decay and the corresponding event. . . . 32
4.2 Placement information contained in a gated spectrum. 34
4.3 Comparison of different sources of intensity information. 35
4.4 Angular correlation patterns for some common γ-ray cascades. 37
4.5 Geometry for direction-polarization correlation measurements. 38
4.6 Direction-polarization correlation patterns for $0,4\rightarrow2\rightarrow0$ cascades. 38
4.7 Direction-polarization correlation patterns for mixed $3^+\rightarrow2^+\rightarrow0^+$ cascades. 39
4.8 The clover detector as a Compton polarimeter. 43
4.9 Schematic representation of the FEST lifetime measurement method. . . . 45
4.10 Detection of delayed annihilation radiation in the BaF_2 detector. 46
4.11 Photograph of the Yale MTC FEST configuration. 48
4.12 Tape transport chamber for FEST experiments at the Yale MTC. 48
4.13 Timing resolution and walk properties of the FEST detector system. 49
4.14 Convolution of the decay curve and the instrument response. 49

5.1 Feeding of a level in thermal neutron capture. 53

6.1 Low-lying positive-parity states in ^{152}Sm. 58
6.2 Spectra gated on transitions feeding the 2^+_{810} and 2^+_{1086} levels in ^{152}Sm. . . 59
6.3 Polarization for the $3^+_{1234} \rightarrow 2^+_{1086} \rightarrow 0^+_0$ cascade in ^{152}Sm. 62
6.4 Doppler-broadened line shapes for transitions in ^{152}Sm. 63

7.1 Spectra from the ^{156}Dy experiment. 66
7.2 Low-lying levels in ^{156}Dy populated in ^{156g}Ho β decay. 68
7.3 Transitions from the 2^+ level at 829 keV in ^{156}Dy. 69
7.4 Transitions from the 4^+ level at 1088 keV in ^{156}Dy. 70
7.5 Gated spectra for the placement of the 554 keV transition in ^{156}Dy. 71
7.6 Gated spectra for transitions from the level at 1515 keV in ^{156}Dy. 72
7.7 Gated spectra for the levels at 1950 keV and 2300 keV in ^{156}Dy. 74

8.1 Yrast band energies and $B(E2)$ values in ^{162}Yb. 79
8.2 Spectra from the ^{162}Yb lifetime measurement. 80

9.1 Cascades involving the 4^+_1 and 0^+_2 states in ^{154}Dy. 84
9.2 FEST data for the 0^+_2 lifetime measurement in ^{154}Dy. 85

10.1 Low-lying positive-parity states in ^{102}Pd. 88
10.2 Gamma-ray spectra from the Yale MTC ^{102}Pd experiment. 89
10.3 Status of $E2$ and $E0$ strengths from low-lying 0^+ excitations in ^{102}Pd. . . . 90
10.4 Evolution of level energies along the Pd and N=56 chains. 91

11.1 Ge detector singles spectrum for ^{162}Er. 95
11.2 Level scheme for the low-spin band members in ^{162}Er. 96
11.3 Gated spectra showing transitions from $K^\pi = 0^+_2$ band members in ^{162}Er. . 98
11.4 Spectra gated on the 900 keV and 418 keV transitions in ^{162}Er. 98
11.5 Spectra from the ^{162}Er lifetime measurement. 100
11.6 Angular correlation data for the $(?)_{1420} \rightarrow 2^+_\gamma \rightarrow 0^+_g$ cascade in ^{162}Er. . . . 102

12.1 Successively deepening and squeezing a potential. 113
12.2 The GCM potential function for d<0. 116
12.3 The shapes of the GCM potential. 118
12.4 Horizontal and vertical scaling of the GCM potential function. 119
12.5 The quantities $S_<$ and $S_>$ as functions of d. 122
12.6 Map of the GCM (d, S) parameter space. 125
12.7 Energy observable predictions for $-5000 \leq d \leq 5$. 126
12.8 $B(E2)$ observable predictions for $-5000 \leq d \leq 5$. 127
12.9 Auxiliary plots for $-5000 \leq d \leq 5$. 127
12.10 Selected predictions of the GCM for $0 \leq d \leq 1$. 130

13.1 Possible shapes of the quadratic-quartic potential. 132
13.2 Energy and $B(E2)$ observables for the quadratic-quartic potential. 135
13.3 Yrast level energies for the quadratic-quartic potential. 135
13.4 E(5)-like structure in the GCM. 136
13.5 Regions for which GCM predictions match those of X(5). 138
13.6 X(5)-like structure in the GCM. 139

14.1 Finite square well potential. 142
14.2 Graphical representation of the finite well eigenvalue problem. 144
14.3 Bound states of the $x_0 = 10$ well. 146
14.4 Evolution of level excitation energies as a function of well size. 148
14.5 Evolution of $B(E2)$ strengths. 149
14.6 Evolution of $B(E0)$ strengths. 149

15.1 Yrast band level energies and $B(E2)$ values for the N=90 isotones. 152
15.2 Evolution of the 4_1^+ and 0_2^+ energies across the N=90 region. 152
15.3 $K^\pi = 0_2^+$ band level energies for the N=90 isotones. 153
15.4 Energy spacing scale of the excited 0^+ sequence across the N=90 region. . 153
15.5 Relative $B(E2)$ strengths for transitions from the $4^+_{K^\pi=0_2^+}$ state in ^{156}Dy. . 155
15.6 Relative $B(E2)$ branching strengths for transitions from the 2^+ state. . . . 156
15.7 Regions for which GCM predictions match ^{152}Sm. 157
15.8 Level scheme for ^{152}Sm, with X(5) and GCM predictions; GCM potential. . 158
15.9 Level scheme for ^{102}Pd, with E(5) and GCM predictions. 161
15.10 Regions for which GCM predictions match ^{102}Pd. 162
15.11 Potential for the GCM calculation for ^{102}Pd. 162

A.1 Level scheme for the E(5) model. 176
A.2 Level scheme for the X(5) model. 177

F.1 Time line for a moving tape collector activity spot. 191
F.2 Number of decays in the detector area per experiment time. 192

G.1 Event processing scheme for `cscan` WNSL sorting routine. 196

H.1 Examples of the extraction of intensities from coincidence data. 199
H.2 Efficiency curve for a clover detector at the Yale MTC. 202
H.3 Ratio of the observed coincident counts to the number expected. 203

List of Tables

6.1 Lifetime ranges deduced from GRID line shapes for levels in ^{152}Sm. 62

8.1 Values for the lifetime of the first excited 2^+ state in ^{162}Yb. 81

10.1 Intensities of transitions from the 2^+_{1534}, 3^+_{2112} and 4^+_{2138} states in ^{102}Pd. . . 90

11.1 Intensities of transitions depopulating the $K^\pi = 0^+_2$ band in ^{162}Er. 97
11.2 Intensities of transitions depopulating the level at 1420 keV in ^{162}Er. 99
11.3 Values for the lifetime of the first excited 2^+ state in ^{162}Er. 101

12.1 Locations and types of extrema in $V(\beta, \gamma)$. 118
12.2 Structures possible for the GCM potential. 121
12.3 Calculational meshes used to generate contour plots. 128

13.1 Calculated branching ratios in X(5) and in the GCM. 140

14.1 Number of bound β solutions for selected x_0. 146
14.2 Excitation energy observables for selected x_0. 148

A.1 Ratio of $B(E2)$ strength to squared intrinsic matrix element (Alaga rules). 173

H.1 Coincident intensities in ^{60}Co, ^{133}Ba, ^{152}Eu, and ^{226}Ra source decay. 204

I.1 Observed γ-ray transitions in ^{156}Dy. 206
I.2 Branching properties of levels populated in ^{156}Dy. 213

Acknowledgements

I would like to acknowledge the many people who collaborated and otherwise contributed throughout the course of this work.

I express my gratitude to Prof. Richard Casten and Dr. Victor Zamfir for being so continuously supportive of this work, and for their extensive involvement and feedback throughout the process. I also especially thank Prof. Cornelius Beausang and Prof. Reiner Krücken for their contributions to the research presented here and to my general experience at the Yale Wright Nuclear Structure Laboratory. The members of the Yale Nuclear Structure Group over the past several years have made this work both possible and enjoyable, and I thank Charles Barton, Daeg Brenner, Libby McCutchan, John Ai, Hanan Amro, Zvi Berant, Gheorghe Căta-Danil, Wen-Tsae Chou, Jeff Cooper, Ron Gill, Gülhan Gürdal, Adam Hecht, Carsten Hutter, Benyuan Liu, Deseree Meyer, Heather Newman, John Novak, Norbert Pietralla, Paddy Regan, Jo Ressler, Zhijun Wang, Alex Wolf, Jing-Ye Zhang, and Lissa Zyromski for their involvement in this work. I am also grateful to the operations and support staff at WNSL — Jeff Ashenfelter, John Baris, Tom Barker, Phil Clarkin, Karen DeFelice, Salvatore DeFrancesco, Sam Ezeokoli, Paula Fox, Walter Garnett, Bob McGrath, Craig Miller, Cheryl Millman, Rusty Reeder, Mary Anne Schulz, Jennifer Tenedine, and Dick Wagner — and to Prof. Peter Parker.

I thank Prof. Francesco Iachello for his suggestions regarding and contributions to the model analysis portions of this work.

I also would like to acknowledge those who contributed to the experiments outside of Yale, including Hans Börner, Milan Krtička, and Paolo Mutti at the Institut Laue-Langevin and Gordon Ball, Peter Jackson, Pierre Amaudruz, John D'Auria, Marik Dombsky, Paul Schmor, and Jean-Charles Thomas at TRIUMF.

I thank Prof. Charles Baltay, Prof. Beausang, Prof. Casten, Prof. Iachello, and Prof. Zamfir for serving on the dissertation committee and Prof. David Warner for acting as outside reader.

Support was provided during this time by the US Department of Energy, under grant DE-FG02-91ER-40609, and by Yale University.

Part I

Introduction

Chapter 1

Investigation of collective nuclear structure

1.1 The nuclear structure problem

The internal structure of the atomic nucleus varies greatly and often suddenly with the number of constituent protons and neutrons. These changes in structure are associated with corresponding changes in the nuclear excitation spectrum and in the decay properties of the excited states. The predominant undertaking of the field of nuclear structure physics is to extract from observed properties of the ground and excited states of the nucleus an understanding of the physical structure of these states and to develop a comprehensive theoretical description of the nuclear system.

The study of nuclei with more than a few constituent nucleons is inherently the problem of interpreting a "complex system", a many-body system with too many constituents to treated by simple few-body techniques and with too few to be adequately treated by pure thermodynamic techniques. Fundamentally, the behavior of the aggregate nuclear system is entirely determined by the interaction of its constituents, but it is largely impossible to deduce even the most basic structural behavior of the system directly from the intrinsic properties of these constituents. This limitation arises in part since the underlying interactions of protons and neutrons in the nuclear medium are not entirely understood, but, more importantly, the computational problem of describing a system of tens or hundreds of interacting protons and neutrons is intractible without the benefit of some additional simplifications. Consequently, there is a need for "phenomenological" models of nuclear structure, which require some degree of empirical input regarding the properties of the nuclear system in order to make predictions of further properties. These models serve at the least to provide a rough conceptual understanding of the properties of nuclei and ideally can allow detailed quantitative descriptions to be obtained.

1.2 Collectivity in nuclear structure

Specific phenomenological models of nuclear structure are applicable only to certain classes of nuclei, and the relevant characteristic for categorization of nuclei is, broadly, the number of nucleons which "participate" in the structure, actively contributing to the ground state properties and excitation modes. The motivation for this classification may be understood in terms of a few elementary properties of the nuclear system.

The nucleus is a system consisting of a fixed number of spin-1/2 particles, the nucleons, and so the space of possible states for the nucleus is the direct product of the single-particle spaces for the individual constituents (*e.g.*, Refs. [1, 2]). This space is spanned by the direct product states

$$\left\{ \left| \mathbf{x}^{(1)} m_s^{(1)} \right\rangle \left| \mathbf{x}^{(2)} m_s^{(2)} \right\rangle \cdots \left| \mathbf{x}^{(A)} m_s^{(A)} \right\rangle_{\mathrm{AS}}, \ \cdots \right\}, \tag{1.1}$$

where A is the total number of nucleons, $\mathbf{x}^{(i)}$ and $m_s^{(i)}$ are the coordinates and spin projection of nucleon i, and the subscript AS indicates antisymmetrization over like nucleons. However, an alternative set of basis states turns out to be more useful for the present purposes. The solutions $\varphi_{nlm_l}(\mathbf{x})$ of the Schrödinger equation for a central potential $V(r)$,

$$\left[-\frac{\hbar^2}{2m} \nabla^2 + V(r) \right] \varphi_{nlm_l}(\mathbf{x}) = \varepsilon_{nlm_l} \varphi_{nlm_l}(\mathbf{x}), \tag{1.2}$$

where n, l, and m_l are radial, orbital angular momentum, and orbital angular momentum projection quantum numbers [1, 2], form a complete set of functions on three-dimensional coordinate space. Consequently, the direct products of the single particle states constructed from these functions constitute a basis for states of the nucleus as a whole,

$$\left\{ \left| nlm_l m_s^{(1)} \right\rangle \left| nlm_l m_s^{(2)} \right\rangle \cdots \left| nlm_l m_s^{(A)} \right\rangle_{\mathrm{AS}}, \ \cdots \right\}. \tag{1.3}$$

This basis has the virtue that, if the Hamiltonian for the nucleus happens to have the special form

$$\hat{H}_0 = \left[\sum_i \frac{\hat{p}_i^2}{2m_i} + V(\hat{r}_i) \right], \tag{1.4}$$

where $\hat{p}_i$ and m_i are the momentum and mass of the ith nucleon, then the nuclear eigenstates will be these very basis states. If the nuclear Hamiltonian is only *approximately* of this form, *i.e.*,

$$\hat{H} = \hat{H}_0 + \hat{V}_{\mathrm{res}}, \tag{1.5}$$

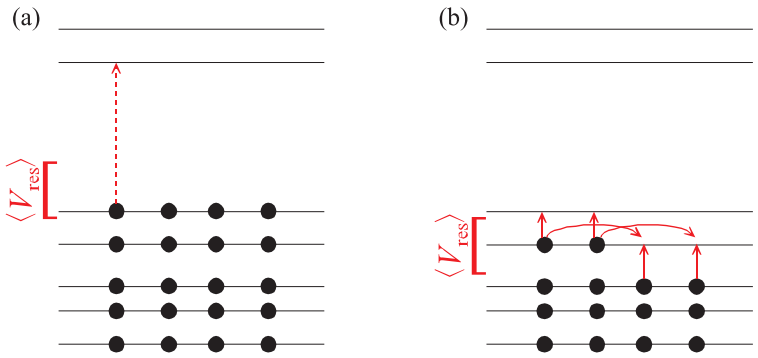

Figure 1.1: Filling of single-particle levels for a single species of nucleon in (a) closed-shell and (b) open-shell nuclei. In an open-shell nucleus, the residual excitation can introduce amplitudes for states with nucleons excited to nearby single-particle levels and/or to different m substates of the same level (spin recoupling).

where the difference is denoted as the "residual" interaction $\hat{V}_{\rm res}$, then the nuclear eigenstates will still *predominantly* be individual direct product states, but with admixtures of the other basis states. Extensive empirical evidence [3] suggests that such a Hamiltonian successfully describes a wide range of nuclear phenomena.

The spacing between the single-particle energy levels $\varepsilon_{nlm_lm_s}$, and whether or not sizeable gaps exist between successive energy levels, is a central factor determining the structure of a nucleus (*e.g.*, Ref. [3]). In the absence of a residual interaction, the nuclear ground state would simply be that direct product state, degenerate in some m_l and m_s, in which nucleons occupy, or "fill", exactly the lowest-energy single-particle energy levels $\varepsilon_{nlm_lm_s}$, as shown schematically in Fig. 1.1(a). The residual interaction can introduce significant amplitudes for occupation of higher-lying single-particle levels only if the spacing between these levels is not much larger than the residual interaction strength. Consequently, depending upon whether or not nucleons have filled all the energy levels below a sizeable gap in the single-particle level spectrum [compare Fig. 1.1(a) and (b)], the ground state and excited spectra of the nucleus will have markedly different properties.

The presence of amplitudes for many direct product states in a single nuclear eigenstate allows for the existence of so-called "collective" phenomena, resulting from the addition of these components with coherent phases. Collective structure corresponds semi-classically to coherent motion of nucleons, including possible bulk motion of nuclear matter. Features identified with collectivity include deformation of the nucleus from spherical shape, smaller spacing between energies of the nuclear states than would arise from the single-particle energy scale, and enhanced electromagnetic transition rates between collec-

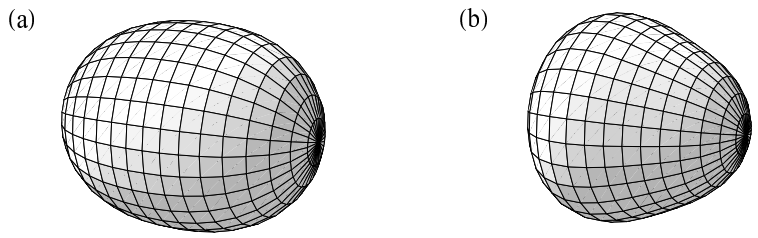

Figure 1.2: Liquid drop shapes with (a) quadrupole and (b) octupole deformation.

tive levels. A wide variety of collective phenomena are possible, ranging from excitations involving small numbers of nucleons to bulk hydrodynamic flow of matter throughout the entire nucleus [4, 5].

The collective structure of nuclear states at low excitation energy is dominated by surface deformations, in which a surface layer of nucleons takes on nonspherical shapes. If the surface shape is described by a multipole expansion of the radius as a function of angle relative to the center of the nucleus,

$$R(\theta,\varphi) = R_0 \left[1 + \frac{1}{\sqrt{4\pi}}\alpha_{00} + \sum_{\mu} \alpha_{2\mu} Y^*_{2\mu}(\theta,\varphi) + \sum_{\mu} \alpha_{3\mu} Y^*_{3\mu}(\theta,\varphi) + \cdots \right], \tag{1.6}$$

then usually the lowest order terms — monopole, quadrupole, and sometimes octupole — are sufficent to describe the phenomena of interest. (The dipole term produces center of mass translation.) Fig. 1.2 illustrates quadrupole-deformed and octupole-deformed shapes. The nucleus does not exist in any one shape but rather in a quantum superposition of shapes: the quantities $\alpha_{2\mu}$ are dynamical variables, for which Schrödinger-like equations can be devised (Chapter 12) and which have probability distributions associated with them. Loosely, however, we may distinguish between "undeformed" nuclei, in which the shape fluctuations are centered about a spherical shape, and "deformed" nuclei, in which the fluctuations are centered about a deformed, usually quadrupole-deformed, shape.

Classically, the modes of excitation available to a nucleus undergoing quadrupole surface deformation are the quadrupole normal modes of a liquid drop [4], and the quantized system shows features recognizably related to these classical modes. For a liquid drop with a spherical shape in equilibrium, the five vibrational modes available, one for each $Y_{2\mu}$, are degenerate, resulting in just one fundamental frequency ω of oscillation. The corresponding quantized energy spectrum consists of a series of phonon excitations, with excitation energies $E = n\hbar\omega$ spaced according to that fundamental frequency [Fig. 1.3(a)]. If a liquid drop instead has a deformed equilibrium shape, the degeneracy of its modes

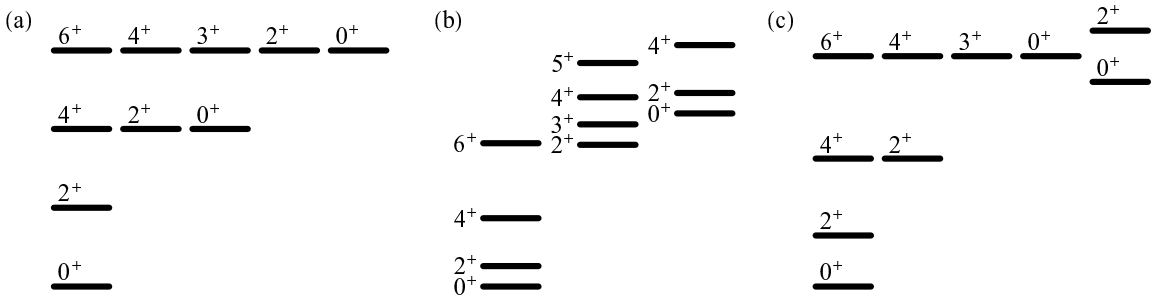

Figure 1.3: Level schemes for quantized liquid drops: (a) spherical oscillator, (b) deformed rotor, and (c) deformed γ-soft. Total angular momentum ("spin") and parity quantum numbers for the levels are indicated.

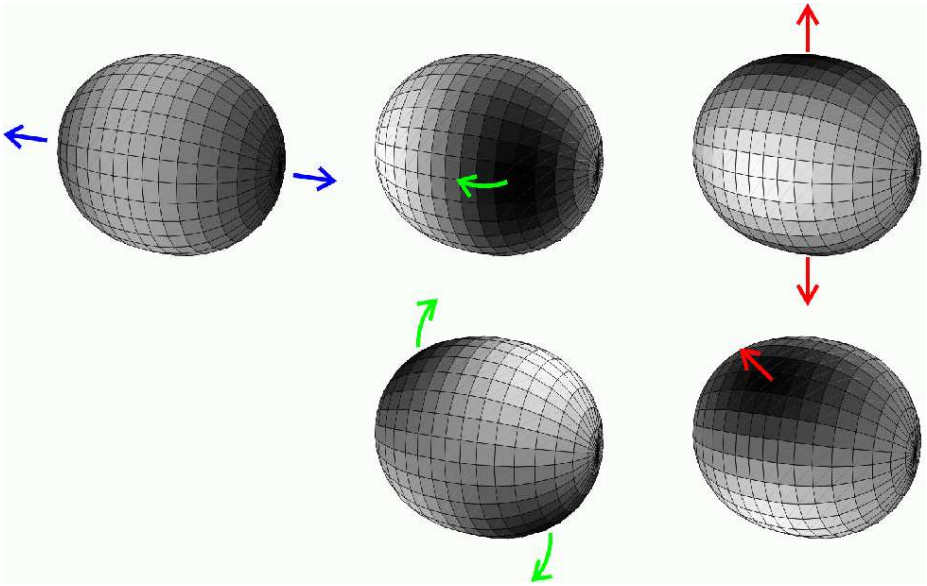

Figure 1.4: Classical quadrupole modes of a liquid drop with deformed equilibrium shape. Dark portions of the surface indicate outward radial motion, and light portions indicate inward radial motion (or vice versa, as an oscillatory function of time). The modes shown are those due to Y_{20} (left), $Y_{2\pm1}$ (middle), and $Y_{2\pm2}$ (right), defined relative to the symmetry axis as the polar axis. The resulting motions are, respectively, oscillations in which the poles and equator alternately expand, rotation of the surface shape, and standing or travelling waves about the equator.

is broken. Fig. 1.4 depicts the surface motion induced by each of the $Y_{2\mu}$ for the case of an axially-symmetric deformed equilibrium shape: Y_{20} induces an oscillation in which the poles and equator alternately expand, $Y_{2\pm1}$ simply induce a rotation of the surface shape, and $Y_{2\pm2}$ produce standing and travelling waves about the equator, causing oscillations about axial symmetry. The quantized spectrum for an axially-symmetric deformed liquid

drop exhibits "bands" of rotationally excited levels with energies following the spacing dictated by quantized angular momentum [$E = (2\mathcal{J})^{-1}|\mathbf{J}|^2 = (2\mathcal{J})^{-1}\hbar^2 J(J+1)$, where $\mathcal{J}$ is a moment of inertia] superposed upon the ground state and upon excitations corresponding to the vibrational modes [Fig. 1.3(b)]. A special case occurs classically for a liquid drop which energetically prefers a deformed shape but which is insensitive to deviations from axial symmetry, since such an object does not support equatorial vibrations. The quantum treatment of such a system (termed "γ-soft" for reasons explained in Appendix A) is especially simple mathematically and is directly relevant to the description of certain nuclei, so its excitation spectrum is also shown [Fig. 1.3(c)].

The forms of quadrupole collective structure just described each thus posess a distinctive, recognizable characteristic pattern of level energies, and there are also specific selection rules and strength patterns followed by the electromagnetic transitions between levels. (The quantitative details are important to discussions throughout the present work and so are summarized in Appendix A.) Several examples exist of nuclei which exhibit, to varying degrees, the properties of a harmonic oscillator, an axially-symmetric rotor, or a deformed γ-soft system (see, *e.g.*, Ref. [6]). These structures are, however, extreme cases, only found when the deformation potential for the nucleus takes on idealized forms, stated more precisely in Appendix A. A description of collective nuclear quadrupole structure must address the phenomena encountered in the "transitional" nuclei, those with structures intermediate between the ideal limits.

Approaches exist which allow treatment of these three extreme forms of structure together with a continuum of transitional cases using a single parametrized model Hamiltonian. Great success in the description of the low-lying levels of a large number of collective nuclei has been achieved using the interacting boson model (IBM) [7]. This is an algebraic model in which the Hamiltonian is built from the Casimir operators of subalgebras of U(6). These operators act upon a bosonic basis for a representation of U(6) consisting of states defined by their occupation numbers for two species of boson: a spin-0 boson with creation operator $s^\dagger$ and a spin-2 boson with creation operator $d^\dagger$. Such a description is appropriate for a system with five coordinate degrees of freedom and thus for a liquid drop undergoing quadrupole deformation [7]. The three limiting structures just discussed correspond to three dynamical symmetries — U(5), O(6), and SU(3) — of the model (Appendix A). A simple "quadrupole" form of the IBM Hamiltonian [8, 9]

$$H = \varepsilon \hat{n}_d - \kappa \hat{Q}^\chi \cdot \hat{Q}^\chi, \tag{1.7}$$

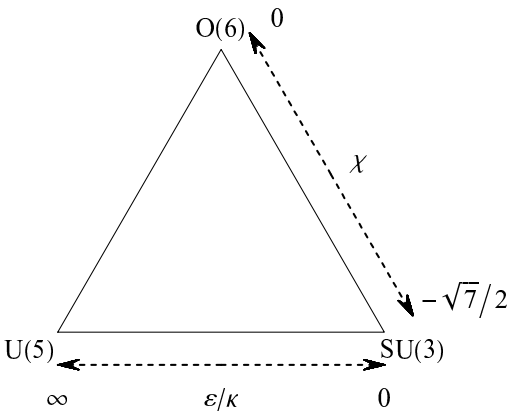

Figure 1.5: Symmetry triangle illustrating the parameter space for the IBM with a quadrupole Hamiltonian. The U(5), SU(3), and O(6) limits correspond to an oscillator, rotor, and deformed γ-soft structure, respectively.

where $\hat{n}_d \equiv (d^\dagger \cdot \tilde{d})$ and $\hat{Q}^\chi \equiv [d^\dagger \times \tilde{s} + s^\dagger \times \tilde{d}]^{(2)} + \chi[d^\dagger \times \tilde{d}]^{(2)}$, reproduces all three limiting structures using only two parameters, ε/κ and χ. The parameter space is commonly illustrated using a symmetry triangle diagram [10], as shown in Fig. 1.5. In the limit of large boson number for the U(6) representation basis, a geometric Hamiltonian is recovered from the IBM [11, 12]. Approaches using a parametrized geometric Hamiltonian are discussed in Chapter 12.

1.3 Transitional phenomena

Some basic aspects of the transition between spherical and deformed shape may be understood schematically from the simple picture already presented. Recent work, outlined in this section, provides components of a more complete understanding. The shape transition occurs over a series of a few "neighboring", *i.e.*, adjacent on the nuclear chart, nuclides. The degree of deformation of a particular nucleus can usually be quite well estimated simply on the basis of the number of protons and neutrons present outside closed shells ("valence nucleons") [13, 14], though the onset of deformation does also depend upon the particular orbitals involved [15–17].

A schematic illustration showing how a shape transition can be expected to evolve is given in Fig. 1.6. For each of several steps along the evolution from spherical to deformed structure, Fig. 1.6 shows the potential energy as a function of a deformation coordinate β. (The quadrupole shape deformation can be reexpressed in terms of a variable β giving

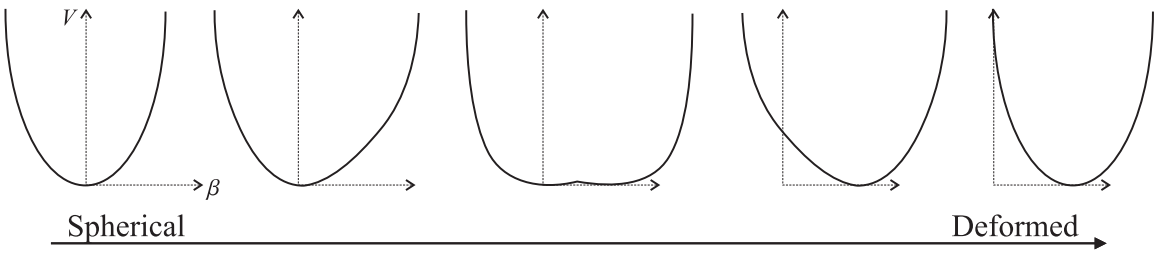

Figure 1.6: Schematic view of the evolution from undeformed to deformed structure, proceeding through anharmonicity, strongly transitional structure, and then softly deformed structure. The potential is shown here simply as a function the deformation coordinate β, though the actual quadrupole shape potential is a function of two variables (see text).

the overall magnitude of deformation and a variable γ describing the deviation from axial symmetry, as defined in Appendix A.)

Two distinct but coupled aspects of the nuclear deformation vary over the course of a shape transition — the magnitude of the deformation and the range of deformation (softness or stiffness) accessible to the nucleus — and it is essential to distinguish these. From a structural point of view, a "spherical" nucleus is one for which a deformation β=0 is strongly energetically preferred, a "deformed" nucleus is one in which a specific deformation $\beta\neq0$ is strongly energetically preferred, and a "transitional" nucleus is one for which β=0 and $\beta\neq0$ are both accessible without significant energetic preference for one over the other. It is this range of accessible β values which determines the qualitative nature of the energy spectrum as being oscillator-like, rotor-like, *etc.*; a nucleus with a harmonic potential centered on β=0 will posess a "spherical" oscillator-like spectrum even if the expectation value for its deformation is large, and a nucleus with a stiff nonzero deformation will behave like a "deformed" rotor even if this deformation is small (see Fig. 1.7). On the other hand, once rotor-like behavior is established, the magnitude of deformation directly controls the moment of inertia of the nucleus and hence the energy scale of rotational excitations. This relationship holds since, for a collective nucleus, only the deformed surface layer of the nucleus is free to participate in rotation. Thus, the moment of inertia is much more directly related to deformation than it is for rigid body rotation and vanishes at zero deformation.

For nuclei with a structure near one of the ideal limits, *i.e.*, near one end of the transition in Fig. 1.6, a perturbative approach is fruitful. The eigenstates for the ideal limit are taken as a zeroth-order approximation to the states of the system, and then the actual perturbed states are obtained as the result of weak mixing between the original

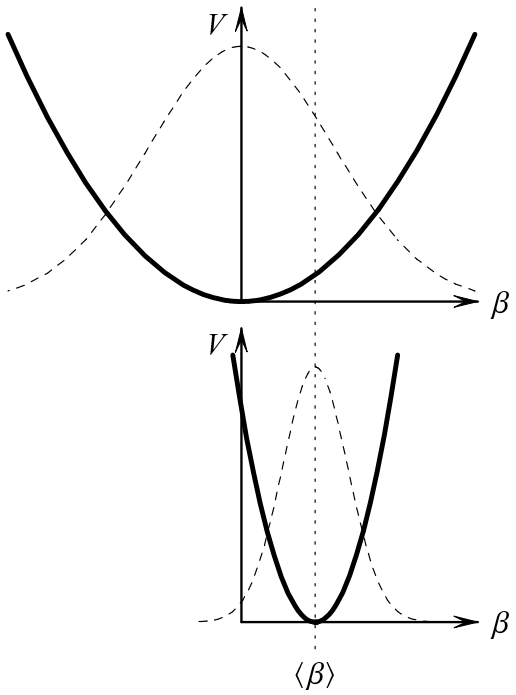

Figure 1.7: Illustration of the distinction between deformation magnitude and structure. A structurally "undeformed" nucleus can have the same average deformation (dotted line) as a structurally "deformed" nucleus. Schematic deformation potentials (solid lines) and wave functions (dashed lines) are shown. [The deformation β is a radial variable (Appendix A) and assumes only positive values, hence the nonzero mean in the upper panel.]

unperturbed states. This description has been very successful for relatively well-deformed rotor nuclei (Section A.4).

In the main part of the transition region, the eigenstates of the transitional nucleus can still be decomposed in terms of the eigenstates of one of the ideal structural limits but will in general have significant amplitudes for a large number of basis states, precluding any simple perturbative approach. Description of the nuclear excitation spectrum must usually be based upon numerical solution of some model Hamiltonian. In transitional nuclei, a given nuclear eigenstate may have a probability distribution spanning a range of deformations. Also, among the spectrum of eigenstates, there may be "coexistence" of states of large deformation with those of small deformation.

Different nuclear observables are sensitive to different aspects of the onset of nuclear deformation. Consider the behavior qualitatively expected for the first excited 2^+ and 0^+ states over the course of the evolution portrayed in Fig. 1.6. For the "stiff" oscillator, starting at the left side of the figure, the 0^+ energy is twice the 2^+ energy,

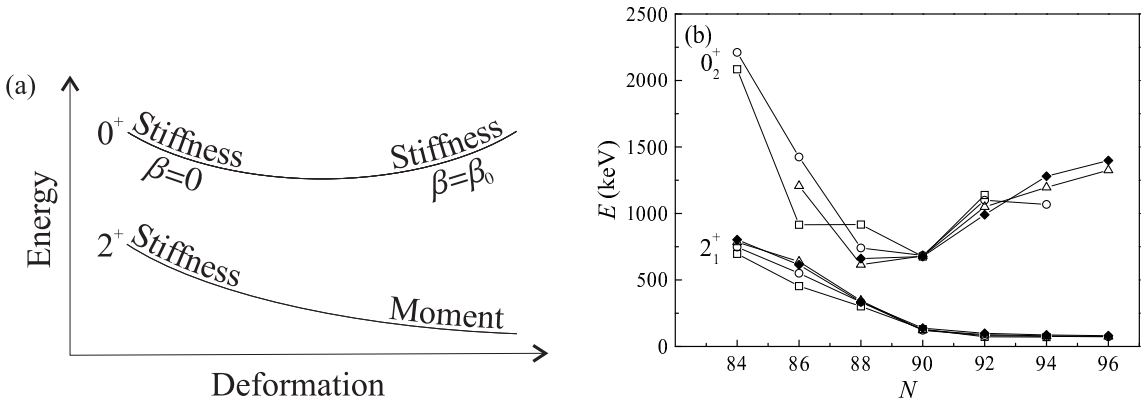

Figure 1.8: Evolution of the 2_1^+ and 0_2^+ states across the spherical to axially-symmetric deformed transition (a) in a schematic picture (see text) and (b) for Nd (□), Sm (○), Gd (△), and Dy (◆) isotopic chains in the $N{\approx}90$ region. Data are from Refs. [18–27]. (The first excited 0^+ state might not be correctly known in all cases and is not necessarily collective.)

and both energies are relatively high. As the potential well becomes wider or "softer", both energies settle lower, and some anharmonicity is likely to be introduced as well. Proceeding further to the right in the figure, rotational behavior sets in, and the first 2^+ state changes in nature from being a vibrational excitation, with an energy determined by the well stiffness, to being a rotational band member, hence with an energy determined by the nuclear moment of inertia. The 2^+ level energy therefore continues to decrease as the deformation, and thus moment of inertia, increase. The 0^+ state, however, retains its vibrational nature, evolving into the β vibrational bandhead (Section A.4). As the potential becomes increasingly stiff, now about a deformed β value, the 0^+ level again rises in energy. This schematic picture of the roles of the 2^+ and 0^+ excitations is summarized in Fig. 1.8(a). Such a general trend in behavior is illustrated with actual data from the $N{\approx}90$ transition region in Fig. 1.8(b). This description should not be viewed as either complete or universally valid — it is qualitative in nature and certainly does not contain the full complexities of a solution of the quadrupole collective Hamiltonian, and, moreover, the lowest 0^+ excitation often lies outside the collective model space — but it does indicate which levels may be sensitive to different aspects of the nuclear structure.

Over the past several years, renewed experimental attention has been directed towards transitional nuclei. The experimental investigation benefits greatly from the development of high-efficiency multi-detector arrays of high-resolution Ge detectors for γ-ray spectroscopy. Greatly improved spectroscopy (Chapter 4) removes a considerable "clut-

ter" of misinformation previously hindering the interpretation of transitional nuclei and also makes possible intensity measurements for weak transitions sensitive to the structure of these nuclei. Measurements of one such transition, the $2_3^+ \rightarrow 0_2^+$ transition in ^{152}Sm (Refs. [28, 29] and Chapter 6), and the discovery of its unexpectedly low strength, significantly constrained model descriptions and encouraged much of the recent theoretical and experimental work. More generally, model analysis benefits from having as full and accurate a set of data available as possible.

Several theoretical ideas have been advanced regarding structural evolution in the transition region. Studies involving the IBM revealed that the transition from spherical to deformed structure has characteristics of a first or second order phase transition [12, 30, 31], depending upon the path taken through parameter space. (The second order phase transition occurs only for the special case in which complete γ softness is maintained along the transition.) Following a very different approach, empirical examination of basic observables, *e.g.*, level energies and separation energies, for large sets of nuclei shows sharp discontinuities in behavior [32, 33] to occur at a specific point along the transition [specifically, where $E(2_1^+)\approx$130–145 keV], again closely resembling the behavior expected for a first order phase transition.

With the new experimental data available, model Hamiltonian parameter values relevant to specific transitional nuclei can be identified much more closely, and several examples have been found of nuclei near the first order phase transition in the IBM. In the immediate region of parameter space surrounding the first order phase transition, individual states can be decomposed as superpositions of two well-defined components — one oscillator-like and one rotor-like — with only a small residual remaining [29]. Among the eigenstates, some with predominantly oscillator-like IBM wave functions are found to coexist with others with predominantly rotor-like wave functions [30, 31]. These observations have led to a treatment, in Ref. [34], of the evolution of structure across the transition region in the IBM as approximately a two-state mixing problem, in which a "spherical" 0^+ state and "deformed" 0^+ state undergo an avoided crossing at the critical point of the transition. The improved data also constrain the appropriate parameter values in geometric models (Chapter 15).

An especially simple geometric description for nuclei near the critical point of the phase transition has been proposed by Iachello [35, 36]. For such nuclei, the deformation potential is expected to be relatively "flat" in β, allowing the nucleus to asuume either

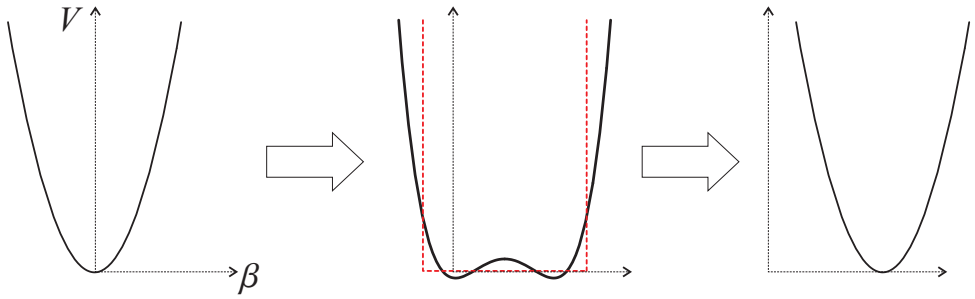

Figure 1.9: The square well as an approximation for the transitional potential. Schematic potentials for the transition from spherical to deformed structure are shown.

a spherical or deformed shape with minimal energy penalty. A flat-bottomed potential can reasonably be approximated by an infinite square well potential, as illustrated in Fig. 1.9. For a square well potential, the solution wave functions are analytic in form (spherical Bessel functions) and the eigenvalues are simply given in terms of the zeros of the Bessel functions. A simple square well in the deformation variable β — termed E(5) — is appropriate to the γ-soft transition. A square well in β with an additional term providing stabilization in the γ degree of freedom — termed X(5) — is used for the description of axially-symmetric transitional nuclei. The E(5) and X(5) models are summarized in Section A.5. Empirical examples of nuclei described by the E(5) and X(5) Hamiltonians have been identified (see Refs. [37–41] and Chapters 6, 7, and 10). The E(5) Hamiltonian has the special property that it exhibits a dynamical symmetry, that of the five-dimensional Euclidan algebra, and is thus the first recognized example a dynamical symmetry based upon a nonsemisimple Lie algebra [36, 42].

The E(5) and X(5) models provide analytical "benchmarks" for the interpretation of transitional nuclei much as the structural limits introduced in Section 1.2 provide benchmarks for the interpretation of undeformed or well-deformed nuclei. The E(5) and X(5) potentials, as functions of the deformations variables β and γ, are shown along with the potentials for the structural limits in Fig. 1.10.

1.4 Overview of the present work

The following chapters present experimental and theoretical investigations of the nuclear quadrupole shape transitions, involving both axially-symmetric and γ-soft structures. The structural domain covered by these studies is plotted in Fig. 1.11, which shows

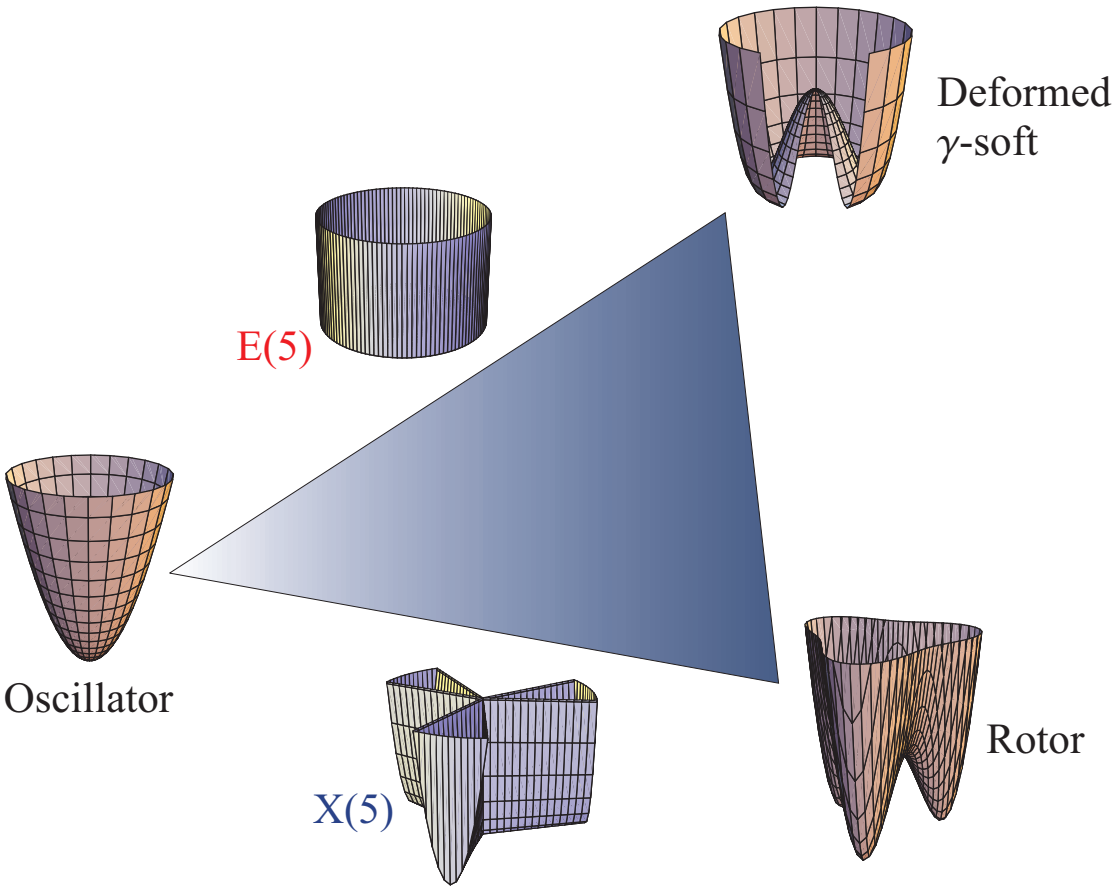

Figure 1.10: Potential energy surfaces producing spherical oscillator, deformed γ-soft, and rotor structures along with the recently-proposed E(5) and X(5) potentials for transitional cases. The radial coordinate for the potential plots is the deformation β, and the angular coordinate is the deviation γ from axial symmetry. (Figure from Ref. [43].)

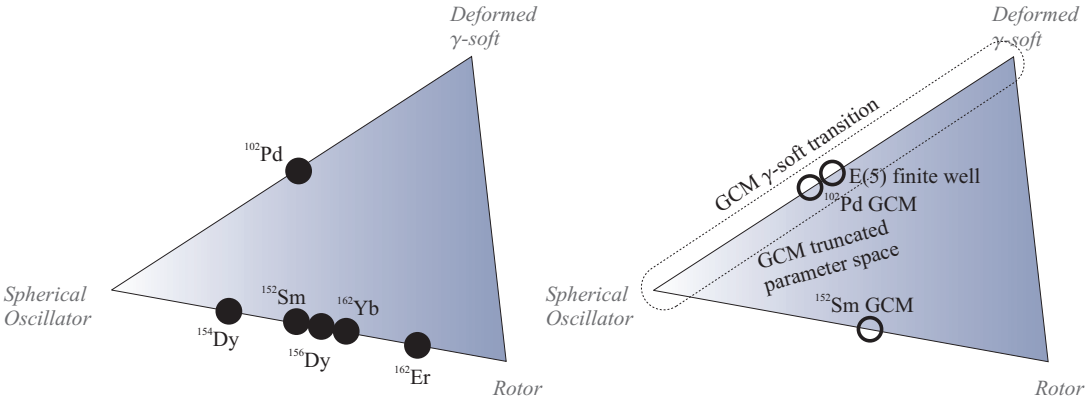

Figure 1.11: Structural investigations discussed in the following chapters, including both experimental work (left) and theoretical studies (right), shown schematically in the context of the axially-symmetric and γ-soft transitions.

where each individual nucleus or model investigation falls on a schematic version of the symmetry triangle diagram.

The experimental work described consists of spectroscopic studies and related measurements making use of γ-ray detection. Experiments concentrated on the $N{\approx}90$ ($A{\approx}150$–160) axially-symmetric transition region and the $A{\approx}100$ (Pd, Ru) γ-soft transition region. A summary of recent experiments involving the Yale nuclear structure group investigating nuclei in these regions, including the work discussed here, is given in Fig. 1.12. Much of the work described in the following chapters was carried out at Yale University's Wright Nuclear Structure Laboratory (WNSL), which houses the 21 MV Extended Stretched Trans-Uranic (ESTU) tandem Van de Graff accelerator [44, 45]. The research presented also includes one of the first experiments to be carried out at the TRIUMF Isotope Separator and Accelerator (ISAC) facility [46] in Vancouver, Canada, and measurements performed at the 58 MW high-flux reactor of the Institut Laue-Langevin in Grenoble, France.

The experimental goals (Chapter 2) and the methods applied are outlined in Part II. Experiments were carried out making use of β decay at stable and radioactive beam facilities (Chapter 3) and of neutron capture (Chapter 5). The availability of high-efficiency multidetector arrays for γ-ray detection requires new approaches to be taken to spectroscopic measurements in decay studies (Chapter 4).

Experimental results for specific nuclei are detailed in Part III. The nuclei discussed include the transitional nuclei ^{152}Sm (Chapter 6), ^{156}Dy (Chapter 7), ^{162}Yb (Chap-

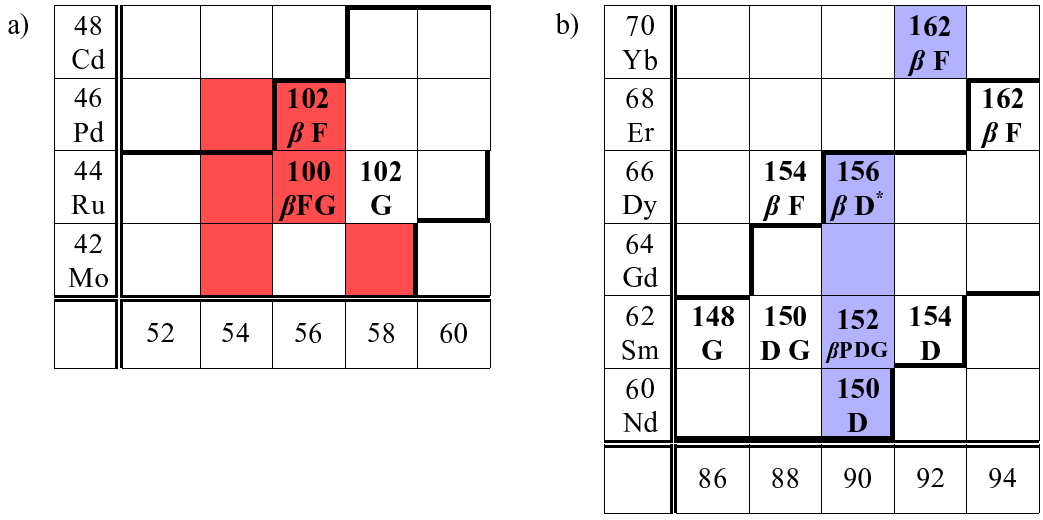

Figure 1.12: Recent experimental work by the Yale nuclear structure group and collaborators investigating low-energy collective modes in the (a) $A\approx100$ and (b) $N\approx90$ ($A\approx150$–160) transitional regions. Nuclei studied are shown on a standard Z *vs*. N nuclear chart. Shaded squares in parts (a) and (b) indicate a 4^+ to 2^+ level energy ratio approximately consistent with the E(5) or X(5) model predictions, respectively. Experimental techniques indicated are $\gamma\gamma$ or $\gamma\gamma(\theta)$ spectroscopy in β decay (β), FEST lifetime measurement in β decay (F), Compton polarimetry in β decay (P), Doppler lifetime measurement following population by Coulomb excitation (D), Doppler lifetime measurement following population by heavy-ion fusion-evaporation (D*), and GRID lifetime measurment and eV-resolution γ-ray spectroscopy following neutron capture (G) (see Part II).

ter 8), ^{154}Dy (Chapter 9), and ^{102}Pd (Chapter 10), as well as the relatively well-deformed rotational nucleus ^{162}Er (Chapter 11) bordering the $N\approx90$ transitional region.

Model investigations are discussed in Part IV. Analytic relations are used to simplify the use of the geometric collective model (GCM) in Chapter 12. These results are used to survey structural evolution throughout the GCM model space. Several special topics — the γ-soft transition in the GCM, and E(5)-like and X(5)-like structure in the GCM — are also considered (Chapter 13). The E(5) model is solved for finite well depth, addressing concerns which had been raised about the application of the E(5) model to actual nuclei [35], and the effects of finite depth on observables are studied (Chapter 14). The phenomenology of the $N\approx90$ transition region is summarized in the context of the X(5) model and GCM predictions, and an analysis of ^{102}Pd using the GCM is carried out (Chapter 15).

Part II

Experimental techniques

Chapter 2

Gamma-ray spectroscopy: Aims and methods

Understanding of nuclear structure is largely obtained through comparison of measured nuclear properties with model predictions. The experimental task is to measure those properties which can most effectively be used to distinguish between different model descriptions or to refine the interpretation using a given model (*e.g.*, find the most suitable set of parameter values). The collective models discussed in Chapter 1 provide predictions for such quantities as the energies of low-lying levels and for electromagnetic matrix elements between these levels, and the study of these is the focus of the present experimental work.

Much successful work has been performed over the past decades populating states through heavy-ion fusion-evaporation reactions [47]. Such reactions tend to initially produce nuclear states at high spin and high energy, which are usually either "yrast" states (*i.e.*, the lowest-energy states of their given spin) or nearly yrast. These states then deexcite by emission of a series low-multipolarity (dipole and quadrupole) γ rays. Each low-multipolarity γ ray emission can induce at most a small change in spin, and higher-energy transitions are enhanced due to the greater available phase space for the radiation. Consequently, at each step in the decay the sequence of levels populated tends ever closer to being yrast, as shown in Fig. 2.1. Population of near-yrast states at high spin thus leads almost exclusively to the population of yrast states at low energy.

The useful predictions of the collective models pertain, though, to the whole set of low-energy collective states, not just the yrast states. Mechanisms other than direct population in fusion-evaporation reactions are necessary for the effective population of non-yrast states. Several such mechanisms exist, including β decay from a low-spin parent nucleus (Chapter 3), neutron capture (Chapter 5), and Coulomb excitation, as well as various forms of transfer reaction and inelastic scattering.

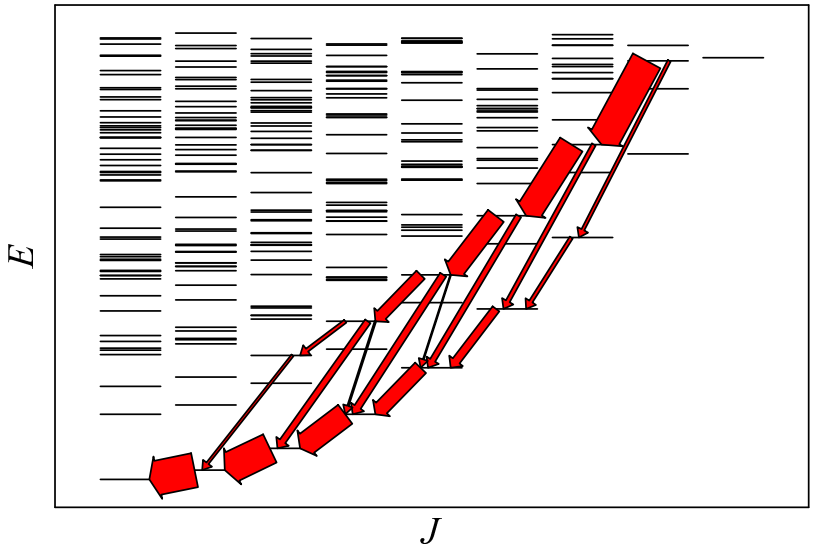

Figure 2.1: Population patterns in heavy-ion fusion-evaporation. Electromagnetic quadrupole transitions can induce a change in spin of at most two units, and larger-energy transitions are preferred, leading to a population pattern in which intensity flow migrates to the yrast states.

Once the levels of interest are populated, these levels must be observed and their properties, especially electromagnetic decay properties, determined. The probability per unit time of deexcitation of one state to another by γ-ray or conversion electron emission (an experimentally accessible quantity) is directly related to electromagnetic multipole operator matrix elements between the two states (quantities predicted by models). Experimentally, several pieces of data are needed to deduce a single matrix element. A given level may be depopulated by several different possible transitions or "branches", including both γ-ray and conversion electron transitions, and the partial transition probabilities for all these branches combine to produce an aggregate decay rate

$$T = \sum_i T_i^{\gamma} + \sum_i T_i^{\text{c.e.}}, \tag{2.1}$$

and hence lifetime $\tau = T^{-1}$, for the level. The problem of measuring the decay rates for individual transitions is broken into two parts: a lifetime measurement and a "spectroscopic" study, in which the relative intensities of the various branches are determined. Each individual γ-ray transition may also proceed by more than one multipolarity, as described by a mixing ratio δ (Appendix B), and this δ must be determined experimentally in order for the contributions from the different multipole matrix elements to be separated. These matters are reviewed in more detail in Appendix B.

Directly or indirectly, a broad variety of information can be obtained through detection of the emitted electromagnetic radiation. The techniques discussed in the following chapters all rely at least partially upon γ-ray detection. Energies of observed γ-ray transitions, and the coincidence relations between these transitions (Section 4.1), allow identification of the levels. Intensities of the emitted γ rays (Section 4.1) provide information on relative electromagnetic transition strengths, and when combined with conversion electron data they can also yield information on γ-ray multipolarities [48]. Angular corelations and polarizations (Section 4.2) of the emitted γ rays provide information on level spins and γ-ray multipolarities. Detection of the γ-rays is also integral to many techniques for the determination of matrix elements in Coulomb excitation [49, 50] and for the measurement of level lifetimes, including electronic timing methods (Section 4.3) and recoil Doppler shift methods (Ref. [51] and Chapter 5).

Chapter 3

Beta decay and tape collector techniques

3.1 Beta decay as a population mechanism

The process of β decay can directly provide certain nuclear physics information, for instance, on weak interaction coupling strengths, nuclear ground-state mass differences, or nuclear spin assignments, but in the following discussion it is considered primarily as a mechanism for populating states to be studied by their subsequent electromagnetic interaction. "Beta decay" is used as a generic term to include the processes of β^- and β^+ emission and electron capture (or ε decay).

Beta decay is a highly spin-selective population mechanism. The beta emission wave function may be decomposed (*e.g.*, Refs. [52, 53]) into multipoles of the orbital angular momentum L of the emitted particles, much as for electromagnetic radiation (*e.g.*, Ref. [54]). The parity change induced by each multipole is $(-)^L$. The angular momentum difference between the parent and daughter nuclei must be carried off by some combination of this orbital angular momentum and the combined spin S of the β and ν (S=0,1). The transition probability for each higher multipole is suppressed by a factor of approximately $(R_{\rm nucl}/\lambda_\beta)^2$, where $R_{\rm nucl}$ is the nuclear radius and λ_β is the β-particle de Broglie wavelength, which is typically $\sim 10^4$. Consequently, most decays from the parent will proceed to daughter states which are accessible by L=0 decay, thus with ΔJ=0,$\pm$1 and no change in parity.

Beta decay from a low-spin parent can therefore populate low-energy, low-spin states in the daughter directly. It can also populate higher-energy, low-spin levels, which then decay primarily by dipole or quadrupole radiation to the lower-energy levels of similar spin; although decays directly to the lowest-energy levels are energetically preferred, decays to intermediate-energy levels may also be considerable. Fig. 3.1 illustrates the resulting γ-decay patterns in the daughter nucleus. These should be compared to the population

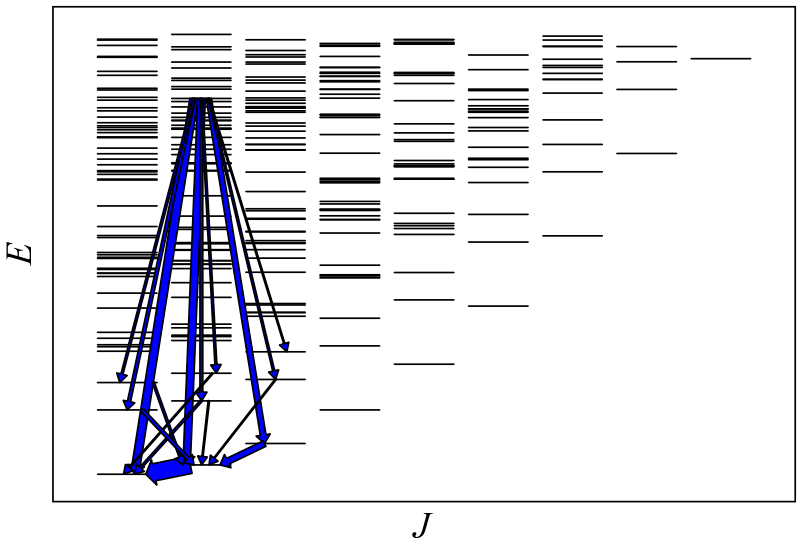

Figure 3.1: Population patterns in a β decay daughter nucleus from a low-spin parent. Transitions from one representative high-lying, low-spin level directly fed by the β decay are shown, along with subsequent transitions among the levels populated.

patterns shown for fusion-evaporation in Fig. 2.1.

Both β^+ decay and electron capture proceed from the same parent nucleus to the same daughter nucleus but do so producing different population patterns of states in the daughter nucleus. In β^+ emission, some of the energy provided by the mass difference between the parent and daugther nucleus must be used to create the β^+ particle; whereas, in electron capture, the mass energy of an atomic electron is liberated. The energy available for excitation of the daughter nucleus in each case is

$$Q_\beta = M_P^{\rm nucl}c^2 - M_D^{\rm nucl}c^2 - m_e c^2 \tag{3.1}$$

and

$$Q_\varepsilon = M_P^{\rm nucl}c^2 - M_D^{\rm nucl}c^2 + m_e c^2, \tag{3.2}$$

where $M_P^{\rm nucl}$ is the parent nuclear mass and $M_D^{\rm nucl}$ is the daughter nuclear mass, excluding minor contributions from atomic binding effects. Consequently, electron capture can populate higher-lying states in the daughter nucleus than can β^+ decay and can even proceed in some cases for which β^+ decay is energetically forbidden ($0<Q_\varepsilon<2m_e c^2$). Where both β^+ decay and ε decay to a given level in the daughter nucleus are possible, the relative probability of these depends upon the maximum β energy for that transition: electron capture dominates for small transition energy (high-lying levels), while β^+ decay dominates

for large transition energy [55]. The distinction between β^+ decay and electron capture is relevant to several applications discussed in the following chapters: radiation from β^+ annihilation can be a significant source of background in coincidence spectroscopy experiments, β^+ particles may be used for timing in lifetime measurements (Section 4.3), and β tagging may be used to separate $\beta^\pm$ decay processes from electron capture processes in contaminated radioactive beam experiments.

3.2 Beta decay in an accelerator environment: The Yale MTC

Electrostatic heavy-ion accelerators are effective tools for the production of proton-rich or near-stable nuclei through a variety of possible reactions, including fusion-evaporation and transfer reactions. Fusion-evaporation *per se* is not an efficient population mechanism for the low-spin, non-yrast states we wish to study, as discussed in Chapter 2. However, fusion-evaporation may be used as a *production* mechanism for β-decay parent nuclei, which then populate such states of interest in the daughter nucleus. Fusion-evaporation is flexible in the nuclei it can create, due to the wide variety of available combinations of beam and target nuclei (which control the compound nucleus produced) and beam energy (which influences the following statistical decay process) [56], and it can provide relatively high reaction cross-sections of hundreds of mb.

In the $A\approx$100–170 region of interest in this work, the particle evaporation following compound nuclear formation is mainly of neutrons, although proton and alpha emission are significant towards the low end of this mass range. For beam energies within a few MeV above the threshold energy for fusion, relatively few particles ($\sim$3–4) are evaporated, and the evaporation process is dominated by a single channel. At energies further above threshold, the total fusion cross section increases until saturation at a geometric limit. The average number of evaporated particles increases with beam energy as well (about one additional particle emitted per few-MeV increase in beam energy), and fluctuation in the number of emitted particles leads to decreased dominance of the main evaporation channel and hence decreased production selectivity. At higher energies still (tens of MeV above threshold), compound nuclear fission begins to occur instead of particle evaporation. As an example of a clean, near threshold fusion-evaporation reaction, one experiment in the present work used ^{148}Sm(^{12}C,4n)^{156}Er at 73 MeV beam energy, or $\sim$20 MeV above

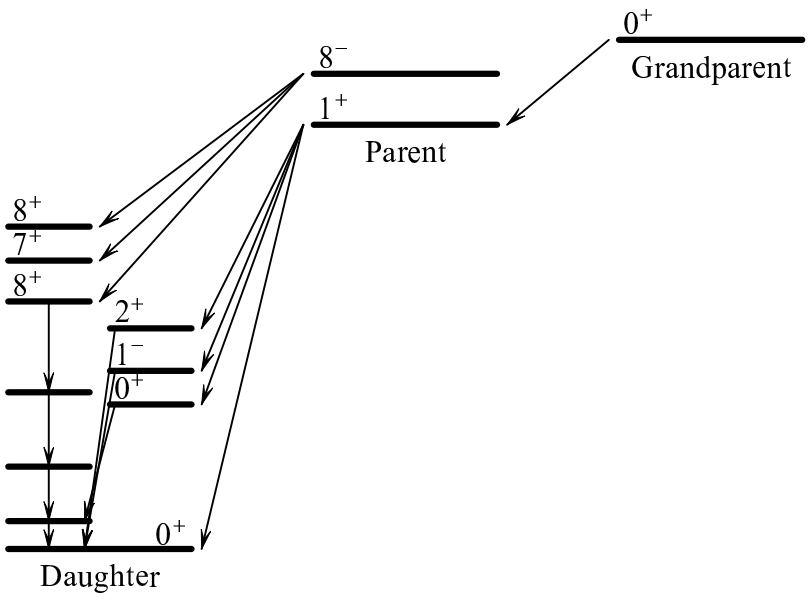

Figure 3.2: Population of an even-even daughter by two-step β decay to avoid β decay from a high-spin isomer in the odd-A parent.

the Coulomb barrier. Of a total $\sim$990 mb cross section for fusion in this reaction, $\sim$74% results in ^{156}Er production, with the neighboring $3n$ and $5n$ channels accounting for most ($\sim$3/4) of the remaining cross section [56, 57].

Beta decay following fusion-evaporation is only effective at populating low-spin, non-yrast states if the parent nucleus, which is created at high-spin, γ-decays to low spin before β-decaying. This is not guaranteed to occur, since the study of even-even daughter nuclei requires the use of odd-odd parent nuclei. These nuclei commonly posess yrast high-spin isomeric states ("yrast traps"), which are strongly populated in fusion-evaporation, and γ decay from these states is often so suppressed that their preferred decay mode is β decay. Alternatively, odd-odd nuclei may have a high-spin ground state strongly populated in fusion-evaporation, with low-spin β-decaying isomers. In either case, the β-decaying parent nucleus state populated in fusion-evaporation has a higher spin than desired. A means of circumventing such difficulties is to use fusion-evaporation to produce the β-decay *grandparent* of the nucleus of interest, which, as an even-even nucleus, will γ decay to its ground state before β decaying. It will therefore predominantly populate the low-spin β-decaying states in the odd-odd parent, be they the ground state or isomeric, and therefore lead to the population of the states of interest in the daughter. The differing population patterns for one-step and two-step β decay are compared in Fig. 3.2.

The Yale Moving Tape Collector (MTC) [58], at the Wright Nuclear Structure Laboratory, is a dedicated setup for the study of β-decay daughters of nuclei produced using beam from the Yale ESTU accelerator. Reaction product nuclei are collected on a tape and transported to a detector area, where their daughter nuclei can be studied using an array of γ-ray and β-particle detectors. A photograph and schematic diagram of the Yale MTC are shown in Fig. 3.3.

The β-decay parent nuclei are produced in a target and recoil out from the downstream side of the target. It is necessary to separate these product nuclei from unreacted beam nuclei which have passed through the target, since direct beam rapidly vaporizes the tape material at the $\sim$1–100 nA beam currents used. The beam spot at the target location is focused to $\lesssim$1 mm diameter by a quadrupole magnet upstream of the target chamber and also passes through 3 mm diameter collimation apertures before reaching the target. The unreacted primary beam nuclei pass largely undeflected through the target and are stopped by a 3 mm diameter gold plug [Fig. 3.4(a)]. In contrast, the fusion-evaporation product nuclei are emitted from the target with an angular distribution spanning several degrees [Fig. 3.4(b)], largely bypass the plug, and are embedded into a 16 mm wide Kapton tape 1.5 cm further downstream. The target-plug separation, typically $\sim$4–8 cm, is chosen on the basis of the angular distribution for each specific reaction: it must be sufficient to allow the nuclei to bypass the plug, but small enough that significant numbers of nuclei do not completely bypass the tape.

The tape transports the collected activity $\sim$3 m to a shielded detector area at regular intervals, chosen according to the parent nucleus half-lives (Appendix F). The time required for the tape to be advanced the necessary few meters, starting from rest, is $\lesssim$1 s. The tape is a continuous loop of 16 mm Kapton motion picture film leader, of $\sim$50 m total length, which after advancing from the target to the detector area continues on to a storage box, where it passes back and forth among a series of rollers. It is strung on plain unsprocketed rollers and driven by a single sprocketed wheel on a stepper motor with adjustable acceleration.

The Yale MTC is equipped with a flexible detector array for γ-γ and β-γ coincidence spectroscopy. Its usual configuration consists of three Compton-suppressed YRAST Ball clover segmented HPGe detectors [60, 61] and one low-energy photon spectrometer (LEPS) planar Ge detector on an angular correlation table. The clover detectors, which are large-volume composite high-purity germanium detectors, provide high-efficiency γ-

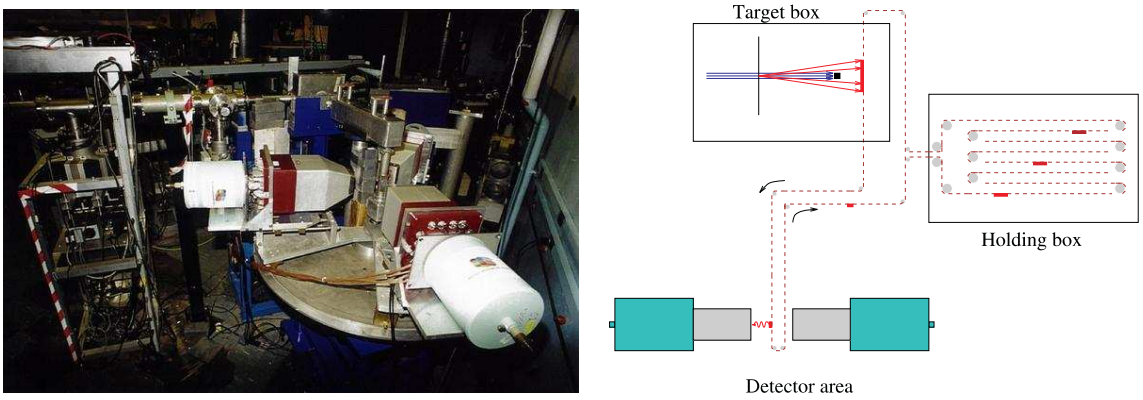

Figure 3.3: Photograph and schematic diagram of the Yale Moving Tape Collector with an array of clover detectors. (Figure from Ref. [59].)

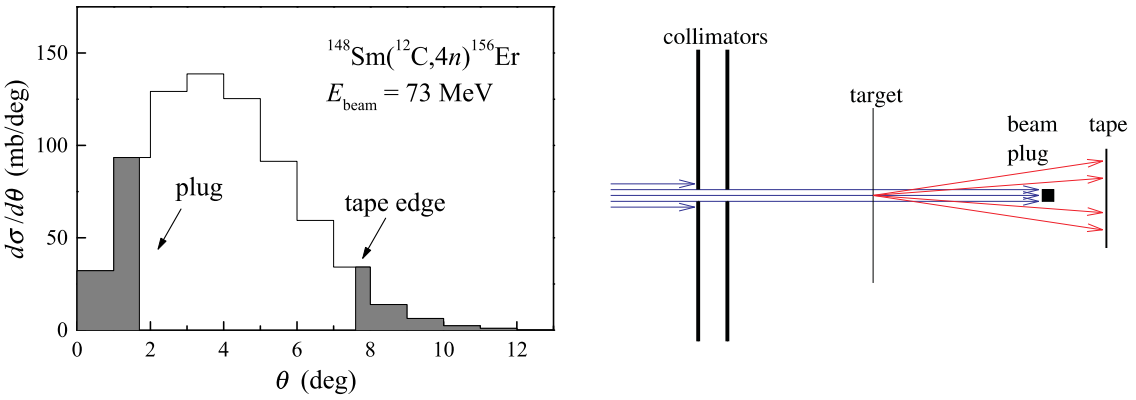

Figure 3.4: Kinematic separation of beam and product nuclei in the Yale MTC: calculated [57] angular distribution of ^{156}Er evaporation residue nuclei from ^{148}Sm(^{12}C,4n)^{156}Er at 73 MeV beam energy (left) and the target chamber configuration (right).

ray detection at energies above ∼50 keV, giving an array efficiency of ∼1.1% at 1.3 MeV. They may be used as Compton polarimeters (Section 4.2) as well. The clover detectors are placed inside bismuth germanate (BGO) Compton suppression detectors, with heavy-metal front collimators, to allow the identification and rejection of clover detector hits in which the incident γ ray is Compton scattered, leaving only a portion of its energy in the clover.

Auxiliary detectors are regularly used with the array to extend its capabilities. Variations upon the standard configuration have included:

1. Three Compton-suppressed clover detectors and a LEPS detector, in combination with a thin plastic scintillation detector and BaF_2 scintillation detector, for sub-nanosecond lifetime measurements by electronic timing (described in Section 4.3).

2. Three Compton-suppressed clover detectors and a LEPS detector, in combination with a thick plastic scintillation detector, for γ-ray gated β energy endpoint measurements [62, 63].

3. Four unshielded clover detectors, for γ-γ angular correlations between individual clover elements and γ-γ Compton polarimetry [64].

4. Four unshielded clover detectors and a thin plastic scintillation detector, for β-γ Compton polarimetry [65].

Electronic pulse processing and data acquisition for the Yale MTC are accomplished using the YRAST Ball electronics suite [61]. The acquisition hardware and sorting software are described in Appendix G.

3.3 Beta decay at an ISOL facility: The ISAC GPS

In an isotope separation on-line (ISOL) ion source, fission or spallation is induced by a proton or light ion beam in a thick production target. Reaction products, including unstable species, escape the target and are ionized, electrostatically extracted as a low energy (tens of keV) beam, and electromagnetically mass separated. Although ISOL radioactive ion sources have existed for several decades [66], a new, much more powerful, generation of facilities is currently beginning operation (*e.g.*, Refs. [46, 67, 68]) with the central purpose of providing high-energy "postaccelerated" beams of unstable nuclei. The

availability of high-purity, high-intensity β-decay activities from these new ISOL radioactive beam production sources promises to provide a major improvement in the quality of γ-ray spectroscopy data on collective excitations, allowing greatly improved measurements on nuclei near stability and making nuclei far from stability accessible to spectroscopy for the first time.

The experiment described in Chapter 11 was one of the first experiments to be performed at the recently commissioned TRIUMF Isotope Separator and Accelerator (ISAC) facility [46], a new-generation ISOL facility. The experiment made use of an existing tape transport system at the General Purpose Station (GPS) [69, 70]. After production in the ISAC surface ion source [71], spallation products are mass separated by the ISAC separator and transported to the GPS at extraction energy, 29 keV for the experiment in Chapter 11.

A photograph and schematic diagram of the GPS are shown in Fig. 3.5. The beam line terminates in a vacuum chamber, in which the beam nuclei are embedded into a 25 mm wide aluminized Mylar tape. Diagnostic scintillation detectors (plastic for β detection and/or NaI for γ detection) at the deposition point are used to monitor the accumulated activity, providing feedback for control of the beam intensity. The tape exits the chamber through 100 μm differentially-pumped slits and transports the activity in air to a detector area. The GPS transport system is based upon a single-pass reel-to-reel tape design and is optimized for high-speed operation with tape cycles of $\lesssim$0.25 s. The tape reels are pneumatically actuated, controlled directly by the acquisition computer, and the tape is fed over air-cushion bearings — curved metal surfaces perforated with numerous holes through which pressurized air is bled [69] — instead of conventional rollers.

The detector configuration used for the γ-γ coincidence spectroscopy experiment of Chapter 11 consisted of two large-volume coaxial Ge detectors of 80% relative efficiency located 12 cm from the source position. The detectors were oriented obliquely with respect to each other and separated by lead shielding, in order to suppress unwanted coincidence events due to β^+ annihilation photon pairs and Compton cross-scattering. The combined photopeak efficiency was 0.8% at 1.3 MeV. A pair of thin plastic scintillation detectors surrounding the tape at the source location provided tagging of decays involving β particle emission.

Detector energy and timing information at the GPS are recorded in event mode using a CAMAC-based acquisition system read out by an Intel/Linux front end computer

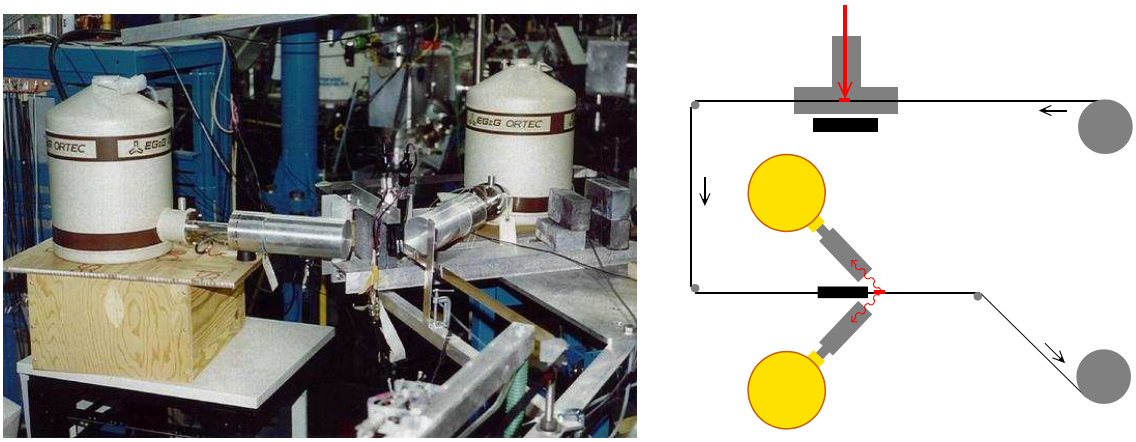

Figure 3.5: Photograph and schematic diagram of the ISAC GPS in its γ-γ spectroscopy configuration.

running PSI/TRIUMF MIDAS [72]. Deposition rates and other diagnostic data are obtained using a CAMAC scaler module, also included in the data stream. The MIDAS system supports unlimited concurrent operations to be performed on the data stream, interchangeably running on the front end or remote networked machines, including data logging to primary and backup storage media, graphical monitoring of experiment rates (*e.g.*, to assist ISAC operations staff in controlling deposition rates), and online sorting.

Experimental β-decay work at an ISOL radioactive beam presents special challenges. A summary of some main considerations follows.

Beam steering and measurement diagnostics can be of limited use or nonexistent, since beam currents of $\lesssim 10^7$ particles/s are too low for conventional current-based devices (Faraday cups, slit boxes, wire scanners, harp monitors) and optical phosphors to be useful, and these devices may also be omitted to prevent the accumulation of contamination. For this reason, the deposition monitoring detectors at the GPS were crucial for controlling beam intensities. However, much more sophisticated radioactive beam diagnostic detectors are currently in use or under development (*e.g.*, Ref. [73]).

ISOL beam purity can vary greatly with nuclide and with production source details. ISOL sources can provide beams of exceptional purity if only one member of the nuclear mass chain selected by the separator escapes easily from the ISOL target or, ideally, if mass separation of the isobars *within* a mass chain is accomplished, as is possible with a sufficiently high-resolution mass separator. In general, however, a beam containing multiple radionuclides ("cocktail" beam) must be expected. Contaminant nuclei with

half lives differing by at least an order of magnitude from that of the parent nucleus of interest do not usually present difficulties, since use of the proper tape advance cycle (Appendix F) strongly suppresses their decay in the detector area relative to the decay of interest. When the contaminant nuclei decay primarily by electron capture and the parent nucleus of interest decays by β^+ or β^- decay, or vice versa, β particle tagging may be useful as a coincidence requirement or veto, respectively. The GPS setup incorporated and tested this capability, but the extremely high beam purity encountered in the actual experiment (Chapter 11) rendered it unnecessary.

Making full use of the intense $\sim 10^{10}$ Bq β-decay activities which can be obtained for copiously-produced species of nuclei near stability presents a challenge to the instrumentation, in the form of an "embarassment of riches". The experiment at the GPS was essentially detector-limited in nature, due to the constraint of maintaining acceptable count rates in individual detectors ($\lesssim$20 kHz): the maximum beam deposition rate which could be accomodated was $\sim 10^5$/s, although a beam intensity of $\sim 10^9$/s was available from the ISAC separator. Arrays with high granularity are less subject to limitation by single detector count rates and thus can benefit more fully from the large beam intensities available. Specifically, coincidence spectroscopy experiments (Section 4.1) require high-statistics two-fold γ-ray coincidence data. For an array of total efficiency ε divided among n similar array elements, these data are collected with a rate $\propto A\varepsilon^2(n-1)/n$, where A is the source activity. The γ absorption rate in an individual array element is $\propto A\varepsilon/n$. If the maximum acceptable count rate for a single element is $R_{\max}$, then the corresponding maximum coincidence data collection rate is $\propto R_{\max} n\varepsilon$, suppressing the $(n-1)/n$ factor relevant only at small n. Improved data collection can be obtained by increasing any of the factors: single-element rate capability, array granularity, or overall efficiency. For this reason, much improved coincidence sensitivity should be obtained as large, Compton-suppressed, multi-detector arrays, such as the Clarion array [74] at ORNL HRIBF or the Miniball array [75] at CERN REX-ISOLDE, are implemented for decay studies at ISOL ion sources.

Chapter 4

Gamma-ray spectroscopy with modern high-efficiency arrays

4.1 Coincidence spectroscopy for transition intensities

Gamma-ray spectroscopy, through the identification of γ-ray transitions and measurement of their intensities, plays a central role in obtaining experimental information necessary for understanding nuclear structure, as described in Chapter 2. One broadly-stated goal in the spectroscopic study of a nucleus is to understand the placement of the observed γ ray lines, in the process establishing the level scheme of the nucleus. Another is to deduce the relative strengths of all transitions depopulating each level of interest, since these relative intensities allow either ratios of $B(\sigma\lambda)$ strengths or, if the level lifetime is known, absolute $B(\sigma\lambda)$ strengths to be determined.

Although usually only the relative intensities of transitions sharing the same parent level are needed for model analysis, it is often more practical to measure the intensities of transitions from all levels populated in the nucleus on a common scale — in β decay, this is the probability of the transition occuring per unit parent nucleus decay. The measurement techniques, with one exception described below, yield separate intensities for each transition individually on this common scale; the relative intensities for the transitions from a given level are only subsequently deduced by comparison of these. Intensities expressed on such a common scale can directly be compared across all experiments which use the exact same mechanism to populate the nucleus. Thus, points of agreement or contradiction between different sets of results can be identified, and results from separate experiments can be assembled into a more comprehensive composite set of information — for instance, a conversion electron intensity from one experiment can be combined with a γ-ray intensity from another to extract a conversion coefficient.

Spectroscopic measurements are indirect measurements of a physical system via an instrument. The physical system being analyzed is an ensemble of nuclei which have

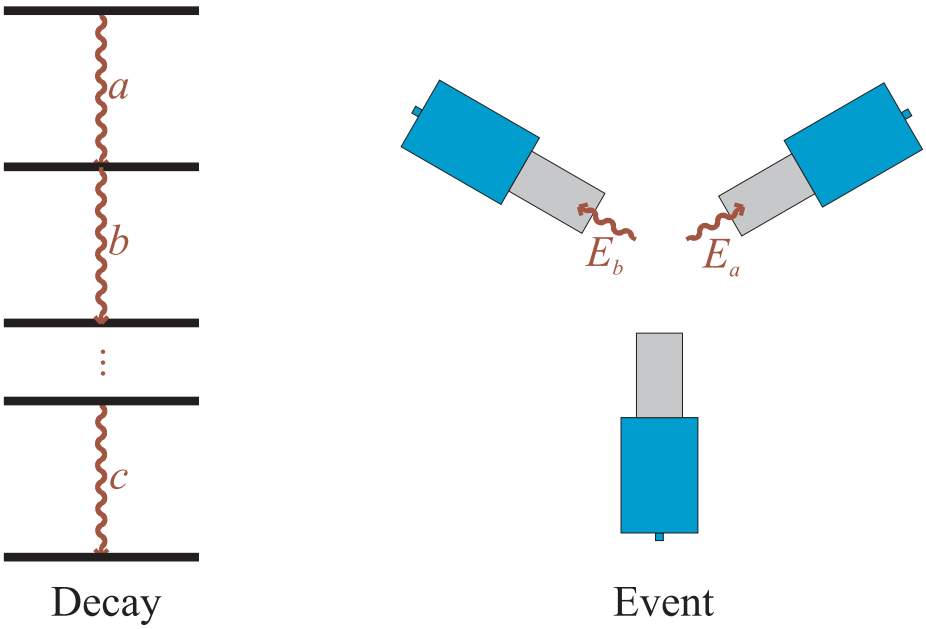

Figure 4.1: Schematic illustration of a nuclear decay (the physical process) and the corresponding event (the observed data).

been populated in various excited states and which then deexcite by emission of a series of radiations. The decay process for each of these individual nuclei may, or may not, result in an observed "event", that is, detection of one or more of the emitted radiations in an array of detectors, as illustrated in Fig. 4.1. The experimental challenge is to understand the instrument response, which maps decays to events, and then, given a set of data, invert this process to extract the properties of the underlying ensemble of decays. Given the rich nature of the data collected, involving simultaneous detection of multiple radiations from the same decay (coincidences), there are often several possible complementary ways of extracting the same piece of information, each of which may be more or less effective according to the circumstances. The following discussion summarizes some basic techniques as applied in pure γ-ray spectroscopy following β decay, but the approaches presented are more generally applicable to a wide range of spectroscopy experiments with multidetector arrays and reasonably low detection multiplicity. Some more technical issues are deferred to Appendix H.

Singles measurements, based upon analysis of a simple aggregate energy spectrum of all γ rays detected, in principle directly provide both energies and intensities for all transitions. However, measurements of intensities from singles data are notoriously prone to error due to the presence of unresolved contaminant transitions. Beta-decay ex-

periments with Q_β values of a few MeV commonly produce several hundred identifiable γ-ray transitions, many of them yielding overlapping or unresolved peaks in the singles spectra. For instance, in ^{162}Er (Chapter 11), five of the ten most strongly populated transitions in β-decay are doublets [27, 76]. Construction of a level scheme from a singles spectrum in such a decay experiment is extremely challenging, since it relies upon the recognition of groups of γ-ray lines with energies which sum to yield the same excited level energy, yet a virtual continuum energies of partially resolved γ-ray lines is observed in the spectrum [see Fig. 7.1 on page 66 and Fig. 11.1 on page 95 for examples]. Historically, decay experiments have relied heavily or exclusively upon singles data. Singles analysis is "efficient", in that it makes use of all detected γ rays, so for experiments performed using only one or a few low-efficiency detectors, or when only a small activity can be obtained, singles measurements may be the only type possible. A preponderance of the studies contributing to the present corpus of decay data in medium-mass and heavy nuclei were carried out several decades ago when only small-volume Ge detectors were available.

The advent of compact, high-efficiency arrays of large-volume Ge detectors has permitted a new generation of γ-ray spectroscopy β-decay experiments which produce high-statistics coincidence data. These data provide much more reliable information on placement of transitions in the decay scheme and allow γ-ray transition intensities to be determined from relatively clean gated spectra. An example gated coincidence spectrum in Fig. 4.2 illustrates how the transitions observed coincident with a γ ray of interest are related to the placement of the transition in the level scheme, showing how the gating transition is coincident both with transitions feeding the initial level and depopulating the final level.

When the transition x of interest directly feeds a level which decays by a γ radiation b for which the intensity branching fraction B_b is known, then the intensity I_x per parent decay can be determined from

$$G_{b:x} = N I_x B_b \varepsilon(E_b, E_x) \tag{4.1}$$

where $G_{b:x}$ is the number of detected coincidences between b and x from a gated spectrum, N is the number of parent decays, and $\varepsilon(E_b, E_x)$ is the coincidence efficiency (Section H.2). The branching fraction B_b is calculated from known intensities as $B_b = I_b/(\sum_i I_i + \sum_i I_i^{\rm ce})$, where the sums are over all γ-ray and conversion electron transitions depopulating the level.

The *relative* intensities of two branches x and y from a level can also be obtained

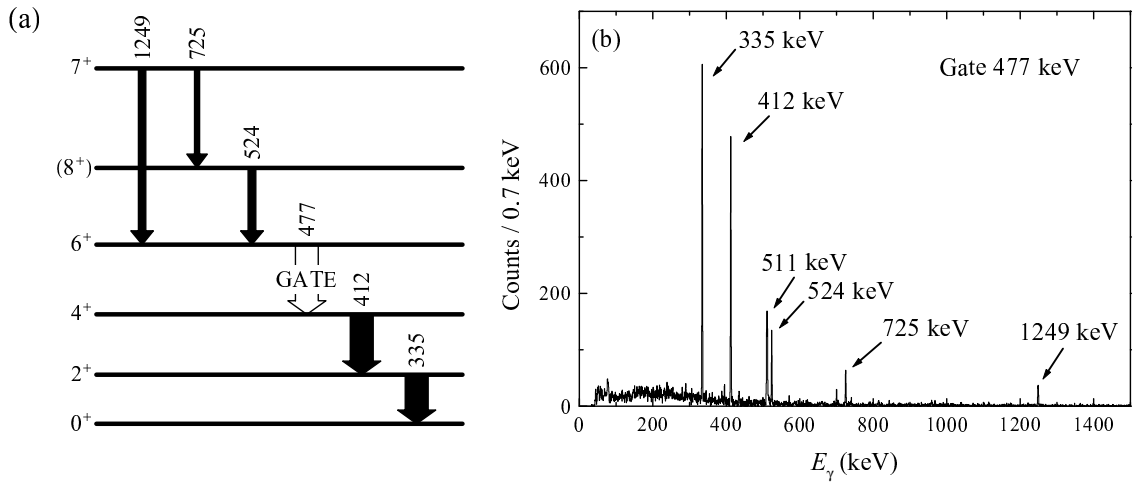

Figure 4.2: Placement information contained in a gated spectrum: (a) level scheme showing transitions feeding or following the gate transition and (b) a gated spectrum showing transitions coincident with this transition. Arrow thicknesses in part (a) are proportional to the expected intensity coincident with the 477 keV transition (Appendix H). The example gate is on the 477 keV transition in ^{154}Dy, populated in ^{154}Ho β^+/ε decay (Chapter 9).

from a spectrum gated on a transition a feeding the level, according to

$$\frac{G_{a:x}}{G_{a:y}} = \frac{I_x \varepsilon(E_a, E_x)}{I_y \varepsilon(E_a, E_y)}. \tag{4.2}$$

Intensities can only be measured in this way if there exist one or more strong discrete feeding transitions to the level, and this method therefore tends to be useful only for levels low in the excitation spectrum. This method in most cases provides lower statistics than can be obtained by gating below the transition of interest — the intensity flow below the transition of interest is typically concentrated in one or two strong branches, but the intensity flow feeding the transition of interest is usually diluted among several weak transitions or may come from direct β feeding. A gate on a feeding transition can only provide intensities *relative* to other branches from the same level.

The relative quality of these different sources of intensity information is illustrated in Fig. 4.3, which shows the data used in the measurement of the intensities of the 617 keV and 884 keV branches from the 3^+ level at 1022 keV in ^{156}Dy (Chapter 7).

All intensity measurements rely upon an accurate knowledge of the array efficiency. Calibration of the singles and coincidence efficiency of an array of detectors is discussed in Section H.2.

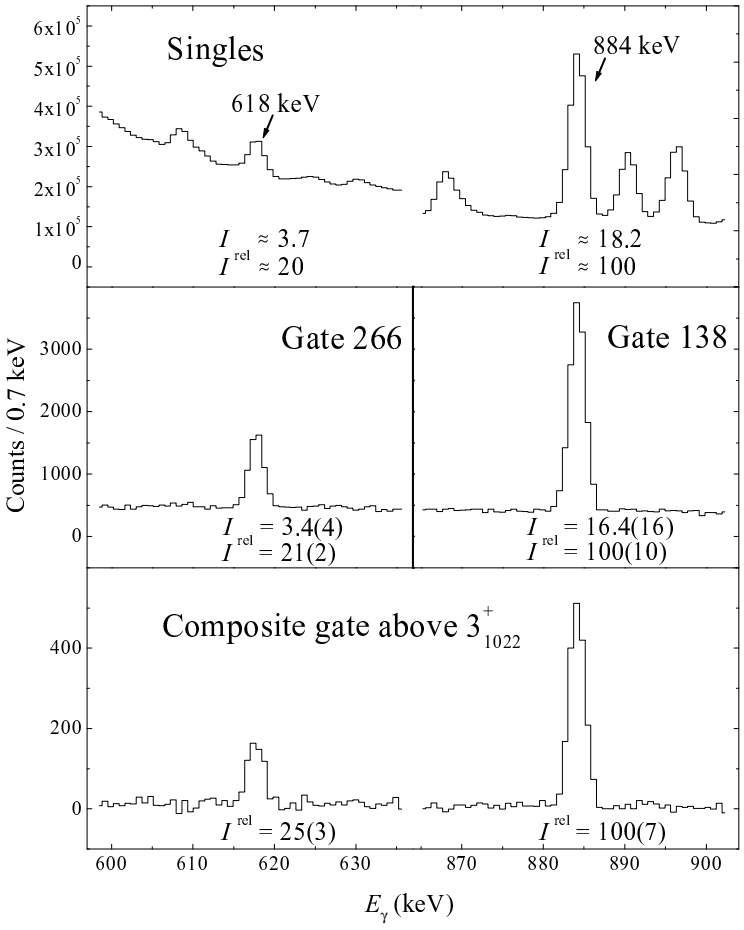

Figure 4.3: Comparison of the different sources of intensity information for the 618 keV and 884 keV branches from the 3^+ level at 1022 keV in ^{156}Dy. The spectra are (top) from singles, (middle) gated below the branch of interest, or (bottom) gated on transitions feeding the 3^+ level. The composite spectrum on the bottom is gated on 655, 819, 1081, 1301, 1310, and 1386 keV transitions. (Figure from Ref. [77].)

4.2 Angular correlation and polarization measurements

4.2.1 Theoretical summary

The angular correlation patterns and polarization properties of radiation emitted by a nucleus are directly related to the spins of the states in the emitting nucleus and to the multipolarities of the emitted radiations (*e.g.*, Refs. [78–80]). Observation of these properties provides information on spin/parity assignments of states as well as on the relative contributions of different multipole matrix elements to the observed transition intensities.

In the β-decay spectroscopy experiments considered here, the sources are unoriented, *i.e.*, posess no preferred direction in space. More precisely, when the β-decay parent nuclei are produced in fusion-evaporation or spallation (Sections 3.2 and 3.3), they are actually created with a preferred direction, namely the beam axis, and posess an anisotropic angular momentum distribution [47], but this orientation is lost well before β decay occurs, on a time scale typically of hundreds of ns [80]. Consequently, all radiations from the β decay are emitted with isotropic angular and polarization *distributions*. However, angular or polarization *correlations* between pairs of emitted radiations are in general anisotropic. In β-decay experiments, either γ-γ correlations or β-γ correlations may be measured.

The basic angular correlation relations are well known [78, 80], so only a brief summary is provided here. For two radiations emitted in cascade, the probability per unit solid angle of emission of radiation 1 in direction Ω_1 and radiation 2 in direction Ω_2 can depend, by isotropy of the source, only upon the relative angle θ between these two directions. The probability distribution can thus be entirely described by an angular correlation function $W(\theta)$ on the interval [0°,180°]. It is convenient to decompose this function as a Legendre series

$$W(\theta) = \sum_{\nu} A_\nu P_\nu(\cos\theta). \tag{4.3}$$

The coefficents A_ν may be expressed in a simple fashion in terms of Clebsch-Gordon and Racah coefficients involving the spins of the nuclear states and the multipolarities of the radiations, and they can be calculated for quite general pairs of radiations (β, γ, conversion electron, ...). For any particular set of spins and multipolarities, the series terminates after only a few terms. Only even-order terms have nonvanishing coefficients (this follows from parity being a good quantum number for the states involved [78]), so the angular distribution is symmetric about θ=90°. Angular correlation patterns for some commonly

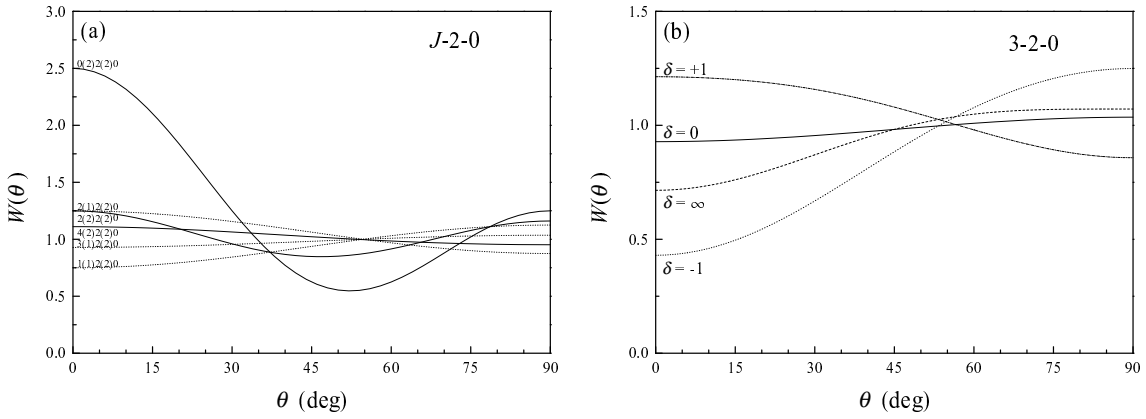

Figure 4.4: Angular correlation patterns for some common γ-ray cascades among low-spin states: (a) Cascades involving transitions of pure dipole or quadrupole multipolarity among levels with spins J-2-0. Curves are designated $J_1(L_1)J(L_2)J_2$. (b) Cascades involving levels of spins 3-2-0, for various $\delta_{E2/M1}$ mixing ratios in the $3 \rightarrow 2$ transition.

encountered spin and multipolarity combinations are shown in Fig. 4.4. Calculation of the correlation functions is discussed in Appendix D.

The angular correlation formalism can account for arbitrary mixtures of contributing radiation multipolarities. As discussed in Chapter 2, γ radiation often consists of an $M\lambda$ and $E(\lambda+1)$ admixture, in which case interference between the two multipoles occurs. The correlation pattern then depends strongly upon the mixing ratio δ [Fig. 4.4(b)].

The distribution of a γ radiation may be considered as a function of γ-ray linear polarization [79] in addition to the direction of emission. For two radiations emitted in a cascade, where one (at least) is a γ ray, the probability of emission of this γ ray with polarization angle γ relative to the plane containing the emission directions of two radiations (Fig. 4.5) is

$$W(\theta,\gamma) = \left[\sum_{\nu} A_\nu P_\nu(\cos\theta)\right] + \left[\sum_{\nu} \mathcal{A}_\nu P_\nu^{(2)}(\cos\theta)\right]\cos 2\gamma, \tag{4.4}$$

where the $\mathcal{A}_\nu$ are again simple functions of the spins and multipolarities involved (Appendix D). By axial symmetry, polarization effects vanish for back-to-back radiations (θ=180°). Polarization effects dominated by the dipole term $[P_2^{(2)}(\cos\theta) = 3\sin^2\theta]$ are most pronounced at an angle of 90° between the emitted radiations. All polarization information is contained in a decomposition of the polarization along the two directions γ=0°

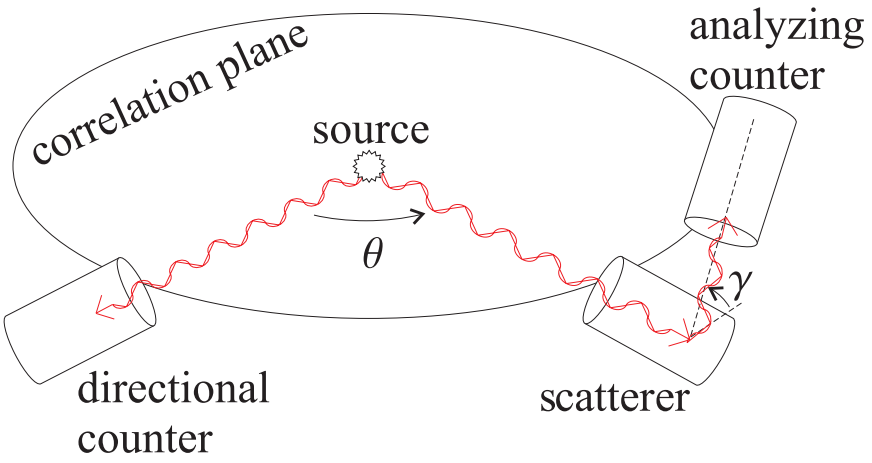

Figure 4.5: Geometry for direction-polarization correlation measurements. The basic experimental components are a directional counter and a Compton polarization analyzer, consisting of a paired scatterer and counter.

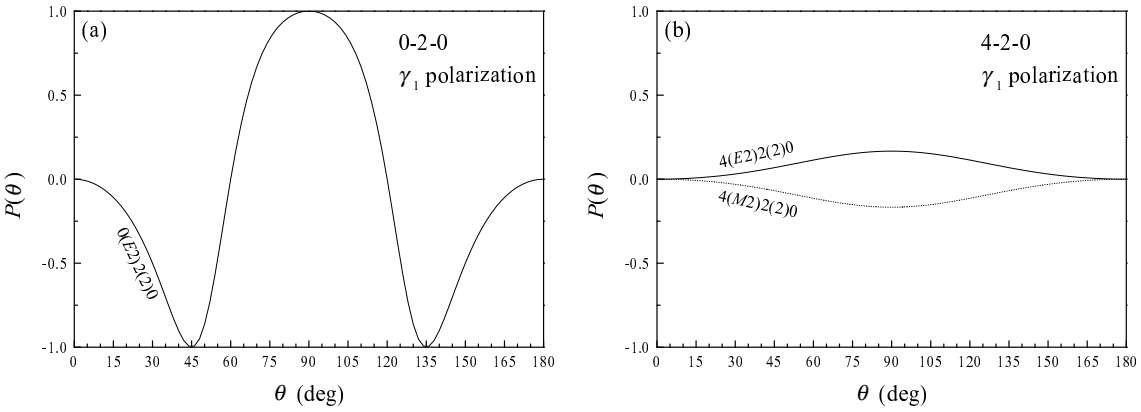

Figure 4.6: Direction-polarization correlation patterns for (a) $0 \xrightarrow[\text{POL}]{E2} 2 \xrightarrow{2} 0$ and (b) $4 \xrightarrow[\text{POL}]{E2 \text{ or } M2} 2 \xrightarrow{2} 0$ cascades, illustrating the complete polarization found in 0–2–0 cascades (useful for identification of 0^+ states) and the overall sign reversal of the polarization depending upon the magnetic or electric nature of the measured radiation (useful for parity determinations when the angular momenta are already known).

and 90°, conventionally summarized by the polarization distribution function

$$P(\theta) = \frac{W(\theta, 0^\circ) - W(\theta, 90^\circ)}{W(\theta, 0^\circ) + W(\theta, 90^\circ)}. \tag{4.5}$$

The polarization functions for some representative spin and multipolarity combinations are shown in Figs. 4.6 and 4.7.

Polarization measurements provide several forms of useful information. The de-

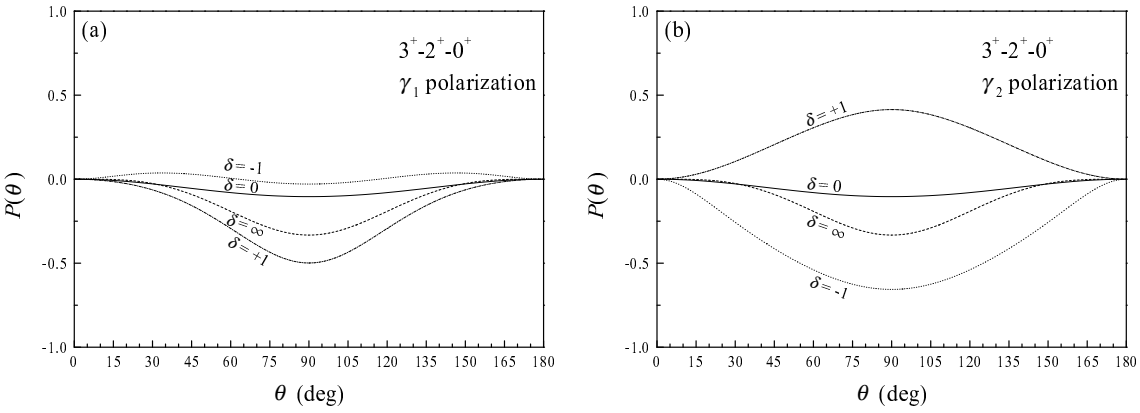

Figure 4.7: Direction-polarization correlation patterns for mixed (a) $3^+ \xrightarrow[\text{POL}]{M1,E2} 2^+ \xrightarrow{E2} 0^+$ and (b) $3^+ \xrightarrow{M1,E2} 2^+ \xrightarrow[\text{POL}]{E2} 0^+$ cascades, illustrating how measurement of the polarization for either transition in the cascade can provide information on the mixing ratio δ of the first transition.

gree of polarization in the spin 0–2–0 quadrupole cascade is very high [Fig. 4.6(a)], reaching complete polarization at the angles of 45°, 90°, and 135° so polarization measurements can aid in the identification of 0^+ states. Unlike the angular correlation function $W(\theta)$, which depends only upon angular momenta, the polarization correlation function $W(\theta, \gamma)$ is highly sensitive to the electric or magnetic nature of the γ radiation. The polarization distribution function for a γ radiation flips sign depending upon whether the radiation is electric or magnetic in character [see (D.3)–(D.5)], as shown in Fig. 4.6(b). Consequently, if all spins and multipolarities are known, polarization measurements can be used to determine the parity of the radiation and thus to obtain level parity assignments [81, 82]. For mixed multipolarity γ radiation, the polarization depends upon the mixing ratio δ (Fig. 4.7). Polarization measurements can be used to resolve ambiguities in measurements of δ from angular correlations.

4.2.2 Experimental considerations

Classic angular correlation measurements [80] commonly determined the function $W(\theta)$ by counting coincidences between a fixed detector and a moveable detector for each of several values of the relative angle θ. This approach has the benefit of simplicity, since, with careful experiment design, detector efficiencies remain constant between measurements at different θ values. Modern angular correlation measurements, in contrast, make use of high-efficiency multidetector arrays. With such arrays, all detectors are held stationary,

and coincidences at multiple relative angles are measured simultaneously. This approach greatly improves the available statistics but introduces some complexities to the data analysis.

For two detectors i and j at relative angle $\theta_{i:j}$, with radiation a detected in one and radiation b detected in the other, the number of coincident counts detected is

$$G_{a:b}^{i:j} = N I_{a:b} W_{a:b}(\theta_{i:j}) \varepsilon^{i:j}(E_a, E_b), \tag{4.6}$$

where N is the number of parent decays, $I_{a:b}$ is the number of coincident radiations a and b emitted per parent decay, and $\varepsilon^{i:j}$ is the detector pair efficiency. In principle, $W_{a:b}(\theta)$ can be extracted from this coincidence measurement directly, since the activity and coincident intensity are known from the spectroscopy experiment (Section 4.1) and the detector efficiency is calibrated.

In practice, however, uncertainties in the intensity and efficiency can be large compared to the necessary accuracy of the $W_{a:b}(\theta)$ measurement. For example, small deviations of the calibration source position from the experimental source position, which have negligible effect on the overall array efficiency calibration, can significantly disrupt the angular correlation pair efficiency. This method also contains no internal check against drift in efficiency. It is therefore useful to have a measurement technique in which as many parameters as possible cancel or are internally calibrated. Several approaches exist for situations in which only coincidence data are available [64, 83]. However, if singles data are taken from all detectors simultaneously with the coincidence data, an especially simple approach is possible, provided that the coincidence efficiency for the two detectors factorizes as $\varepsilon^{i:j}(E_a, E_b) = \varepsilon^i(E_a)\varepsilon^j(E_b)$ (Section H.2). When *ratios* of coincidence counts for radiations a and b in different detector pairs are used to obtain *ratios* of $W_{a:b}(\theta)$ values, the singles counts in the individual detectors [$S_a^i = N\varepsilon^i(E_a)I_a$] provide an internal calibration of the detector efficiencies, and all efficiencies required in (4.6) cancel:

$$\frac{G_{a:b}^{i:j}}{G_{a:b}^{k:l}} = \frac{W_{a:b}(\theta_{i:j}) S_a^i S_b^j}{W_{a:b}(\theta_{k:l}) S_a^k S_b^l}. \tag{4.7}$$

The internal consistency of this method can be checked by comparing values obtained for different detector pairs at the same angles, including comparison of the "reverse" gates in the same detector pair [$W_{a:b}(\theta_{i:j}) = W_{a:b}(\theta_{j:i})$].

With an array of clover detectors, as at the Yale Moving Tape Collector, two approaches may be taken for angular correlation measurements. Each clover may be treated

as four independent coaxial detectors within a common cryostat (as in Ref. [64]), and angular correlation measurements are in this case carried out simultaneously for all pairs of clover elements in the array, excluding pairs within the same detector since these are subject to excessive Compton cross scatter. An array of three clover detectors arranged in a plane at equal distances from the source provides 48 correlation pairs at 18 distinct angles, once symmetries of the element positions within the clovers are taken into account. Alternatively, each clover as a whole may be treated as a single detector (as in the experiment of Chapter 11), in which case an array of three clover detectors provides only three correlation pairs. This approach is sufficient if the goal of the experiment is simply to distinguish spin 0–2–0 quadrupole cascades from other cascades, due to the highly pronounced 0–2–0 correlation pattern (Fig. 4.4). For this purpose, it is preferable to have one clover pair positioned at a relative angle of $\sim 180^\circ$, equivalent to the first-quadrant angle of 0° in Fig. 4.4, since this is the location of the maximum of $W(\theta)$ for a 0–2–0 cascade. The remaining clover can then be inserted between these at an angle of approximately 52° relative to one of the first two clovers, the location of the minimum of $W(\theta)$, and the remaining angle is then automatically the supplementary angle 128°, also equivalent to 52°. However, this configuration is not optimal for spectroscopy, since two clovers diametrically opposite each other are susceptible to unwanted coincidence events due to β^+ annihilation photon pairs and Compton cross-scattering.

The effects of finite detector opening angle and source size must be considered in angular correlation experiments. The measured angular correlation $W^{\mathrm{expt}}(\theta)$ is the result of the convolution of the true angular correlation with the extended angular acceptances of the detectors. A single clover element spans $\sim 25^\circ$ at a distance of 10 cm from the source; the additional spread due to the $\lesssim 1$ cm source size contributes negligibly. For a pair of cylindrically symmetric detectors, the addition theorem for spherical harmonics dictates that the convolution results simply in a term-by-term multiplicative correction [84]

$$W^{\mathrm{expt}}(\theta) = \sum_{\nu} A_\nu Q_\nu^i Q_\nu^j P_\nu(\cos\theta), \tag{4.8}$$

where the solid angle correction factors Q_ν^i and Q_ν^j for the two detectors are energy dependent and can be calculated by integrations of the detector efficiency over the detector volume [85, 86]. These results are applicable to correlations of individual clover elements, since these are approximately cylindrical, but not to the entire clover used as a detector for angular correlations. The entire clover has a much reduced symmetry — namely symmetry under horizontal and vertical reflection — which is sufficient to guarantee that

the convolution process will not introduce odd-order Legendre polynomials or higher-order terms than those already present [87] but provides little additional simplification. Fortunately, for the 0–2–0 cascade and the optimized detector configuration described above, averaging over even tens of degrees of acceptance still leaves the 0–2–0 cascade clearly distinguishable from the other likely cascades (Fig. 4.4), and sophisticated corrections are unnecessary.

The linear polarization of a γ ray is most easily measured by means of "Compton polarimetry" [79, 80], a method based upon the polarization dependence of the Compton scattering cross section. The Compton scattering probability, given by the Klein-Nishina formula, is dependent upon the angle between the scattering direction and the plane perpendicular to the incident γ-ray polarization vector — it is maximal in this plane and lowest directly out of this plane. A minimal apparatus for Compton polarimetry consists of a scatterer and a pair of analyzing counters to measure the relative probability of scattering in two perpendicular planes.

The clover detector may be used as a Compton polarimeter [60, 88, 89] in which each leaf acts both as a scatterer and as an analyzing counter to measure scattering from the other two adjacent leaves (see Fig. 4.8). In software analysis of the clover hit, the total energy of the incident γ-ray is obtained as the sum of the energies deposited in the two leaves, and the Compton scattering direction is identified as being either in the correlation plane or perpendicular, depending upon which pair of adjacent leaves fired (hits involving scattering between diagonally opposite leaves are discarded). The incident γ rays with out-of-plane polarization preferentially scatter between in-plane pairs of leaves, and vice versa, but both polarizations (parallel or perpendicular) contribute to both types of scattering (parallel or perpendicular). Consequently, the observed numbers of scattered counts depend upon a total of four efficiencies:

$$N_{\parallel} = \varepsilon_{\parallel}(\parallel) I_{\parallel} + \varepsilon_{\parallel}(\perp) I_{\perp}, \tag{4.9}$$

$$N_{\perp} = \varepsilon_{\perp}(\parallel) I_{\parallel} + \varepsilon_{\perp}(\perp) I_{\perp}, \tag{4.10}$$

where $N_{\parallel(\perp)}$ is the number of scatterings between in-plane (out-of-plane) pairs of leaves, $I_{\parallel(\perp)}$ is the in-plane (out-of-plane) polarization component, and $\epsilon_x(y)$ is the efficiency for a photon with polarization y to result in an observed scattering of type x. The efficiencies are energy dependent, due both to the intrinsic energy dependence in the Klein-Nishina formula and to the detector properties. Inverting these relations provides an expression

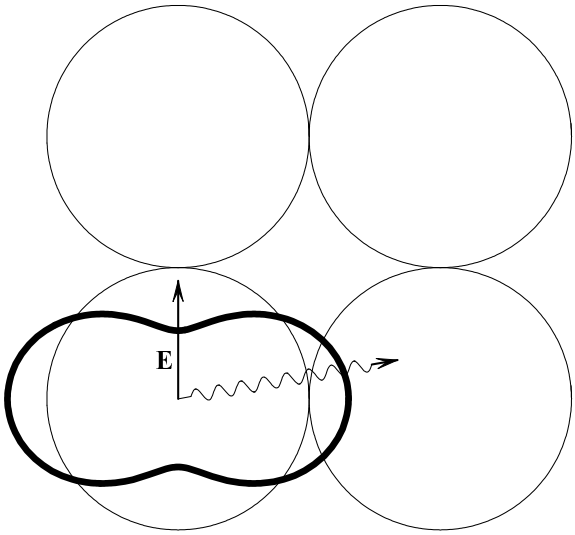

Figure 4.8: The clover detector as a Compton polarimeter, viewed from the source position. Each leaf serves as both a scatterer and an analyzing counter. A representative angular distribution pattern for the scattered photon is indicated, illustrating the preference for scattering perpendicular to the incident photon polarization vector.

for the polarization (4.5) in terms of experimental quantities

$$P = \frac{[\varepsilon_\perp(\perp) + \varepsilon_\perp(\parallel)]N_\parallel - [\varepsilon_\parallel(\perp) + \varepsilon_\parallel(\parallel)]N_\perp}{[\varepsilon_\perp(\perp) - \varepsilon_\perp(\parallel)]N_\parallel - [\varepsilon_\parallel(\perp) - \varepsilon_\parallel(\parallel)]N_\perp}. \tag{4.11}$$

For an ideal clover with four identical leaves, $\varepsilon_\parallel(\perp) = \varepsilon_\perp(\parallel)\,(\equiv \varepsilon_>)$ and $\varepsilon_\parallel(\parallel) = \varepsilon_\perp(\perp)\,(\equiv \varepsilon_<)$, so the polarization is simply extracted as

$$P = \frac{(1 + \varepsilon_</\varepsilon_>)}{(1 - \varepsilon_</\varepsilon_>)}\frac{N_\perp - N_\parallel}{N_\perp + N_\parallel}. \tag{4.12}$$

The reciprocal of the first factor, a measure of the polarimeter's sensitivity, is commonly denoted by Q, and the second factor is referred to as the experimental asymmetry ratio A. Q is energy dependent and may be calibrated using a γ ray of known polarization near the energy of interest or may be calculated in detector simulations [89]. The deviation of a polarimeter from ideal symmetric response is conventionally absorbed into an *ad hoc* instrumental asymmetry correction parameter [90], by which $N_\perp$ must be multiplied in (4.12), so

$$P = \frac{1}{Q}\frac{aN_\perp - N_\parallel}{aN_\perp + N_\parallel}. \tag{4.13}$$

[This procedure is motivated by assuming a specific form for the asymmetry, $\varepsilon_\parallel(\perp) = a\varepsilon_\perp(\parallel)$ and $\varepsilon_\parallel(\parallel) = a\varepsilon_\perp(\perp)$.] The intrumental asymmetry correction is calibrated by

exposing the detector to known unpolarized γ rays, for which A should be vanishing: these may be singles γ rays, γ rays coincident at θ=180°, or γ rays coincident with uncorrelated radiations, such as atomic x rays or annihilation radiation. An experimental example is given in Chapter 6.

4.3 Fast electronic scintillation timing measurements

It is desirable to be able to measure the lifetimes of excited nuclear states, since electromagnetic transition strengths are deduced from these in combination with the γ-ray branching information. For a state populated in some form of decay process, the lifetime may be determined by measuring the time difference between detection of a radiation emitted in the process of population of the level and of a radiation emitted as part of the subsequent decay of that level.

For measurement of short lifetimes, the timing response of the detection system must be optimized in two respects: to minimize statistical fluctuations in the timing response for the detected radiations (timing jitter) and to minimize variation of this response with respect to the energy of the detected radiation (timing walk). To optimize either of these aspects of timing, it is generally necessary that detectors be used which produce as short an output pulse rise time as possible.

The fast electronic scintillation timing (FEST) techniques developed by Mach, Moszyński, Gill and collaborators [91–93] make possible lifetime measurements for levels populated in β decay with lifetimes as short as several ps. These methods are based upon electronic timing of the interval between β-particle emission, detected with a fast plastic scintillation detector, and the subseqent γ-ray decay, detected with a BaF_2 detector. It is also often useful to require a coincidence with an additional γ ray in a Ge detector. A schematic representation of the method is shown in Fig. 4.9. To accomplish the measurement of such short lifetimes, several special techniques are used.

The fast-timing β detection in FEST makes use of the ΔE signal produced by the β particle as it traverses a thin slice of fast plastic scintillation material. The energy dependence of a timing signal results primarily from the pulse-height dependence of the electronic timing discrimination process. The advantage to using the ΔE signal from a thin scintillator is that the ΔE signal is largely independent of incident β-particle energy [94], and thus the timing has minimal dependence upon the β-particle energy. The energy spectrum of emitted β particles is continuous up to an end-point energy, and so use of a

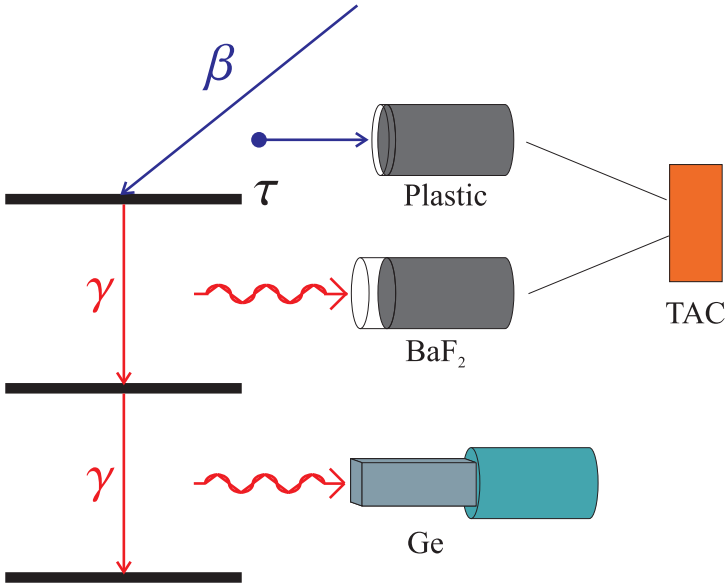

Figure 4.9: Schematic representation of FEST lifetime measurement method. The β radiation is detected in a fast-timing plastic scintillation detector and a γ ray is detected in a fast-timing BaF_2 detector. An additional γ ray detected in a Ge detector may be used when the energy resolution of the BaF_2 detector is insuffient to isolate the γ ray of interest in singles or for special purposes involving cascade selection (*e.g.*, Fig. 9.1). The plastic-BaF_2 relative timing is used for the determination of the level lifetime τ.

β-particle full-energy absorption signal from a thick scintillator would in contrast require timing of signals covering a broad dynamic range. Plastic scintillation materials with rise times as short as hundreds of ps are available [95]. The NE111 scintillators used for many FEST experiments have a measured rise time of 200 ps and decay time of 1.7 ns [96].

For fast timing γ-ray detection, it is preferable to use a high-Z inorganic scintillator to provide appreciable efficiency for full-energy γ detection. The timing performance of inorganic scintillators typically lags that of organic scintillators by orders of magnitude (*e.g.*, Ref. [95]). To acheive the necessary timing performance, FEST relies upon the fast ultraviolet component of scintillation light from BaF_2 [97], which has a decay constant of $\sim$600 ps. BaF_2 provides an energy resolution marginally inferior to that obtained with NaI, due to its lower photon yield.

A coincidence with an additional γ ray detected in a Ge detector can be required as a gating condition. A Ge gating condition is valuable when the energy resolution of the BaF_2 detector is insuffient to isolate the γ ray of interest in singles, as is often the case. Gating may also be used for cascade selection to choose specific γ-ray feeding paths for

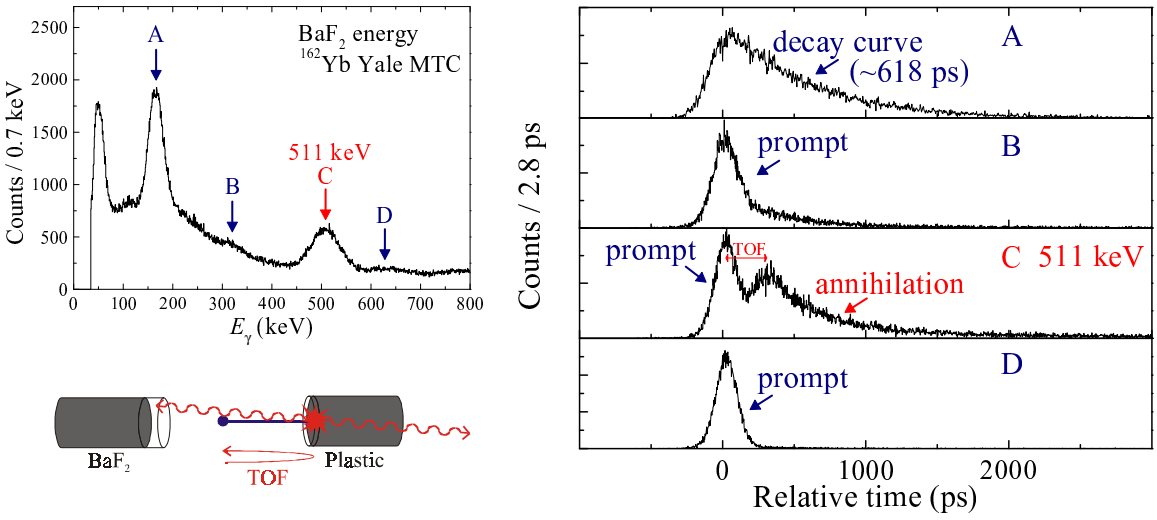

Figure 4.10: Detection of delayed β-coincident annihilation radiation in the BaF_2 detector for FEST experiments in β^+ decay. For gates on each of the BaF_2 energies indicated by lettered arrows (top left), the corresponding BaF_2-plastic TAC spectra are shown (right). The earliest-arriving annihilation radiation is delayed relative to the prompt location by an additional β and γ time of flight (TOF) (bottom left).

the lifetime measurement, as in Chapter 9.

Additional technical innovations can contribute further moderate performance improvements to FEST detector systems. These include the use of specially-shaped truncated conical BaF_2 crystals to control the reflection of scintillation light into the photomultiplier tube [98] and extraction of the timing signal from an early dynode stage of a modified photomultiplier voltage divider chain [99].

The FEST method was orginally designed for use with neutron-rich nuclei provided by reactors or ISOL-type sources, but it has also been successfully applied to the study of proton-rich nuclei [100–102], as in the present measurements at the Yale MTC (Chapters 8, 9, and 11). Challenges associated with measurements of proton-rich nuclei include the presence of delayed coincident background radiation from β^+ annihilation, with a time profile (Fig. 4.10) which extends into the ns range and is strongly dependent upon detector geometry and absorber materials [103], and competition from electron capture, in which no emitted β^+ particle is available for timing [104].

The FEST system implemented at the Yale MTC uses an integrated multidetector array consisting of three Compton-suppressed clover detectors, a LEPS detector, and the plastic and BaF_2 fast timing detectors (Fig. 4.11). This configuration allows $\gamma\gamma$ spectroscopy, angular correlation and polarization, and FEST measurements to be carried out

simultaneously. Fast timing β particle detection is accomplished with a disk of NE111A plastic scintillation material (1.3 cm diameter and 3 mm thick) coupled to a Photonis XP2020 photomultiplier tube and covered only by a 20 μm aluminum foil, to minimize energy loss of β particles entering the detector. Fast timing γ-ray detection is carried out with a BaF_2 crystal in the shape of a conical frustum (1.91 cm forward diameter, 2.54 cm length, and 2.54 cm rear diameter) coupled using Viscasil silicone fluid [105, 106] for transmission of the fast ultraviolet scintillation light to a quartz-windowed Photonis XP2020Q photomultiplier tube. The voltage divider chains for both photomultiplier tubes are modified to provide timing signals from the ninth dynode. The tape carrying the activity passes through the detector area inside a flat aluminum transport duct, designed to allow the FEST detectors to be placed facing each other across the tape with minimal separation (Fig. 4.12). The β particles exit the chamber through a 51 μm polypropylene vacuum window [107].

The fast timing detectors are incorporated into the YRAST Ball electronics suite [61]. Conventional energy and logic/timing signals are acquired as for the Ge detectors. Timing discrimination for the fast-timing detectors is carried out using Tennelec TC454 constant fraction discriminators with minimal (3 cm) external wire delays. The critical plastic-BaF_2 time difference is measured using an Ortec 567 TAC acquired through an ADC, calibrated using known delays.

The timing properties of the Yale MTC FEST system are shown in Fig. 4.13. These are obtained using coincidences between the 1173 keV and 1332 keV γ rays emitted in ^{60}Co decay, making use of the plastic scintillator's albeit limited efficiency for γ-ray detection through Compton interaction. Compton and full energy deposition interactions provide a continuum of energies in the BaF_2 detector, allowing the timing characteristics to be measured as a function of BaF_2 energy up to $\sim$1332 keV. The energy dependence of the BaF_2-plastic relative time distribution centroid and width are shown in Fig. 4.13 as measures of the timing walk and resolution, respectively. The timing resolution under experimental conditions, with ΔE signals from high-energy β particles in the plastic detector, is $\sim$140 ps FWHM at γ-ray energies $\gtrsim$1.5 MeV.

The measured distribution for the relative time between β and γ emission is the convolution of the true time distribution (a decaying exponential) with the instrumental response [Fig. 4.14(a)].The level lifetime can be extracted by a nonlinear least-squares fitting procedure, the "deconvolution method" [91, 108, 109], provided the instrumental

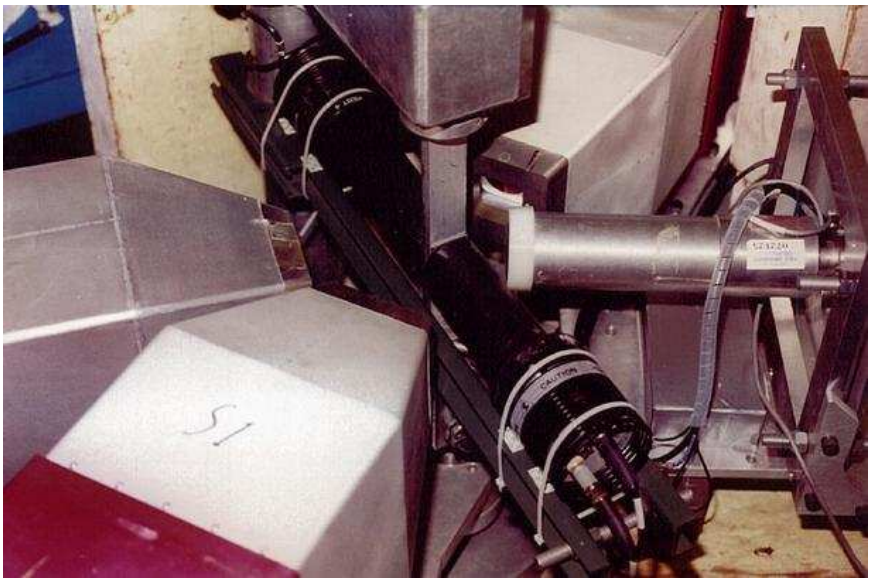

Figure 4.11: Photograph of the Yale MTC FEST configuration.

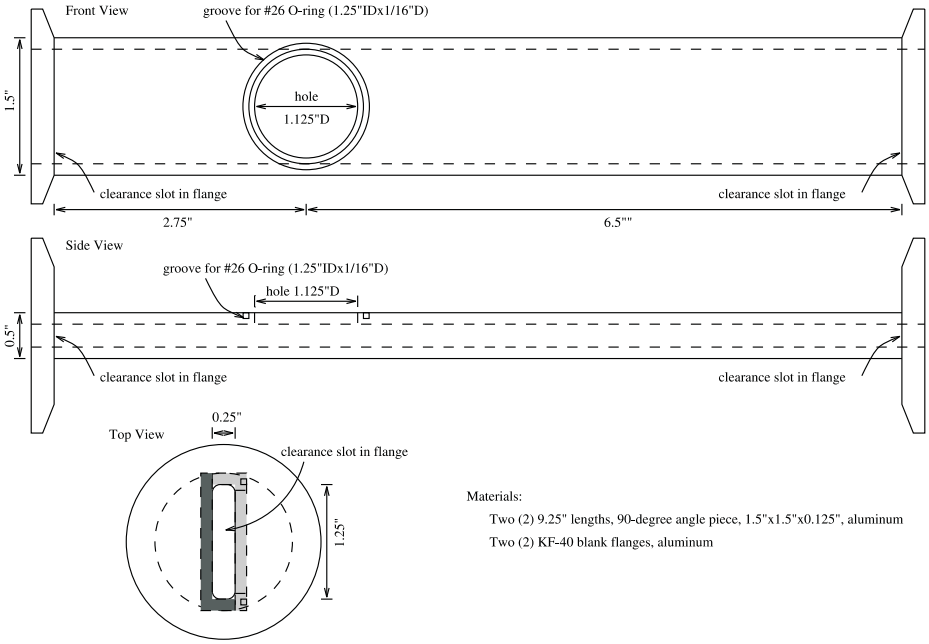

Figure 4.12: Tape transport chamber for FEST experiments at the Yale MTC.

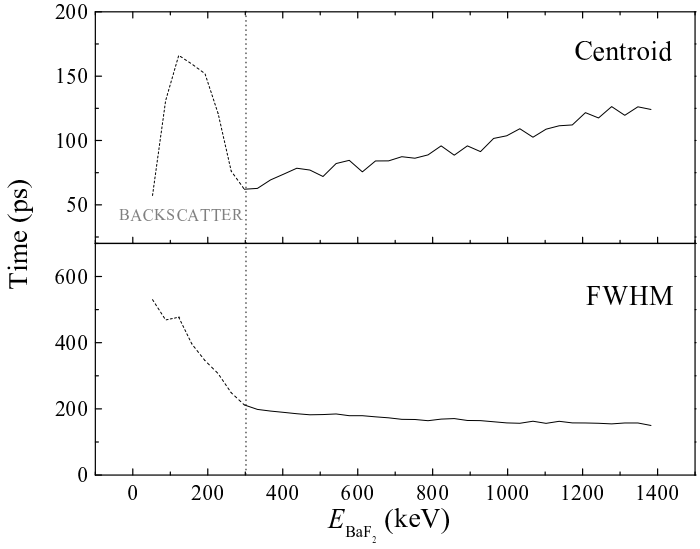

Figure 4.13: Timing resolution and walk properties of the Yale MTC FEST detector system, as determined from ^{60}Co γ-ray coincidences (see text). Some of the ^{60}Co γ rays which deposit energy in the plastic scintillator backscatter and are detected in the BaF_2 detector, producing a coincidence involving a delay due to the extra time of flight between the detectors. These γ rays have an energy after scattering of $\sim$210 keV, so the timing response measured near this energy is artificially delayed and broadened relative to the true response.

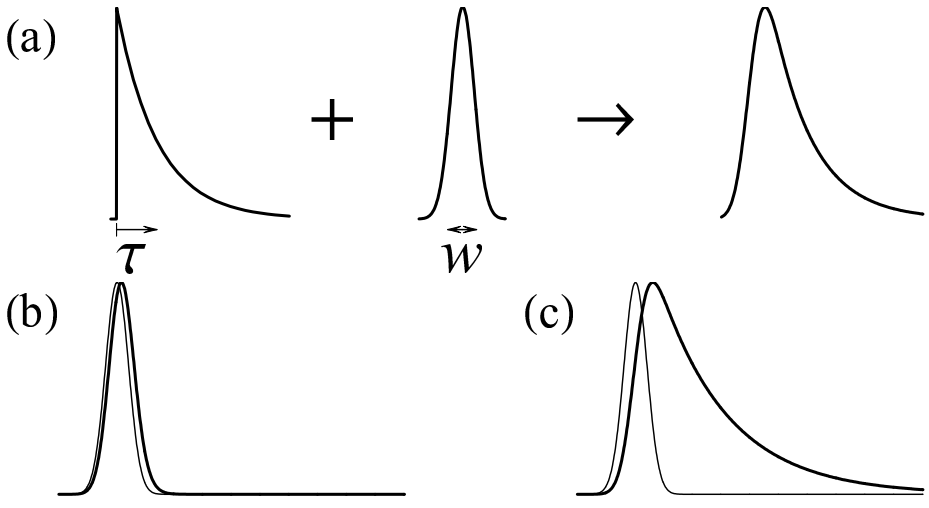

Figure 4.14: Convolution of the decay curve and the instrument response: (a) schematic diagram for lifetime τ and width w, (b) for a short lifetime ($\tau \ll w$), and (c) for a long lifetime ($\tau \gtrsim w$).

response is sufficiently well known. In practice, however, two specialized approaches, the "centroid shift" and "slope" methods, can be used for the extraction of relatively short or relatively long lifetimes.

The $\beta\gamma$ delayed time distribution has a centroid shifted relative to that of a prompt distribution by a time equal to the lifetime of the intervening level. If the experimental prompt centroid time is known for a given γ-ray energy, then the lifetime of a level depopulated by a γ-ray transition of that energy can be measured simply by observing the shift of its centroid [91] relative to the prompt centroid [Fig. 4.14(b)]. Accurate calibration of the prompt peak position can in general be challenging (see, *e.g.*, Ref. [91] for a detailed discussion), but such calibration is not always necessary for the analysis (Chapter 9). This centroid shift method is effective for the lifetimes ranging from $\sim$10 ps to $\sim$100 ps. For long lifetimes, the centroid shift method becomes impractical, since a wide range of channels must be included in the centroid analysis, and small fluctuations in the number of background counts in the tail region have a large effect on the calculated centroid. The centroid shift method is also difficult to apply if a significant prompt contamination is present in the time spectrum.

For decay times much longer than the width of the instrument response, the tail of the measured decay curve approximates a true decaying exponential. The lifetime can then be extracted from the logarithmic slope of this tail, most conveniently by linear least-squares fitting of the logarithmic number of counts. The slope method is insensitive to prompt contamination, so long as the prompt region is excluded from fitting. Incorporation of time channels containing a small number of counts into the analysis tends to skew the extracted lifetime, since a simple square-root error weighting can place far too much weight on such a channel. A practical solution is to exclude the extreme tail region from fitting and to repeatedly compress the spectrum, so that each individual channel has more counts, until the deduced lifetime is stable against further compression.

Chapter 5

Gamma-ray induced Doppler broadening measurements

Thermal neutron capture [6, 110] on a target nucleus can be an effective mechanism for populating low-spin states of interest in the resulting product nucleus. Since a thermal neutron contributes a kinetic energy of $\lesssim$0.1 eV to the system, the product nucleus is produced at a tightly constrained excitation energy very near the neutron separation energy ($\sim$5–10 MeV). Consequently, the capture reaction proceeds with significant strength only to the one resonance (or at most a few resonances) nearest this excitation energy in the product nucleus; this resonance usually has a spin close ($\pm 1/2$) to that of the target ground state, since s-wave capture dominates. The capture resonance then decays by γ-ray emission to lower-lying levels. A few percent of this decay intensity proceeds for by strong high-energy γ-ray transitions ("primary γ rays") from the capture resonance to low-lying levels, while the rest proceeds by cascades through the many densely-spaced levels present above $\sim$2 MeV excitation energy ("statistical cascades"). At any given excitation energy, the level population intensity is spin dependent, and states with spins near that of the capture resonance are most strongly populated (*e.g.*, Ref. [111]).

Tremendous production rates can be achieved through thermal neutron bombardment of bulk samples in a fission reactor. Available neutron fluxes are as high as $\sim 10^{14}\,\mathrm{cm^{-2}s^{-1}}$, and neutron capture cross sections typically are in the range $\sim$1–10^5 b. The correspondingly high γ-ray fluxes produced make feasible the use of crystal spectrometers [112] for γ-ray energy measurements. These devices can acheive extraordinarily fine energy resolutions, on the order of eV, but at the cost of having detection efficiencies orders of magnitude below those of conventional scintillation or semiconductor detectors. Crystal spectrometers rely upon the dispersive nature of Bragg diffraction of γ rays by the internal lattice structure of crystals, such as Si or Ge. A beam of photons to be analyzed is collimated and passed through a series of crystals and collimators configured so that

only γ rays with a very specific Bragg scattering angle, and hence specific energy, successfully transit the system. These γ rays are then counted with a conventional detector, for which the energy resolution is not critical. To construct a spectrum of the γ-ray intensity as a function of energy, the crystal orientations are scanned to select a series of different energies, and the γ ray intensity is counted at each energy.

The GAMS4 spectrometer [113–115], located at the 58 MW high-flux reactor of the Institut Laue-Langevin (ILL) in Grenoble, France, achieves energy resolutions of $\sim$2 parts per million. The target sample is located 50 cm from the reactor core, where the neutron flux is 5×10^{14} cm^{-2}s^{-1}. Capture γ rays are collimated into a beam by a 2 mm $\times$ 25 mm slit collimator and travel 15 m to the spectrometer, where they are transmitted through a series of two flat $\sim$5 mm thick Si or Ge crystals separated by 50 cm. The analyzed γ rays exit through another collimator and are counted by a Ge detector. The crystal orientations are monitored using an optical interferometer system, which allows the diffraction angles, $\sim10^{-3}$ rad, to be determined to a precision of $\sim10^{-10}$ rad. The γ-ray detection efficiency of the system is $\lesssim10^{-11}$. The comparatively low efficiency of crystal spectrometers such as GAMS4 arises from the extremely low acceptance in the initial collimation stage, as well as the low probability of Bragg scattering in the analyzing crystals.

The parts-per-million γ-ray energy resolution available with GAMS4, and related spectrometers at the ILL, allows lifetimes of levels populated in thermal neutron capture to be measured using the gamma-ray induced doppler broadening (GRID) technique [115]. The capture product nucleus is essentially at rest, except for thermal motion, when it is first created in its capture resonance state. Emission of a primary γ ray imparts to the nucleus a recoil velocity v given by

$$\frac{v}{c} = \frac{E_\gamma}{Mc^2}, \tag{5.1}$$

where E_γ is the primary γ-ray energy and M is the nuclear mass (*e.g.*, E_γ=5 MeV and M=100 u yield $v/c\approx5\times10^{-5}$). If the resonance decays through a statistical cascade, a recoil velocity will similarly be imparted; in this case the velocity is somewhat lower for the same total energy emitted, since the recoil momenta imparted by the cascade γ rays are not colinear but rather add as a random walk. The nucleus subsequently loses its recoil velocity by collisions with neighboring nuclei in the target material. The time scale at which slowing starts is the time required to reach the nearest atomic neighbor, or $\sim$10 fs. If the level populated by the primary or cascade γ rays emits a secondary γ ray while the nucleus is still recoiling, this γ ray will be Doppler shifted (Fig. 5.1). The recoil

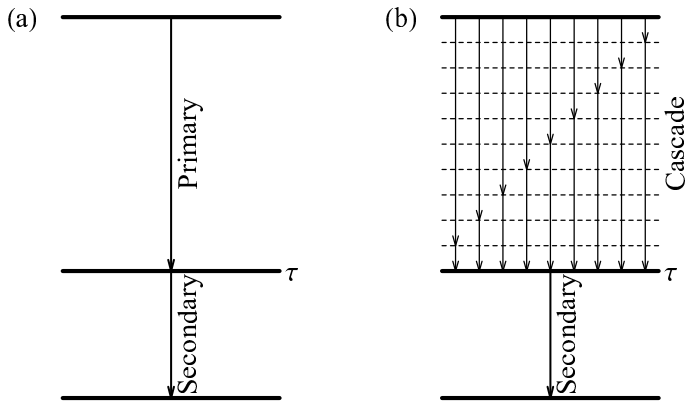

Figure 5.1: Feeding of a level in thermal neutron capture by (a) direct primary feeding or (b) cascade feeding. The feeding γ rays impart a recoil momentum to the nucleus, so that the secondary γ ray is emitted with a Doppler shift.

directions in the target are isotropic relative to the emission direction of the secondary γ ray detected in the spectrometer (excepting effects due to angular correlations between the primary γ rays and the γ rays observed by the spectrometer, which are negligible in most cases [115]), so the shift observed by the spectrometer will be averaged over a full 4π solid angle, resulting in a symmetric Doppler broadening of the measured γ-ray line. If, however, the level lifetime is comparable to slowing time of the recoiling nucleus, not all emitted γ rays will be fully Doppler shifted, and the level lifetime can be extracted from the observed line shape (for examples, see Section 6.3). This method is practical for the determination of lifetimes ranging from a few fs to a few ps. Scanning a single γ-ray transition with a mesh of $\sim$40 diffraction angles, accumulating the few thousand counts total needed for a GRID measurement, typically requires several hours to one day of experiment time.

The dominant source of uncertainty in lifetime values determined with the GRID method is usually the limited knowledge of the initial recoil velocity distribution imparted to the level of interest at the time it is populated. This distribution depends both on the γ-ray energies and intermediate level lifetimes for the feeding cascades. The analysis can be carried out using extreme bounds on the velocity distribution in order to place upper and lower limits on the deduced lifetime: the scenario in which all the indirect feeding is via a single two-step cascade through a level with zero lifetime (no slowing) provides an upper bound (5.1) on the recoil velocity, and a conservative scenario involving a cascade through a long-lived low-lying level (see Ref. [115] for details) gives a lower bound on

the recoil velocity. However, the lifetimes deduced in these limiting cases typically differ by more than a factor of two, leaving the actual lifetime poorly determined. Statistical models of the cascade feeding can be used to extract a more specific lifetime value. A straightforward approach [116] for estimating the feeding effects is based the consideration that all levels being analyzed in a given nucleus usually lie withing a narrow window of spins and excitation energies, compared to the energy of the neutron capture resonance, and so should be subject to similar statistical feeding patterns. If the lifetimes of one or more levels being analyzed by GRID are already known from other methods, these lifetimes can be used to calibrate the GRID feeding assumptions. Usually it has been found that the upper lifetime limit, or lower velocity scenario, described above provides a good estimate of the actual value.

Part III

Experimental results

Chapter 6

^{152}Sm

6.1 Experimental motivation

The nucleus ^{152}Sm, with N=90 and Z=62, lies intermediate between nuclei of known spherical shape and well-deformed axially-symmetric rotor structure. A sudden change in deformation occurs at $N\approx$88–90 for the Sm and neighboring isotopic chains [see Fig. 1.8(b) on page 11]. The nucleus ^{152}Sm has played a central role in the recent developments in the treatment of transitional structure outlined in Section 1.3. The energies of the first 2^+ and 4^+ states in ^{152}Sm place it near the phenomenological "critical point" (see Section 1.3) of the transition between spherical and axially-symmetric deformed structure. New data obtained by Casten *et al.* [28] (as well as the results of Section 6.2) constrain the description of this nucleus within the IBM to parameter values near the critical point of the transition from oscillator to rotor structure [30]. The nucleus ^{152}Sm was the first to be proposed for description by the X(5) model [38].

The nucleus ^{152}Sm, especially among the $N\approx$88–90 transitional nuclei, has historically drawn attention due to the availability of extensive and varied experimental data. The common γ-ray calibration source ^{152}Eu populates excited states in ^{152}Sm through β^+/ε decay, so spectroscopic data from this decay has long been available. The nucleus ^{152}Sm is stable, with a reasonably high abundance (27%), and the neighboring even-mass isotopes ^{150}Sm and ^{154}Sm are both stable as well. These circumstances make ^{152}Sm accessible to studies by Coulomb excitation, inelastic scattering of various projectiles, (t,p) and (p,t) two-neutron transfer reactions, and neutron capture via double capture on ^{150}Sm, among other population mechanisms (see Ref. [22]).

The excited states of ^{152}Sm exhibit a band structure roughly similar to that of a rotational nucleus, but with significant differences, suggesting it to be a transitional nucleus. As early as the 1960s, a full-fledged three-band mixing calculation performed using

detailed data from β decay [117] failed to determine consistent mixing parameters within the conventional rotational picture. Experiments using (p,t) and (t,p) transfer reactions suggested the "coexistence" of well-deformed states with undeformed states in ^{152}Sm as well as the presence of large shape fluctuations in the ground state [118–120]. The observation of unusually large electric monopole matrix elements in ^{152}Sm provides corroborating evidence indicating that both the ground state and excited states may contain admixtures of configurations of differing deformations [121].

The recent developments provided motivation for several new experiments involving ^{152}Sm. Although the γ-ray transitions most strongly populated in β-decay had been well studied as calibration standards, many of the weaker lines were subject to the inaccuracies inherent to older experiments carried out without high-statistics coincidence data (Section 4.1), suggesting that model analyses of ^{152}Sm might well be based in part upon inaccurate data. The γ-ray spectroscopy experiment in β-decay by Casten *et al.* [28] revealed that there was a genuine need for careful remeasurement of observables involving the low-lying states of ^{152}Sm. For full model treatments, it became apparent that further lifetime and mixing ratio measurements were needed as well.

The following sections present results from experiments involving the population of ^{152}Sm in β decay and neutron capture. These results were reported in Refs. [29, 122]. New lifetime values have also been determined by Klug *et al.* [123] from recoil decay method (RDM) measurements on states populated by Coulomb excitation. Interpretation of the experimental results is deferred to Chapter 15.

6.2 Spectroscopic measurements

A high-statistics γ-ray coincidence spectroscopy experiment on ^{152}Sm was performed at the Yale YRAST Ball array [61]. For this experiment, the array consisted of three clover detectors with BGO Compton suppression shields, 17 coaxial Ge detectors ($\sim$25% relative efficiency, except for one with a relative efficiency of 70%) with BGO or NaI suppression shields, and one LEPS detector. The array efficiency was 1.7% at 1.3 MeV. States in ^{152}Sm were populated through β^+/ε decay of the 3^- ground state of ^{152}Eu ($T_{1/2}$=13.5 y), from a 7 μCi commercial calibration source. Data were acquired with a γ-ray singles (or higher fold) trigger, using the YRAST Ball FERA/VME acquisition system, for a period of 25 d. The experiment yielded 2.0×10^9 singles counts and 1.3×10^8 coincidence pairs.

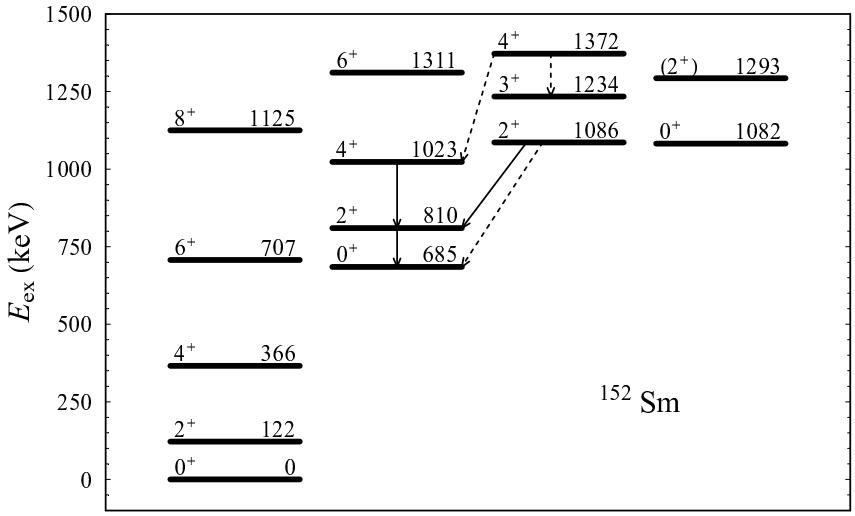

Figure 6.1: Low-lying positive-parity states in ^{152}Sm. Transitions for which intensity values or limits from the YRAST Ball data are discussed in the text are indicated by solid and dashed arrows, respectively.

Since the intensities for most of the stronger transitions from each of the low-lying levels in ^{152}Sm are reliably known, as are precise lifetime values for several of these levels [22], the following discussion will mainly serve to highlight specific experimental issues regarding individual γ-ray transitions of interest. The low-lying levels of ^{152}Sm are summarized in Fig. 6.1. In the following discussion, the notation $J^{\pi}_{E_{\rm ex}\ ({\rm keV})}$ is used to denote the level of spin assignment J^{π} at excitation energy $E_{\rm ex}$. Relative intensities are normalized to $I^{\rm rel}$=100 for the strongest branch from each level.

2^{+}_{810}: The in-band 126 keV $2^{+}_{810} \rightarrow 0^{+}_{685}$ transition was previously attributed a relative intensity $I^{\rm rel}_{126}$=1.9(6) [22] (normalized to the $2^{+}_{810} \rightarrow 2^{+}_{122}$ transition), based upon γ-ray singles measurements in β^{+}/ε decay from Refs. [124, 125]. Combined with the level lifetime value of 10.7(9) ps from Coulomb excitation (see Ref. [22]), this yielded a $B(E2; 2^{+}_{810} \rightarrow 0^{+}_{685})$ strength of 520(170) W.u. Such a strong $2^{+} \rightarrow 0^{+}$ transition is unprecedented in the rare earth nuclei and would be very difficult to explain. For comparison, the yrast $2^{+} \rightarrow 0^{+}$ transition strength in this nucleus is only 144(3) W.u. [22]. In the YRAST Ball experiment, the 126 keV transition is measured to have an intensity $I^{\rm rel}_{126}$=0.4(1), significantly lower than previously reported, from a composite gate on transitions feeding the 2^{+}_{810} level [Fig. 6.2(a)]. It is largely, but not completely, resolved from the strong 122 keV yrast $2^{+} \rightarrow 0^{+}$ transition in that gate. Klug *et al.* [123] confirm the prior level lifetime measurement, obtaining a value of 10.8(9) ps. The resulting

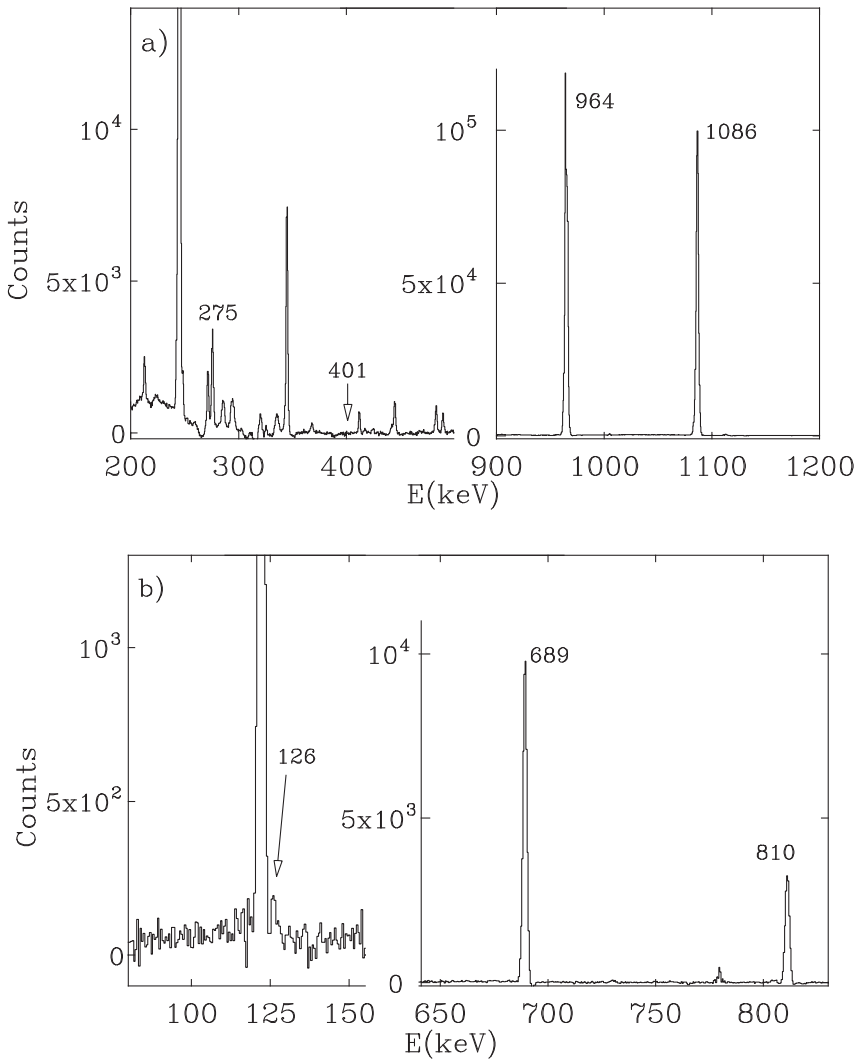

Figure 6.2: Composite coincidence spectra gated on (a) the 444, 494, 644, and 671 keV transitions feeding the 2^+_{810} level and (b) the 275, 482, 769, and 839 keV transitions feeding the 2^+_{1086} level in ^{152}Sm, used to deduce relative intensities for branches from these levels (see text). (Figure adapted from Ref. [29].)

$B(E2; 2^+_{810} \rightarrow 0^+_{685})$ value is a much more reasonable 111(28) W.u.

4^+_{1023}: The prior intensity value for the 213 keV $4^+_{1023} \rightarrow 2^+_{810}$ in-band transition was $I^{\rm rel}_{213}$=13(4) from β decay, normalized to the $4^+_{1023} \rightarrow 4^+_{366}$ transition, but discrepant values had been reported in various in-beam reactions (see Ref. [22]). Only an estimate for the level lifetime, of $\sim$7 ps, had been obtained from multiple Coulomb excitation [126]. The YRAST Ball data yield $I^{\rm rel}_{213}$=11(1), consistent with the prior value. Klug *et al.* [123] obtain an actual lifetime measurement for the 4^+_{1023} level of 12.0(19) ps. Together, these

yield $B(E2; 4^+_{1023} \rightarrow 0^+_{810})$=203(38) W.u., about half the strength which would be obtained from the prior values.

2^+_{1086}: The present interest in ^{152}Sm stemmed in part from the attempt by Casten *et al.* [28] to deduce an explicit limit for the intensity of the unobserved 401 keV $2^+_{1086} \rightarrow 0^+_{685}$ transition. In Ref. [28], a peak was observed in the singles spectrum with an area corresponding to $I^{\rm rel}_{401}$=0.023(2), normalized to the $2^+_{1086} \rightarrow 2^+_{122}$ transition, but this peak contained a contribution from the 401.258(14) keV line in ^{154}Eu decay [23]. The YRAST Ball coincidence data [Fig. 6.2(b)] provide a more stringent limit $I^{\rm rel}_{401}$<0.014. The lifetime of the 2^+_{1086} level is evaluated in Ref. [22] to be 1.26(6) ps, from a weighted average of Coulomb excitation measurements. (The 2^+_{1086} lifetime is too short for RDM to be an optimal measurement technique. Klug *et al.* [123] obtain an approximately consistent lifetime value of 1.57(20) ps with inclusion of a correction for the nonzero stopping time of the recoils. See also Section 6.3 for GRID results.) Together, these values yield $B(E2; 2^+_{1086} \rightarrow 0^+_{685})$<0.11 W.u.

The 275 keV $2^+_{1086} \rightarrow 2^+_{810}$ transition was previously attributed a predominantly $M1$ character [22], since the measured γ-ray intensity in β^+/ε decay from Refs. [124, 125] combined with the measured K conversion intensity from Ref. [127] yielded a K conversion coefficient α^K_{275}=0.106(20) [22], closely matching the theoretical [48] value 0.090 for $M1$ multipolarity. The YRAST Ball data [Fig. 6.2(b)], however, show the γ-ray intensity to be substantially larger than previously reported [$I^{\rm rel}_{275}$=0.56(7), rather than $I^{\rm rel}_{275}$=0.229(15) [22]], decreasing the experimental conversion coefficient to α^K_{275}=0.046(8), which is more consistent with the theoretical value 0.059 for pure $E2$ multipolarity. The resulting strength is $B(E2; 2^+_{1086} \rightarrow 2^+_{810})$=27(4) W.u.

4^+_{1372}: Two spin-allowed transitions from this level — the interband 349 keV $4^+_{1372} \rightarrow 4^+_{1023}$ transition and the in-band 138 keV $4^+_{1372} \rightarrow 3^+_{1324}$ transition — had not been reported in prior studies. The YRAST Ball data were used to provide explicit intensity limits $I^{\rm rel}_{349}$<3 and $I^{\rm rel}_{138}$<0.2, normalized to the $4^+_{1372} \rightarrow 4^+_{366}$ transition. The level lifetime is known to be 2.0(6) ps from Coulomb excitation [126], as approximately confirmed by the GRID measurement (Section 6.3). Using this lifetime value, the intensity limits correspond to $B(E2; 4^+_{1372} \rightarrow 4^+_{1023})$<35 W.u. and $B(E2; 4^+_{1372} \rightarrow 3^+_{1324})$<250 W.u.

The spectroscopic results of this section substantially improve the quality of the available data on transitions between low-lying states in ^{152}Sm. The transition strengths obtained are necessary for the interpretation and model analysis discussed in Chapter 15.

6.3 Lifetime and polarization measurements

Gamma-ray direction-polarization correlation measurements were carried out in a β^+/ε decay experiment at the Yale SPEEDY array [128], using seven YRAST Ball clover detectors and one coaxial Ge detector (70% relative efficiency). The clover detectors were used as Compton polarimeters, as described in Section 4.2. The total array efficiency was ∼2% at 1.3 MeV. The detector positions in the SPEEDY array, which are optimized for Doppler-shift lifetime measurements, are also well-suited for direction-polarization correlation measurements, providing four detector pairs at a 98° relative angle. A 7 μCi commercial ^{152}Eu calibration source, as used in the YRAST Ball experiment, was placed at the center of the array, and data were acuired with a γ-ray doubles (or higher fold) trigger, using the YRAST Ball FERA/VME acquisition system, for a period of 10 d.

The experiment provided useful data on the multipolarity of the 148 keV $3^+_{1234} \rightarrow 2^+_{1086}$ in-band transition, for which no information had previously been available. The polarization of the 1086 keV $2^+_{1086} \rightarrow 0^+_0$ transition was measured in coincidence with the 148 keV transition in the detector pairs at 98° relative angle. In the analysis, events involving Compton cross-scatter between clover elements *within* the coincidence plane of each detector pair were aggregated and compared to the sum of those involving Compton cross-scatter *perpendicular to* the coincidence plane. The instrumental asymmetry (Section 4.2) at a γ-ray energy of 1.1 MeV was calibrated using coincidences involving pairs of detectors at a relative angle of 180°, for which the polarization must be vanishing by axial symmetry, and was found to be $a(1.1\,\mathrm{MeV})$=1.00(3). The instrumental polarization sensitivity (Section 4.2) at this energy was calibrated using coincidences between the 1112 keV and 121 keV γ-rays, for which the multipolarities are well known [22], yielding $Q(1.1\,\mathrm{MeV})$=0.115(12), in good agreement with Monte Carlo simulations [89]. The experiment yielded a polarization $P(98^\circ) = 0.96(65)$.

The predicted polarization for a $3^+ \xrightarrow{M1,E2} 2^+ \xrightarrow[\mathrm{POL}]{E2} 0^+$ cascade [given by (D.5)] is shown as a function of mixing ratio in Fig. 6.3, where it is overlayed, for comparison, with the experimental value and one-σ error band. The experimental error band is consistent with an $E2/M1$ mixing ratio for the 148 keV transition of $\delta_{E2/M1}$=1.0(6). However, it should be noted that, given the properties of the polarization function in Fig. 6.3, a relatively small increase in uncertainty would admit a much larger range of δ values.

Gamma-ray induced doppler broadening (GRID) lifetime measurements on levels in ^{152}Sm were carried out using the GAMS4 spectrometer (Chapter 5). An isotopi-

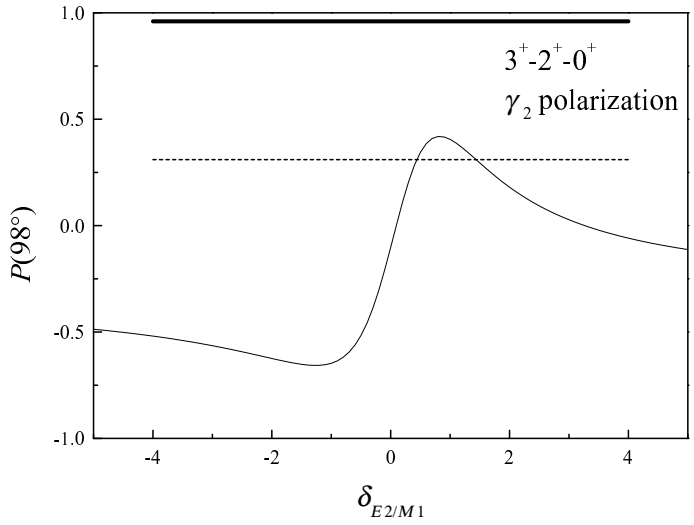

Figure 6.3: Polarization at a relative angle of 98° for the $3^+ \xrightarrow{M1,E2} 2^+ \xrightarrow[\text{POL}]{E2} 0^+$ cascade as a function of $E2/M1$ mixing ratio. The experimental value for the $3^+_{1234} \rightarrow 2^+_{1086} \rightarrow 0^+_0$ cascade in ^{152}Sm is shown (solid line) together with the one-σ error limit (dotted line).

J^π	E_{ex} (keV)	E_γ (keV)	τ_{GRID} (ps)	τ_{lit} (ps)
2^+	1086	964	0.46–1.55	1.26(6)/1.57(20)
3^+	1234	1112	0.44–1.08	
4^+	1372	1005	0.54–1.78	2.0(6)

Table 6.1: Lifetime ranges deduced from GRID line shapes for levels in ^{152}Sm and literature values (see text) for comparison. The limits of the ranges correpond to the extreme feeding assumptions (Chapter 5).

cally enriched ^{150}Sm target was placed near the reactor core, subject to a neutron flux of 5×10^{14} cm^{-2}s^{-1}. The surface layer of this material was converted through neutron capture ($\sigma\approx1.0\times10^2$ b) to long-lived ^{151}Sm ($T_{1/2}$=90 y), and ^{152}Sm nuclei were produced through subsequent neutron capture ($\sigma\approx1.5\times10^4$ b). The lifetime of the 3^+_{1234} state was previously unknown; an upper limit of 9 ps, from BaF_2-BaF_2 electronic timing of γ-γ coincidences [129], had been reported. Lifetime measurements for the 2^+, 3^+, and 4^+ members of the $K^\pi = 2^+$ band are summarized in Table 6.1. Doppler-broadened line shapes for the 964 keV $2^+_{1086} \rightarrow 2^+_{122}$ and 1112 keV $3^+_{1234} \rightarrow 2^+_{122}$ transitions used in this analysis are shown in Fig. 6.4. As discussed in Chapter 5, GRID measurements produce a range of

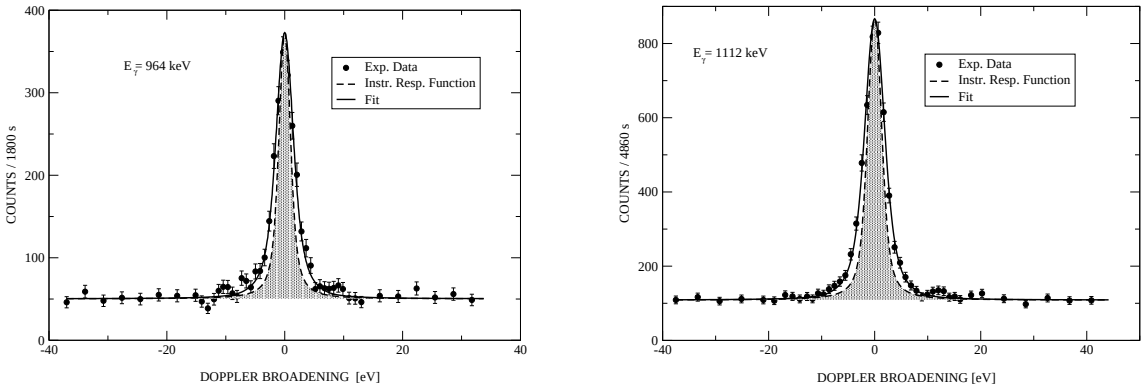

Figure 6.4: Doppler-broadened line shapes for the (a) 964 keV $2^+_{1086} \rightarrow 2^+_{122}$ and (b) 1112 keV $3^+_{1234} \rightarrow 2^+_{122}$ transitions in ^{152}Sm. The dotted line shows the instrumental response, and the solid line represents the fit to the data incorporating Doppler broadening. (Left panel courtesy of H. Börner. Right panel from Ref. [122].)

possible lifetime values, depending upon the feeding scenario assumed, but a value near the upper end of the range provides the best estimate under typical feeding conditions. Comparison of the limits obtained for the 2^+_{1086} lifetime with the prior measurements (Table 6.1) supports this feeding scenario for ^{152}Sm. Consequently, a more specific estimate $\tau(3^+_{1234})\approx$1.1 ps can be made. Similar use of the upper end of the lifetime range allows an estimate $\tau(4^+_{1372})\approx$1.8 ps, supporting a value near the center of the uncertainty range for the prior value of 2.0(6) ps from Coulomb excitation [126].

The lifetime and multipolarity measurements discussed in this section involve the 2^+_{1086}, 3^+_{1243}, and 4^+_{1372} states, all of which are members of the first excited K^π=2^+ band, and so will provide data for comparison with the X(5) predictions for the n_γ=1 band [130]. Predictions of the GCM are discussed in Chapter 15.

Chapter 7

^{156}Dy

7.1 Experimental motivation

The nucleus ^{156}Dy, with N=90 and Z=66, shows strong similarities to the lower-Z N=90 transitional nuclei, both in level energies and in transition strengths. The yrast band level energies closely match those of ^{150}Nd, ^{152}Sm, and ^{154}Gd and are nearly identical to the X(5) model predictions [Fig. 15.1(a) on page 152]. These and other basic observables involving low-lying levels suggest that ^{156}Dy warrants further examination as a candidate for description using the X(5) model (see Chapter 15).

Further interpretation of the structure of ^{156}Dy, however, requires accurate information on the branching properties of the low-lying non-yrast states. The previous spectroscopic studies of ^{156}Dy, both from in-beam data and decay data, present seriously contradictory results for some of the most basic observables concerning the low-lying off-yrast states: values stated in the literature for the intensities of some branching transitions from the lowest excited 2^+ and 4^+ states [24] disagree by factors of five or more, and values for others have uncertainties which are too large for useful analysis.

The following sections describe the results of a spectroscopic study of ^{156}Dy performed to address some of the issues regarding transition strengths in ^{156}Dy and to provide a detailed data set to serve as a basis for interpretation of ^{156}Dy. The high-statistics γ-ray coincidence spectroscopy data allow many of the ambiguities (*e.g.*, contaminant transitions, unresolved doublets) inherent to singles studies to be largely avoided. From this study, not only are substantially improved measurements of the branching properties of low-lying levels obtained, resolving the outstanding conflicts in the literature, but much of the previous level scheme for excitation energies above $\sim$1200 keV is found to be in error. Results from this experiment were reported in Refs. [59, 77].

7.2 Spectroscopy experiment overview

A $\gamma\gamma$ spectroscopy experiment to study ^{156}Dy in β^+/ε decay was carried out at the Yale MTC. Parent ^{156}Er nuclei were produced through the reaction $^{148}\mathrm{Sm}(^{12}\mathrm{C}, 4n)^{156}\mathrm{Er}$ at a beam energy of 73 MeV, using an ∼10 pnA beam provided by the Yale ESTU tandem accelerator incident upon a 1.8 mg/cm^2 96%-isotopically-enriched target. The nucleus ^{156}Er decays with a 19.5 min half life to ^{156}Ho [J^π=(4$^+$)], which in turn decays with a 56 min half life to ^{156}Dy [24]. Two-step decay was chosen since β decay from the 0$^+$ ground state of ^{156}Er avoids population of β-decaying high spin isomeric states in ^{156}Ho and thus enhances the population of low-spin off-yrast states in ^{156}Dy, as discussed in Section 3.1. The tape was advanced, carrying the deposited activity to the detector area, at 1 h intervals.

The Yale MTC was in its basic $\gamma\gamma$ spectroscopy configuration (Section 3.2) for this experiment, with three Compton-suppressed clover detectors and one LEPS detector. The array photopeak efficiency was 1.1% at 1.3 MeV and the dynamic range extended from ∼35 keV to 2650 keV. Data were acquired in event mode with a singles (or higher fold) trigger, using the YRAST Ball FERA/VME acquisition system [61]. The experiment yielded 7.2×10^8 clover singles events and 1.7×10^7 clover-clover coincidence pairs in 125 h. The combined clover singles spectrum from this experiment is shown in Fig. 7.1, along with an example gated spectrum. The main contaminant nuclei present in the experiment were in the neighboring A=157 mass chain, with γ-ray energies largely below ∼500 keV.

The nucleus ^{156}Dy is populated in β^+/ε decay with a Q_ε value of ∼5 MeV [24]. As described in Section 4.1, such population results in the production of several hundred identifiable transitions, many of them yielding overlapping or unresolved peaks in the singles spectra, and measurements of intensities from such singles data are therefore not generally reliable. All intensity values reported in the present work were deduced from the high-statistics coincidence data. Information was extracted from coincidences both with feeding transitions and with transitions below the transition of interest whenever possible. The singles data were used primarily to provide corroboration of these intensities and to deduce limits on the intensities of certain unobserved transitions. Details of these methods for measuring intensities are discussed in Sections 4.1 and H.1.

An accurate knowledge of the array singles and coincidence efficiencies is essential for intensity measurements. The array singles and coincidence efficiencies were determined as descibed in Section H.2. The coincidence efficiency calibration for this experiment was

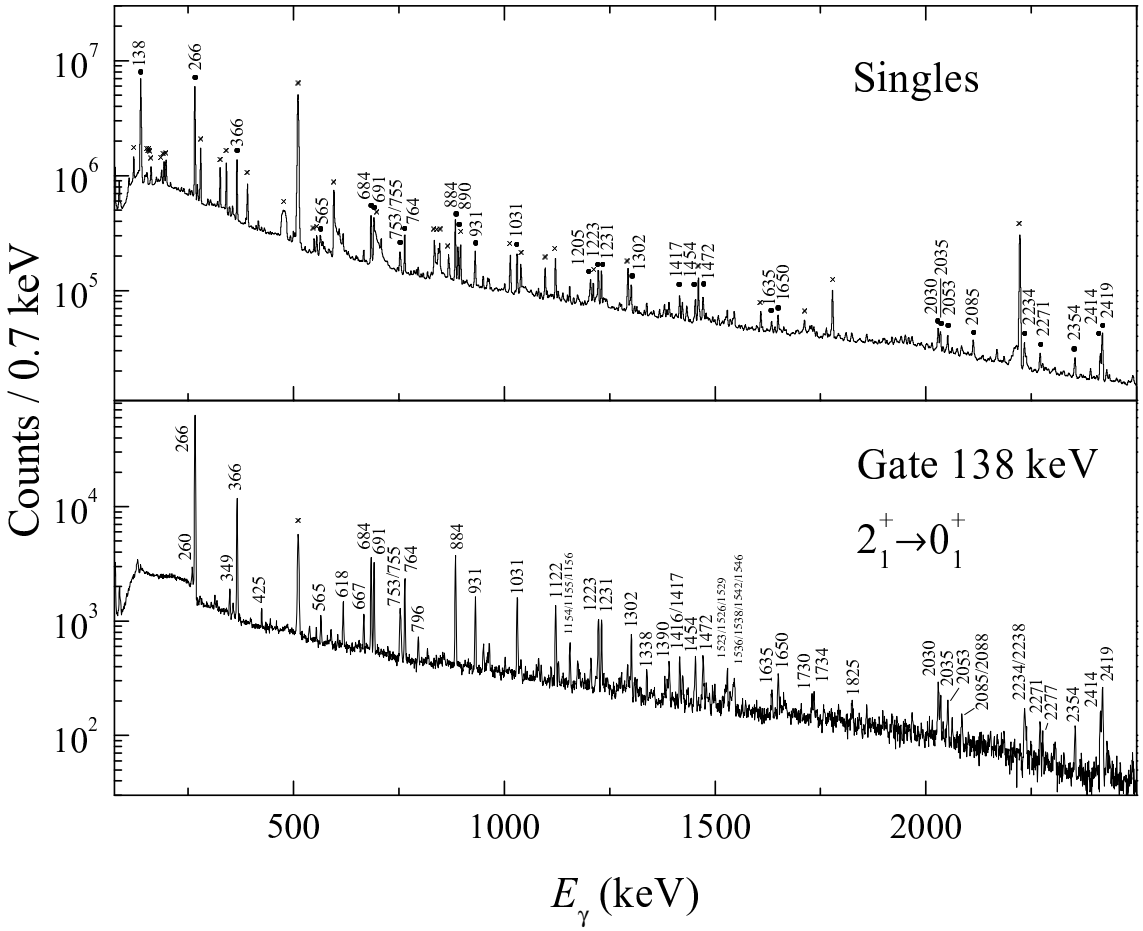

Figure 7.1: Spectra from the ^{156}Dy experiment. (Top) Clover singles spectrum. Transitions from ^{156}Dy are marked with a circle (●), and contaminant lines from ^{157}Ho, ^{157}Dy, room or neutron-induced background, and positron annihilation are indicated with a cross (×). (Bottom) Clover-clover coincidence spectrum gated on the 138 keV $2_1^+ \rightarrow 0_1^+$ transition. Annihilation radiation is marked with a cross (×). (Figure from Ref. [77].)

made using 35 known coincidences in ^{152}Sm and ^{152}Gd from ^{152}Eu calibration source decay [22]. Use was also made of "internal" calibrator coincidences from the ^{156}Dy data involving transitions in the yrast cascade, since for these transitions the branching fractions depend only upon $E2$ internal conversion coefficients, which are reliably known from atomic physics. The array exhibited a coincidence efficiency attenuation at low γ-ray energies (see Section H.2), with an attenuation factor of $w \approx 0.65$ for γ-ray energies of $\sim$100 keV, and reached ideal efficiency ($w \approx 1$) for energies above $\sim$300 keV.

Intensities measured by coincidence methods can also be affected by angular correlations between the emitted γ rays. For the clover detector pair angles used in the

present experiment (approximately 110°–125°), the effect on the γ-ray intensity measurement is $\sim$24% for a spin 0–2–0 cascade and substantially smaller ($\lesssim$5%) for other common cascades. Since reliable multipolarity information is not consistently available, intensities reported here are not corrected for angular correlation effects.

The coincidence data provide placement and intensity information on over 250 γ-ray transitions in ^{156}Dy, and the level scheme obtained constitutes a substantial revision to that found in the literature [24]. Over 50 new levels are identified, numerous levels previously claimed from β-decay data are found to be unsubstantiated, and the decay properties of many of the remaining levels are substantially modified. The γ-ray transition energies, placements, and absolute and relative intensities deduced in this experiment are summarized in Tables I.1 and I.2. Intensity limits for unobserved transitions, valuable for model analysis, are systematically included for low-lying levels (Table I.2). In the tables and in the following discussion, all absolute intensities are normalized to $I_{138} \equiv 100$ for the $2_1^+ \rightarrow 0_1^+$ transition intensity, and relative intensities are quoted normalized to $I^{\rm rel}$=100 for the strongest branch from each level. The level scheme for levels populated below 1500 keV is shown in Fig. 7.2.

7.3 Transitions depopulating low-lying levels

This section summarizes the experimental results for levels which are of current interest in the structural interpretation of ^{156}Dy, elaborating upon the basic information presented in Table I.2. The notation $J^\pi_{E_{\rm ex}\ ({\rm keV})}$ is used to denote the level of spin assignment J^π at excitation energy $E_{\rm ex}$. Spin assignments are taken from Ref. [24] unless information affecting the spin assignment has been obtained from the present experiment.

2^+_{829}: Measurement of the branching properties of this level provided much of the initial motivation for the present experiment, as this level is central to interpretation of the low-lying collective structure of ^{156}Dy and considerable ambiguities existed in the literature (Table I.2). The relative intensities of the two strongest branches from this level, to the 2^+ and 4^+ members of the yrast band, were confirmed. However, the 829 keV transition to the ground state is highly suppressed, in spite of its having a larger transition energy than the other branches. Only a limit on its intensity could be obtained, $I^{\rm rel}_{829} < 4$, from spectra gated on transitions feeding 2^+_{829} [Fig. 7.3(a)]. Previously an intensity $I^{\rm rel}_{829} = 16(18)$ had been proposed from an $(\alpha, 4n)$ study [131].

Wildly discrepant intensities for the 153 keV $2^+_{829} \rightarrow 0^+_{676}$ transition have been

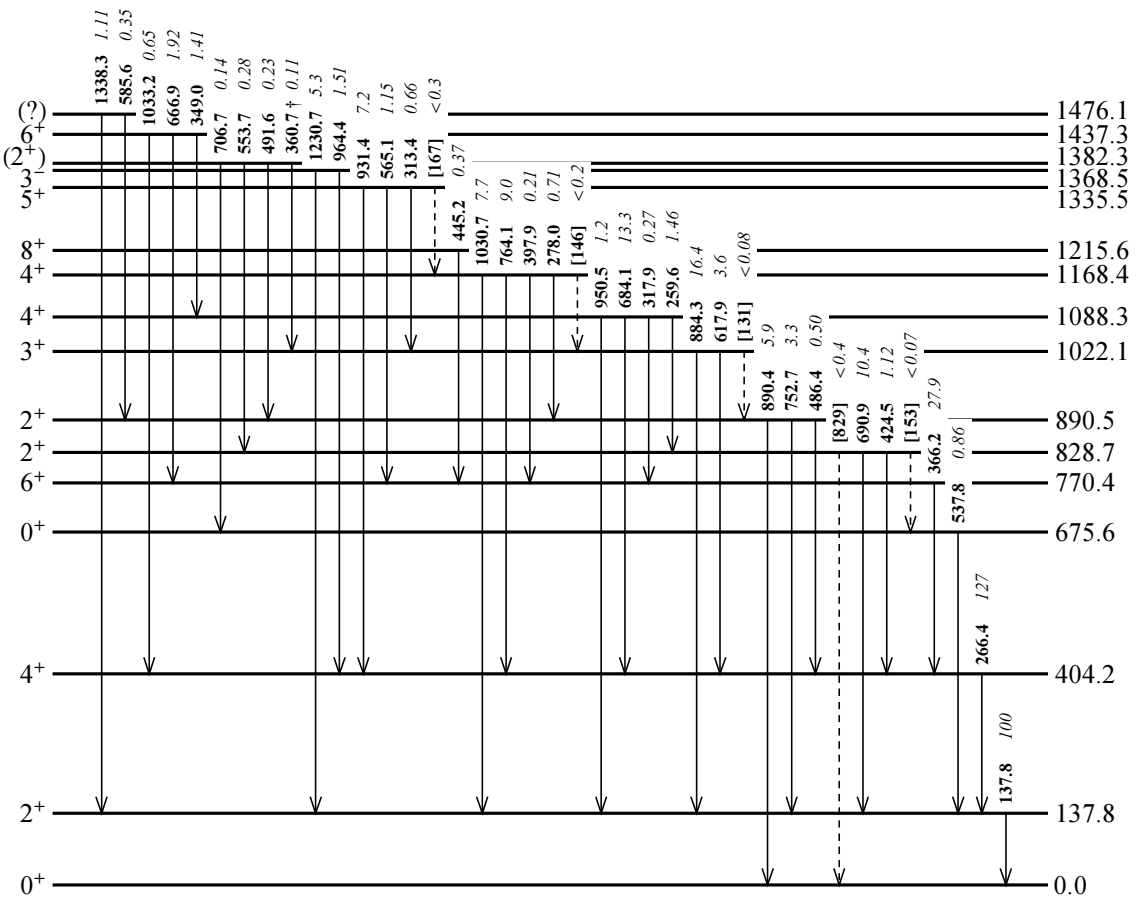

Figure 7.2: Low-lying levels in ^{156}Dy populated in ^{156g}Ho β decay and their depopulating γ-ray transitions. Unobserved transitions for which intensity limits are obtained contradicting previously reported values are indicated by dashed arrows, and a dagger (†) indicates tentative placement. Level energies (in keV), transition energies (in keV), and transition intensities in β decay (normalized to the $2^+_{138} \rightarrow 0^+_0$ transition) are from Table I.2. Level spin assignments are from Ref. [24] except as noted in the text. (Figure from Ref. [77].)

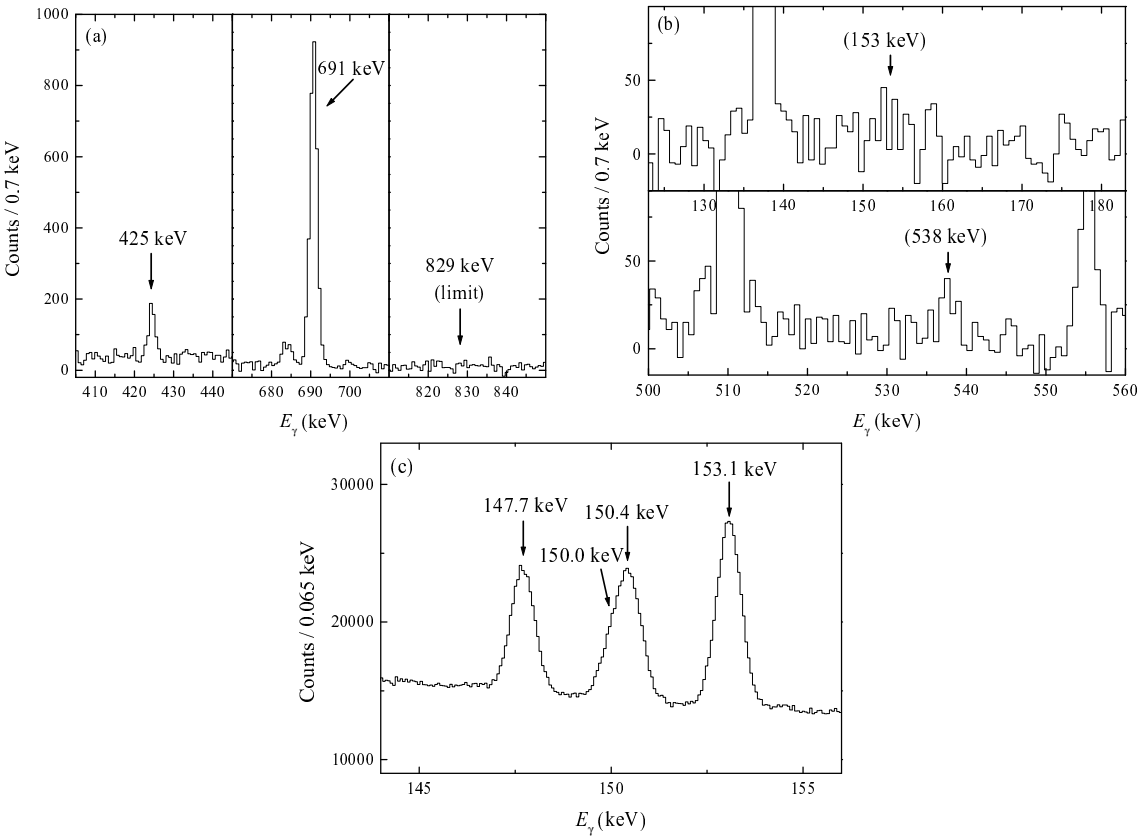

Figure 7.3: Transitions from the 2^+ level at 829 keV in ^{156}Dy. (a) Composite spectrum gated on 260, 796, 1416, and 1479 keV transitions feeding the 2^+_{829} level, showing the 424, 691, and unobserved 829 keV branches from this level. (b) Spectra gated on the 538 keV $0^+_{676} \rightarrow 2^+_{138}$ transition (top) and on the expected energy of the 153 keV $2^+_{829} \rightarrow 0^+_{676}$ transition (bottom), which allow a limit to be placed upon coincidences between these transitions. (c) LEPS detector singles spectrum showing the strong contaminant peaks at 147.7 keV (^{157}Dy), 150.0 keV (^{157}Ho), 150.4 keV (^{157}Dy), and 153.1 keV (^{157}Dy). (Figure from Ref. [77].)

reported. Much of the confusion probably results from the presence of a strong 153.0 keV transition in ^{157}Dy — relative intensities as large as $I^{\rm rel}_{153} \approx 144$ were found in experiments subject to ^{157}Dy contamination [131, 132]. The prior β-decay work [133] estimated $I^{\rm rel}_{153} \approx 1.9$ from conversion electron singles data. In singles, the γ-ray spectrum at this energy in the present experiment is overwhelmingly dominated by the contaminant transition in ^{157}Dy [Fig. 7.3(c)]. Coincidences with the 538 keV $0^+_{676} \rightarrow 2^+_{138}$ transition were not observed [Fig. 7.3(b)], allowing a limit of $I^{\rm rel}<0.7$ to be placed on the intensity of the $2^+_{829} \rightarrow 0^+_{676}$ transition, which eliminates the various previously claimed intensities (Table I.2) for this transition.

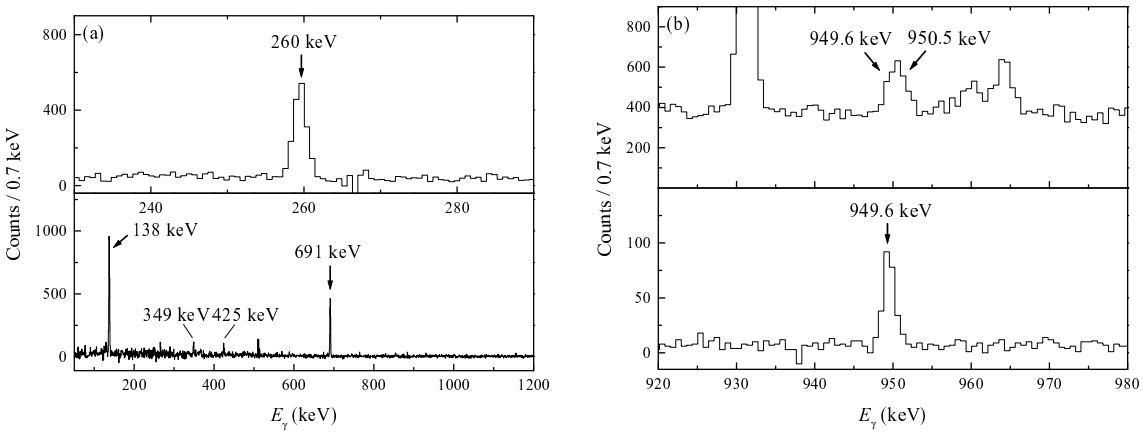

Figure 7.4: Transitions from the 4^+ level at 1088 keV in ^{156}Dy. (a) Spectra gated on the 691 keV $2^+_{829} \rightarrow 2^+_{138}$ (top) and 260 keV $4^+_{1088} \rightarrow 2^+_{829}$ (bottom) transitions, supporting the placement of the 260 keV transition and allowing measurement of its intensity. (b) Spectra gated on the 138 keV $2^+_{138} \rightarrow 0^+_0$ (top) and 890 keV $2^+_{890} \rightarrow 0^+_0$ (bottom) transitions, illustrating the 950.5 keV branch from the 4^+_{1088} level and the doublet 949.6 keV $(?)_{1840} \rightarrow 2^+_{890}$ transition. (Figure from Ref. [77].)

2^+_{890}: The reported intensities for the transitions to the yrast 0^+, 2^+, and 4^+ states are essentially confirmed, with some reduction in uncertainty for the intensity of the 486 keV $2^+_{890} \rightarrow 4^+_{404}$ transition. A weak (∼5%) doublet contribution is found in the 890 keV $2^+_{890} \rightarrow 0^+_0$ transition. Limits are placed upon any possible transitions to the 0^+_{676} and 2^+_{829} states. A $2^+_{890} \rightarrow 2^+_{829}$ γ-ray transition deduced in Ref. [133] on the basis of conversion electron data is not excluded by the present limit.

4^+_{1088}: The most important result obtained for this level is the confirmation of the existence of the "in-band" 260 keV $4^+_{1088} \rightarrow 2^+_{829}$ transition, together with a reliable intensity measurement [$I^{\rm rel}_{260}$=11.0(10)]. Coincidences between this transition and transitions depopulating the 2^+_{829} level or feeding the 4^+_{1088} level are shown in Fig. 7.4(a). Prior values for the relative intensity had ranged from about 11 to 45 [131, 132], with nonobservation in β decay [133].

The intensities of the transitions from the 4^+_{1088} state to the yrast band members are also different from those previously reported. The 950 keV $4^+_{1088} \rightarrow 2^+_{138}$ transition is found to contain a $(?)_{1840} \rightarrow 2^+_{890}$ doublet contributing ∼37% of the total intensity [Table I.1 and Fig. 7.4(b)], and the uncertainty in the intensity of the 318 keV $4^+_{1088} \rightarrow 6^+_{770}$ transition is considerably reduced.

4^+_{1168}: The strong 1031 keV and 764 keV branches to the yrast 2^+ and 4^+ states are essentially unchanged from Ref. [133], although the 1031 keV transition is found to

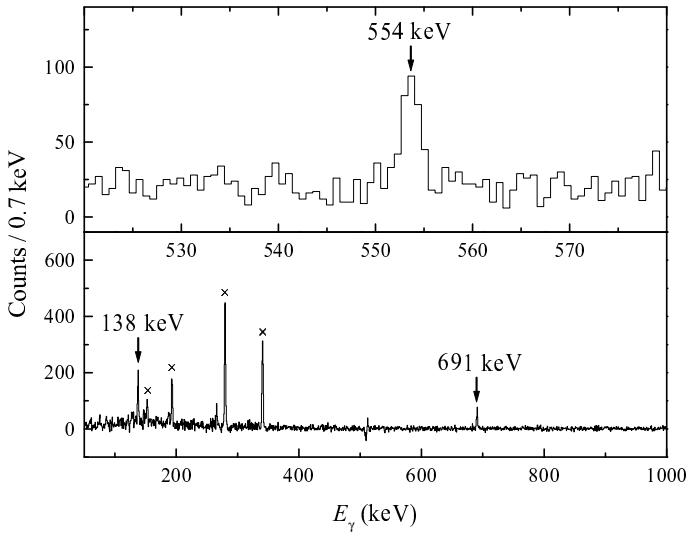

Figure 7.5: Gated coincidence spectra providing evidence for the placement of the 554 keV transition as a branch from the $(2^+)_{1382}$ level to the 2^+_{829} level in ^{156}Dy. Spectra gated on the 691 keV $2^+_{829} \rightarrow 2^+_{138}$ (top) and 554 keV (bottom) transitions. Contaminant transitions coincident with the 555 keV transition in ^{157}Dy are indicated with a cross ($\times$). (Figure from Ref. [77].)

have a weak ($\sim$1.4%) doublet contribution. The 398 keV $4^+_{1168} \rightarrow 6^+_{770}$ branch is now clearly identified [$I^{\rm rel}_{398}$=2.3(6)] from coincidences. Previous claims for the intensity of this transition had disagreed radically, with nonobservation in β decay [133]. The intensity measured for the "in-band" 278 keV $4^+_{1168} \rightarrow 2^+_{890}$ branch is modified ($\sim$37% decrease) relative to the value from Ref. [133]. A limit placed on the possible 146 keV branch to the 3^+_{1022} level ($I^{\rm rel}_{146} < 3$) excludes an extremely large relative intensity ($\sim$530) reported in $(\alpha, 4n)$ [131], which perhaps resulted from contamination by the 147.7 keV transition in ^{157}Dy [Fig. 7.3(c)]. A weaker γ-ray transition deduced from conversion electron data [133] is not excluded by the present limit.

$(2^+)_{1382}$: A weakly-populated level is identified at 1382.3(2) keV on the basis of γ-ray branches to the 0^+_{676}, 2^+_{829}, 2^+_{890}, and possibly 3^+_{1022} levels deduced from coincidences with the transitions depopulating these respective levels (Fig. 7.5 and Table I.1). The present level may be identified with the (3^-) level at 1385(5) keV [24], previously only reported in the (p, t) reaction [134], for which no prior γ-ray information was known. Observation of the γ-ray branch to an excited 0^+ state, together with the tentative transition to a 3^+ state, suggests a (2^+) spin assignment instead, although a spin of 3^- cannot be excluded if the transition to the 0^+_{676} state is taken to be of $E3$ multipolarity.

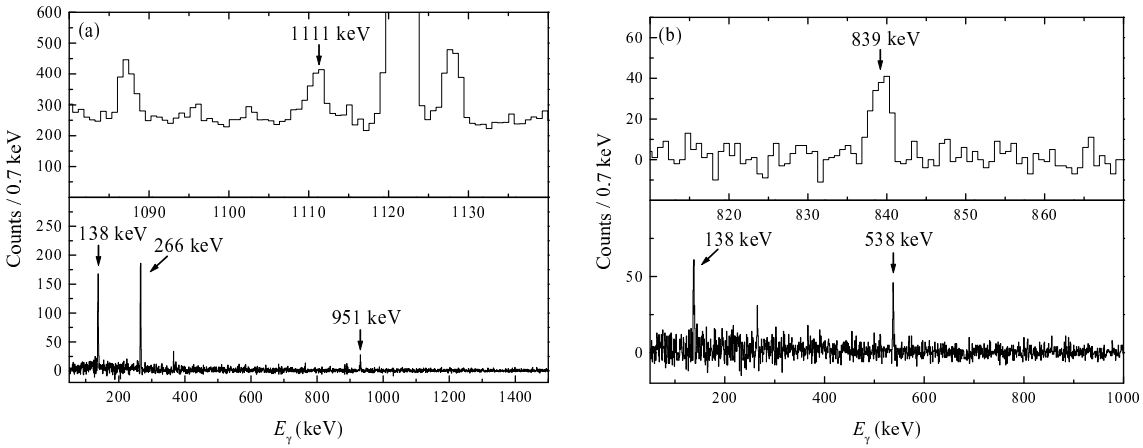

Figure 7.6: Gated coincidence spectra providing evidence for branching transitions from the level at 1515 keV in ^{156}Dy to 4^+ and 0^+ levels, suggesting a (2^+) spin assignment. (a) Spectra gated on the 266 keV $4^+_{404} \rightarrow 2^+_{138}$ transition (top) and 1111.2 keV $(2^+)_{1515} \rightarrow 4^+_{404}$ transition (bottom), supporting the placement of the latter transition. The 1111 keV peak in the top spectrum is a doublet, containing a contribution from the 1110.7 keV $(?)_{2445} \rightarrow 5^+_{1336}$ transition, which also produces the coincidence with the 951 keV $5^+_{1336} \rightarrow 4^+_{404}$ transition observed in the bottom spectrum. (b) Spectra gated on the 538 keV $0^+_{676} \rightarrow 2^+_{128}$ transition (top) and 839 keV $(2^+)_{1515} \rightarrow 0^+_{676}$ transition (bottom), supporting the placement of the latter transition. (Figure from Ref. [77].)

6^+_{1437}: The intensities found for the strong 667 keV and 349 keV branches to the 6^+_{770} and 4^+_{1088} levels are in agreement with the literature. However, the intensity of the 1033 keV $6^+_{1437} \rightarrow 4^+_{404}$ transition, which was previously not observed in β-decay, is found to have about twice the value obtained from $(\alpha, 4n)$ [131].

$(2^+)_{1515}$: A level at 1515.0(2) keV is identified on the basis of transitions to the 4^+_{404}, 0^+_{676}, and 2^+_{890} states. These transitions suggest a 2^+ spin assignment (Fig. 7.6), although a spin of 3^- cannot be excluded if $E3$ multipolarity is considered.

6^+_{1525} and $(5^-)_{1526}$: A closely spaced pair of levels lies at 1525.3(2) keV and 1526.0(2) keV. All transitions feeding or depopulating these levels are potentially doublets at $\sim$0.7 keV separation, and division of the intensities has been a challenge to all studies of these levels [131, 132]. In fact, the prior published β-decay work [133] failed to identify the lower of the two levels, but unpublished β-decay work [135] cited in Ref. [131] did observe both levels. At least one of these levels decays to each of the levels 4^+_{404}, 6^+_{770}, 4^+_{1088}, and 4^+_{1168}. The 190 keV branch to the 5^+_{1336} level reported in $(\alpha, 4n)$ [131] is excluded by the present data. The present data are likewise inconclusive about the assignment of intensities. However, the centroid energies of the observed peaks in gated spectra suggest

that most of the intensity in the 755 keV transition to the 6^+_{770} level and in the 356 keV transition to the 4^+_{1168} level is depopulating the 6^+_{1525} level, while most of the observed intensity in the 1122 keV transition to the 4^+_{404} level and in the 438 keV transition to the 4^+_{1088} level is depopulating the $(5^-)_{1526}$ level. (Estimated limits on the intensity in the other portion of each potential doublet are given in Table I.2.) Note that the adopted spin assignments [24] of the two levels, which are based upon measured conversion coefficients for the depopulating transitions, are rather speculative given the uncertainties in γ-ray intensities.

Among the higher-lying levels, several previously reported in β decay [133] are observed — $(3)^-_{1609}$, $(4)^+_{1627}$, 2^+_{2090}, 4^+_{2307}, $(?)_{2409}$ [previously (2^-)], $(?)_{2517}$ [previously $(1)^-$], $(?)_{2818}$, and $(?)_{2823}$ — albeit some with significantly modified decay properties. Three levels previously only identified in in-beam studies [131, 132, 136] — 7^+_{1729}, 7^-_{1810}, and $(6)_{1898}$ [previously $(6, 7^-)$] — are also observed, yielding new information on their branching properties. The following comments address only a few of the confirmed higher-lying levels, those for which the new data modify the spin assignment, but detailed data for all may be found in Table I.2.

$(6)_{1898}$: The adopted level at 1898.64(10) keV [24] had been assigned a spin of $(6, 7^-)$ based upon results from $(\alpha, 4n)$, $(p, 4n)$, and (HI, xn) studies [131, 136]. The present data show a transition to a 5^+ level, which eliminates the possible 7^- assignment.

$(?)_{2409}$: The adopted level at 2409.64(20) keV [24] had been assigned a spin of (2^-), based upon a supposed 880 keV $M1$ γ-ray transition to a (1^-) level at 1529 keV and the presence of γ-ray transitions to 4^+ levels. This spin assignment would have required both transitions to 4^+ levels to be $E3$ in character, constituting a fairly unusual situation. However, the present data show that there is no evidence for the (1^-) level at 1529 keV (see the following section) or for the 880 keV branch to this level. Several new branches from the $(?)_{2409}$ level are observed, and all branches to levels of known spin are to 2^+, $3^\pm$, or 4^+ levels.

$(?)_{2517}$: The present level at 2516.6(7) keV may be identified with the adopted level at 2517.55(16) keV [24], which had a spin assignment of (1^-) based upon a supposed $E2$ γ-ray transition to a $(3)^-$ level and a γ-ray transition to a 0^+ level. (There is an observed transition to a 4^+ level, which this assignment would have required to be $E3$ in nature.) However, the present data eliminate the claimed 907 keV transition to the $(3)^-_{1609}$ level and 1841 keV transition to the 0^+_{676} level. This leaves only transitions to 2^+, 3^+,

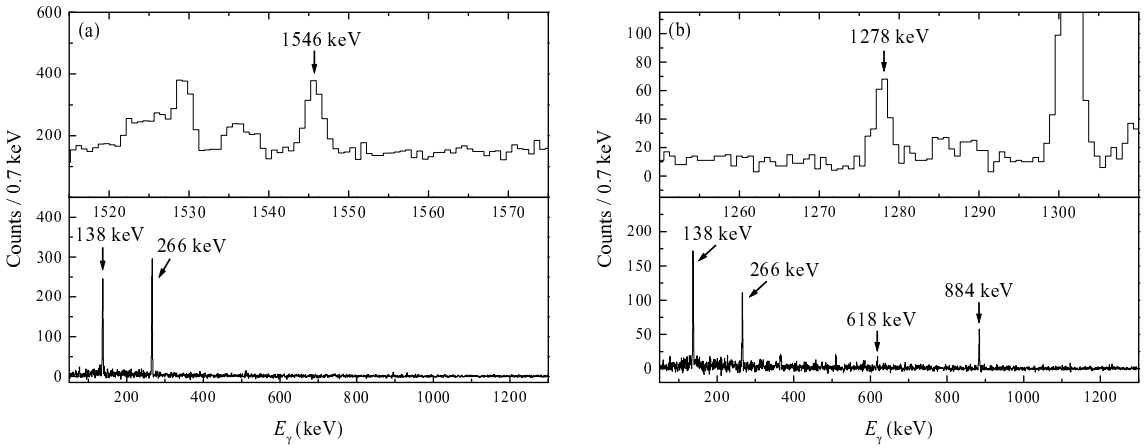

Figure 7.7: Gated coincidence spectra providing evidence for the existence of levels at 1950 keV and 2300 keV in ^{156}Dy. (a) Spectra gated on the 266 keV $4^+_{404} \rightarrow 2^+_{128}$ transition (top) and 1546 keV $(?)_{1950} \rightarrow 4^+_{404}$ transition (bottom). (b) Spectra gated on the 884 keV $3^+_{1022} \rightarrow 2^+_{138}$ transition (top) and 1278 keV $(?)_{2300} \rightarrow 3^+_{1022}$ transition (bottom), supporting its placement as directly feeding the 3^+_{1022} level. (Figure from Ref. [77].)

and 4^+ levels, and possibly a transition to a 3^- level (Table I.2). It also should be noted that the level energy calculated from the transition energy of the 1493.8(10) keV branch from this level (as measured in a spectrum gated on the 884 keV transition) disagrees with that calculated from the transition energy of the 1348.9(5) keV branch (as measured in spectra gated on the 764 and 1031 keV transitions) and from the other two tentatively-placed branches. Even though the discrepancy ($\sim$1.4 keV) is within the extreme range of the energy uncertainties, it calls into question the identity of the level as a single level.

Several new levels are identified as well (Table I.2). Many of the new levels are identified on the basis of several corroborating branching or feeding transitions, each independently placed from coincidence data. Other levels are identified on the basis of only one or two branches. These have been retained in the tabulation when there is fairly strong evidence for their placement from coincidence relations (see Fig. 7.7). Some of the "new" levels below 2250 keV likely correspond to levels previously reported in (d, d') or (p, t) studies [134, 137], but the low energy resolution of such studies precludes the establishment of an unambiguous correspondence.

7.4 Previously reported levels from β decay for which no evidence is found

The previous β-decay study [133] of ^{156}Dy identified levels on the basis primarily of singles γ-ray data, together with singles conversion electron data and some very limited coincidence data. Each level was invoked to explain several γ rays observed in singles. As outlined in Section 4.1, this process relies upon the recognition of groups of γ-ray lines with energies which sum to yield the same excited level energy and is extremely challenging when the singles spectrum is a near continuum of unresolved or overlapping lines. In contrast, the high-statistics coincidence data available in the present study provide placement information directly from coincidence relations.

A large number of levels previously proposed on the basis of data from β decay are found to be unsubstantiated by the present data, so it is worth summarizing the evidence used in dismissing these levels. The previously proposed placements of γ rays implied coincidences relations involving these γ rays, and the present data are used to verify whether or not these coincidences are actually present with the necessary strength. Also, if substantially all of the singles intensity for a γ ray line is now accounted for by one or more new placements from coincidence information, the need for the original proposed placement is obviated. Detailed discussions of a few of the most important low-lying dismissed levels follow.

$(1, 2^+)_{1219}$: This level was proposed in β decay [133] to explain six γ-ray transitions, placed as two branches and four feeding transitions. The prior study identifies a 1218.9(4) keV line of intensity 0.74(11), which it places as a branch to the ground state. The present coincidence data show this intensity to be accounted for, within uncertainties, by two new transitions: a 1217.2(3) keV $(?)_{2386} \rightarrow 4^+_{1168}$ transition of intensity 0.25(7) and a 1218.9(5) keV $4^+_{2307} \rightarrow 4^+_{1088}$ transition of intensity 0.39(10). Ref. [133] also reports a 1081.38(20) keV line of intensity 1.01(6), which it places as a branch to the 2^+_{138} level, supported by an observed qualitative coincidence with the $2^+_{138} \rightarrow 0^+_0$ transition. The present coincidence data show there to be a 1081.18(9) keV $(?)_{2103} \rightarrow 3^+_{1022}$ transition of intensity 0.64(5). This leaves a residual intensity of 0.4(2) feeding the 2^+_{138} level in this energy region, observed in a spectrum gated on the 138 keV transition after subtraction of the known placement. The two stronger supposed feeding transitions, a 582.6(4) keV transition of intensity 0.24(4) and a 2428.0(5) keV transition of intensity 0.35(4), are noncoincident with the depopulating transitions at a level inconsistent with the prior decay scheme. (Specif-

ically, from the present data, the coincident intensity of any possible 583 keV transition with a 1081 keV transition is found to be <0.08, and that with a 1219 keV transition is <0.05. The coincident intensity of any 2428 keV transition with a 1081 keV transition is <0.06, and that with a 1219 keV transition is <0.07.) The 2428 keV γ-ray line is now replaced by a 2429.5(7) keV $(?)_{2833} \rightarrow 4^+_{404}$ transition of intensity 0.63(9).

1^-_{1293}: This level was identified in β decay [133] on the basis of two depopulating transitions and five feeding transitions. (A discrepancy of ∼0.67 keV existed, however, between the level energies deduced from the two different depopulating transitions.) Ref. [133] reported a 1292.85(22) keV transition of intensity 1.28(6), which it gave a $1^-_{1293} \rightarrow 0^+_0$ placement. However, this singles intensity is now fully accounted for by three transitions (Table I.1) — a 1292.3(3) keV $(?)_{2818} \rightarrow (5^-)_{1526}$ transition, a 1293.0(5) keV $(?)_{2184} \rightarrow 2^+_{890}$ transition (tentative), and a 1293.4(15) keV $(?)_{2818} \rightarrow 6^+_{1525}$ transition — with a combined intensity of 1.28(14). Most (∼85%) of the singles intensity observed at this energy in the present experiment comes from a 1293.7(2) keV contaminant transition from ^{116}Sn, most likely arising from ^{115}In neutron capture followed by ^{116m}In β decay to ^{116}Sn [138], identified by its coincidences with the 818, 1097, 1507, and 1753 keV transitions in that nucleus. Ref. [133] also reported a 1155.72(14) keV transition of intensity 2.14(5), qualitatively coincident with the $2^+_{138} \rightarrow 0^+_0$ transition, which it assigned a $1^-_{1293} \rightarrow 2^+_{138}$ placement. This intensity is now mostly accounted for by three transitions — an 1154.4(8) keV $(?)_{2490} \rightarrow 5^+_{1336}$ transition (tentative), an 1155.3(2) $(?)_{2324} \rightarrow 4^+_{1168}$ transition, and an 1156.4 keV $(?)_{2245} \rightarrow 4^+_{1088}$ transition — with a combined intensity of 1.72(13). The intensities of all five feeding transitions are also accounted for (Table I.1), and all are found to be noncoincident with 1293 keV and 1156 keV transitions at intensity limits contradicting the earlier placements.

$(2^+)_{1447}$: This level was reported only in the $(a, 4n)$ and $(p, 4n)$ literature [131], but the placement given in that work was justified using information from an earlier unpublished β-decay study [135]. No evidence is found for the existence of this level in the present experiment.

2^+_{1518}: This level was identified in β decay [133] on the basis of two depopulating transitions and two feeding transitions. The reported singles intensities of these transitions are now accounted for by other placements (Table I.1), and both feeding transitions are noncoincident with the depopulating transitions at intensity limits contradicting the earlier placements.

$(1^-)_{1529}$: This level was proposed in β decay [133] to explain seven γ-ray transitions, placed as two depopulating and five feeding transitions. The reported intensities of the 1529 and 1392 keV branching transitions and the 1274, 1542, and 1900 keV feeding transitions are now accounted for by other placements (Table I.1), and all feeding transitions are noncoincident with both depopulating transitions at intensity limits contradicting the earlier placements.

By similar arguments, there is no evidence for the existence of the levels claimed from β decay [133] at 1801, 1944, 2006, 2169, 2216, 2476, 2514, 2637, 2661, and 2803 keV or above 2900 keV excitation energy.

The level scheme and γ-ray decay data for ^{156}Dy are considerably modified by the results presented in this chapter. The results which have the most direct implications for the structural interpretation of ^{156}Dy are the intensity measurements for transitions between low-lying levels and the clarification of existence or nonexistence for several of the low-lying levels. These results are discussed within the context of the phenomenology of the $N\approx90$ region and the X(5) model in Chapter 15.

Chapter 8

^{162}Yb

The nucleus ^{162}Yb shows a similar spin dependence in its yrast band energies to the N=90 X(5) candidate nuclei [Fig. 8.1(a)]. However, difficulties arise in interpreting other aspects of the existing data, including $B(E2)$ values and off-yrast structure, in terms of an X(5) picture, as shown in Fig. 8.1(b). Since the overall scale of the X(5) predictions is arbitrary, the experimental $B(E2)$ values are normalized to the $B(E2; 2_1^+ \rightarrow 0_1^+)$ value for comparison, and an accurate $B(E2; 2_1^+ \rightarrow 0_1^+)$ value is essential to such a comparison. A β-decay experiment on ^{162}Yb was performed to obtain a FEST measurement of the 2_1^+ level lifetime. (The experiment also yielded spectroscopic and angular correlation information on low-lying non-yrast states, reported elsewhere [139].) This lifetime measurement has been reported in Ref. [140].

The experiment was carried out in β^+/ε decay at the Yale MTC in its FEST configuration (Section 4.3), consisting of three Compton-suppressed clover detectors, a LEPS detector, and the plastic and BaF_2 fast-timing detectors. Parent ^{162}Lu nuclei were produced through the reaction ^{147}Sm(^{19}F,4n)^{162}Lu at a beam energy of 95 MeV, using an $\sim$7 pnA beam incident upon a 1.8 mg/cm^2 98%-isotopically-enriched target. The ^{162}Lu parent nucleus decays to ^{162}Yb with a half life of $\sim$1.4 min [27]. The tape was advanced at 125 s intervals.

This experiment was one of the first to make use of a new VME-based acquisition system for WNSL nuclear structure experiments, with readout by an Intel/Linux front end computer. The data acquisition and sorting software presently used for nuclear structure experiments at WNSL (see Appendix G) was written in preparation for and first tested in this experiment. Data were acquired in event mode with a Ge singles (or higher fold) or plastic scintillation detector trigger. In 79 h, the experiment yielded 1.2×10^6 plastic-BaF_2 coincidence events, including 1.5×10^5 Ge-plastic-BaF_2 coincidence events.

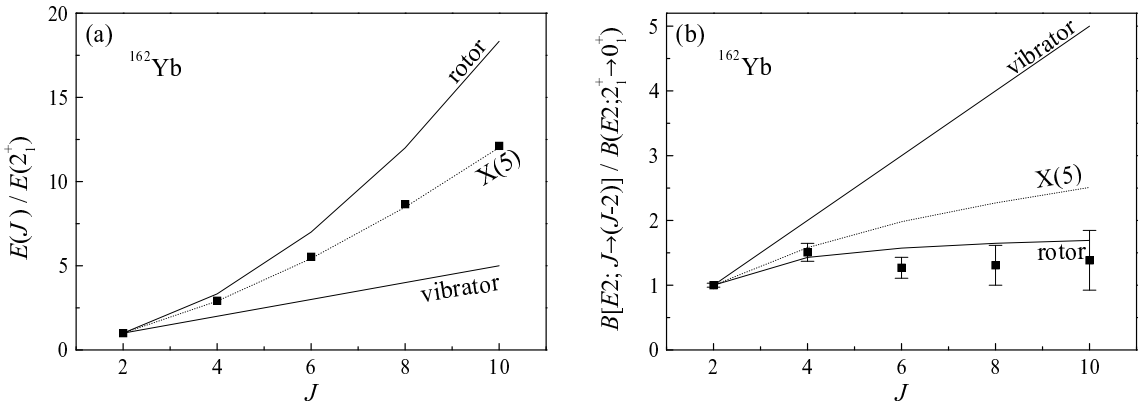

Figure 8.1: Yrast band (a) energies, normalized to the 2^+ band member, and (b) $B(E2)$ values, normalized to the $2_1^+ \rightarrow 0_1^+$ transition, in ^{162}Yb. The rotor, X(5), and vibrator predictions are shown for comparison. The experimental $B(E2)$ values are from Ref. [27]. [For the $B(E2; 2_1^+ \rightarrow 0_1^+)$ value, see text.]

The 167 keV $2_1^+ \rightarrow 0_1^+$ γ-ray transition in ^{162}Yb is by far the most intense observed transition in the β^+ decay of ^{162}Lu [Fig. 8.2(a)]. Consequently, a high-statistics measurement of its decay time can be carried out from the full plastic-BaF_2 coincidence data, without it being necessary to require triple coincidences with a feeding γ-ray transition detected in the Ge detector.

The time distribution obtained for a 17 keV wide energy gate on the 167 keV transition in the BaF_2 detector, with a local background subtraction on both the Ge and BaF_2 gates, is shown in Fig. 8.2(b). The prompt timing response at this energy is shown for comparison. (This curve is obtained using $\gamma\gamma$ coincidences from ^{60}Co decay, with Compton energy deposition in both timing detectors, shifted [92] so that the time response centroids at higher energies coincide with those for prompt Compton events in the ^{162}Yb data.) The plastic-BaF_2 time spectrum obtained for $\sim$167 keV energy deposition in the BaF_2 detector contains both a prompt background from partial-energy deposition by higher-energy γ rays from ^{162}Yb and a small delayed background from partial-energy deposition by 511 keV annihilation γ rays.

The decay time of the 167 keV transition deduced using the slope method is 618(19) ps, where the uncertainty accounts for both statistical and systematic contributions, including walk [93] and weighting uncertainties in the background subtraction. The slope was obtained by a Gaussian-error-weighted least-squares fit of the time spectrum, sufficiently compressed to provide a deduced lifetime stable against counting fluctuations (Section 4.3), over a range of time channels excluding the prompt region and extreme

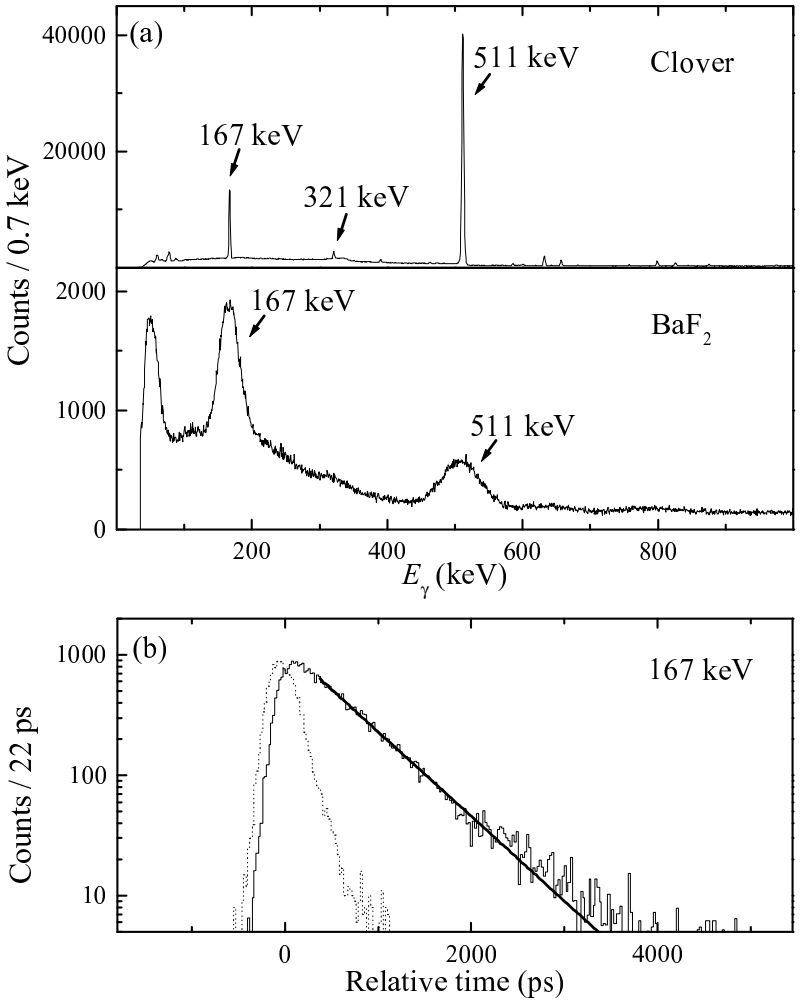

Figure 8.2: Spectra from the ^{162}Yb lifetime measurement. (a) Clover and BaF_2 detector energy spectra coincident with β^+ ΔE signals, showing the 167 keV $2_1^+ \rightarrow 0_1^+$ and 321 keV $4_1^+ \rightarrow 2_1^+$ γ-ray transitions as well as 511 keV annihilation radiation. (b) Measured time distribution for the 167 keV BaF_2 detector γ-ray time signal relative to the β^+ time signal, together with the fitted τ=618 ps decay curve (heavy line). The prompt response curve (dotted) is shown for comparison (see text). (Figure from Ref. [140].)

τ (ps)	Reference	Method
633(53)	Ref. [141]	Recoil conversion electron shadow
577(19)	Ref. [142]	Recoil Doppler
618(19)	Present	

Table 8.1: Values for the lifetime of the first excited 2^+ state in ^{162}Yb as determined by various methods in prior experiments and in the present work.

tail region. Corroborating results were obtained, but with larger statistical uncertainties, using time spectra gated on specific feeding γ-ray transitions detected in the Ge array as well as on 511 keV annihilation radiation detected in the Ge array, which selects events in which the partner annihilation γ ray does *not* enter the BaF_2 detector, providing a reduced background for the 167 keV γ ray.

The decay time of the 167 keV transition can be interpreted directly as the lifetime of the 2_1^+ level it depopulates, due to comparatively short decay times of the higher-lying feeding transitions. Approximately 10% of the β^+-coincident feeding of the 2_1^+ level comes through the 321 keV $4_1^+ \rightarrow 2_1^+$ transition [Fig. 8.2(a)], and so the 15.3(14) ps lifetime of the 4_1^+ level [27] introduces a small feeding delay to the population of the 2_1^+ level. However, the contribution of this delay to the effective lifetime, or reciprocal of the logarithmic slope of the decay curve, for the 167 keV transition is much less than 1 ps in the time region used for the analysis. The measured 2_1^+ lifetime is comparable to prior reported values (Table 8.1) and has a low uncertainty due to the high statistics obtained and simplicity of the background.

The spin dependence of the yrast band $B(E2)$ values in ^{162}Yb presents great difficulties for model interpretation. The lifetime measured in this experiment, combined with a total electron conversion coefficient of 0.503 [27], yields a $B(E2; 2_1^+ \rightarrow 0_1^+)$ value of 130(4) W.u. Figure 8.1(b) shows the $B(E2)$ values for transitions in the yrast band normalized to this strength. The data for $J>2$ are from Ref. [27], based upon the recoil Doppler method data of Refs. [142, 143]. The $B(E2)$ strengths depopulating the 6^+ and higher band members fall not only well below the X(5) predictions but even below the rotor predictions. With the 2_1^+ lifetime well established, it would be valuable to have verification of the lifetimes for higher band members from an experiment making use of modern gated coincidence Doppler shift techniques [144].

Chapter 9

^{154}Dy

The nucleus ^{154}Dy, with N=88 and Z=66, is structurally intermediate between the oscillator nuclei and the N=90 transitional nuclei. This nucleus is therefore of interest as part of the program to trace structural evolution in transitional regions, especially in conjunction with the new data for the neighboring isotope ^{156}Dy described in Chapter 7. The first excited 0^+ state plays a special role in indicating the evolution of β-deformation and β-softness, as discussed in Section 1.3 [see Fig. 1.8 on page 11]. Lifetimes for excited 0^+ states in unstable, proton-rich nuclei (such as ^{154}Dy) are not commonly known, unless some form of isomerism makes the 0^+ lifetime accessible to electronic timing (as for ^{102}Pd in Chapter 10), since Coulomb excitation, (n, n') scattering, and neutron capture are not available as population mechanisms for these nuclei. The excited 0^+ states in ^{154}Dy were not significantly populated in (HI,xn) Doppler shift lifetime measurements (see Ref. [23]). However, the 0_2^+ state in ^{154}Dy can be populated in β decay, and the 0_2^+-2_1^+ energy difference in ^{154}Dy is unusually low (326 keV), so even with collective decay strength to the 2_1^+ state (tens of W.u.), this state should have a lifetime near 100 ps. This is long enough to be accessible to a FEST measurement.

A $\gamma\gamma$ spectroscopy and FEST lifetime measurement experiment on ^{154}Dy was carried out in β^+/ε decay at the Yale MTC in its FEST configuration (Section 4.3). Parent ^{154}Er nuclei were produced through the reaction ^{144}Sm(^{13}C,3n)^{154}Er at a beam energy of 62 MeV, with a beam current of $\sim$20 pnA. A target stack containing a total of $\sim$713 μg/cm^2 thickness of ^{144}Sm (unknown enrichment) and 60 μg/cm^2 thickness of C backing material was used. However, mechanical damage was evident in some of the layers, leading this target to be replaced by a sandwich target consisting of 10.6 mg/cm^2 ^{209}Bi (placed upstream), 2.2 mg/cm^2 ^{144}Sm, and 60 μg/cm^2 Au for the final portion of the experiment. The beam energy was adjusted to 73 MeV to allow for energy loss in

the Bi and current was limited to $\lesssim$4 pnA by target heating considerations. The detector array consisted of three Compton-suppressed clovers and a LEPS detector, as well as the fast-timing detectors, but the array efficiency was much lower than usual ($\sim$0.51% at 1.3 MeV), since an interim mounting used for the fast-timing detectors imposed constraints on detector positioning. Data were acquired in event mode with a Ge singles (or higher fold) trigger using the YRAST Ball FERA/VME data acquisition system [61]. In $\sim$50 h, the experiment yielded 4.4×10^8 Ge singles counts and 2.3×10^5 Ge-plastic-BaF_2 triple-coincidence events.

The nucleus ^{154}Er ($T_{1/2}$=3.7 min) decays to ^{154}Ho, primarily populating the 2^- ($T_{1/2}$=11.8 min) ground state [23], and so a 25 min tape advance cycle was used for the MTC. The nucleus ^{154}Ho also posesses a low-lying 8^+ ($T_{1/2}$=3.1 min) β-decaying isomer [23]. The γ-ray and conversion electron spectroscopy of ^{154}Dy following the β^+/ε decay of both ground state and isomeric ^{154}Ho has been studied in detail by Zolnowski *et al.* [145], making heavy use of $\gamma\gamma$ coincidence data. The level scheme and branching intensity results of Ref. [145] are generally supported by the present γ-ray data. Levels indicated in Ref. [145] to be populated in ^{154}Ho ground state decay following ^{154}Er decay were, as expected, strongly populated. However, higher-spin states reported in Ref. [145] as being present only in ^{154}Ho isomer decay were strongly populated as well (see Fig. 4.2 on page 34). This might be attributable to direct production of isomeric ^{154}Ho in the present experiment through the ^{144}Sm(^{13}C,$p2n$)^{154}Ho reaction channel, although this reaction channel was calculated [57] to constitute only $\sim$21 mb out of the total $\sim$600 mb reaction cross section, compared to $\sim$470 mb for the main ^{144}Sm(^{13}C,$3n$)^{154}Er channel. The long tape-advance cycle used should also have strongly emphasized the two-step decay over the one-step isomer decay.

The 0_2^+ level lifetime is short compared to the FEST system time resolution, and so it must be determined by a centroid shift measurement. The decay scheme of ^{154}Dy is such that the lifetime can be extracted by using the Ge detectors to select specific feeding paths and observing the difference between the timing curve centroids for a *single* γ-ray transition, the 335 keV $2_1^+ \rightarrow 0_1^+$ transition, subject to two different Ge detector gating conditions [Fig. 9.1]. If a coincidence with the 412 keV $4_1^+ \rightarrow 2_1^+$ transition is required [Fig. 9.1(a)], the timing centroid for the 335 keV γ ray detected in the BaF_2 detector is

$$x_{\text{gate 412}} = x_{\text{prompt}}(335\,\text{keV}) + \tau_{4_1^+} + \tau_{2_1^+}. \tag{9.1}$$

If, instead, a coincidence with the 326 keV $0_2^+ \rightarrow 2_1^+$ transition is required [Fig. 9.1(b)],

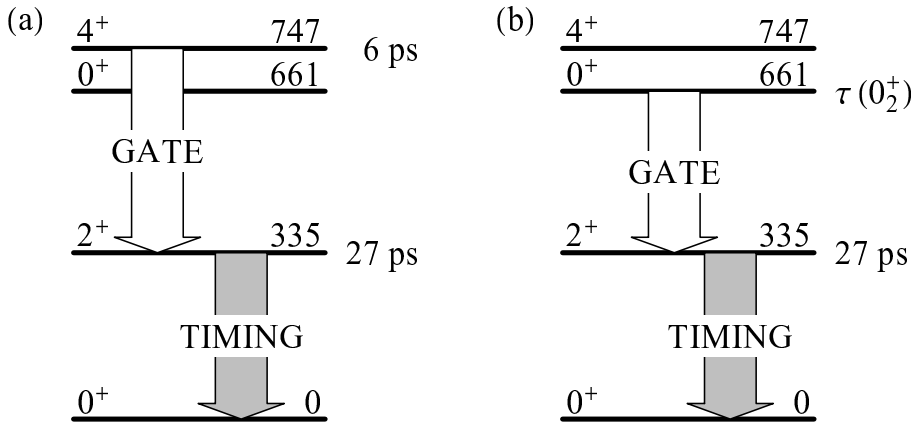

Figure 9.1: Cascades involving the (a) 4_1^+ and (b) 0_2^+ states, selected by a Ge gating condition, for measurement of the 0_2^+ lifetime in ^{154}Dy.

the timing centroid for the 335 keV γ ray detected in the BaF_2 detector is

$$x_{\text{gate 326}} = x_{\text{prompt}}(335\,\text{keV}) + \tau_{0_2^+} + \tau_{2_1^+}. \tag{9.2}$$

(These expressions assume that the feedings of the 4_1^+ and 0_2^+ levels contribute negligible additional delay.) The same γ-ray energy is used for timing in both cases, so the prompt position is the same for each, and the 2_1^+ level lifetime contributes the same delay in both cases, so the difference in centroids is simply

$$x_{\text{gate 326}} - x_{\text{gate 412}} = \tau_{0_2^+} - \tau_{4_1^+}. \tag{9.3}$$

The 4_1^+ level lifetime is known to be 6.9(5) ps (see Ref. [23]), leaving the 0_2^+ lifetime as the only unknown quantity. A measurement in which two different delayed centroids are compared to each other without reference to the prompt centroid position is termed a "relative" measurement. Such a measurement has the significant benefit that knowledge of the prompt centroid position is irrelevant; the prompt centroid calibration can otherwise be the dominant source of uncertainty.

Whereas the 4_1^+ level receives considerable direct β^+/ε feeding, the feeding of the 0_2^+ level is essentially all via higher-lying levels ranging in excitation energy from 905 keV to 2272 keV [145]. Since ^{154}Ho ground state decay occurs with a Q_ε value of 5751(11) keV, the β^+ fraction for feeding of these levels falls off rapidly with excitation energy [23], and the average emitted β^+ particle energy is lower. Consequently, much less of the 0_2^+ level feeding is found to be coincident with a β^+ particle over 500 keV in energy than is the case for the 4_1^+ level, hindering timing with the plastic scintillation detector ΔE signal.

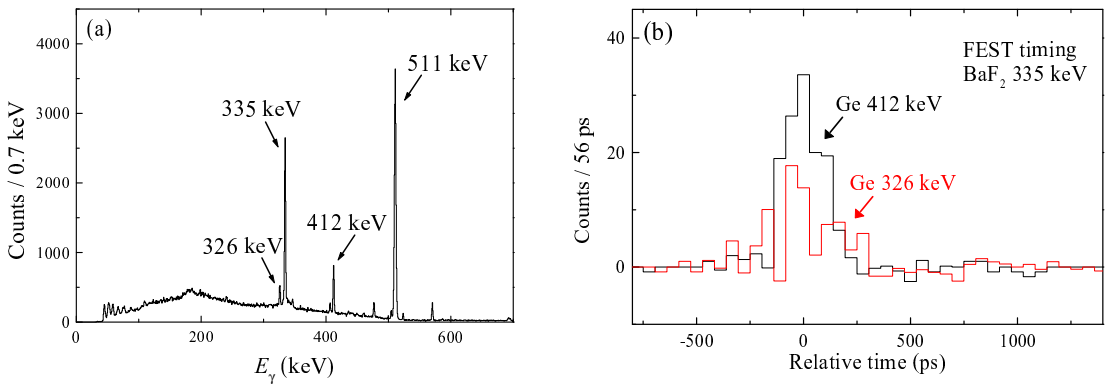

Figure 9.2: FEST data for the 0_2^+ lifetime measurement in ^{154}Dy. (a) Clover detector energy projection for all clover-BaF_2-plastic triple coincidence events, showing the 326 keV $0_2^+ \rightarrow 2_1^+$, 335 keV $2_1^+ \rightarrow 0_1^+$, and 412 keV $4_1^+ \rightarrow 2_1^+$ transitions. (b) FEST timing distributions for the 335 keV γ ray subject to clover detector gates on the 326 keV and 412 keV transitions.

The 326, 335, and 412 keV γ-ray lines are shown in the clover spectrum of Fig. 9.2(a). The BaF_2 detector timing distributions for the 335 keV transition subject to 412 keV and 326 keV clover detector gating conditions, with local background subtractions for the Ge and BaF_2 detectors, are shown in Fig. 9.2(b). For increased stastics, these were obtained with no energy cut placed on the plastic scintillation detector signal. Therefore, a significant background from γ rays Compton scattered in the plastic scintillator is present, and timing walk effects over the broad energy range accepted degrade the timing performance obtained from this detector.

The statistics obtained are insufficient for a meaningful measurement of the 0_2^+ level lifetime. The absence of a visible difference between the centroids of the time distributions in Fig. 9.2(b) suggests a 0_2^+ level lifetime of under $\sim$100 ps, but the use of low-energy signals in the plastic scintillation detector likely introduces systematic errors. The decay of the 0_2^+ level proceeds not only by the 326 keV γ-ray transition [$I^{\rm rel}$=100(16) [145]] and its associated conversion electrons, but by an $E0$ transition to the ground state as well [$I^{\rm ce,rel}$=9.5(5) [23, 145]]. With this branching information, an upper limit of 100 ps on the 0_2^+ lifetime corresponds to a transition strength $B(E2; 0_2^+ \rightarrow 2_1^+)$>26 W.u. By way of comparison, the $B(E2; 0_2^+ \rightarrow 2_1^+)$ strengths in the lower-Z N=88 isotones ^{148}Nd, ^{150}Sm, and ^{152}Gd have been measured to be 31.4(22) W.u., 54(5) W.u., and 180(40) W.u., respectively (see Refs. [20–22]). It is likely that in a full-length $\sim$100 h experiment, with more optimal target and detector array conditions, about a factor of ten more data could be obtained

than in the present experiment, allowing extraction of a value or useful limit for the 0_2^+ level lifetime in ^{154}Dy.

Chapter 10

^{102}Pd

A nucleus with an $R_{4/2}$ value near 2.20 in a known spherical to γ-soft transition region is immediately of interest as a prospective E(5) nucleus. It must then be seen to what extent the excited levels follow the energy and transition properties expected for the E(5) multiplet structure (Section 1.3) and whether or not an excited 0^+ level with its associated family of levels can be found.

The Pd isotopes constitute an example of such a spherical to γ-soft transition region and have been extensively modeled as transitional nuclei using the IBM [146–148], the IBM-2 [149–151], and other models [152]. The nucleus ^{102}Pd lies in the correct position along the isotopic chain to be a promising candidate for E(5) structure. This nucleus has an $R_{4/2}$ value of 2.29, and the levels form an approximate O(5) multiplet structure (Section A.3), with levels at the correct energies to constitute the 4^+-2^+ members of a τ=2 multiplet and the 6^+-4^+-3^+ members of a τ=3 multiplet (Fig. 10.1). Two 0^+ levels are present at energies close to that expected for the head of the first excited (ξ=2) family in the E(5) description. However, difficulties are encountered with such an interpretation of the structure of ^{102}Pd. Several of the transitions predicted by E(5) to be enhanced transitions were missing from the known decay scheme [153], suggesting the need for a spectroscopy experiment either to identify these transitions or to place limits on their existence.

An experiment was carried out in β^+/ε decay at the Yale MTC in its standard spectroscopy configuration (Section 3.2), consisting of three Compton-suppressed clover detectors and a LEPS detector. Parent ^{102}Ag nuclei were produced through the reaction ^{89}Y(^{16}O,3n)^{102}Ag at a beam energy of 75 MeV, using an $\sim$20 pnA beam incident upon a $\sim$5 mg/cm^2 ^{89}Y target (monoisotopic element) on a 2 mg/cm^2 Au backing. Production in heavy-ion fusion-evaporation preferentially populates the higher-spin 5^+ ground state

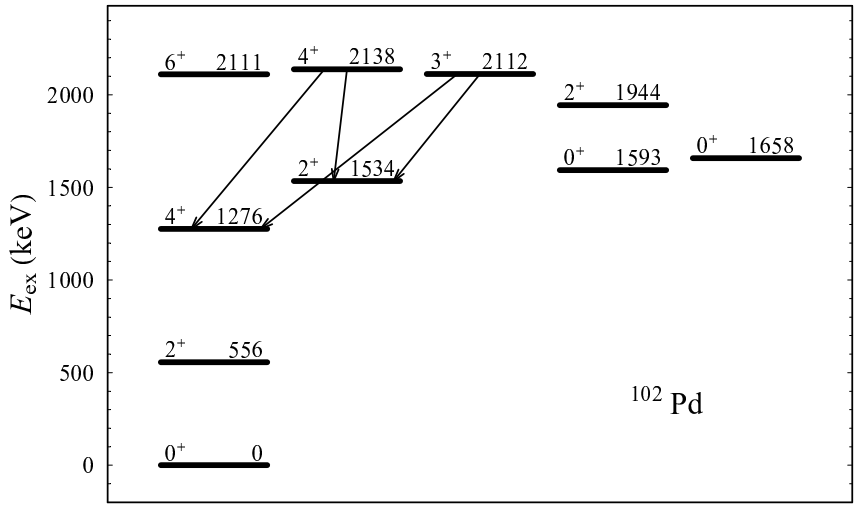

Figure 10.1: Low-lying positive-parity states in ^{102}Pd. Transitions for which intensity values from the present data are discussed in the text are indicated by arrows.

($T_{1/2}$=12.9 min) of Ag rather than the 2^+ β-decaying isomer ($T_{1/2}$=7.7 min) [153]. The tape was advanced at 20 min intervals. Data were acquired in event mode with a Ge singles (or higher fold) trigger using the YRAST Ball FERA/VME data acquisition system [61]. The experiment provided 3.6×10^8 singles counts and 9.4×10^6 coincidence pairs in $\sim$100 h (Fig. 10.2). The results were reported in Ref. [154].

The following discussion summarizes the spectroscopic information obtained most relevant to the interpretation of the low-lying postitive-parity structure of ^{102}Pd.

3^+_{2112}: The 3^+_{2112} state was previously reported (see Ref. [153]) only to decay by a 1555 keV transition to the 2^+_{556} state. In the context of the E(5) description, or in any picture involving O(5) symmetry, this is the *forbidden* ($\Delta\tau$=-2) transition. In the present data, an 836 keV $3^+_{2112} \rightarrow 4^+_{1276}$ transition and a 577 keV $3^+_{2112} \rightarrow 2^+_{1534}$ transition are observed. These transitions show a substantial $B(E2)$ enhancement relative to the $3^+_{2112} \rightarrow 2^+_{556}$ transition, as expected for $\Delta\tau$=-1 transitions, provided $E2$ character is assumed for these transitions (see Table 10.1).

4^+_{2138}: The 1581 keV $4^+_{2138} \rightarrow 2^+_{556}$ transition was previously known, and the 603 keV $4^+_{2138} \rightarrow 2^+_{1534}$ had been reported as well, with a relatively large ($\sim$33%) uncertainty on its intensity (see Ref. [153]). Other transitions had been proposed from the 4^+_{2138} level but with uncertain placements [153]. The present coincidence data show the existence of an 862 keV $4^+_{2138} \rightarrow 4^+_{1276}$ transition and provide a much more precise determination of the 603 keV transition intensity (Table 10.1). The intensity data com-

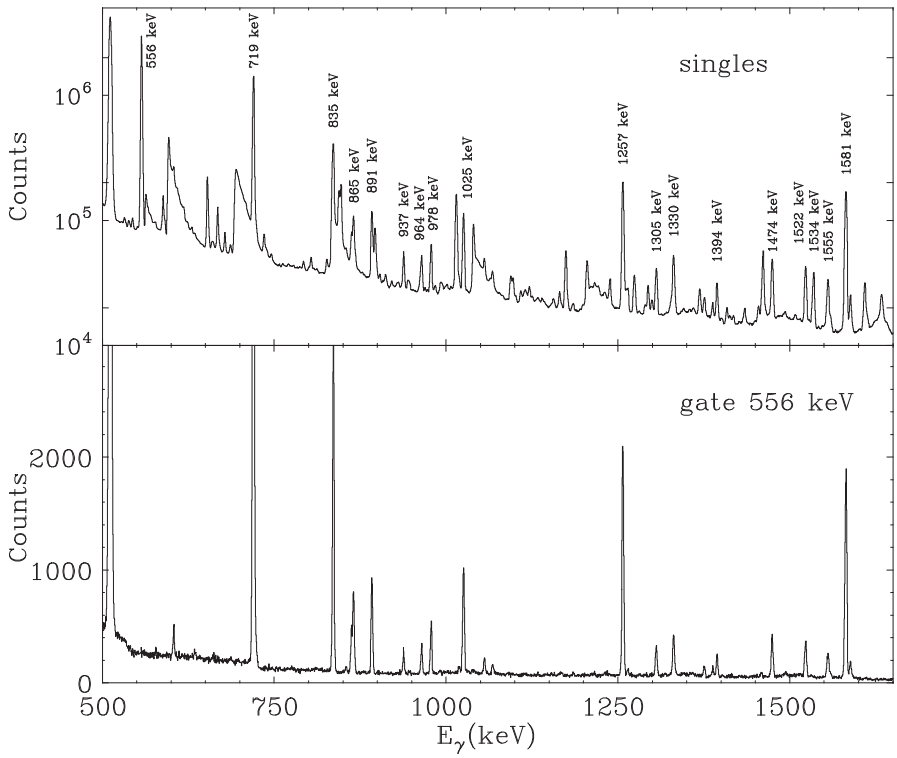

Figure 10.2: Gamma-ray singles spectrum (top) and coincidence spectrum gated on the 556 keV $2^+_{556} \rightarrow 0^+_0$ transition (bottom) from the Yale MTC ^{102}Pd experiment. (Figure adapted from Ref. [154].)

bined with the $B(E2; 4^+_{2138} \rightarrow 2^+_{556})$ value of 3.0(6) W.u. from Coulomb excitation [158] yield $B(E2; 4^+_{2138} \rightarrow 2^+_{1534})$=46(11) W.u., in good agreement with the E(5) prediction of 51(4) W.u. [based upon a $B(E2; 2^+_{556} \rightarrow 0^+_0)$ strength of 32.6(23) W.u. [153]]. The $4^+_{2138} \rightarrow 4^+_{1276}$ transition is somewhat weaker than expected (Table 10.1). Again, the transitions which are characterized as $\Delta\tau$=-1 transitions in the E(5) picture show enhanced $B(E2)$ strength over the forbidden $\Delta\tau$=-2 $4^+_{2138} \rightarrow 2^+_{556}$ transition.

The nucleus ^{102}Pd provides an example of an important consideration relating to the interpretation of excited states, especially low-lying 0^+ states, namely the possibility of intruder character. The low-lying 0^+ states of ^{102}Pd are not significantly populated in β decay from the ^{102}Ag 5^+ ground state. However, these states have been well-studied in several experiments involving ^{102}Ag 2^+ decay [159, 160], the $(p, 2n)$ transfer reaction [158], (p, p') scattering [158, 161, 162], and Coulomb excitation [158]. The reported $E2$ and $E0$ decay properties of these states are summarized in Fig. 10.3. The lowest excited 0^+ state (0^+_{1593}) is an isomer, with a lifetime of 21(6) ns [153]. It decays primarily by $E0$ decay to the

	Experiment			E(5)
Transition	E_γ (keV)	I	$B(E2)^{\rm rel}$	$B(E2)^{\rm rel}$
$2^+_{1534} \rightarrow 0^+_0$	1534.3(1)	1.9(2)	12.6(14)	
2^+_{556}	977.75(5)	1.81(16)	100(9)[a]	100
$3^+_{2112} \rightarrow 2^+_{556}$	1555.1(1)	1.44(15)	6.0(6)[b,c]	
4^+_{1276}	836.0(5)	0.15(8)	14(7)[b]	40
2^+_{1534}	577.1(1)	0.17(3)	100(18)[b]	100
$4^+_{2138} \rightarrow 2^+_{556}$	1581.1(1)	12.9(8)	6.5(4)	
4^+_{1276}	861.9(1)	1.59(14)	16.6(15)[b]	90
2^+_{1534}	603.32(6)	1.61(14)	100(9)	100

[a] Calculated using δ=2.8(2) from low-temperature nuclear orientation [155].
[b] Calculated assuming pure $E2$ character.
[c] The reported δ is 0.24(16) or >15 from the γ-ray singles angular distribution in (HI,xn) [156], and $p\gamma$ angular correlations in (p,p') scattering support the latter [157].

Table 10.1: Intensities and relative $B(E2)$ strengths of transitions from the 3^+_{2112} and 4^+_{2138} states in ^{102}Pd, compared with the E(5) multiplet member predictions. All intensities are from the present β^+/ε decay data, normalized to 100 for the 556 keV $2^+_{556} \rightarrow 0^+_0$ transition.

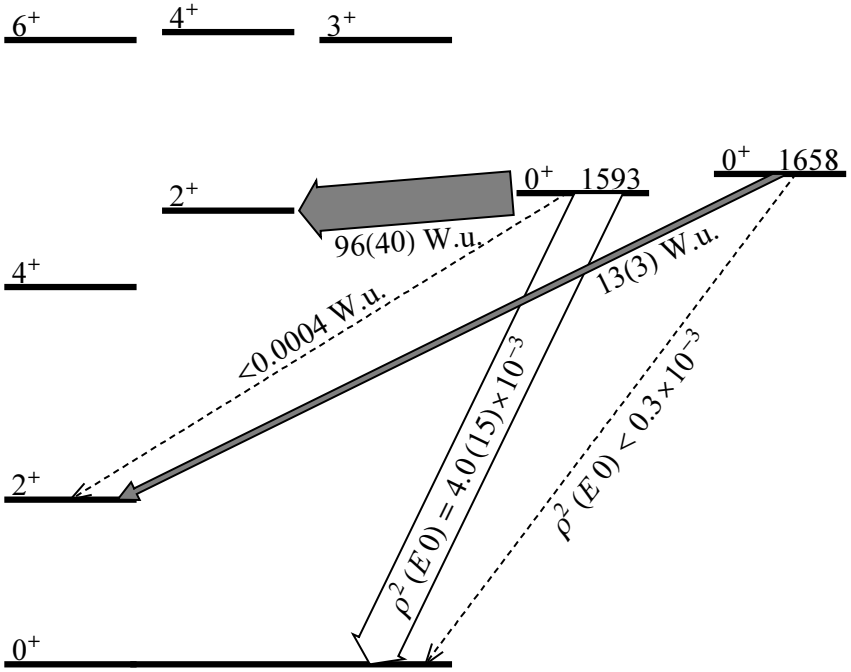

Figure 10.3: Status of $E2$ and $E0$ strengths from low-lying 0^+ excitations in ^{102}Pd, based upon data from Ref. [158] (see text).

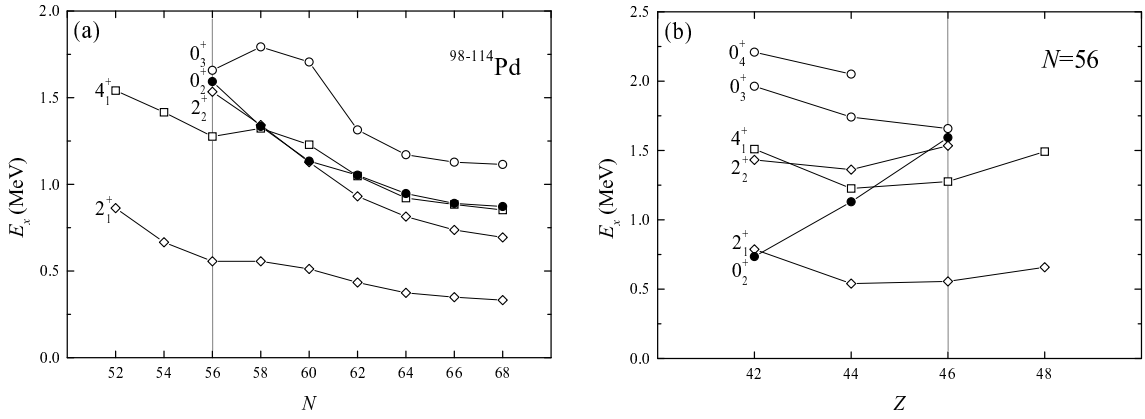

Figure 10.4: Evolution of level energies for low-lying states along (a) the Pd (Z=46) isotopic chain and (b) N=56 isotonic chain. The contrary behavior of the 0_2^+ state (filled symbols) in part (b), with a decreasing energy towards the Z=40 shell closure, indicates a cross-shell intruder nature.

ground state. An exceedingly stringent limit has been deduced on any $E2$ strength to the 2^+_{556} level, and a low-energy transition to the 2^+_{1534} level has been reported [158]. A 0^+ level at this low energy, with these decay properties, is completely inexplicable within the E(5) picture. However, an inspection of the evolution of level energies for the low-lying levels (Fig. 10.4) along the isotopic and isotonic chains containing ^{102}Pd indicates an anomalous behavior for the first excited 0^+ state along the N=56 isotonic chain. The energy *decreases* towards the Z=40 shell closure, indicating that this is not an ordinary collective state constructed from the Z=40–50 valence space. The evolution is consistent with that of a collective excitation involving the entire Z=28–50 shell, breaking the subshell closure at Z=40. Collective intruder 0^+ states have previously been identified in the higher-N Pd isotopes [163]. The next excited 0^+ level (0^+_{1658}) lies at an energy [$E(0^+_{1658})$=2.98$E(2^+_{556})$] in near perfect agreement with the E(5) prediction [$E(0^+_2)$=3.03$E(2^+_1)$]. This level decays with collective $E2$ strength to the 2^+_{556} level $B(E2; 0^+_{1658} \rightarrow 2^+_{556})$=13.3 W.u., as expected for the head of the ξ=2 family, though this strength is lower than predicted [28(2) W.u.] in E(5).

The E(5) model reproduces many of the characteristics of the low-lying levels of ^{102}Pd. The main deviations from the E(5) picture include the splitting between the 4^+ and 2^+ members of the τ=2 multiplet and several quantitative differences between predicted and observed $B(E2)$ strengths, which are enumerated more fully in Section 15.2. The divergences from the E(5) model predictions are generally consistent with a slight prefer-

ence for axial symmetry, signaling the incipient formation of a γ band. This possibility is addressed quantitatively in Section 15.2.

Chapter 11

^{162}Er

11.1 Experimental motivation

The nucleus ^{162}Er, with N=94, is the lowest neutron number member of the Er isotopic chain for which the ground state band observables indicate a well-deformed rotational structure, with a 2^+_g level energy of 102 keV, an $E(4^+_g)/E(2^+_g)$ energy ratio of 3.23, and a $B(E2; 2^+_g \rightarrow 0^+_g)$ strength of 191(1) W.u. [27]. This nucleus is therefore of interest as a bridge between the transitional nuclei and true rotor nuclei (Section 1.3). The β-vibrational mode (see Section A.4) has been widely accepted as a benchmark for the interpretation of the lowest $K^\pi = 0^+$ excitation in rotational nuclei. However, difficulties arise in the categorical interpretation of the lowest $K^\pi = 0^+$ excitation as a β vibrational or as any form of collective excitation at all [164–166]. The conclusive identification of examples of β-vibrational excitations in rotational nuclei — especially as the lowest-lying $K = 0^+$ excitation — has been elusive. Substantial evidence has been obtained in only a few cases [164, 167], including for a high-lying β-vibrational excitation in the higher-N Er isotope ^{166}Er [168].

The nucleus ^{162}Er is of special interest since the 2^+ state at 1171 keV, assigned [76] to the $K^\pi = 0^+_2$ band, is reported [169] to decay to the ground state band with a collective $B(E2)$ strength corresponding to a squared intrinsic matrix element $|\langle K^\pi = 0^+_2 | \mathfrak{M}'(E2) | K^\pi = 0^+_g \rangle|^2$=8.0(13) W.u. This is comparable to the largest such values for any $K^\pi = 0^+$ excitation in the rare earth region [164] and fully half as large as for the γ-vibrational excitation in this nucleus $|\langle K^\pi = 2^+_\gamma | E2 | K^\pi = 0^+_g \rangle|^2$=15.5(13) W.u. [169]. However, the reported relative $B(E2)$ strengths [76] of the transitions depopulating this level deviate from the Alaga rules by nearly an order of magnitude and can be reconciled with the Alaga rules through mixing of the ground and $K^\pi = 0^+_2$ bands only by invoking interaction strengths ($\sim$50 keV) for the 2^+ state an order of magnitude stronger than are

typical for rotation-vibration interactions in the rare earth region. The decay properties of this level thus precluded any simple interpretaton of the 2^+ level and consequently of the $K = 0_2^+$ excitation.

A γ-ray spectroscopy experiment was carried out under the TRIUMF E801 proposal [170], with the original intent of looking for significant strengths for transitions from the $K^\pi = 0_2^+$ band members to the γ band members, which would indicate possible two-phonon γ vibrational character (Section A.4). Such strong interband strengths have been identified for excitations in the higher-mass isotopes ^{166,168}Er [171–174]. Although limits on these strengths were obtained, the most interesting data turned out to be of an entirely different nature (Section 11.2). Subseqently, FEST and angular correlation measurements were carried out at the Yale MTC (Section 11.3). Interpretation of the $K^\pi = 0_2^+$ excitation based upon the present data is discussed in Section 11.4.

11.2 Spectroscopic measurements

The nucleus ^{162}Er was populated in β^+/ϵ decay and studied through γ-ray coincidence spectroscopy in one of the first experiments to be carried out at the ISAC radioactive ion beam facility. The results of this experiment were reported in Ref. [175].

A beam of ^{162}Yb parent nuclei was produced in the ISAC ion source, through spallation of a Ta production target by a 500 MeV proton beam from the TRIUMF Cyclotron, and transported to the GPS tape collector end station. Details of the experimental configuration are given in Section 3.3. The beam was of very high purity, and no contaminants were present at observable levels. Beam intensities for ^{162}Yb of $\sim 10^9$/s were available from the ion source, but, as discussed in Section 3.3, the maximum beam deposition rate which could be accommodated was $\sim 10^5$/s due to detector limitations.

The nucleus ^{162}Yb decays with an 18.9 m half life through β^+/ϵ decay to ^{162}Tm, the ground state of which in turn decays with a 21.7 m half life to ^{162}Er [27]. The GPS tape was therefore advanced, carrying the deposited activity to the detector area, at approximately 1 h intervals. Data were taken with a Ge singles trigger for 16 h, yielding 1.5×10^8 events, and with a doubles trigger for 120 h, yielding 6×10^7 coincidence events. A Ge detector singles spectrum from the experiment is shown in Fig. 11.1. Transitions from both members of the decay chain — ^{162}Tm and ^{162}Er — are clearly visible, with essentially no other background.

Two members of the $K^\pi = 0_2^+$ band are populated in β decay: the 0^+ level at

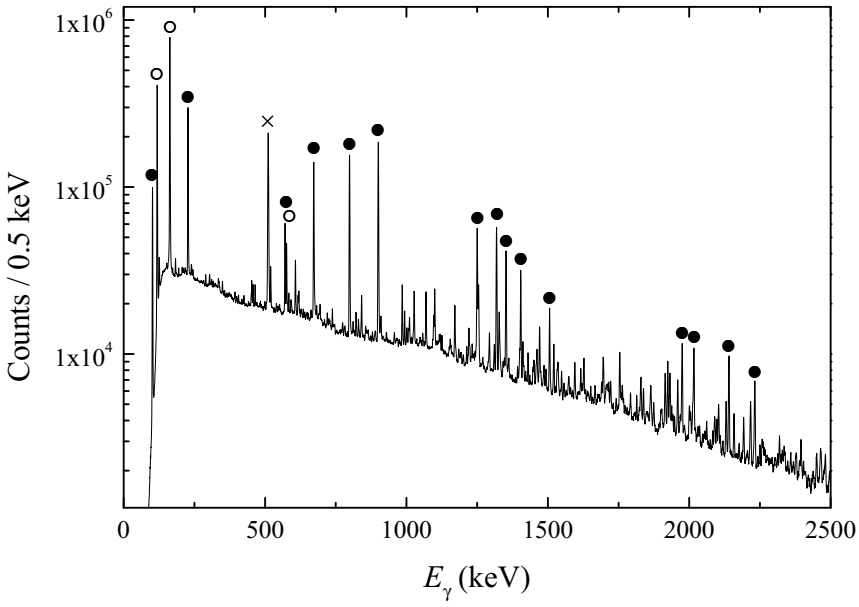

Figure 11.1: Ge detector singles spectrum for ^{162}Er. Intense transitions from ^{162}Tm (open circles) and ^{162}Er (filled circles) and 511 keV annihilation radiation (cross) are marked. (Figure from Ref. [175].)

1087 keV and the 2^+ level at 1171 keV. The level scheme for the low-spin members of the γ and $K^\pi = 0_2^+$ bands, including these levels, is shown in Fig. 11.2. The coincidence data yield intensities for the transitions depopulating these levels, as well as limits for the intensities of transitions which are not observed, summarized in Table 11.1.

Substantially revised γ-ray branching properties are measured for the $2^+_{K=0_2}$ level. The intensity of the 1171 keV $2^+_{K=0_2} \rightarrow 0^+_g$ transition, relative to the other branches depopulating the $2^+_{K=0_2}$ level, can be obtained in a straightforward fashion from spectra gated on transitions feeding this level [Fig. 11.3(a)]. The data provide a relative intensity about 7 times greater than previously reported. (Most of the singles intensity of the 1171 keV line was previously assigned [76] to a placement elsewhere in the level scheme, which the present coincidence data eliminate.) With this newly measured transition intensity, the relative $B(E2)$ values for the branches from the $2^+_{K=0_2}$ level are now found to be in reasonably good agreement with the Alaga rules (Table 11.1), as is discussed further in Section 11.4.

The other low-lying $K^\pi = 0^+$ excitation in ^{162}Er identified in the literature is based upon a spin assignment of (0^+) for the level at 1420 keV. This excitation, from its reported decay properties, would have been of interest as a possible two-γ-phonon

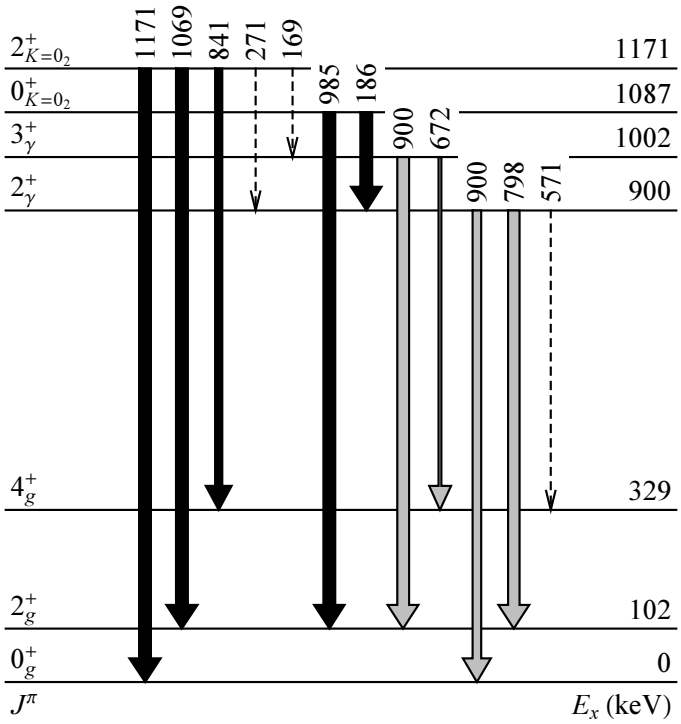

Figure 11.2: Level scheme for the low-spin members of the ground, γ, and $K^\pi = 0^+_2$ bands in ^{162}Er with transition intensities obtained from the present work. Transitions from the $K^\pi = 0^+_2$ band members (black arrows) and from the γ band members (gray arrows) are shown. Arrow widths are proportional to γ-ray intensity, normalized to the strongest transition from each level. Unobserved transitions for which intensity limits were obtained are indicated by dashed arrows. (Figure adapted from Ref. [175].)

excitation candidate.

There are several reasons given in Ref. [76] for a 0^+ assignment for the level at 1420 keV. The only observed γ rays were to 2^+ states — 2^+_g and 2^+_γ. Conversion electron data suggested a possible $E2$ character for the $(0^+)_{1420} \rightarrow 2^+_g$ transition [α_K=1.6(7)$\times 10^{-3}$], although the stated uncertainty does not exclude $E1$ character at two standard deviations. There was also a possible $E0$ transition from this level to the ground state, though this transition was at the limit of observation. Because of the uncertainties in these arguments, Ref. [76] also suggests 2^- as a possible spin for this level.

The present coincidence data show the existence of a weak 418.1(2) keV transition from the level at 1420 keV to the 3^+ member of the γ band (Fig. 11.4). The existence of such a transition is inconsistent with a 0^+ assignment for the level at 1420 keV. (Corroborating evidence that this level does not have spin 0^+ is obtained from angular correlation results described in Section 11.3.) A summary of intensities for transitions depopulating

Transition	Experiment			Alaga
	E_γ (keV)	$I^{\rm rel}$	$B(E2)$ (W.u.)	$B(E2)$ (W.u.)
$0^+_{K=0_2} \rightarrow 2^+_g$	985.2(2)	100(5)		
2^+_γ	[186]	<3.4		
$2^+_{K=0_2} \rightarrow 0^+_g$	1171.05(15)	100(5)	$\equiv$1.6(3)[a]	$\equiv$1.6[a]
2^+_g	1069.05(15)	100(5)	2.5(5)[b,c]	2.3
4^+_g	841.37(18)	59(3)	4.9(10)[b]	4.1
2^+_γ	[271]	<1.5	<37	
3^+_γ	[169]	<2.6	<6.6×10^2	

[a] Normalized to the literature $B(E2; 0^+_g \rightarrow 2^+_{K=0_2})$ value of 8.0(13) W.u. [169] (see text).
[b] The dominant contribution to the uncertainties in deduced $B(E2)$ values is from normalization to the $B(E2; 0^+_g \rightarrow 2^+_{K=0_2})$ value of Ref. [169]. Ratios of these $B(E2)$ values, *e.g.*, for comparison with the Alaga rules or use in the mixing analysis (see text), may be obtained with much smaller uncertainties directly from the intensity values in column 3.
[c] $B(E2)$ value calculated assuming pure $E2$ multipolarity.

Table 11.1: Relative intensities of transitions depopulating members of the $K^\pi = 0^+_2$ band in ^{162}Er and intensity limits for unobserved transitions. The $B(E2)$ strengths obtained by combining these with the $B(E2; 0^+_g \rightarrow 2^+_{K=0_2})$ value from Coulomb excitatation are shown, along with the Alaga rule predictions.

the level at 1420 keV is given in Table 11.2.

A spin assignment of 2^- for the level at 1420 keV is reasonable in the context of the systematics of octupole excitations in the deformed rare earth region, where a $K^\pi = 2^-$ band at comparable excitation energy is known in several of the neighboring nuclei [176]. The $B(E1; 2^-_{K=2} \rightarrow 3^+_\gamma)/B(E1; 2^-_{K=2} \rightarrow 2^+_\gamma)$ ratios for the neighboring nuclei cluster in the range 0.4–0.6, close to the Alaga value of 0.5. In ^{162}Er, this ratio has a somewhat lower value of 0.15(2), as extracted from the intensities in Table 11.2.

11.3 Lifetime and angular correlation measurements

A complementary experiment, also in β^+/ε decay, was carried out at the Yale MTC in its FEST configuration (Section 4.3), consisting of three Compton-suppressed clover detectors, a LEPS detector, and the plastic and BaF_2 fast-timing detectors. This experiment allowed measurement of the 2^+_1 level lifetime by FEST and also provided angular correlation data sensitive to 0^+–2^+–0^+ cascades. The lifetime measurement has

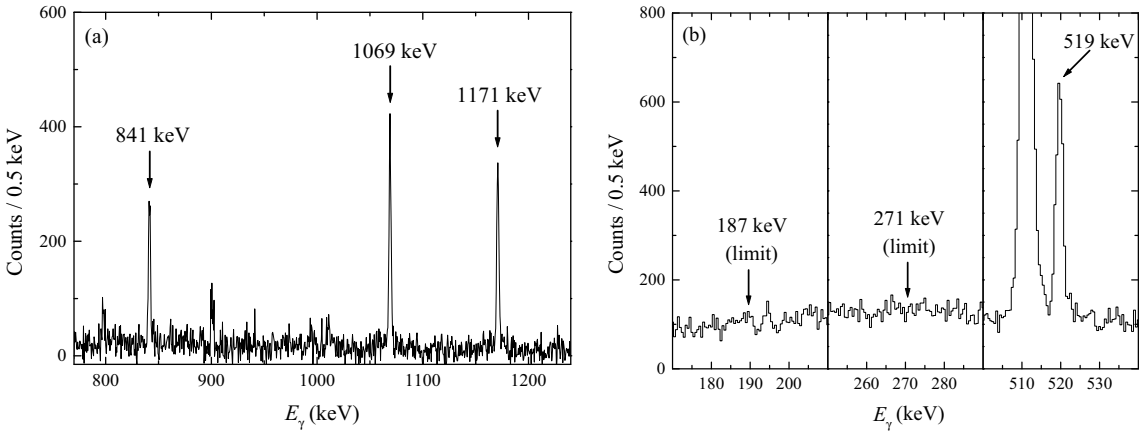

Figure 11.3: Gated spectra showing transitions from $K^\pi = 0_2^+$ band members in ^{162}Er. (a) Composite spectrum gated on 551, 639, 1224, 1236, and 2096 keV transitions feeding the $2^+_{K=0_2}$ level at 1171 keV, showing the 841, 1069, and 1171 keV branches from this level. (b) Spectrum gated on the 798 keV $2^+_\gamma \rightarrow 2^+_g$ transition. Nonobservation of 186 or 271 keV transitions from $0^+_{K=0_2}$ or $2^+_{K=0_2}$ to 2^+_γ in this spectrum allows limits to be placed upon their intensities. The observed 519 keV transition (see Table 11.2) from the misassigned (0^+) level at 1420 keV is shown for comparison. (Figure from Ref. [175].)

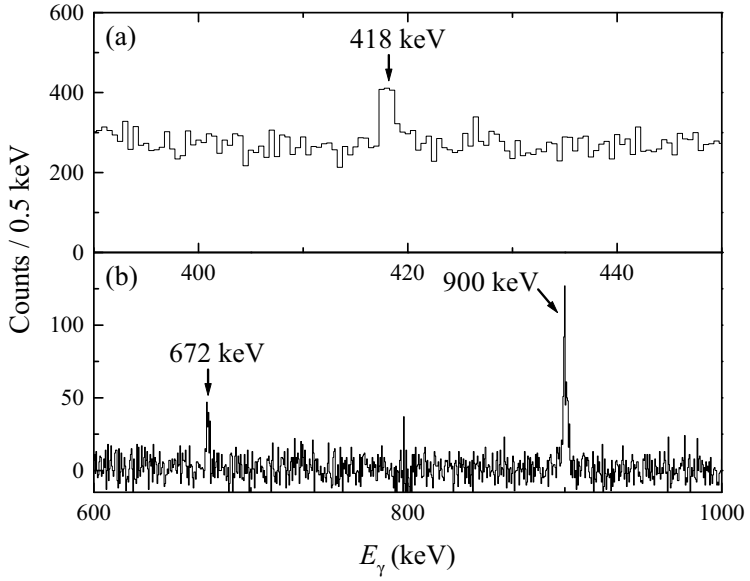

Figure 11.4: Specta gated on the (a) 900 keV and (b) 418 keV transitions in ^{162}Er, supporting the placement of the 418 keV transition as directly feeding the 3^+_γ level (see Fig. 11.2). (Figure from Ref. [175].)

Transition	E_γ (keV)	$I_{\rm rel}$
$(2^-) \rightarrow 0^+_g$	[1420]	<1.1
2^+_g	1318.42(11)	100(4)
4^+_g	[1090]	<0.6
6^+_g	[753]	<0.15
2^+_γ	519.54(13)	11.9(4)
3^+_γ	418.1(2)	0.95(13)
$0^+_{K=0_2}$	[333]	<0.18
4^+_γ	[292]	<0.8
$2^+_{K=0_2}$	[249]	<0.9

Table 11.2: Relative intensities of transitions depopulating the level at 1420 keV in ^{162}Er, including intensity limits on unobserved transitions.

been reported in Ref. [140].

Parent ^{162}Yb nuclei were produced through the reaction ^{155}Gd(^{12}C,5n)^{162}Yb at a beam energy of 86 MeV, with an ∼20 pnA beam incident upon a 5 mg/cm^2 99.8%-isotopically-enriched target. The tape was advanced at 1 h intervals, as in the ISAC GPS experiment. Data were acquired in event mode with a Ge singles (or higher fold) trigger using the YRAST Ball FERA/VME data acquisition system [61], yielding 1.0×10^9 clover singles events and 1.3×10^7 clover-clover coincidences in 110 h. The experiment produced 5.3×10^5 Ge-plastic-BaF_2 triple coincidence events for the FEST analysis.

The lifetime of the 2^+_g level in ^{162}Er is deduced from $\beta\gamma$ coincidences involving the 102 keV $2^+_g \rightarrow 0^+_g$ transition by an analysis similar to that described in Chapter 8. The decay of ^{162}Tm to ^{162}Er proceeds predominantly by electron capture, with a β^+ decay fraction of only ∼6% [177]. Since in the vast majority of decays only γ-rays are present, the detection of true β^+ ΔE signals in the plastic scintillation detector competes with a substantial background of γ-ray Compton scattering interations in the plastic scintillator depositing energies in the same energy range. Detection of the corresponding Compton-scattered γ rays in the BaF_2 detector gives rise to a strong coincident backscatter peak in the BaF_2 energy spectrum [Fig. 11.5(a)]. However, the 102 keV $2^+_1 \rightarrow 0^+_1$ transition is largely resolved from the backscatter peak in the BaF_2 spectrum [Fig. 11.5(a)], and the time spectrum from the backscatter events is essentially prompt, with an excess flight time of only ∼100 ps relative to prompt γ rays, so this background has little influence on the

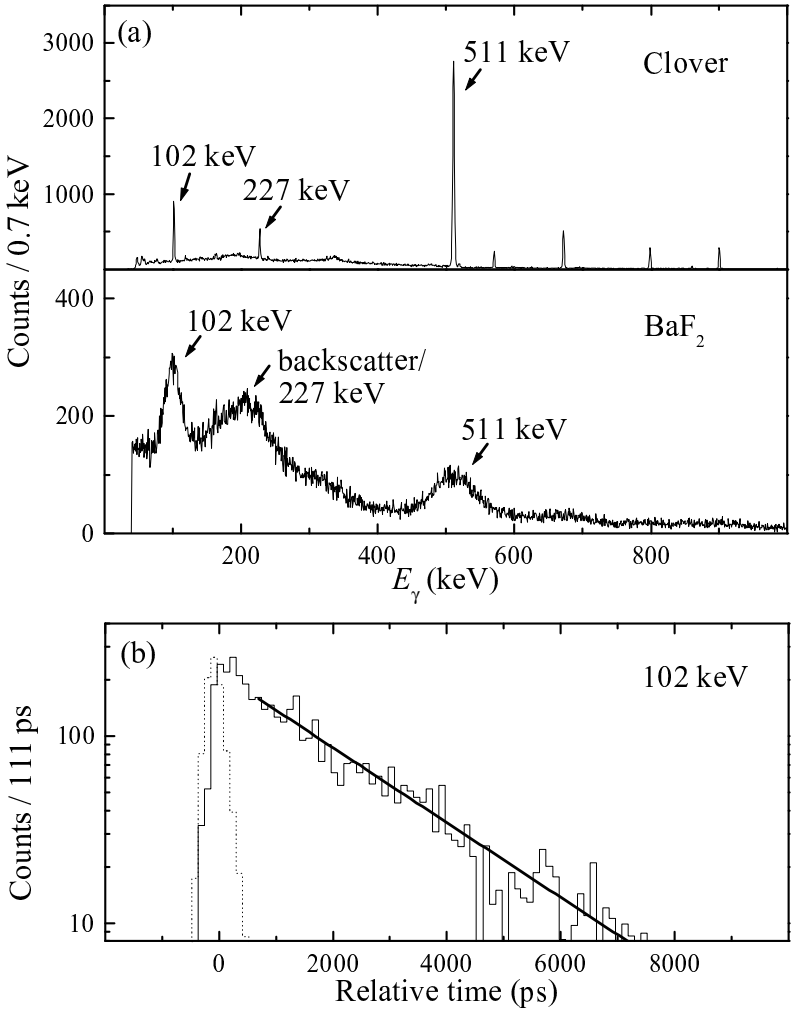

Figure 11.5: Spectra from the ^{162}Er lifetime measurement. (a) Clover and BaF_2 detector energy spectra from clover-plastic-BaF_2 triples events, 102 keV $2_g^+ \rightarrow 0_g^+$ and 227 keV $4_g^+ \rightarrow 2_g^+$ γ-ray transitions as well as 511 keV annihilation radiation and backscatter (see text). (b) Measured time distribution for 102 keV γ-ray detection in the BaF_2 detector relative to the β^+ time signal, shown with the fitted τ=2.2 ns decay curve (heavy line). The prompt response curve (dotted) is shown for comparison (see Chapter 8). (Figure from Ref. [140].)

τ (ns)	Reference	Method
1.69(14)	Ref. [178]	Electronic timing
1.96(6) [a]	Ref. [179]	Coulomb excitation
2.2(4)	Present	

[a] Deduced from the reported $B(E2; 0_g^+ \rightarrow 2_g^+)$ value using a total electron conversion coefficient of 2.76(8) [27].

Table 11.3: Values for the lifetime of the first excited 2^+ state in ^{162}Er as determined by various methods in prior experiments and in the present work.

lifetime measurement. The time distribution obtained for a 30 keV wide energy gate on the 102 keV transition in the BaF_2 detector with a local background subtraction is shown in Fig. 11.5(b).

The lifetime deduced for the 2_g^+ level in ^{162}Er, using the slope method, is 2.2(4) ns. The larger relative uncertainty obtained for this lifetime compared to the lifetime in ^{162}Yb (Chapter 8) is a result both of lower statistics and uncertainties in the local background subtraction in the BaF_2 detector due to the adjacent backscatter peak. The present measurement is compared with prior values in Table 11.3. Due to its large uncertainty, this measurement does not resolve the discrepancy between the prior values.

The clover detectors for this experiment were positioned at relative angles optimized for the identification of spin 0–2–0 cascades, as described in Section 4.2, separated by angles of 65°, 112°, and 177°. These are equivalent for angular correlation analysis to first quadrant angles of 3°, 65°, and 68°. The clover detectors were located with their faces 13 cm from the activity, giving an array efficiency of 0.6% at 1.3 MeV.

Angular correlation data for the 519 keV and 900 keV γ rays of the $(?)_{1420} \rightarrow 2_\gamma^+ \rightarrow 0_g^+$ cascade are shown in Fig. 11.6. Ratios of $W(\theta)$ values were obtained according to the singles internal calibration procedure of Section 4.2. [The overall normalization for the experimental $W(\theta)$ values shown in Fig. 11.6 is therefore arbitrary and has been adjusted to approximately match the 0^+–2^+–0^+ and 2^-–2^+–0^+ theoretical functions at $\sim$65° for comparison purposes.] For each clover detector pair, coincidences involving detection of the 519 keV γ ray in one detector and the 900 keV γ ray in the other have been distinguished from the reverse ordering, yielding a total of six data points each involving $\sim$50 counts. The angular correlation pattern is inconsistent with a spin assignment of 0^+ for the level at 1420 keV but consistent with the suggested assignment of 2^-, as well as with other assignments (Fig. 4.4). Insufficient statistics are available in the $(?)_{1420} \rightarrow 2_g^+ \rightarrow 0_g^+$

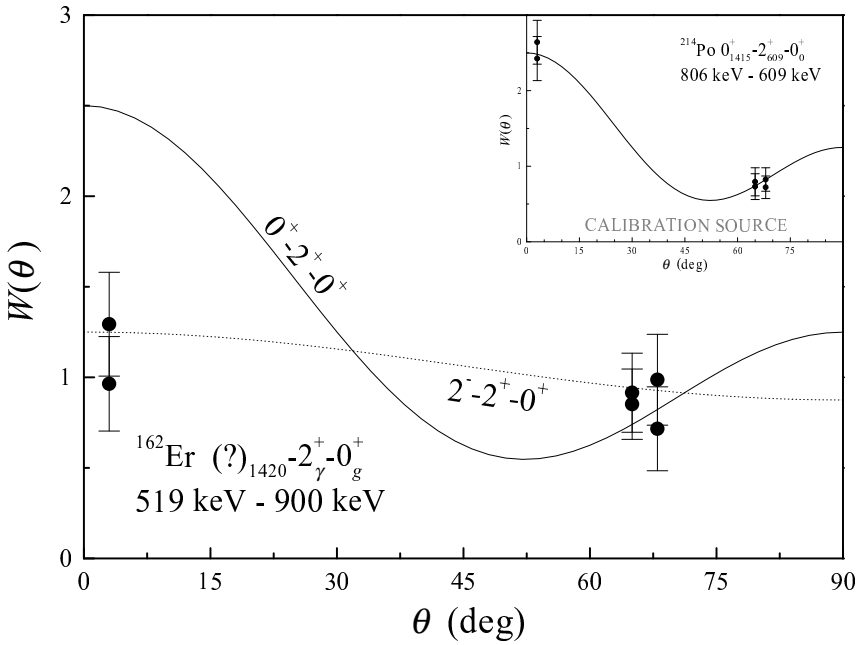

Figure 11.6: Angular correlation data for the $(?)_{1420} \rightarrow 2^+_\gamma \rightarrow 0^+_g$ cascade in ^{162}Er (see text), together with the theoretical curves for the previously proposed 0^+ or 2^- spin assignments. The correlation pattern measured with the same array geometry for the known $0^+_{1415} \rightarrow 2^+_{609} \rightarrow 0^+_0$ cascade in ^{214}Po, involving similar γ-ray energies, is shown for comparison (inset).

cascade for useful analysis in this experiment, but results from perturbed angular correlations in β decay [180] indicate that the $(?)_{1420} \rightarrow 2^+_g \rightarrow 0^+_g$ γ-ray cascade similarly does not exhibit the characteristic 0^+–2^+–0^+ angular correlation pattern.

11.4 Interpretation

The revised branching data for the $2^+_{K=0_2}$ level qualititively affect several different aspects of the interpretation of this level. The intensity values from Table 11.1 yield a $B(E2; 2^+_{K=0_2} \rightarrow 4^+_g)/B(E2; 2^+_{K=0_2} \rightarrow 0^+_g)$ ratio of 3.1(2). The deviation of this from the Alaga value of 2.6 can be attributed to relatively minor mixing effects. In contrast, the prior data [76] corresponded to a $B(E2)$ ratio of 20(15), which would have suggested an order of magnitude larger mixing and thus would have rendered implausible any straightforward interpretation of the 2^+ level as a simple $K^\pi = 0^+$ level. The γ-ray branching data also have major effects on the interpretation of the existing Coulomb excitation and conversion electron data.

The $B(E2; 0^+_g \rightarrow 2^+_{K=0_2})$ transition strength is reported from a Coulomb excitation cross section measurement [169] to be 8.0(13) W.u. The procedure used in Ref. [169] for extracting the $B(E2; 0^+_g \rightarrow 2^+_{K=0_2})$ value from the Coulomb excitation cross section was noted, in Ref. [121], to be suspect since it ignores multi-step processes. However, since the present branching ratio data show the relative $2^+_{K=0_2} \rightarrow 0^+_g$ γ-ray branch to be much stronger than previously thought, direct excitation is greatly enhanced over any possible two-step excitation. Coulomb excitation yield calculations using the present intensities and the semiclassical formalism of Alder and Winther [181, 182] show that excitation via the 2^+_g state and reorientation effects can produce at most a 10% change in the $B(E2)$ value obtained.

A new $\rho^2(E0; 2^+_{K=0_2} \rightarrow 2^+_g)$ value can be deduced by combining existing conversion electron data with the present γ-ray data. The K-conversion intensity for the $2^+_{K=0_2} \rightarrow 2^+_g$ transition in ^{162g}Tm β decay was obtained from singles conversion electron data in Ref. [76]. The value in that reference is given indirectly, as a γ-ray intensity together with a K-conversion coefficient, but it is straightforward to extract the result $I^K(2^+_{K=0_2} \rightarrow 2^+_g)$=0.43(5), normalized to $I^\gamma(4^+_g \rightarrow 2^+_g)\equiv$100. In these same units, the present γ-ray intensity for the $2^+_{K=0_2} \rightarrow 0^+_g$ transition is 17.3(15). Since the ratio of the intensities of two transitions depopulating a level is equal to the ratio of their transition probabilities per unit time,

$$\frac{I^K(E0; 2^+_{K=0_2} \rightarrow 2^+_g)}{I^\gamma(E2; 2^+_{K=0_2} \rightarrow 0^+_g)} = \frac{T^K(E0; 2^+_{K=0_2} \rightarrow 2^+_g)}{T^\gamma(E2; 2^+_{K=0_2} \rightarrow 0^+_g)}. \tag{11.1}$$

Of these quantities, electron and γ-ray intensities have just been discussed and the transition probability per unit time for the $E2$ γ-ray is directly related to the known $B(E2; 2^+_{K=0_2} \rightarrow 0^+_g)$ value by (B.1). The transition probability per unit time for K-shell $E0$ electron emission is related to $\rho^2(E0)$ by

$$T^K(E0) = \rho^2(E0)\Omega_K, \tag{11.2}$$

where Ω_K is the K-shell electronic factor for the $E0$ transition [183]. Thus, the $\rho^2(E0; 2^+_{K=0_2} \rightarrow 2^+_g)$ value may be expressed in terms of measured quantities as

$$\rho^2(E0; 2^+_{K=0_2} \rightarrow 2^+_g) = \frac{T^\gamma(E2; 2^+_{K=0_2} \rightarrow 0^+_g)}{\Omega_K(2^+_{K=0_2} \rightarrow 2^+_g)} \frac{I^K(E0; 2^+_{K=0_2} \rightarrow 2^+_g)}{I^\gamma(E2; 2^+_{K=0_2} \rightarrow 0^+_g)}. \tag{11.3}$$

[It is best to express $\rho^2(E0; 2^+_{K=0_2} \rightarrow 2^+_g)$ directly in terms of the measured quantities in this fashion, rather than first converting the data to a lifetime for the $2^+_{K=0_2}$ level and using

this lifetime to deduce $\rho^2(E0; 2^+_{K=0_2} \rightarrow 2^+_g)$, since use of the lifetime as an intermediate result leads to a greatly exaggererated uncertainty estimate unless correlated uncertainties are properly taken into account.] The experimental $2^+_{K=0_2} \rightarrow 2^+_g$ K-shell electron intensity includes $E0$, $M1$, and $E2$ contributions, and so the $M1$ and $E2$ contributions [48] must be subtracted on the basis of the known $2^+_{K=0_2} \rightarrow 2^+_g$ γ-ray intensity in order to recover the $E0$ contribution. The $M1/E2$ mixing ratio for this transition is not known, but the value of the mixing ratio affects the calculated $\rho^2(E0)$ by at most 10%. Assuming no $M1$ contribution, the extracted $\rho^2(E0)$ is 0.061(14). In comparison, the previously existing branching data would have led to a $\rho^2(E0)$ value of 0.5(4), far larger than any other reported $\rho^2(E0)$ value in the deformed rare earth nuclei [121].

If the $K^\pi = 0^+_2$ excitation is assumed to be a β vibration, the rotation vibration model (RVM) [184] relates the $E0$ strength to $E2$ strengths as [121]

$$\rho^2(E0; \beta \rightarrow g) = \frac{4B(E2; 0^+_g \rightarrow 2^+_\beta)\beta_0^2}{e^2 r_0^4 A^{4/3}}, \tag{11.4}$$

where the equilibrium quadrupole deformation β_0 can be extracted from the ground state intraband $B(E2; 2^+_g \rightarrow 0^+_g)$ strength [4]. The RVM value of 0.077(12) for $\rho^2(E0; \beta \rightarrow g)$ is in excellent agreement with the present experimental value of 0.061(14).

It is useful to assess the extent to which $\Delta K = 0$ mixing between the $K^\pi = 0^+_2$ and ground state bands affects the value deduced for the intrinsic interband matrix element. The necessary relations are summarized or derived in Appendix C. The mixing parameter a_0 deduced from the observed $B(E2; 2^+_{K=0_2} \rightarrow 4^+_g)/B(E2; 2^+_{K=0_2} \rightarrow 0^+_g)$ ratio, using (C.10), is a_0=-0.0044(19). (This would be induced by an intrinsic interaction strength $|\langle K^\pi = 0^+_2 | h_0 | K^\pi = 0^+_g \rangle|$=0.44(19) keV and corresponds to a mixing matrix element of ∼2.6 keV for the 2^+ state.) With this mixing, the squared intrinsic matrix element $|\langle K^\pi = 0^+_2 | \mathfrak{M}'(E2) | K^\pi = 0^+_g \rangle|^2$ is 8.4(16) W.u.

While it would be interesting to have the results of a full three-band mixing calculation [117, 185] involving the ground, γ, and $K^\pi = 0^+_2$ excitations, there is currently insufficient information on higher-lying band members and on $M1/E2$ mixing ratios [27] for such an analysis to be feasible. Mixing between the γ and $K^\pi = 0^+_2$ bands is only expected to have a significant effect upon the $K^\pi = 0^+_2$ to ground state band transition strengths in nuclei for which the $K^\pi = 0^+_2$ and γ bands are nearly degenerate. For mixing between the γ and $K^\pi = 0^+_2$ bands to account for the observed $B(E2; 2^+_{K=0_2} \rightarrow 0^+_g)$ strength in ^{162}Er would require nearly complete mixing of the $2^+_{K=0_2}$ and 2^+_γ states, corresponding to an interaction matrix element of ∼100 keV. Such mixing would also

result in a strong $2^+_{K=0_2} \rightarrow 2^+_\gamma$ transition with $B(E2; 2^+_{K=0_2} \rightarrow 2^+_\gamma) \approx 176$ W.u. This would correspond to a γ-ray intensity for the 271 keV $2^+_{K=0_2} \rightarrow 2^+_\gamma$ transition about 7% as strong as for the 1171 keV $2^+_{K=0_2} \rightarrow 0^+_g$ transition. Experimentally, no γ-ray transition was observed between the $2^+_{K=0_2}$ and 2^+_γ states [Fig. 11.3(b)], and the intensity limit obtained (Table 11.1) is inconsistent with such a mixing picture.

Transitions between the $K^\pi = 0^+_2$ and γ bands are also important for interpretation within the framework of the interacting boson model (IBM), since the IBM can predict substantial transition strengths between these two bands [166, 186]. For IBM parameter values relevant to ^{162}Er [187], the predicted interband to in-band transition strength ratio is $B(E2; 2^+_{K=0_2} \rightarrow 2^+_\gamma)/B(E2; 2^+_{K=0_2} \rightarrow 2^+_g) \approx 6$, which is not inconsistent with the present experimental limit of <15 (Table 11.1).

In summary, revised γ-ray branching data show that the decays from the 2^+ state at 1171 keV in ^{162}Er are in good agreement with the Alaga rules for a $K^\pi = 0^+$ excitation, and the analysis used in obtaining the previously measured $B(E2; 0^+_g \rightarrow 2^+_{K=0_2})$ value [8.0(15) W.u.] from Coulomb excitation [169] is validated by the present branching results. These results provide evidence for a collective intrinsic matrix element between the ground and $K^\pi = 0^+_2$ excitations, as expected for a β vibration. This case is therefore one of only a few in which strong evidence for such β-vibrational structure exists, especially for the lowest 0^+ excitation. Also, the resulting $\rho^2(E0)$ value is in agreement with the RVM prediction for a β vibration, and moderately restrictive limits are placed upon transitions to the γ band. Since the structural interpretation of the $K^\pi = 0^+_2$ excitation depends heavily upon a single $B(E2)$ determination, it would, however, be valuable to obtain confirmation of the $2^+_{K=0_2}$ lifetime, either from Coulomb excitation or by direct measurement.

The present results highlight the need to obtain a more complete set of information on the low-lying excitations of ^{162}Er. The 4^+ member of the $K^\pi = 0^+_2$ band has only tentatively been reported [188] and none of the higher band members are known. Since the spin assignment of the previously reported $K^\pi = (0^+_3)$ excitation was altered by the present results, the $K^\pi = 0^+_2$ excitation is left as the only identified low-lying $K^\pi = 0^+$ excitation in ^{162}Er. However, the neighboring higher-mass Er isotopes (^{164,166,168}Er) are all known [168, 171, 172, 189] to have several excited 0^+ states below 2 MeV, and so it is likely that ^{162}Er does as well. Recent results elsewhere in the rare earth region of nuclei [167] indicate that a low-lying β-vibrational excitation can be accompanied by a well-defined higher-lying two-phonon β-vibrational excitation. Further experiments using other low-

spin population mechanisms, such as (p,t) transfer reactions or $(n,n'\gamma)$ scattering, will be required to obtain this information.

Identification of the $K^\pi = 0_2^+$ excitation in ^{162}Er as having probable β-vibrational character is, in and of itself, relevant to the study of the existence and properties of vibrational modes in deformed nuclei. From a broader perspective, though, confirmation of the collective character of this excitation allows the evolution of the lowest collective 0^+ excitation to be traced across the $N{\approx}90$ transition region to the well-deformed rotor nuclei.

Part IV

Model analysis

Chapter 12

The geometric collective model parameter space

12.1 Introduction to the GCM

12.1.1 The geometric Hamiltonian

For a collective nucleus undergoing quadrupole deformation (Section 1.2), it is natural to describe the dynamics of the system by using the deformation coordinates $\alpha_{2\mu}$ as the relevant dynamical variables. In order for predictions of the nuclear excitation properties to be made, an expression for the nuclear Hamiltonian in terms of these deformation variables must somehow be deduced or postulated. This Hamiltonian can then be solved for its eigenvalues and eigenfunctions.

The Hamiltonian will in general be a function of both the coordinates $\alpha_{2\mu}$ and their conjugate momenta $\pi_{2\mu}$. The geometric collective model (GCM), developed by Gneuss, Mosel, and Greiner [190–192], is based upon an approach in which the Hamiltonian is expanded as a power series in the coordinates and momenta. The requirements of rotational, reflection, and time reversal invariance constrain the possible terms which may be present in this Hamiltonian, yielding a series of the form

$$\begin{aligned} H =& \frac{1}{B_2}[\pi \times \pi]^{(0)} + B_3[[\pi \times \alpha]^{(2)} \times \pi]^{(0)} + \cdots \\ &+ C_2[\alpha \times \alpha]^{(0)} + C_3[[\alpha \times \alpha]^{(2)} \times \alpha]^{(0)} + \cdots . \end{aligned} \tag{12.1}$$

The terms may be classified as either "kinetic energy" terms, involving the momenta π, or "potential energy" terms, involving only the coordinates α.

The leading-order kinetic energy term, known as the "harmonic" term, arises directly when the classical expression for the kinetic energy of a liquid drop undergoing small-amplitude vibrations is quantized [5]. If only this term is used as the kinetic energy operator, then the canonical momenta are $\pi_{2\mu}{=}{-}i\hbar\partial/\partial\alpha_{2\mu}$, and the kinetic energy

operator is thus

$$-\frac{\hbar^2}{\sqrt{5}B_2}\sum_\mu \frac{\partial^2}{\partial\alpha_{2\mu}\partial\alpha^*_{2\mu}}. \tag{12.2}$$

The eigenproblem for a Hamiltonian with this kinetic energy operator is equivalent to the Schrödinger equation in Cartesian coordinates in five-dimensional space (Appendix E). The harmonic kinetic energy operator may alternatively be written (see Ref. [5]) in terms of the Euler angles θ_i and the shape coordinates β and γ (Section A.1) as

$$-\frac{\hbar^2}{2B}\left[\frac{1}{\beta^4}\frac{\partial}{\partial\beta}\beta^4\frac{\partial}{\partial\beta} + \frac{1}{\beta^2\sin 3\gamma}\frac{\partial}{\partial\gamma}\sin 3\gamma\frac{\partial}{\partial\gamma} - \frac{1}{4\beta^2}\sum_\kappa \frac{M_\kappa^2}{\sin^2(\gamma-\frac{2}{3}\pi\kappa)}\right], \tag{12.3}$$

where $B \equiv \sqrt{5}B_2/2$ and the M_κ are angular momentum operators which may be expressed in terms of the θ_i and $\partial/\partial\theta_i$. This expression for the kinetic energy was first used in the Bohr Hamiltonian [193], for the description of rotational nuclei.

The potential energy depends only upon the shape of the nucleus, not its orientation in space, and so the potential can be expressed purely in terms of the shape coordinates β and γ. The series expression for the potential energy in terms of these variables is

$$\begin{aligned} V(\beta,\gamma) = \frac{1}{\sqrt{5}}C_2\beta^2 - \sqrt{\frac{2}{35}}C_3\beta^3\cos 3\gamma + \frac{1}{5}C_4\beta^4 \\ - \sqrt{\frac{2}{175}}C_5\beta^5\cos 3\gamma + \frac{2}{35}C_6\beta^6\cos^2 3\gamma + \frac{1}{5\sqrt{5}}D_6\beta^6 + \cdots . \end{aligned} \tag{12.4}$$

Once wave functions for the nuclear eigenstates are calculated (Subsection 12.1.2), electromagnetic matrix elements between these states can be calculated. This requires that the electromagnetic multipole operators, which depend upon the charge and current distributions in the nucleus, be expressed in terms of the quadrupole collective coordinates, something for which there is no unambiguous recipe without a full knowledge of the underlying single-particle dynamics. The most commonly used expression for the electric quadrupole operator is deduced using the mathematically simple, but somewhat arbitrary, assumption that the nuclear charge is uniformly distributed within a radius $R = R_0(1 + \sum_\mu \alpha_{2\mu}Y^*_{2\mu})$ [5, 194]. This charge distribution leads to a series expression in powers of α

$$Q_{2\mu} = \frac{3ZR_0^2}{4\pi}\left[\alpha^*_{2\mu} - \frac{10}{\sqrt{70\pi}}[\alpha\times\alpha]^{(2)\,*}_\mu + \cdots\right], \tag{12.5}$$

where $R_0 \equiv r_0A^{1/3}$ (with $r_0 = 1.1\,\mathrm{fm}$ in Ref. [194]).

12.1.2 Numerical solution of the GCM eigenproblem

The geometric Hamiltonian (12.1) is defined as a differential operator in coordinate space. The Schrödinger-like partial differential equation for this Hamiltonian may be solved directly by finite difference methods. Such a technique has been applied by Kumar and Barranger [195]. However, an alternative approach, which can be considerably more computationally efficient, is to first calculate the matrix elements of the Hamiltonian with respect to a complete set of functions on the coordinate space and to then diagonalize the Hamiltonian in this basis. The eigenfunctions of the five-dimensional harmonic oscillator constitute an especially convenient basis for diagonalization, since these are known in closed form (Section A.2), and group-theoretic results can be applied in calculation of matrix elements of various operators with respect to this basis. Essentially all calculations using the GCM have been performed using the oscillator basis [190–192].

The GCM calculations disscussed in the present work were performed using a computer code written by Troltenier, Maruhn, and Hess [196] which calculates the GCM Hamiltonian eigenvalues and eigenstates by diagonalization in a truncated basis of oscillator eigenfunctions. The code constructs matrix elements of the Hamiltonian operator (12.1) from precomputed matrix elements for each of the potential and kinetic energy terms, which were originally obtained either analytically or by numerical integration [196, 197]. The code includes the necessary matrix elements for calculations using basis functions with phonon numbers up to N=30 and angular momenta up to L=10. The code accomodates calculations with kinetic energy terms through second order in π and potential energy terms through sixth order in β. It calculates electric quadrupole matrix elements between eigenstates using the first two terms of the operator given in (12.5) and deduces $E2$ transition strengths and quadrupole moments from these. For the present work, the code has been adapted to also perform calculations using only the linear term, for reasons discussed in Section 12.2.

If diagonalization of the GCM Hamiltonian in a truncated basis is to yield eigenvalues and eigenfunctions which reasonably reproduce the true ones, the set of basis functions chosen should be adequately matched to the eigenfunctions they are being used to approximate. The eigenfunctions of the harmonic oscillator Hamiltonian

$$H_{\mathrm{osc}} = \frac{1}{B_2}\left([\pi \times \pi]^{(0)} + B_2 C_2 [\alpha \times \alpha]^{(0)}\right), \tag{12.6}$$

depend upon the "stiffness" $s \equiv (B_2 C_2/\hbar^2)^{1/4}$ of the oscillator from which they are con-

structed. The oscillator eigenfunctions for different stiffnesses are related to each other by simple dilation, $\Phi^s(\beta,\gamma,\underline{\theta}) = s^{5/2}\Phi(s\beta,\gamma,\underline{\theta})$ (Section A.2), so the stiffness parameter controls the radial (β) extent of these functions. For diagonalization in a truncated basis to produce accurate results, the s for the basis must chosen so that the radial extent of the basis functions matches the radial extent of the GCM eigenfunctions they are being used to approximate. The code of Ref. [196] uses variational procedures [198] to automatically optimize s for each calculation.

Even if the stiffness of the basis functions is chosen as well as possible, the diagonalization process will fail to produce accurate results if the basis is truncated at too low a phonon number. Solution wave functions which are sharply peaked at some nonzero deformation must be obtained from basis functions which vary rapidly at that deformation, and superposition of a large number of basis functions is required in order for cancellation to be obtained throughout the region of β less than that deformation. Thus, stiffly-deformed wave functions are likely to require basis functions of high phonon number for their description. Basis functions of high phonon number are also needed to produce γ-rigid angular wave functions. For successfully convergent diagonalizations, most of the probability density is usually accounted for by the lowest $\sim$10% of the basis functions in order of increasing phonon number [192, 198]. Significant probability in the highest basis functions is an indicator that the solution may have "overflowed" the truncated basis, requiring additional basis functions for proper description, and that the results of the diagonalization are not reliable. Detailed discussions, and illustrative plots, of the dependence of convergence properties upon the basis s and $N_{\max}$ may be found in Refs. [192, 198].

12.1.3 Application of the GCM

Attempts have been made to derive the parameters in the collective Hamiltonian operator (12.1) from models of the underlying single particle dynamics (*e.g.*, Refs. [199–201]). However, the necessary theory is not sufficiently well developed to provide a full description of the nuclear phenomenology. An alternative, more pragmatic, approach is to choose the collective Hamiltonian so as to best reproduce observed nuclear properties.

The GCM Hamiltonian with eight parameters (B_2, B_3, C_2, C_3, C_4, C_5, C_6, and D_6) accomodated by the existing codes is capable of describing a rich variety of nuclear structures and can flexibly reproduce many details of potential energy surface

shapes [5, 202]. Manual selection of parameter values in this full eight-parameter model is impractical, so parameter values for the description of a particular nucleus must be found through automated fitting [196, 197] of the nuclear observables. This process introduces technical difficulties associated with reliable minimization in eight-dimensional space, and often the parameter values appropriate to a nucleus are underdetermined by the available observables [5]. This is not necessarily an impediment to physical interpretation of the fitted nuclei, since, as discussed in Ref. [197], the available data are usually sufficient to establish the qualitative nature of the GCM potential and determine the coefficients of lower order terms, while the uncertainties in the values of higher-order parameters represent only fine adjustments in the predicted structure. However, a more tractable form of the model is desirable.

A GCM Hamiltonian truncated to the harmonic term in the kinetic energy and to the three lowest-order terms in the potential,

$$V(\beta,\gamma) = \frac{1}{\sqrt{5}}C_2\beta^2 - \sqrt{\frac{2}{35}}C_3\beta^3\cos 3\gamma + \frac{1}{5}C_4\beta^4, \tag{12.7}$$

is sufficient (see Refs. [5, 203]) to produce the rotor, oscillator, and γ-soft structures discussed in Section 1.2 as well as various more exotic possibilities involving shape coexistence. With fewer parameters in the Hamiltonian, it is more feasible to survey the full range of phenomena accessible in the parameter space, and the parameter values applicable to a given nucleus are much more fully determined by the available observables. These benefits must be weighed against the limitations inherent in using the truncated model: the full generality of the GCM is forsaken, precluding, for instance, the description of rigid triaxiality (*e.g.*, Refs. [204, 205]), and, even within its qualitative domain of applicability, the truncated model can be expected to have reduced flexibility in reproducing subtleties of the potential energy surface.

12.2 Scaling properties for the GCM

The truncated form of the GCM, with potential (12.7), still contains four parameters (B_2, C_2, C_3, and C_4). The relationship between a set of values for these parameters and the structure of the resulting predictions is not evident without detailed calculations. It would be useful to have a model which covers the full range of features needed for description of the physical system but which simultaneously has a dependence upon its parameters which is simple, qualitatively predictable by inspection, and directly under-

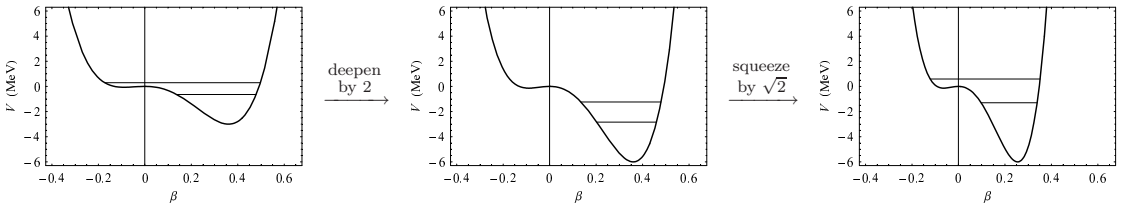

Figure 12.1: Successively deepening and squeezing a potential in the correct proportion (see text) have effects which exactly cancel each other, in that the level energies are simply renormalized and all wave functions (not shown) are dilated by the same amount. Under the scaling transformation, the potential energy function is multiplied by the same factor as the level energies. The rightmost panel can thus be obtained simply by magnifying the vertical axis and compressing the horizontal axis of the leftmost panel. (This is *not* not the case for the intermediate stage shown in the middle panel.)

standable. It is therefore desirable to further simplify the GCM parameter space, but *without* additional truncation of the model.

The GCM predictions for different sets of parameter values are not entirely independent. Proper use of analytic relations can considerably simplify the use of the model.

First, observe that an essentially trivial manipulation saves considerable computational effort. Overall multiplication of any Hamiltonian by a constant factor b results in multiplication of all eigenvalues by b and leaves the eigenstates unchanged. This transformation thus leaves unchanged all energy *ratios*, as well as all observables which depend only upon the wave functions. A practical consequence is that the truncated GCM Hamiltonian is reduced from having four active parameters to effectively having three parameters. The transformation

$$B_2' = \frac{1}{b} B_2 \qquad C_2' = bC_2 \qquad C_3' = bC_3 \qquad C_4' = bC_4 \tag{12.8}$$

has the effect only of rescaling all energies by b. Therefore, all calculations can be performed for some reference value of B_2, varying only C_2, C_3, and C_4, and any calculation with another value of B_2 would be equivalent to one of these to within a rescaling of energies.

There is a second simplification which can be made. It is a well-known heuristic that "deepening" a potential lowers the energies of levels confined within the potential, while "narrowing" a potential raises the level energies. It would thus be expected that successively deepening and then squeezing a given potential, if performed in the correct proportion, could have effects which roughly offset each other, as illustrated in Fig. 12.1.

For a large class of problems, of which the GCM Hamiltonian with harmonic

kinetic energy is a special case (Appendix E), there is an exact analytic result to this effect. Consider the transformation in which the potential is multiplied by a factor a^2 while also dilated by a factor $1/a$, *i.e.*, multiplying β by a in the argument to V,

$$V'(\beta, \gamma) = a^2 V(a\beta, \gamma). \tag{12.9}$$

The effect of this transformation is simply to multiply all eigenvalues by a factor a^2 and radially dilate the wave functions by $1/a$, as shown in Appendix E. Thus, for the truncated GCM Hamiltonian, the transformation

$$B_2' = B_2 \qquad C_2' = a^4 C_2 \qquad C_3' = a^5 C_3 \qquad C_4' = a^6 C_4 \tag{12.10}$$

results in a rescaling of all level energies by a^2 and dilation of all the solution wave functions by $1/a$. This is illustrated in Fig. 12.1. Observe that, since level energies are multiplied by the same scaling factor a^2 as the potential itself, they retain their positions relative to the recognizable "features" of the potential, such as barriers or inflection points.

If the electric quadrupole transition operator (12.5) is truncated to its linear term, then all matrix elements of this operator change by the same factor under wave function dilation (Appendix E), so $B(E2)$ ratios are left unchanged. Many GCM studies have retained the second-order term [196], but, since the different terms in (12.5) scale by different powers of a under dilation (see Appendix E), inclusion of the second-order or higher-order terms destroys the simple invariance of $B(E2)$ ratios. The second-order term usually provides only a small correction to the linear term, and the correct coefficient by which it should be normalized is highly uncertain [5, 194]. Comparative studies by Petkov, Dewald, and Andrejtscheff [206] have shown no clear benefit to its inclusion. In light of the simple scaling properties obtained by its omission, calculations of $B(E2)$ strengths are carried out using a linear electric quadrupole operator throughout the present work.

A scaling result equivalent to that just discussed has been used in earlier work [196, 207, 208] to simplify the automated fitting of experimental data with the full eight-parameter GCM Hamiltonian. In that work, the canonical transformation $\pi \rightarrow \frac{1}{a}\pi$ and $x \rightarrow ax$ [196] was used to produce wave function dilation with no change in energy scale, equivalent to the transformation (E.2) followed by an overall multiplication of the Hamiltonian by a^{-2}. Since in Refs. [196, 207, 208] the second-order form of the quadrupole operator was used, $B(E2)$ ratios *were* changed under scaling. Therefore, the fitting procedure was carried out using only energy ratios, and, after fitting, the wave functions were dilated to reproduce a single $B(E2)$ strength or quadrupole moment.

Systematic use of the scaling relations just discussed is facilitated by the adoption of a simple reparametrization of the GCM potential. Specifically, let us rewrite (12.7) as

$$V(\beta,\gamma) = f\left[\frac{9}{112}d\left(\frac{\beta}{e}\right)^2 - \sqrt{\frac{2}{35}}\left(\frac{\beta}{e}\right)^3\cos 3\gamma + \frac{1}{5}\left(\frac{\beta}{e}\right)^4\right]. \tag{12.11}$$

This expression has been constructed so that varying each of the parameters d, e, and f controls one specific aspect of the potential:

> d – describes the shape of the potential, *i.e.*, d uniquely defines the shape to within a horizontal and vertical scaling
>
> e – expands the potential horizontally, *i.e.*, varying e scales V in the radial coordinate β
>
> f – is a factor multiplying the entire potential, *i.e.*, varying f scales the magnitude of V.

Comparison of the coefficients in (12.11) with those in the original parametrization (12.7) yields the conversion formulae

$$\begin{aligned} d &= \frac{112}{9\sqrt{5}}\frac{C_2C_4}{C_3^2} \qquad e = \frac{C_3}{C_4} \qquad f = \frac{C_3^4}{C_4^3} \\ C_2 &= \frac{9\sqrt{5}}{112}\frac{fd}{e^2} \qquad C_3 = \frac{f}{e^3} \qquad C_4 = \frac{f}{e^4}. \end{aligned} \tag{12.12}$$

The extremum structure of the truncated GCM potential, investigated in Refs. [209, 210], can be expressed very concisely in terms of the present parametrization (12.11). Extrema occur where $V(\beta,\gamma)$ is locally extremal with respect to both β and γ individually. Thus, they are possible where $\cos 3\gamma$ attains its maximum value of +1 (γ=0°, 120°, and 240°) or its minimum value of -1 (γ=60°, 180°, and 300°). Since the potential (12.11) repeats every 120° in γ, it suffices to locate the extrema on one particular ray in the $\beta\gamma$-plane with $\cos 3\gamma$=+1 (*e.g.*, γ=0°) and on one ray with $\cos 3\gamma$=-1 (*e.g.*, γ=180°). Thus, extrema need only be sought on a cut through the potential along the a_0-axis, and these extrema will then be duplicated along the other rays of $\cos 3\gamma=\pm 1$, as illustrated in Fig. 12.2.

Extrema along the two rays γ=0° and γ=180° are found by identification of the zeroes of $\partial V/\partial\beta$ for $\cos 3\gamma$=+1 and for $\cos 3\gamma$=-1. The variable β is a radial coordinate (see Section A.1) and so takes on only positive values. However, the form of the following results is considerably simplified by noting that the only occurrence of $\cos 3\gamma$ in (12.11) is in a product also containing the only occurrence of an odd power of β, so substituting $\cos 3\gamma$=-1 is algebraically equivalent to setting $\cos 3\gamma$=+1 and negating β. Any extremum

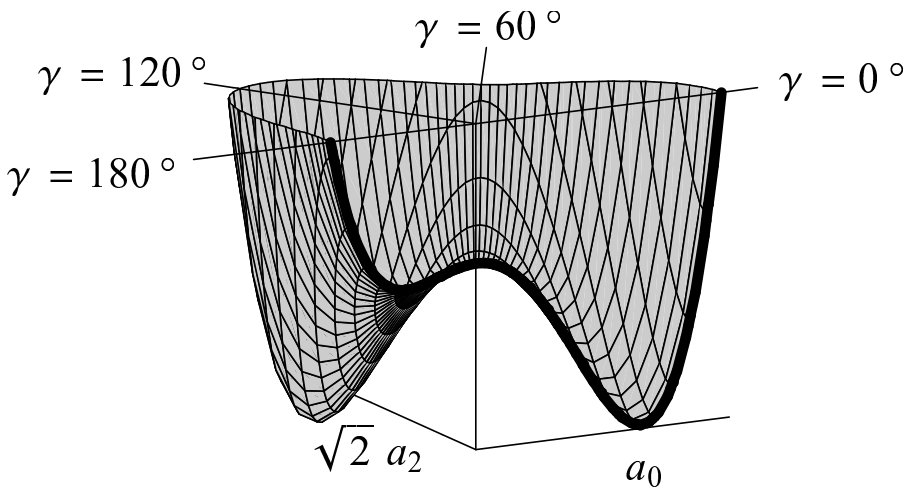

Figure 12.2: The GCM potential function for $d<0$ posesses a global minimum, a saddle point, and a local maximum at $\beta = 0$. The case $d = -5$ is shown here as an example, plotted as a function of the Cartesian coordinates $(a_0, \sqrt{2}a_2)$ or polar coordinates (β, γ), for γ=0° to 180°. The cut along the a_0-axis (thick line) is the same as is shown in the second panel of Fig. 12.3. The global minimum is visible in this figure at γ=0° and 120°, and the saddle point is visible at γ=60° and 180°. The saddle point is a local minimum with respect to β and a local maximum with respect to γ.

occuring for $\cos 3\gamma$=-1 will thus be found when the extrema for $\cos 3\gamma$=+1 are sought, but at a fictitious "negative" β value. A simple expression for the β values yielding extrema along γ=0° follows, but it must be interpreted with the proviso that when a negative β value is encountered it actually represents a positive β value along γ=180°. The only extrema of V along the a_0-axis cut are located at

$$\begin{aligned} \beta &= 0 \qquad && \text{any } d \\ \beta &= \beta_- \qquad && d \le 1 \\ \beta &= \beta_+ \qquad && d \le 1, \end{aligned}$$

where

$$\beta_\pm = \frac{3}{4}\sqrt{\frac{5}{14}}\,(1 \pm r)\,e, \tag{12.13}$$

in terms of $r \equiv \sqrt{1-d}$. The extremal values of the potential are

$$V(\beta_\pm) = -\frac{135}{50176}(r \pm 1)^3(3r \mp 1)f. \tag{12.14}$$

The nature of the extrema — whether they are minima, maxima, saddle points, or inflection points — can be ascertained from the signs of the partial derivatives. The extremum structure of the potential depends only upon the value of d, as summarized in

Table 12.1 and Fig. 12.3. For $d<0$, the potential has both a global minimum and a saddle point at nonzero β (Fig. 12.2). For $0<d<1$, minima are present at both at nonzero β and at $\beta=0$, with the deformed minimum lower for $0<d<8/9$ and the undeformed minimum lower for $8/9<d<1$. For $d>1$, there is only one minimum, located at $\beta=0$.

Let us briefly address the ranges of definition for the parameters e and f. Negating e reflects the potential about $\beta=0$. A positive value of e places the deformed minimum on the prolate side of the cut ($\beta_+>0$), while negative e places the deformed minimum on the oblate side of the cut ($\beta_+<0$). All model predictions for energies and transition strengths are unchanged under interchange of prolate and oblate deformations, and only the signs of quadrupole matrix elements and thus quadrupole moments are affected. Throughout the discussions and examples in the present work, e will be taken positive without loss of generality. Only positive values of f are meaningful, since for f negative the coefficient on the β^4 term in the potential is negative. This makes $V \to -\infty$ as $\beta \to \infty$, leaving the system globally unbound. The effects on the potential of varying the parameters e and f are illustrated in Fig. 12.4.

In terms of the new parameters, overall multiplication of the Hamiltonian by b is obtained by the transformation

$$B_2' = \frac{1}{b}B_2 \qquad d' = d \qquad e' = e \qquad f' = bf, \tag{12.15}$$

and deepening the potential by a^2 while dilating by $1/a$ is accomplished by the transformation

$$B_2' = B_2 \qquad d' = d \qquad e' = \frac{1}{a}e \qquad f' = a^2 f. \tag{12.16}$$

If two sets of parameter values, call them (B_2, d, e, f) and (B_2', d', e', f'), can be transformed into each other by any combination of these scaling relations, the solutions for these parameter sets will be identical, to within energy normalization and wave function dilation. If, however, (B_2, d, e, f) and (B_2', d', e', f') cannot be transformed into each other, the solutions for these parameters will be distinct. Parameter sets are thus naturally grouped into "families", where (B_2, d, e, f) and (B_2', d', e', f') are members of the same family if and only if they are related by the scaling transformations (12.15) and (12.16).

We are now equipped to construct a "structure parameter" S which is invariant under the transformations (12.15) and (12.16). Let

$$S \equiv \frac{1}{B_2 e^2 f}. \tag{12.17}$$

d	β	Extremum type	d	β	Extremum type
(-∞,0)	β_- (<0)[a]	Saddle point[b]	(8/9,1)	0	Minimum (global)
	0	Maximum		β_-	Saddle[c]
	β_+	Minimum (global)		β_+	Minimum (not global)
0	0 (=β_-)	Inflection point	1	0	Minimum (global)
	β_+	Minimum (global)		β_- (=β_+)	Inflection point
(0,8/9)	0	Minimum (not global)	(1,∞)	0	Minimum (global)
	β_-	Saddle point[c]			
	β_+	Minimum (global)			
8/9	0	Minimum (global)			
	β_-	Saddle point[c]			
	β_+	Minimum (global)			

[a] A "negative" solution for β indicates an extremum at γ=180°, *i.e.*, on the negative a_0-axis (see text).
[b] Local minimum with respect to β and local maximum with respect to γ.
[c] Local maximum with respect to β and local minimum with respect to γ.

Table 12.1: The locations and types of each of the extrema in $V(\beta, \gamma)$ along the a_0-axis cut, for the different ranges of d values. Extrema are given in order along the a_0-axis cut.

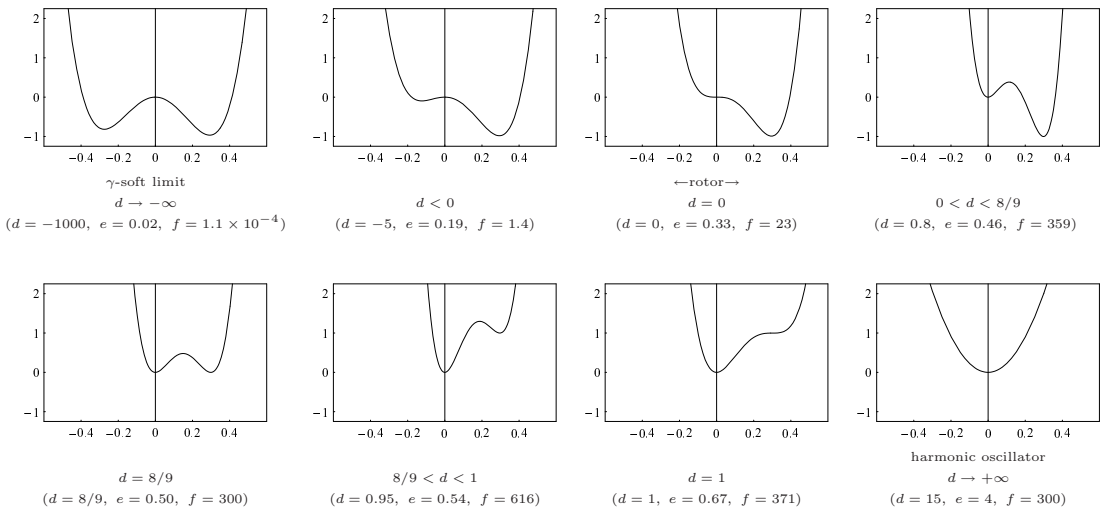

Figure 12.3: Illustration of the qualitatively different shapes of the GCM potential function (12.11) obtained for different ranges of values for the parameter d. Potentials are shown as a function of β along the a_0-axis cut (see text). For f in MeV, the energy scale is also in MeV.

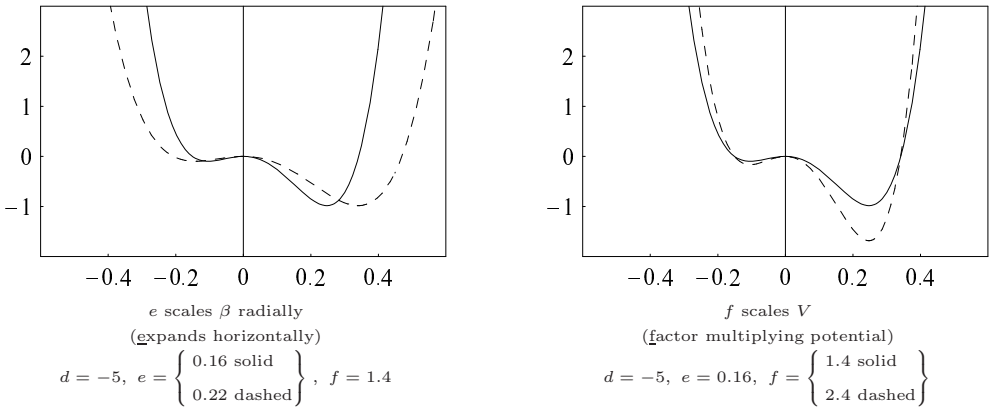

Figure 12.4: Horizontal and vertical scaling of the GCM potential function (12.11), obtained as the effects of changing the values of the parameters e and f, respectively. Potentials are shown as a function of β along the a_0-axis cut (see text). For f in MeV, the energy scale is also in MeV.

Under overall multiplication of the Hamiltonian (12.15),

$$\begin{aligned} S' &= \frac{1}{\left(\frac{1}{b}B_2\right)(e)^2\,(bf)} \\ &= \frac{1}{B_2 e^2 f} = S, \end{aligned} \tag{12.18}$$

and, under deepening and narrowing of the potential (12.16),

$$\begin{aligned} S' &= \frac{1}{(B_2)\left(\frac{1}{a}e\right)^2(a^2 f)} \\ &= \frac{1}{B_2 e^2 f} = S, \end{aligned} \tag{12.19}$$

so S is unchanged under both transformations. If two points in parameter space are characterized by the same values of d and S, they yield identical energy spectra, to within an overall normalization factor, and identical wave functions, to within dilation, and consequently identical $B(E2)$ ratios. Two points characterized by different values of d or of S will in general give different energy spectra, wave functions, and $B(E2)$ ratios. Increasing S corresponds to decreasing the mass parameter B_2, making the potential narrower, or making the potential shallower, all of which have the effect of raising the energy levels within the potential. Thus, for a given potential shape, given by d, the parameter S determines how "high" the levels lie relative to the features of the potential.

12.3 Mapping the GCM parameter space

The truncated GCM described in Section 12.2 is effectively a *two-parameter* model, with parameters d and S. The two other degrees of freedom remaining from the four original parameters provide only an overall normalization factor on the energy scale and a radial scaling for the wave functions in the coordinate β. Because of the simplicity of this model, the behavior of an observable over the *entire model space* can be summarized on a single contour plot. However, the parameter values needed to cover the structural features of interest span many orders of magnitude, so it is necessary to make some preliminary analytic estimates to guide the numerical calculations if an effective and comprehensive survey of the parameter space is to be made.

Let us first consider what qualitatively different types of behavior are possible within the model space. Each of the different potential "shapes" depicted in Fig. 12.3 can give rise to a several different types of structure, depending upon the excitation energy of the ground state and other low-lying levels relative to the minimum of the potential. These structural regimes are illustrated in Table 12.2. For potentials with $d<0$:

> 1. If level energies lie well below the saddle point, the states will be energetically confined to the deformed minimum, yielding rotational behavior.
>
> 2. If level energies lie between the saddle point and the local maximum at $\beta=0$, all γ values will be energetically accessible, but $\beta=0$ will still not be accessible. In this case, deformed γ-soft structure is possible.
>
> 3. If level energies lie well above the local maximum at $\beta=0$, the potential controlling the behavior of these states is dominantly a β^4 quartic oscillator well.

For potentials with $0<d<1$, two minima are present, one at zero deformation and one at nonzero deformation:

> 1. If level energies lie well below the higher minimum, the states will be energetically confined to the global minimum, yielding rotational behavior for $0<d<8/9$ or approximately harmonic oscillator behavior for $8/9<d<1$.
>
> 2. If level energies lie above both minima but below the saddle point barrier, the energetically-accessible regions around the two minima will be separated from each other by this barrier. States involving mixing through the barrier may be possible.
>
> 3. If level energies lie well above the barrier, the behavior again approaches that of a quartic oscillator.

	$d \leq 0$	$0 \leq d \leq 8/9$	$8/9 \leq d \leq 1$	$d \geq 1$
	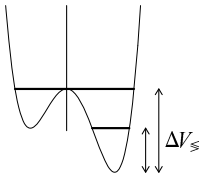	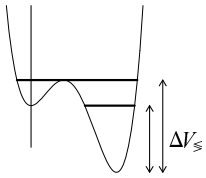	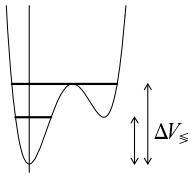	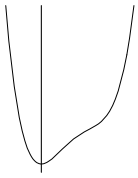
$\Delta V_<$	$V(\beta_-) - V(\beta_+)$	$-V(\beta_+)$	$V(\beta_+)$	—
$\Delta V_>$	$-V(\beta_+)$	$V(\beta_-) - V(\beta_+)$	$V(\beta_-)$	—

Table 12.2: Structures possible for each of the qualitatively different shapes of the truncated GCM potential, shown on the cut along the a_0-axis. The quantities $\Delta V_{\lessgtr}$ represent the approximate ground state energies, relative to the global minimum of the potential, at which the boundaries between the structural regimes occur. For energies substantially less than $\Delta V_<$, the low-lying levels are "trapped" in the global minimum. For energies substantially greater than $\Delta V_>$, quartic anharmonic vibrational structure dominates.

Finally, for potentials with d>1, deformed structure is not possible. If level energies are low in the well, so the states are confined to a region of small β, where the β^2 term in the potential dominates, harmonic oscillator behavior arises, but for level energies much higher in the well the β^4 term dominates, yielding quartic oscillator behavior.

Thus, for the potentials with d<1, the qualitative nature of the low-lying levels is expected to depend upon the excitation energy of these levels relative to specific extremum features of the potential well, and three possible different structural regimes are possible at each given value of d. We can estimate the values for S, at a given d, at which we expect the transition to occur from the lowest-energy structural regime to the intermediate regime [call this $S_<(d)$] and at which we expect the transition to occur from this intermediate regime to the anharmonic oscillator regime [call this $S_>(d)$]. The energy which the ground state must have, relative to the lowest point of the potential, in order to be at the approximate boundary between each type of structure is given Table 12.2, where it is denoted $\Delta V_<$ or $\Delta V_>$, respectively. The Wentzel-Kramers-Brillouin approximation (*e.g.*, Ref. [2]) yields a quantization condition

$$\int_0^{\beta_{\max}} d\beta \sqrt{B[E - V(\beta)]} \approx \left(n + \frac{3}{4}\right) \hbar\pi \qquad n = 0, 1, 2, \ldots \tag{12.20}$$

on the radial coordinate in the five-dimensional Schrödinger equation, ignoring here the five-dimensional equivalent of the centrifugal potential, where the mass B appearing in the usual form of the Schrödinger equation is $\sqrt{5}B_2/2$ (Appendix E). Since we seek only an

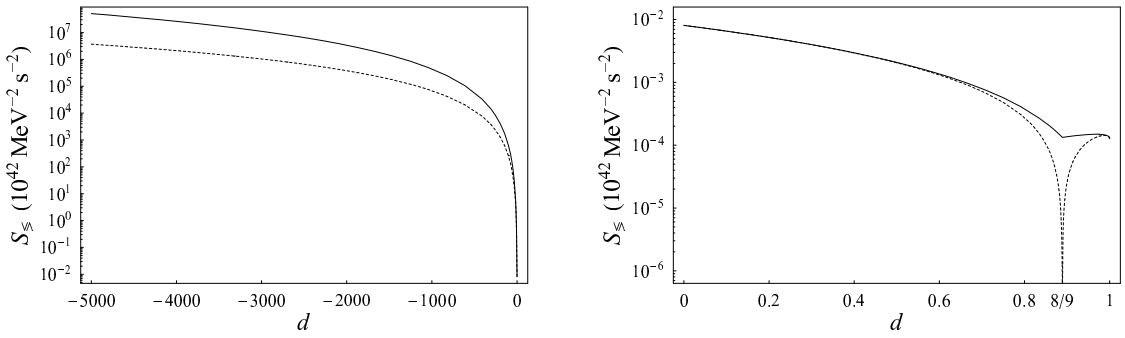

Figure 12.5: The quantities $S_<$ (dotted line) and $S_>$ (solid line) as functions of d. The intervals $d \leq 0$ and $0 \leq d \leq 1$ are plotted separately for clarity.

order-of-magnitude estimate, let us consider only the ground state and replace $E - V(\beta)$ in this equation by a constant value $E - \overline{V}$ representing the excitation energy relative to the "average" floor of the well. Then (12.20) reduces to the relation,

$$\beta_{\max} \approx \frac{1}{2} \frac{2\pi\hbar}{\sqrt{2B(E-\overline{V})}}, \tag{12.21}$$

which simply states that, for the ground state, approximately one-half of a de Broglie wavelength must fit within the width $\beta_{\max}$ of the well. For the GCM potential, let us approximate the width of the well by β_+ and require that the ground state lie at the energy $\Delta V_<$ or $\Delta V_>$ relative to the floor of the well. This provides the desired estimates for the parameter values at which the transition between structural regimes occurs,

$$S_{\lessgtr} \approx \frac{1}{\pi^2\hbar^2} \left(\frac{\Delta V_{\lessgtr}}{f}\right) \left(\frac{\beta_+}{e}\right)^2, \tag{12.22}$$

where factors of order unity have been suppressed in this derivation. The values of $S_{\lessgtr}(d)$ obtained by substituting the expressions for $\Delta V_{\lessgtr}$ from Table 12.2 are plotted in Fig. 12.5

For $d<8/9$, rotational behavior occurs when the levels are at a sufficiently low energy with respect to the potential. For these rotational nuclei, several useful analytic estimates can be made of the quantitative dependence of observables on d and S. For states sufficiently low-lying (well-confined) in the deformed minimum, the structure approaches that of small oscillations about a deformed equilibrium, which is described analytically in the rotation-vibration model (RVM) [184]. The potential in the region of the minimum is treated as a paraboloid, and, to first approximation, pure harmonic oscillations occur in the β and γ degrees of freedom. Using the leading-order approximations from this model,

the 2^+ state energy for the yrast band is determined by the moment of inertia, giving

$$E_{2g} \approx \frac{\hbar^2}{B\beta_0^2}, \tag{12.23}$$

where β_0 is the equilibrium deformation.

The β-vibrational and γ-vibrational excitation energies are determined by the curvature of the potential in each of these degrees of freedom, yielding

$$E_\beta \approx \hbar\sqrt{\frac{V_{\beta\beta}}{B}} \qquad E_\gamma \approx \hbar\sqrt{\frac{V_{\gamma\gamma}}{B\beta_0^2}}, \tag{12.24}$$

where $V_{\beta\beta} \equiv \partial^2 V/\partial\beta^2$ and $V_{\gamma\gamma} \equiv \partial^2 V/\partial\gamma^2$. The bandhead state energies are related to E_β and E_γ by $E(0_\beta^+) \approx E_\beta$ and $E(2_\gamma^+) \approx E_\gamma + \frac{1}{3}E_{2g}$ [184]. For the GCM potential (12.11), the curvatures in the β and γ directions, evaluated at the global minimum $\beta = \beta+$, are

$$V_{\beta\beta}(\beta_+, 0) = \frac{9}{28} r(1+r)\frac{f}{e^2} \tag{12.25}$$

$$\beta_+^{-2} V_{\gamma\gamma}(\beta_+, 0) = \frac{27}{28}(1+r)\frac{f}{e^2}, \tag{12.26}$$

in terms of $r = \sqrt{1-d}$. Note that these β and γ curvatures have *different* dependences upon d, through r, so their *ratio* varies with d. Substituting these expressions for $V_{\beta\beta}$ and $\beta^{-2}V_{\gamma\gamma}$, along with the value $\beta_0 \approx \beta_+$, into (12.24) yields the estimates

$$E_{2g} \approx \frac{224}{45}\frac{1}{(1+r)^2}\frac{\hbar^2}{Be^2} \tag{12.27}$$

$$E_\beta \approx \sqrt{\frac{9}{28}}\sqrt{r(1+r)\frac{\hbar^2 f}{Be^2}} \tag{12.28}$$

$$E_\gamma \approx \sqrt{\frac{27}{28}}\sqrt{(1+r)\frac{\hbar^2 f}{Be^2}}. \tag{12.29}$$

From the ratios of these expressions, the vibrational energies normalized to the yrast 2^+ energy are

$$\frac{E_\beta}{E_{2g}} \approx \frac{135}{448\sqrt{7}}\sqrt{\frac{r(1+r)^5}{\hbar^2 S}} \tag{12.30}$$

$$\frac{E_\gamma}{E_{2g}} \approx \frac{135\sqrt{3}}{448\sqrt{7}}\sqrt{\frac{(1+r)^5}{\hbar^2 S}}, \tag{12.31}$$

and the ratio of the β and γ vibration excitation energies is simply

$$\frac{E_\beta}{E_\gamma} \approx \sqrt{\frac{r}{3}}. \tag{12.32}$$

These ratios of energies (12.30)–(12.32) depend only upon d and S, as expected from the scaling properties of Section 12.2. These estimates provide guidance (needed below) as to both the range of d values of physical interest and the appropriate axis scale or calculational mesh spacing for the parameter d. Observe that, by (12.32), it is expected that "β-stiff" rotors, with $E_\beta > E_\gamma$, occur for d<-8, while "γ-stiff" rotors, with $E_\gamma > E_\beta$, occur for d>-8.

The combined results of this section give a detailed picture of the qualitative characteristics expected for predictions of the truncated GCM and provide quantitative estimates as to where in the (d, S) parameter space these properties are to be found. The results are summarized graphically as a "map" of the parameter space in Fig. 12.6.

Contour plots of several observables over the (d, S) parameter space are shown in Figs. 12.7–12.8. All observables plotted are *ratios* of energies or of $B(E2)$ values. As discussed in the previous section, at a given (d, S) any desired overall normalization for the energy and $B(E2)$ scales can then be obtained by proper rescaling of the well width, well depth, and mass parameter.

The d-axis in Figs. 12.7–12.8 extends from d=-5000 to 5. Inclusion of the low end of this range is necessary to allow description of rotational nuclei with high-lying β vibrations (12.32). In order to encompass this full range while maintaining a reasonably detailed view of the region around d=0 in the plots, it is helpful to use a nonlinear d-axis scale for $d < 0$. The estimate (12.32) indicates that for rotor-vibrator nuclei the observable E_β/E_γ varies as $(1-d)^{1/4}$, so for $d < 0$ the d-axis of Figs. 12.7–12.8 is chosen to be linear in $(1-d)^{1/4}$.

In the range of d values being considered, the S values resulting in pheonomena of interest span approximately *fourteen* orders of magnitude, as is seen from Fig. 12.5. This occurs since S is defined in terms of e and f, and the values of these parameters needed to construct a reasonably-sized potential vary greatly with d (see Fig. 12.3 for examples). However, at any particular value of d, only about three decades in S, those immediately surrounding S=$S_>(d)$, contain predictions of interest. To make effective use of plotting space, the S-axis in Figs. 12.7–12.8 is expanded to show only $10^{-2}S_>(d) \leq S \leq 10^{+1}S_>(d)$ at each point along the d-axis. Fig. 12.9(a) facilitates the reading of S directly off the contour plots.

Details of the calculational mesh used to generate Figs. 12.7–12.8 are given in Table 12.3. A single point in (d, S) space corresponds to an entire two-parameter family

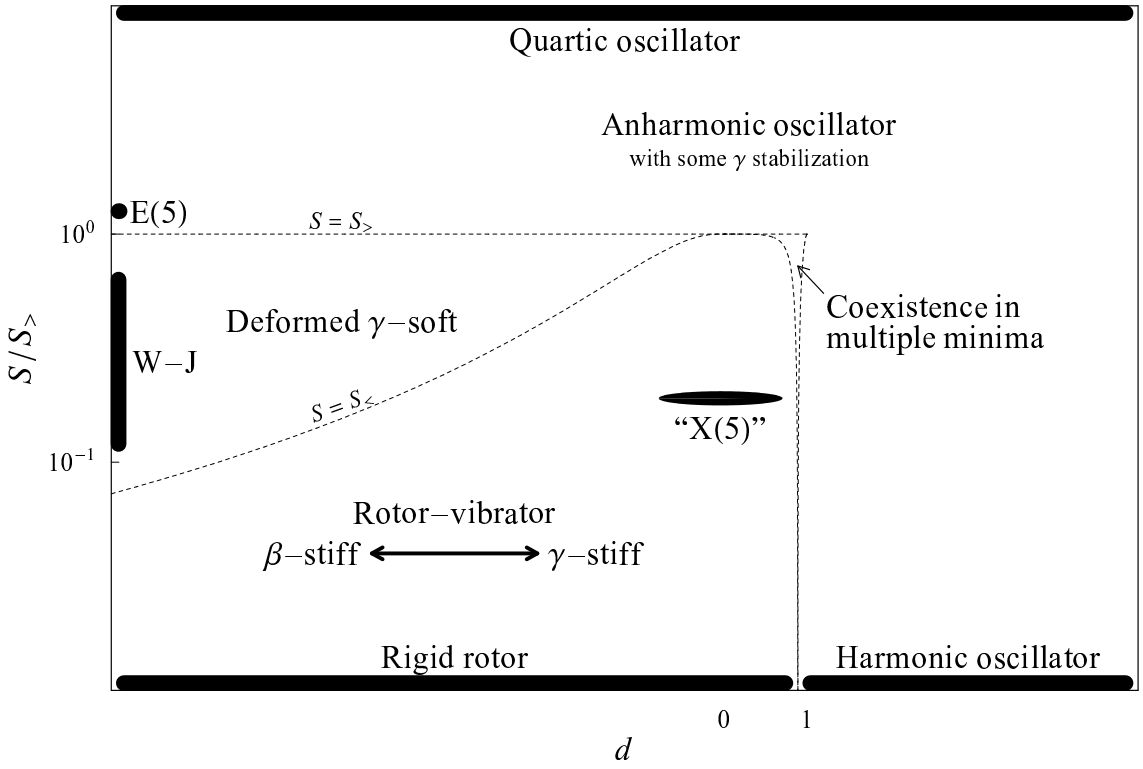

Figure 12.6: Map of the GCM (d, S) parameter space. The regions in which qualitatively different structures occur are indicated. The curves $S = S_<$ and $S = S_>$ (dotted lines) provide estimates for the approximate boundaries between these regions. Within the rotor-vibrator region, the stiffness for β and γ vibrations varies with d (double arrow) with a dependence given approximately by (12.32). Bars along the edges of the plot represent structures which occur in their ideal form at $d \to \pm\infty$ or $S \to 0$ or ∞, as discussed in more detail in Section 13.1. ("W-J" denotes Wilets-Jean rigidly-deformed γ-soft structure.) Parameter values which reproduce E(5)-like and X(5)-like structures are also investigated in Chapter 13. The d- and S-axis scales match those of Figs. 12.7–12.8 (see text) to facilitate direct comparison.

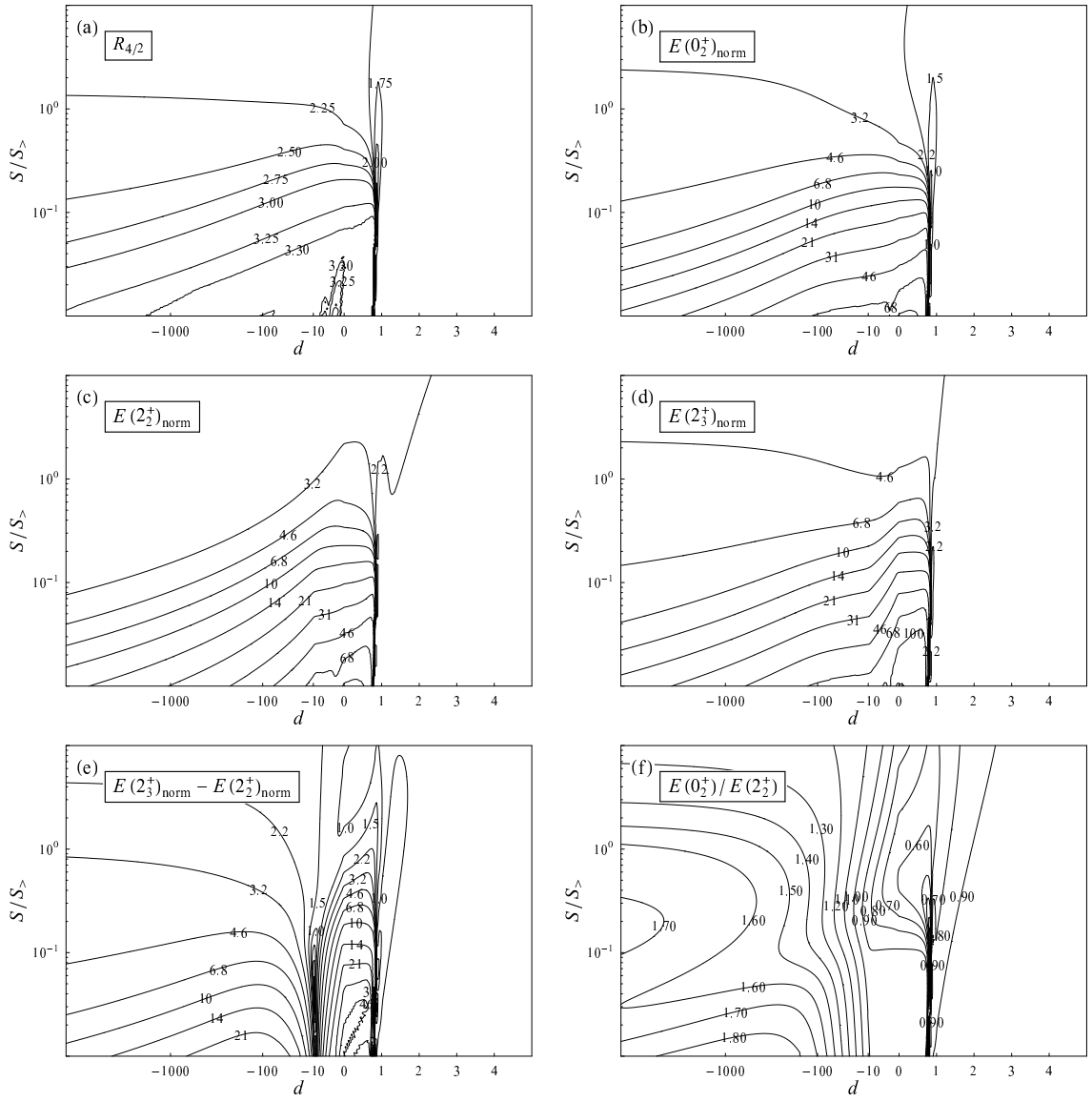

Figure 12.7: Energy observable predictions of the GCM for $-5000 \leq d \leq 5$ and $10^{-2}S_> \leq S \leq 10^{+1}S_>$: (a) $R_{4/2} \equiv E(4_1^+)/E(2_1^+)$, (b) $E(0_2^+)/E(2_1^+)$, (c) $E(2_2^+)/E(2_1^+)$, and (d) $E(2_3^+)/E(2_1^+)$. The observables (e) $[E(2_3^+) - E(2_2^+)]/E(2_1^+)$ and (f) $E(0_2^+)/E(2_2^+)$ can be deduced from these.

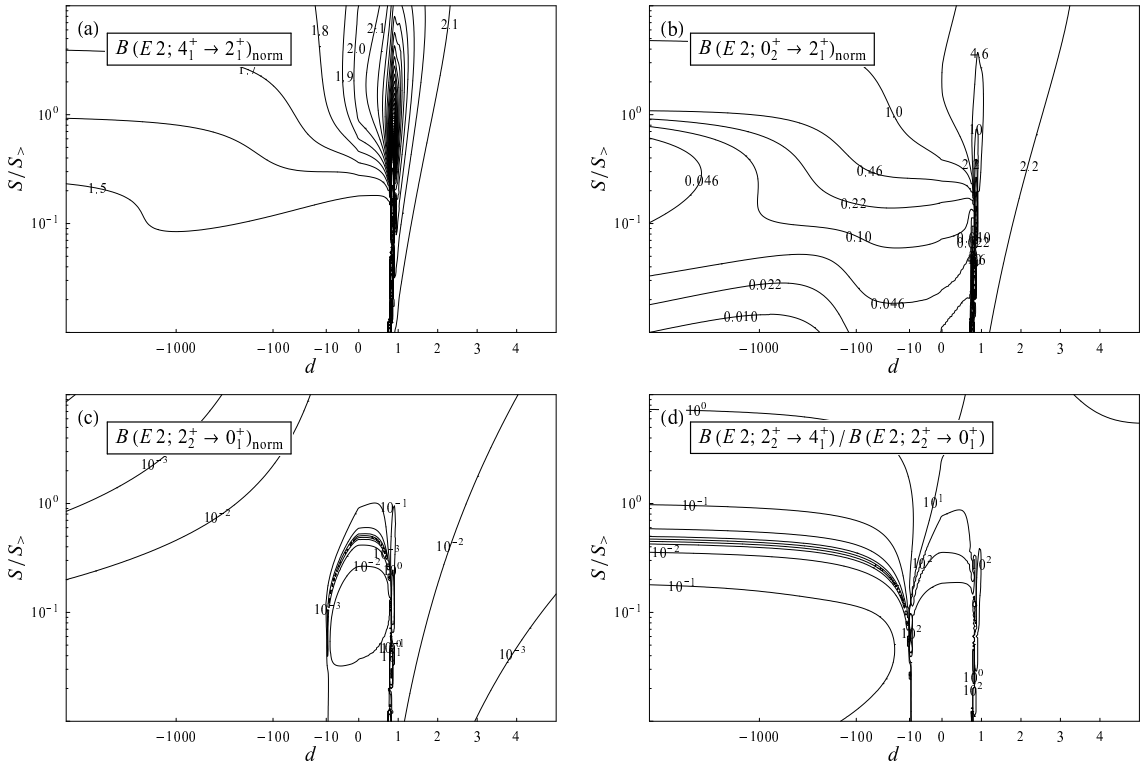

Figure 12.8: $B(E2)$ observable predictions of the GCM for $-5000 \leq d \leq 5$ and $10^{-2}S_> \leq S \leq 10^{+1}S_>$: (a) $B(E2; 4_1^+ \to 2_1^+)/B(E2; 2_1^+ \to 0_1^+)$, (b) $B(E2; 0_2^+ \to 2_1^+)/B(E2; 2_1^+ \to 0_1^+)$, (c) $B(E2; 2_2^+ \to 0_1^+)/B(E2; 2_1^+ \to 0_1^+)$, and (d) $B(E2; 2_2^+ \to 4_1^+)/B(E2; 2_2^+ \to 0_1^+)$.

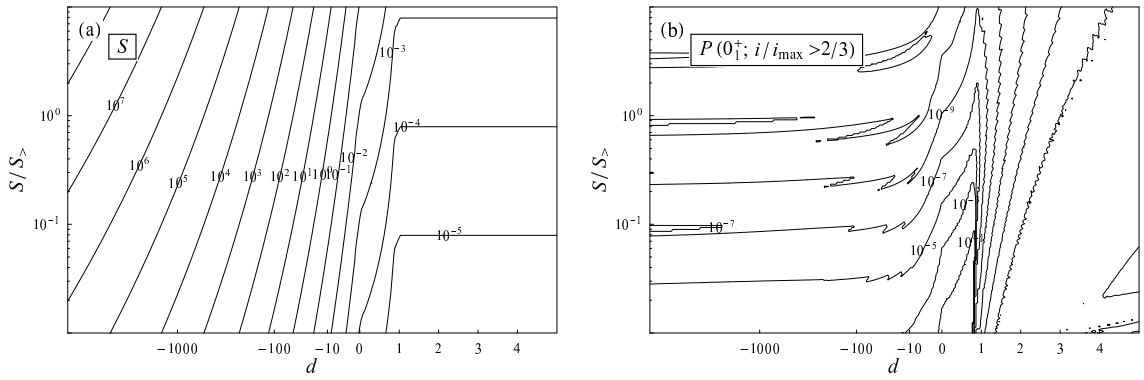

Figure 12.9: Auxiliary plots for $-5000 \leq d \leq 5$ and $10^{-2}S_> \leq S \leq 10^{+1}S_>$: (a) S values for the calculations of Figs. 12.7–12.8, to allow S parameter values to be read directly, rather than as $S/S_>$, for points on these plots, and (b) the total probability content of the highest-indexed 1/3 of basis states for the calculated 0_1^+ state, as an indicator of convergence (see text).

Figure	Axis	Range	Steps	Distribution function
Figs. 12.7–12.9	d	-5000 – 5	300	$\begin{cases} 1-(1-d)^{1/4} & d<0 \\ d & d\geq 0 \end{cases}$
	S	$10^{-2}S_{>}$ – $10^{+1}S_{>}$	200	$\log S$
Fig. 12.10	d	0 – 1	100	d
	S	$10^{-2}S_{>}$ – $10^{+1}S_{>}$	50	$\log S$

Table 12.3: Calculational meshes used to generate the contour plots of Figs. 12.7–12.10. Calculation mesh points are equally spaced with respect to the distribution function in the rightmost column.

of points related by scaling transformations in the (B_2, C_2, C_3, C_4) parameter space, but for numerical diagonalization to be carried out by the code of Ref. [196] a specific set of values for the Hamiltonian coefficients B_2, C_2, C_3, and C_4 must be chosen. The choice is largely irrelevant, but the diagonalization code [196] can fail to produce convergent results if the eigenstates have $\langle\beta\rangle$ many orders of magnitude away from 1. The actual calculations for Figs. 12.7–12.8 were performed by setting B_2=50 MeV. For $d \leq 1$, e was chosen such that β_+=0.3, and, for $d > 1$, e was set to 0.669.

Convergence failure of the code occurs for some of the most sharply deformed structures covered by Figs. 12.7–12.8. At very low S values in the rotor region, where the most clearly well-deformed structure occurs and $R_{4/2}$ should approach 3.33, the numerical calculations instead exhibit sporadic patches of sharp fall-off in the $R_{4/2}$ value [Fig. 12.7(a), at $d \lesssim 0$]. As outlined in Subsection 12.1.2, an indication of the convergence properties of a calculation is given by the total fraction of the probability contained in the high-phonon-number basis states. Fig. 12.9(b) provides a contour plot of the probability content of the highest 1/3 of basis states, in order of increasing phonon number [196], for the calculated 0_1^+ state. The calculations in the region of convergence failure exhibit relatively high values ($\gtrsim 10^{-3}$) for this quantity.

Since many observables vary rapidly in the interval $0<d<1$, a few selected contour plots showing an expanded view of this region are given in Fig. 12.10. Caution must be exercised in using the results produced by the code of Ref. [196] for parameter sets near $d = 0.8$, since Fig. 12.10(f) indicates possible convergence failure in this region. Detailed convergence studies must be carried out to determine whether, and to what extent, this is attributable to a failure in the automatic optimization of the basis stiffness or to a genuine

need for basis functions with $N > 30$ in the diagonalization (Subsection 12.1.2).

Energy observables are shown in Fig. 12.7. The values of the ratio $R_{4/2} \equiv E(4_1^+)/E(2_1^+)$ [Fig. 12.7(a)], an observable which serves as a basic indicator of structure (Appendix A), closely match the values expected from the $S_<$ and $S_>$ estimates. The region with $2.2<R_{4/2}<2.6$ corresponds approximately to that between the dotted lines representing $S_<$ and $S_>$ in Fig. 12.6, the region in which deformed γ-soft structure is expected. For the rotational-vibrational nuclei, found in the lower left-hand region of the plots, the observables $E(0_2^+)/E(2_1^+)$, $E(2_2^+)/E(2_1^+)$, and $E(2_3^+)/E(2_1^+)$ [Fig. 12.7(b-d)] reflect the basic dependences of the β and γ excitation energies estimated in (12.30) and (12.32). At a given d, the excited band energies increase relative to $E(2_1^+)$ as S decreases. Degeneracy of the β and γ excitations is expected at $d\approx -8$, and this behavior is clearly visible from the sharp minimum in $[E(2_3^+)-E(2_2^+)]/E(2_1^+)$ [Fig. 12.7(e)], where an avoided level crossing occurs. To the left of this division, the 2_2^+ state is the γ-vibrational bandhead; whereas, to the right of this division, the 2_2^+ state is the β-vibrational 2^+ band member. Proceeding to the left of the band crossing, the 0_2^+ level energy rises relative to the 2_2^+ energy [Fig. 12.7(f)], as expected, due to increasing β stiffness. The 0_2^+ energy saturates at $\lesssim 2E(2_2^+)$, however, since as the β vibrational excitation continues to rise it leaves the two-phonon γ-vibrational state as the lowest $K = 0$ excitation (see Ref. [184]).

$B(E2)$ observable predictions are shown in Fig. 12.8. The ratio $B(E2; 4_1^+ \rightarrow 2_1^+)/B(E2; 2_1^+ \rightarrow 0_1^+)$ [Fig. 12.8(a)] varies essentially smoothly from rotational values to harmonic oscillator values (Appendix A), except that extreme large and small values are encountered in a narrow region between $d \approx 0.8$ and $d \approx 0.9$. In this region, structures involving coexistence in multiple minima are expected, so the 2_1^+ and 4_1^+ levels do not necessarily correspond to the same structure. Numerical convergence may also not be occurring for certain calculations in this region, as discussed above. The observable $B(E2; 0_2^+ \rightarrow 2_1^+)/B(E2; 2_1^+ \rightarrow 0_1^+)$ [Fig. 12.8(b)] is of interest as the β-vibrational decay strength for rotational nuclei. In the region $d \lesssim -8$, $B(E2; 2_2^+ \rightarrow 0_1^+)/B(E2; 2_1^+ \rightarrow 0_1^+)$ [Fig. 12.8(c)] is the γ-vibrational decay strength. The predictions for the observable $B(E2; 2_2^+ \rightarrow 4_1^+)/B(E2; 2_2^+ \rightarrow 0_1^+)$ [Fig. 12.8(d)] may be compared with the "Alaga ratio" predictions for true rotors (Section A.4), those for the 2_γ^+ state if $d \lesssim -8$ or for the 2_β^+ state if $d \gtrsim -8$.

The general approach and specific techniques discussed in this chapter recast the GCM, with truncated Hamiltonian, as a very tractable model for theoretical studies and

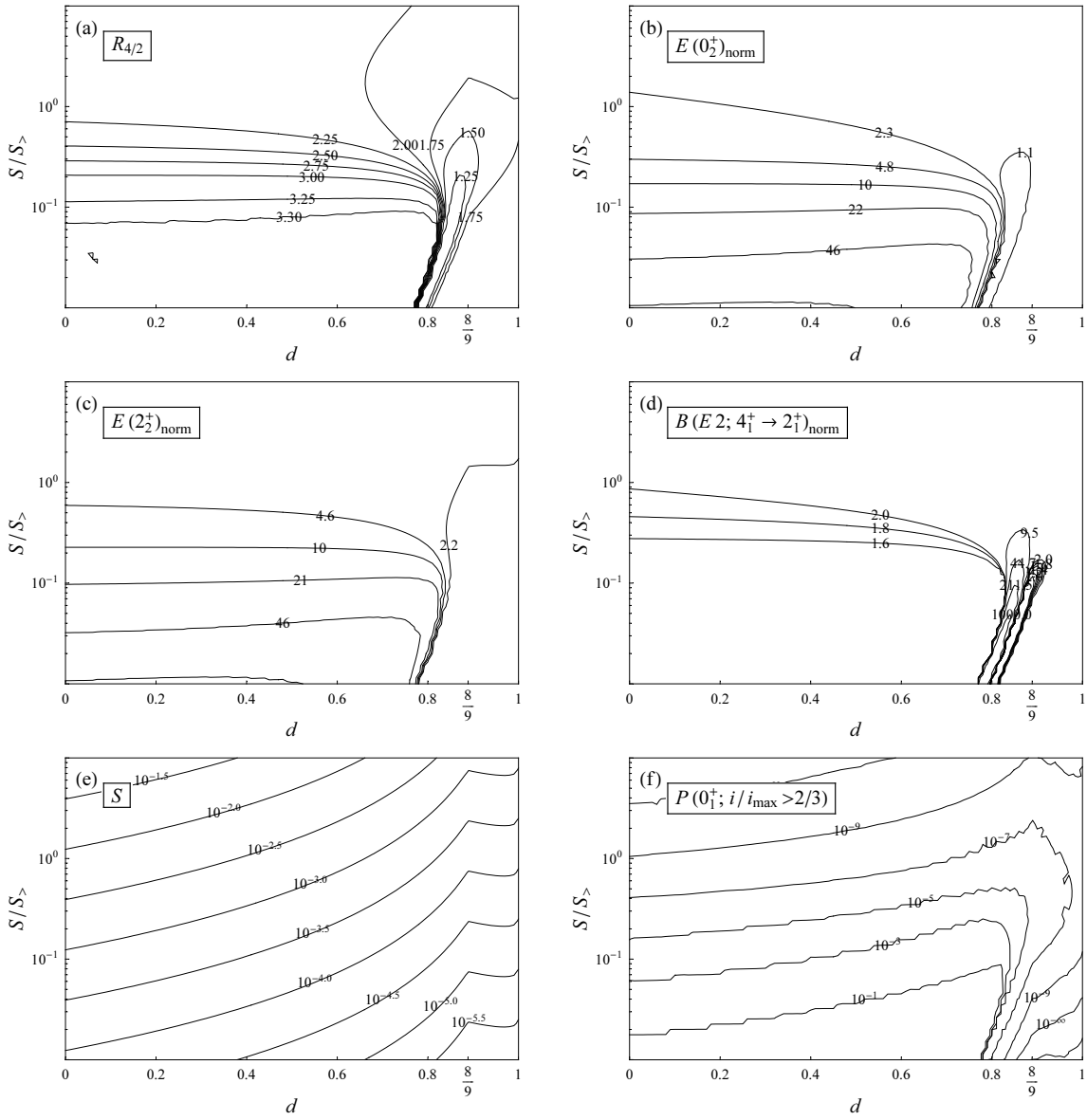

Figure 12.10: Selected prediction of the GCM for $0 \leq d \leq 1$ and $10^{-2}S_> \leq S \leq 10^{+1}S_>$, with additional auxiliary plots: (a) $R_{4/2} \equiv E(4_1^+)/E(2_1^+)$, (b) $E(0_2^+)/E(2_1^+)$, (c) $E(2_2^+)/E(2_1^+)$, (d) $B(E2;4_1^+ \to 2_1^+)/B(E2;2_1^+ \to 0_1^+)$, (e) S, (f) probability content of the highest-indexed 1/3 of basis states for the 0_1^+ state calculation, as an indicator of convergence.

practical application.* The parameter values most appropriate for the description of a given nucleus can be deduced by inspection of contour plots such as those in Figs. 12.7–12.10. Some specialized results pertaining to specific classes of potential are addressed in the following chapter. Examples of the phenomenological application of the model are discussed in Chapter 15.

*The results of this chapter were subsequently reported in M. A. Caprio, Phys. Rev. C **68**, 054303 (2003).

Chapter 13

Special potentials in the geometric collective model

13.1 The quadratic-quartic potential

Gamma-independent potentials have special symmetry properties. The Hamiltonian consisting of a γ-independent potential with the harmonic kinetic energy operator is invariant under the group O(5) of rotations in the five-dimensional space of the coordinates $\alpha_{2\mu}$ (Section A.3). This has several consequences, including that the level energies follow a multiplet structure and the wave functions are separable into radial and angular factors. The harmonic oscillator, E(5), and well-deformed γ-soft structures introduced in Sections 1.2 and 1.3 are all generated by γ-independent potentials.

If the coefficient C_3 in the truncated GCM potential (12.7) is chosen equal to zero, so

$$V(\beta,\gamma) = \frac{1}{\sqrt{5}}C_2\beta^2 + \frac{1}{5}C_4\beta^4, \tag{13.1}$$

then the potential is γ-independent. When C_2 is positive and C_4 is positive [Fig. 13.1(a)], the potential has only a minimum at β=0. The quadratic term dominates at small β, and the quartic term dominates at large β. For C_2=0 [Fig. 13.1(b)], the special case of a quartic oscillator occurs. (This potential has recently found application in the description of anharmonic oscillator nuclei [211].) When C_2 is negative and C_4 is positive [Fig. 13.1(c)],

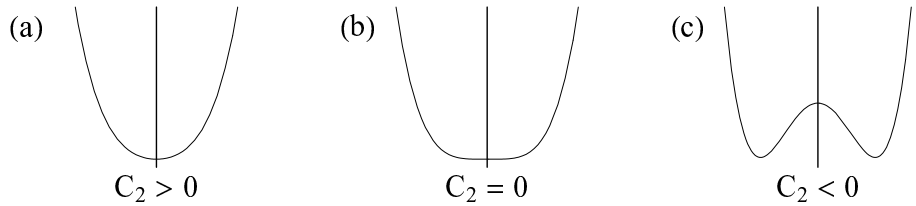

Figure 13.1: Possible shapes of the quadratic-quartic potential, shown along the a_0-axis cut: (a) $C_2 > 0$, (b) $C_2 = 0$, and (c) $C_2 < 0$. C_4 is positive in all cases.

the β^2 term produces an inverted paraboloid "hump" at small β, while the positive quartic term ensures that the system is globally bound. The resulting potential has a continuous "ring" of minima, located at the same β value,

$$\beta_0 = \sqrt{-\frac{\sqrt{5}}{2}\frac{C_2}{C_4}}, \tag{13.2}$$

and at all possible γ values. The depth for these minima is

$$V(\beta_0) = -\frac{1}{4}C_2^2 C_4. \tag{13.3}$$

In principle, the quadratic-quartic GCM potential (13.1) can be treated using the parameters d, e, and f, as well as the structure parameter $S = 1/(B_2 e^2 f)$, of Section 12.2. Potentials with C_3=0 can be approached to any desired degree of numerical accuracy by taking $d \to \pm\infty$, $e \to 0$, and $f \to +\infty$, as is seen from the conversion formulae (12.12).

However, if strictly potentials with $C_3 = 0$ are of interest, it is more straightforward to apply the scaling properties of Section 12.2 directly to the parameters C_2 and C_4. Overall multiplication of the Hamiltonian by a factor b is obtained by the parameter transformation

$$B_2' = \frac{1}{b}B_2 \qquad C_2' = bC_2 \qquad C_4' = bC_4, \tag{13.4}$$

while deepening the potential by a^2 and narrowing it by a is accomplished by the parameter transformation

$$B_2' = B_2 \qquad C_2' = a^4 C_2 \qquad C_4' = a^6 C_4. \tag{13.5}$$

Since these two scaling tranformations leave energy spectra unchanged, to within overall normalization, and wave functions unchanged, to within dilation, there remains only one degree of freedom in the parameter space to control the structure of the solutions. Let us define a structure parameter

$$S_\gamma \equiv -\frac{B_2 C_2^3}{C_4^2}, \tag{13.6}$$

analogous to the parameter S of Section 12.2. It is easily verified that S_γ is invariant under both tranformations (13.4) and (13.5).

The model consisting of a quadratic-quartic potential together with the harmonic kinetic energy term is therefore a *one-parameter* model, producing results which are dependent only upon S_γ to within overall normalization for the energies and wave function dilation. Let us consider the qualitative dependence of the predicted structure on S_γ. For S_γ large negative, C_2 is positive, giving the potential of Fig. 13.1(a), and the levels

are low-lying in the potential, where the β^2 term dominates. Thus, harmonic oscillator structure arises. As S_γ increases towards zero, the levels rise in the potential, and so the quartic term induces increasingly anharmonic behavior. At S_γ=0, the potential is a pure quartic potential [Fig. 13.1(b)]. For S_γ positive, C_2 is negative, producing the potential of Fig. 13.1(c). As S_γ increases from zero, the levels become progressively lower in this potential, and for sufficiently large S_γ the states are confined in the β-deformed minimum. In the limit $S_\gamma \rightarrow \infty$, the rigidly-deformed γ-soft structure described analytically by Wilets and Jean (Section A.3) is obtained. Observe that the structures obtained by varying S_γ from $-\infty$ to $+\infty$ occur, as limiting cases of the (d, S) model, successively along the right, top, and upper left edges of the parameter space "map" diagram (Fig. 12.6).

The behavior of an observable over the entire model space can be summarized on a single graph as a function of S_γ. Plots of some basic energy and $B(E2)$ observables are shown in Fig. 13.2. The observables $R_{4/2}$ and $B(E2; 4_1^+ \rightarrow 2_1^+)/B(E2; 2_1^+ \rightarrow 0_1^+)$ [Fig. 13.2(a,c)] vary monotonically from their values for the harmonic oscillator to their values for the Wilets-Jean rigidly-deformed structure. Observables involving the 0_2^+ state exhibit a kink [Fig. 13.2(b)] or discontinuity [Fig. 13.2(d)] at $S_\gamma \approx 14\times10^{-42}\,\mathrm{MeV^2 s^2}$ due to the occurence of a crossing of the 0_2^+ and 0_3^+ levels. For S_γ less than this value, the 0_2^+ state is the $\tau = 0$ head of the second family of levels, but, for S_γ greater than this value, the 0_2^+ state is the $\tau = 3$ multiplet member of the first family of level. The curve of yrast energies as a function of spin or, equivalently, of multiplet number τ, is given in Fig. 13.3.

It is of interest to see to what extent, and for what parameter values, $E(5)$-like behavior can be reproduced with the quadratic-quartic potential in the GCM. These results were reported in part in Ref. [212]. $R_{4/2}$ values of 2.18–2.22, approximately the value for E(5), occur for $S_\gamma \approx 3.2$–$6.4\times10^{-42}\,\mathrm{MeV^2 s^2}$ [Fig. 13.2(a)]. The level scheme for $S_\gamma = 4.8\times10^{-42}\,\mathrm{MeV^2 s^2}$ is shown alongside the E(5) predictions (Section A.5) in Fig. 13.4(a). The predictions, especially those for level energies and transition strengths within the ground state family of levels, match those for the E(5) potential quite well. The properties of successively higher-lying families of levels reproduce those of E(5) less closely. Note that the transitions which are strictly forbidden under the $\Delta\tau = \pm1$ selection rule for the E(5) model with linear transition operator (Section A.3) are strictly forbidden in the present calculations as well, but use of a second-order transition operator in either model [40, 212] leads to nonvanishing strengths in these transitions.

The S_γ value used to produce this E(5)-like behavior results in a ground state

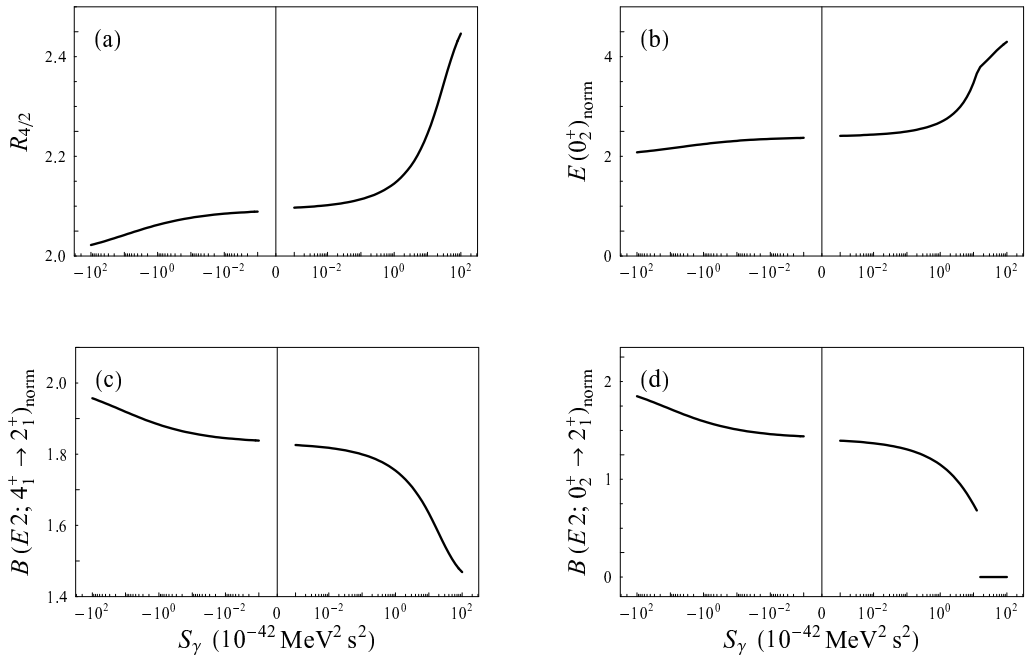

Figure 13.2: Some basic energy and $B(E2)$ observables for the quadratic-quartic potential, as a function of S_γ: (a) $R_{4/2} \equiv E(4_1^+)/E(2_1^+)$, (b) $E(0_2^+)/E(2_1^+)$, (c) $B(E2; 4_1^+ \rightarrow 2_1^+)/B(E2; 2_1^+ \rightarrow 0_1^+)$, and (d) $B(E2; 0_2^+ \rightarrow 2_1^+)/B(E2; 2_1^+ \rightarrow 0_1^+)$.

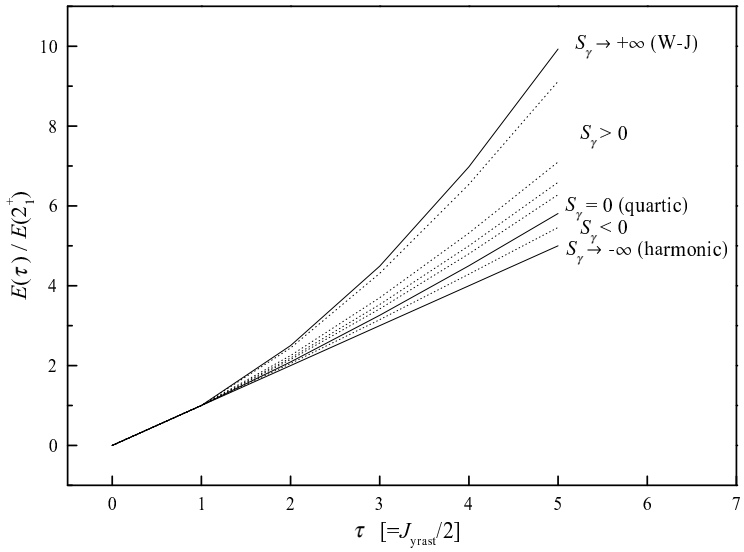

Figure 13.3: Yrast level energies predicted by for the quadratic-quartic potential as a function of multiplet number τ, or, equivalently, $J_{\max}/2$, for various values of S_γ. This curve is a straight line at $S_\gamma = -\infty$ (harmonic oscillator) but becomes continuously more upward-curving as S_γ is increased towards $S_\gamma = +\infty$ (Wilets-Jean limit). (Figure adapted from Ref. [211].)

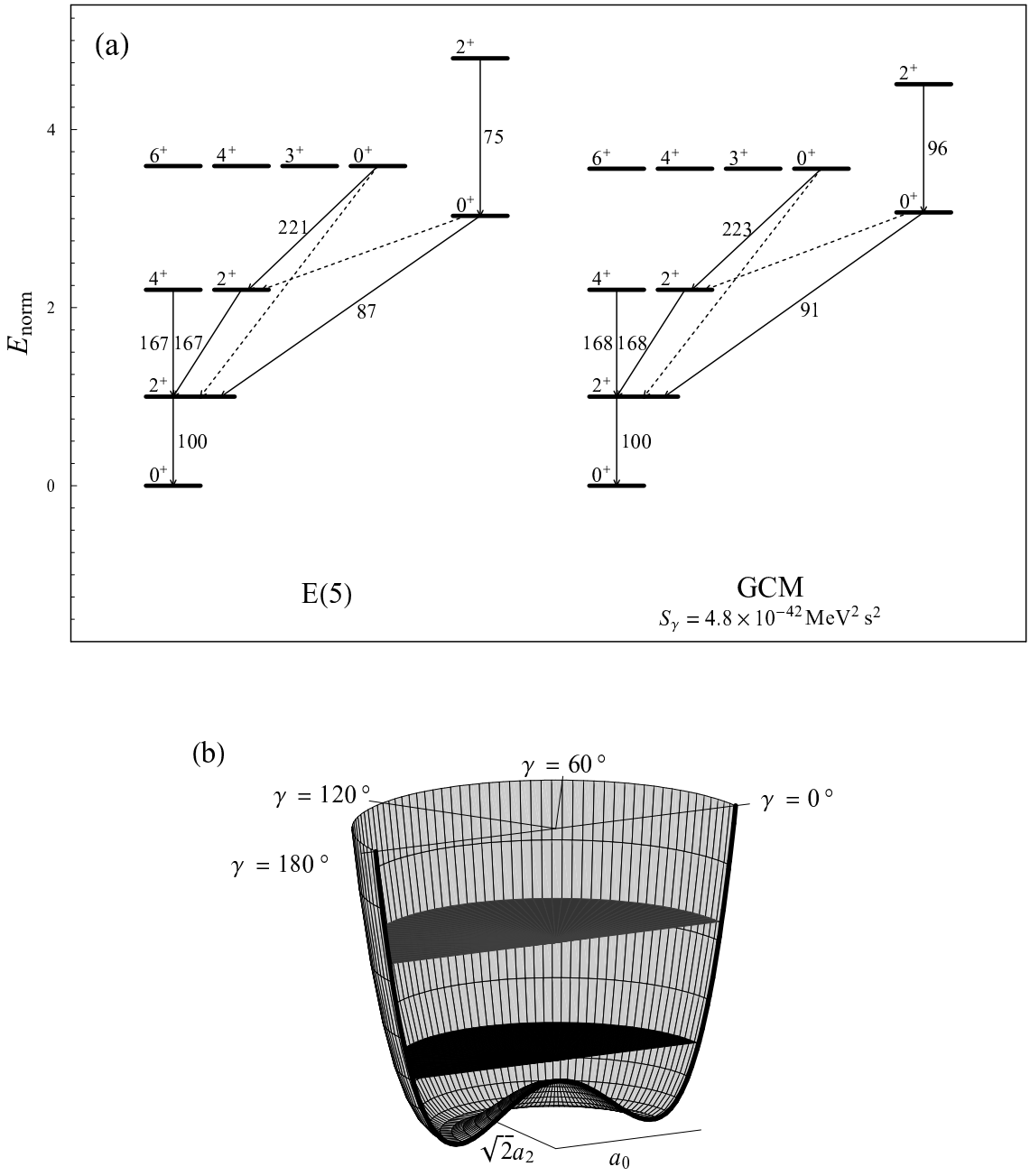

Figure 13.4: E(5)-like structure in the GCM, for S_γ=4.8×10^{-42} MeV^{2}s^2: (a) Level energies and $B(E2)$ strengths predicted in E(5) and the GCM, normalized to $E(2_1^+)$ and $B(E2; 2_1^+ \rightarrow 0_1^+)$. Dotted arrows represent forbidden transitions. (b) A plot of the potential for the GCM calculation as a function of the shape coordinates, showing 0_1^+ and 0_2^+ level energies (black and gray laminae).

energy lying somewhat above the local maximum in the potential at β=0 [Fig. 13.4(b)]. The effect of the maximum and minimum structure is essentially to provide a relatively flat region in the potential before the walls of the well rise sharply at large β. The potential, for excitation energies in this region, is thus conceptually similar to the square well potential (see also Fig. 1.9).

13.2 X(5)-like structure

The X(5) model is based upon the assumptions of a square well potential with respect to β, extending from 0 to some $\beta_{\rm max}$, stability about γ=0°, and complete decoupling of the β and γ degrees of freedom. The resulting level structure consists of a series of $K^\pi = 0^+$ bands, but with energy spacings and $B(E2)$ strengths different from those of a conventional rotor (Section A.5). Similar structural properties would seem most likely to occur in the GCM for potentials which provide strong γ confinement, and hence energetic separation between the β and γ degrees of freedom, while being relatively flat with respect to β. These criteria are met by the potentials with $d \approx 8/9$ [Fig. 12.3 on page 118], provided that the low-lying levels occur at energies moderately above the extrema of the potential but well below the onset of quartic oscillator structure, *i.e.*, for S of roughly the same order of magnitude as $S_>$.

Two basic predictions of the X(5) model are that $R_{4/2}$=2.91 and $E(0_2^+)/E(2_1^+)$=5.67. There is only one point in the truncated GCM parameter space, d=0.70 and S=0.00016×10^{42} MeV^{-2}s^{-2} ($S/S_>$=0.20), for which the GCM predictions for both these quantities match the X(5) predictions simultanously (see Fig. 13.5), although reasonably close agreement can be found along a trajectory in parameter space extending to $d \approx -10$.

Let us compare the predictions of the GCM for d=0.70 and S=0.00016×10^{42} MeV^{-2}s^{-2} with those of X(5). Excitation energies and transition strengths for the low-lying levels are shown in Fig. 13.6(a). The energies of the ground state and 0_2^+ state are shown within a plot of the potential in Fig. 13.6(b). It is seen that both states have energies which make both zero and nonzero β accessible but with γ confinement at the nonzero β, consistent with the qualitative discussion above. For the GCM calculation, energies and $B(E2)$ strengths within the yrast band are similar to those of X(5), though with noticeable differences at higher spins. The bandhead of the third K=0 band has an energy in this calculation [$E(0_3^+)/E(2_1^+)$=13.6] which

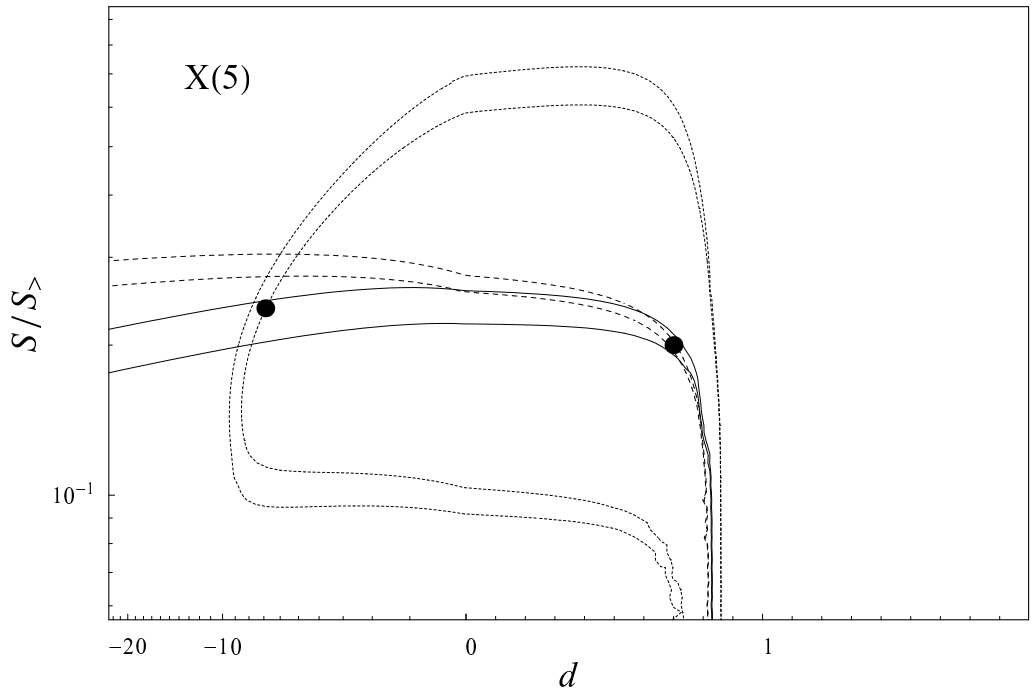

Figure 13.5: Regions in the (d,S) parameter space for which the GCM predictions of selected observables match those of X(5): $R_{4/2}$=2.91 to within 2% (solid line), $E(0_2^+)/E(2_1^+)$=5.67 to within 5% (dashed line), and $[E(2_2^+)-E(0_2^+)]/E(2_1^+)$=1.80 to within 5% (dotted line). The solid circles indicate the points in parameter space corresponding to the calculations discussed in the text.

closely matches that in X(5). The qualitative features of reduced $R_{4/2}$ ratio, increased $2^+ - 0^+$ level spacing, and reduced $B(E2; 2^+ \rightarrow 0^+)$ strength within the excited bands relative to the yrast band also appear, but in a greatly exaggerated fashion: the $R_{4/2}$ for the second band is only 1.81, the $2^+ - 0^+$ level spacing is 5.05 times that of the yrast band, and the $B(E2; 2^+ \rightarrow 0^+)$ strength is only $\sim 1/3$ that in the yrast band. These are far more extreme changes relative to the yrast band than are encountered in X(5) (Fig. 13.6). Absolute interband and intraband transition $B(E2)$ strengths involving the low-lying excited bands agree only to within a factor of three or so between the two models. However, the *ratios* of interband transition strengths are extremely similar in both calculations, showing a characteristic pattern of suppression of the spin-descending transitions. A quantitative comparison is given in Table 13.1.

The GCM calculation just described closely reproduces several X(5) predictions but exhibits extreme discrepancies from X(5) in the energy and transition strength scales for the excited bands. It is possible to seek a point in parameter space for which the

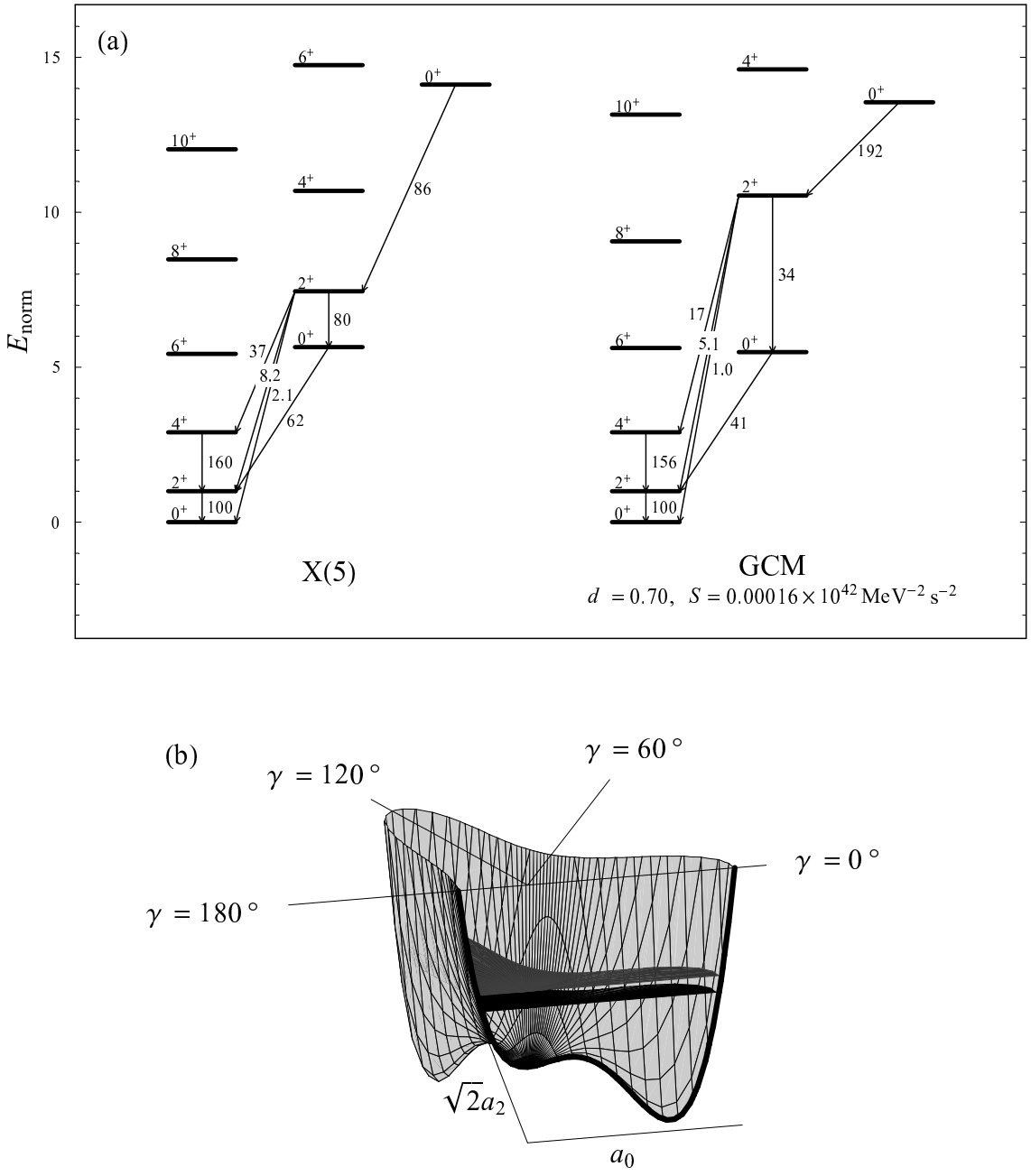

Figure 13.6: X(5)-like structure in the GCM, for $d = 0.70$ and $S = 0.00016 \times 10^{42}\,\mathrm{MeV}^{-2}\mathrm{s}^{-2}$: (a) level energies and $B(E2)$ strengths predicted in X(5) and the GCM, normalized to $E(2_1^+)$ and $B(E2; 2_1^+ \rightarrow 0_1^+)$, and (b) a plot of the potential for the GCM calculation as a function of the shape coordinates, showing 0_1^+ and 0_2^+ level energies.

	$B(E2)^{\rm rel}$	
Transition	X(5)	GCM
$2_2^+ \rightarrow 0_1^+$	100	100
2_1^+	22	30
4_1^+	5.8	6.0
$4_2^+ \rightarrow 2_1^+$	100	100
4_1^+	22	28
6_1^+	3.4	9.2

Table 13.1: Calculated $E2$ branching ratios, from $K^\pi = 0_2^+$ band members to $K^\pi = 0_1^+$ band members, in X(5) and in the GCM for $d = 0.70$ and S =0.00016×10^{42} MeV^{-2}s^{-2}.

calculated $R_{4/2}$ and $E(0_2^+)/E(2_1^+)$ values match those of X(5) less closely but for which the scale $[E(2_2^+) - E(0_2^+)]/E(2_1^+)$ is similar to that in X(5). An example of such a point, $d \approx$-6.9 and $S \approx$0.18×10^{42} MeV^{-2}s^{-2}, is indicated in Fig. 13.5. However, the structural situation in this region of parameter space differs substantially from that encountered in the X(5) picture. As discussed in Section 12.3, degeneracy of the β and γ bands for rotational nuclei occurs at $d \approx$-8 [see (12.32) and Fig. 12.7(e)]. Although the 2_2^+-0_2^+ energy difference does match that of X(5), the 2_2^+ state properties indicate that this state involves a substantial mixing of $K^\pi = 0$ and $K^\pi = 2$ contributions. For instance, $B(E2; 2_2^+ \rightarrow 0_2^+)$ and $B(E2; 2_3^+ \rightarrow 0_2^+)$ are both of "in-band" strength and differ from each other by less than a factor of two.

Thus, while the E(5) predictions could be matched very well by a GCM calculation, it appears that the X(5) predictions can only be identified with a general region in the truncated GCM parameter space. Other examples of GCM calculations for parameter values in this general region are considered in the context of the N=90 transitional nuclei in Chapter 15.

Chapter 14

Finite well solution for the E(5) Hamiltonian

The E(5) model (Sections 1.3 and A.5), recently proposed by Iachello [35], provides an analytic description of structure near the critical point of the transition between spherical oscillator structure and rigidly-deformed γ-soft structure. This description is obtained by considering the geometric Hamiltonian (Section 12.1) with a potential function which is an infinite square well in quadrupole deformation space. The solution wave functions are analytic in form, consisting of the spherical Bessel functions, and the eigenvalues are simply given in terms of the zeros of the Bessel functions (Section A.5). The use of an infinite well potential is a convenient calculational approximation, allowing extremely simple solutions to be obtained. However, actual potentials describing nuclei are expected to be finite, not infinite in depth, and the interacting boson model at finite boson number along the U(5)–SO(6) transition [148] leads to potentials which may be approximated by a finite-depth square well. It is therefore of interest, as suggested in Ref. [35], to assess the extent to which the results from the E(5) description are sensitive to finite well depth. In the present work, the evolution of nuclear observables as a function of well depth is investigated, and observables sensitive to finite well depth are identified. These results were reported in Ref. [213].

The five-dimensional finite square well potential (Figure 14.1),

$$V(\beta) = \begin{cases} V_0 & \beta \leq \beta_w \\ 0 & \beta > \beta_w, \end{cases} \tag{14.1}$$

is, like the E(5) potential, independent of γ. Consequently, the Hamiltonian,

$$-\frac{\hbar^2}{2B}\sum_{\mu}\frac{\partial^2}{\partial\alpha_{2\mu}\partial\alpha^*_{2\mu}} + V(\beta), \tag{14.2}$$

is separable (Section A.3), and the eigenfunctions are of the form $f(\beta)\Phi(\gamma,\underline{\theta})$. The solutions for the "angular" (γ,$\underline{\theta}$) wave functions [214] are common to all γ-soft problems, while

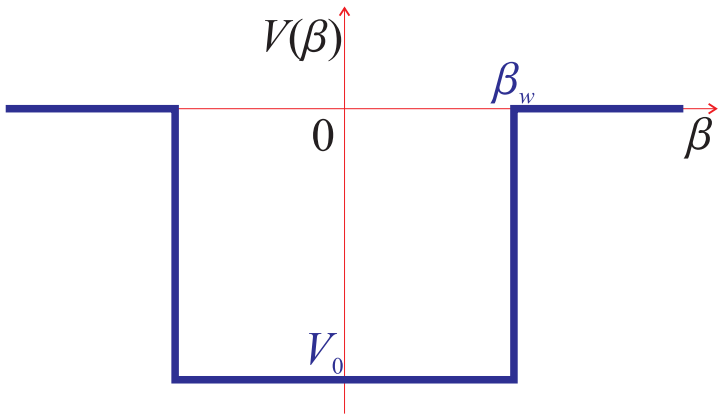

Figure 14.1: Finite square well potential in deformation space, shown along the a_0-axis cut.

the dependence upon the potential $V(\beta)$ is isolated in the "radial" (β) wave function. The equation for $f(\beta)$ is

$$\left[\frac{\hbar^2}{2B}\left(-\frac{1}{\beta^4}\frac{\partial}{\partial\beta}\beta^4\frac{\partial}{\partial\beta}+\frac{\tau(\tau+3)}{\beta^2}\right)+V(\beta)\right]f(\beta)=Ef(\beta), \tag{14.3}$$

where the separation constant τ assumes the values $\tau = 0, 1, \ldots$. The notation is simplified if an overall factor of $\hbar^2/(2B)$ is extracted from the Hamiltonian, leaving the equation in terms of the reduced eigenvalue $\varepsilon \equiv \frac{2B}{\hbar^2}E$ and the reduced potential $v(\beta) \equiv \frac{2B}{\hbar^2}V(\beta)$, of depth $v_0 \equiv \frac{2B}{\hbar^2}V_0$. Bound state solutions can only occur with eigenvalues in the range $v_0 < \varepsilon < 0$. Each solution of the β equation results in a multiplet of solutions to the full problem, degenerate with respect to angular momentum according to the γ-soft τ multiplet structure (Section A.3). The notation $J^+_{\xi,\tau}$ is used to designate the states corresponding to the ξth radial solution for separation constant τ.

The finite well potential is piecewise constant as a function of β. Within a region of constant potential, the radial equation (14.3) reduces to the Bessel equation of half-integer order, as outlined in Ref. [35]. In the interior of the well ($\beta < \beta_w$), where the difference $\varepsilon - v_0$ is positive, the solutions involve the ordinary Bessel functions, while in the classically forbidden region exterior to the well ($\beta > \beta_w$), where the difference $\varepsilon - v_0$ is negative, the solutions involve the modified Bessel functions. Although the equations are satisfied for an arbitrary linear combination of the Bessel functions of the first and second kind, the solution chosen for the interior region must have the correct convergence properties at the origin [215], and the solution for the exterior region must have the proper asymptotic behavior (convergence at $\beta \to \infty$). The Bessel functions of half-integer

order may be expressed in terms of the spherical Bessel functions of integer order (*e.g.*, Refs. [216, 217]), and the correct combinations for this problem involve

$$j_n(x) \equiv \sqrt{\frac{\pi}{2}} x^{-1/2} J_{n+1/2}(x) \qquad k_n(x) \equiv \sqrt{\frac{2}{\pi}} x^{-1/2} K_{n+1/2}(x). \tag{14.4}$$

The wave function in β for the ξth solution with separation constant τ is

$$f_{\xi,\tau}(\beta) = \begin{cases} A_{\xi,\tau} \beta^{-1} j_{\tau+1}[(\varepsilon_{\xi,\tau} - v_0)^{1/2} \beta] & \beta \leq \beta_w \\ B_{\xi,\tau} \beta^{-1} k_{\tau+1}[(-\varepsilon_{\xi,\tau})^{1/2} \beta] & \beta > \beta_w. \end{cases} \tag{14.5}$$

The eigenvalues for the finite well are determined by the requirement that $f(\beta)$ be continuous and smooth at the matching point $\beta = \beta_w$. The eigenvalue condition for ε can be obtained in a manner analogous to that for the three-dimensional square well (*e.g.*, Ref. [215]). Since the spherical Bessel functions may be expressed in terms of trigonometric and exponential functions, the matching condition assumes the form of a transcendental equation. This condition may be derived by direct algebraic manipulation, for each value of τ, as in Ref. [215]. However, the resulting expressions rapidly become cumbersome beyond the lowest few values for τ. It is more convenient to instead derive a general form for the condition, expressed in terms of the coefficients in polynomial expansions of the spherical Bessel functions. Let us define a dimensionless energy variable,

$$\eta(\varepsilon) \equiv \left[1 - \frac{\varepsilon}{v_0} \right]^{1/2}, \tag{14.6}$$

and a "well size" parameter,

$$x_0 \equiv (-v_0)^{1/2} \beta_w. \tag{14.7}$$

The matching condition, in terms of these quantities, is the transcendental equation

$$-\frac{\sum_{i,j=0}^{\tau+2} \left[c_{(\tau+1)i} e'_{(\tau+1)(j+1)} - c'_{(\tau+1)(i+1)} e_{(\tau+1)j} \right] x_0^{-i-j} \eta^{-i} [(1-\eta^2)^{1/2}]^{-j}}{\sum_{i,j=0}^{\tau+2} \left[s_{(\tau+1)i} e'_{(\tau+1)(j+1)} - s'_{(\tau+1)(i+1)} e_{(\tau+1)j} \right] x_0^{-i-j} \eta^{-i} [(1-\eta^2)^{1/2}]^{-j}} = \tan(x_0 \eta), \tag{14.8}$$

where c_{ni}, s_{ni}, and e_{ni} are the coefficients in the expansions

$$\begin{aligned} j_n(x) &= \left(\sum_{i=1}^{n+1} c_{ni} x^{-i} \right) \cos x + \left(\sum_{i=1}^{n+1} s_{ni} x^{-i} \right) \sin x \\ k_n(x) &= \left(\sum_{i=1}^{n+1} e_{ni} x^{-i} \right) e^{-x}, \end{aligned} \tag{14.9}$$

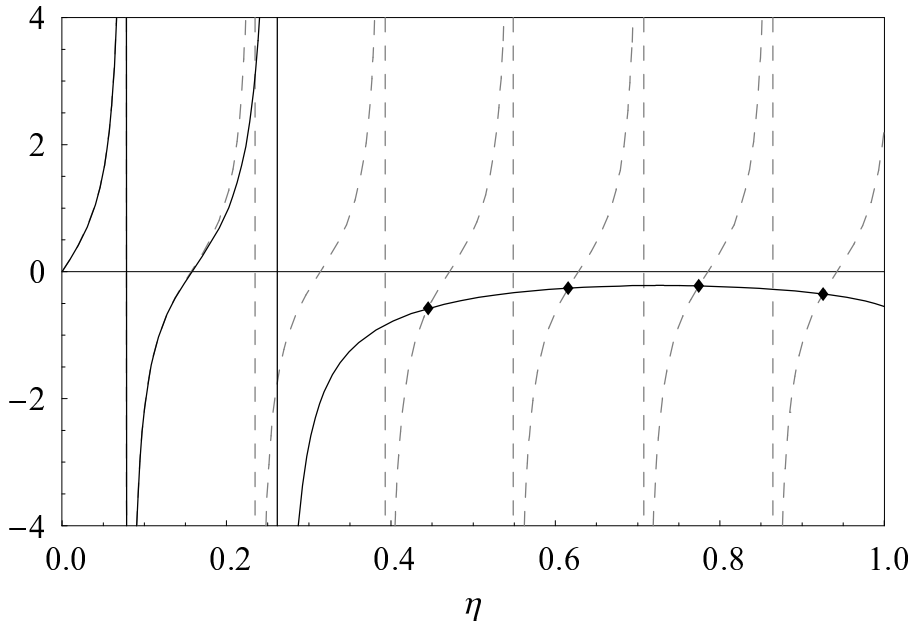

Figure 14.2: Graphical representation of the finite well eigenvalue problem, for x_0=20 and τ=4. The left hand side (solid line) and right hand side (dashed line) of the eigenvalue equation (14.8) are plotted as functions of η. The intersection points (diamonds) indicate eigenvalues.

and c'_{ni}, s'_{ni}, and e'_{ni} are defined similarly for the derivative functions $j'_n(x)$ and $k'_n(x)$. Recurrence relations for the calculation of these coefficients may be derived in a straightforward fashion from the Bessel function recurrence relations.

The equation (14.8) must be solved numerically for the eigenvalues of ε. An example case is shown graphically in Fig. 14.2. Once an eigenvalue $\varepsilon_{\xi,\tau}$ is found, the coefficients $A_{\xi,\tau}$ and $B_{\xi,\tau}$ follow from the continuity condition at $\beta = \beta_w$ and the normalization condition $\int_0^\infty \beta^4 d\beta |f(\beta)|^2 = 1$. The normalization integrals can be evaluated analytically, giving

$$\begin{aligned} c_1 &\equiv \int_0^{\beta_w} \beta^4 d\beta \left[\beta^{-1} j_{\tau+1}[(\varepsilon - v_0)^{1/2}\beta]\right]^2 \\ &= \frac{\beta_w^3}{2}\left[j_{\tau+1}[(\varepsilon - v_0)^{1/2}\beta_w]^2 - j_\tau[(\varepsilon - v_0)^{1/2}\beta_w] j_{\tau+2}[(\varepsilon - v_0)^{1/2}\beta_w]\right] \end{aligned} \tag{14.10}$$

and

$$\begin{aligned} c_2 &\equiv \int_{\beta_w}^\infty \beta^4 d\beta \left[\beta^{-1} k_{\tau+1}[(-\varepsilon)^{1/2}\beta]\right]^2 \\ &= -\frac{\beta_w^3}{2}\left[k_{\tau+1}[(-\varepsilon)^{1/2}\beta_w]^2 - k_\tau[(-\varepsilon)^{1/2}\beta_w] k_{\tau+2}[(-\varepsilon)^{1/2}\beta_w]\right]. \end{aligned} \tag{14.11}$$

In terms of c_1, c_2, $y_1 \equiv \beta_w^{-1} j_{\tau+1}[(\varepsilon - v_0)^{1/2}\beta_w]$, and $y_2 \equiv \beta_w^{-1} k_{\tau+1}[(-\varepsilon)^{1/2}\beta_w]$, the continuity and normalization conditions are $Ay_1 = By_2$ and $A^2 c_1 + B^2 c_2 = 1$. The coefficients satifying these are

$$A = \pm \frac{y_2}{[y_1^2 c_2 + y_2^2 c_1]^{1/2}} \qquad B = \pm \frac{y_1}{[y_1^2 c_2 + y_2^2 c_1]^{1/2}}. \tag{14.12}$$

Note that the numerical values for these coefficients depend upon the normalization convention (14.4) chosen for the spherical Bessel functions, which varies in the literature.

The eigenvalue spectrum of the solution depends upon the parameters β_w and v_0 exclusively in the combination x_0, as can be seen from the eigenvalue equation (14.8). That is, if two wells (β_w, v_0) and (β'_w, v'_0) have the same value for x_0, they will have identical energy spectra, to within an overall normalization factor. Two wells with different x_0 values will have different energy spectra. The parameter x_0 is invariant under multiplication of the potential by a factor a^2 followed by dilation by $1/a$, so this result is actually a special case of the scaling relation discussed in Appendix E, and x_0 plays a role analogous to the structure parameters S and S_γ of the preceding chapters.

Therefore, for a given value of x_0, the numerical solution procedure need only be carried out once, at some "reference" choice of the well width and depth (*e.g.*, $\beta_w = 1$), and the solution for any other well of the same x_0 can be deduced by a simple rescaling of all energies and dilation of all wave functions. To state the relations explicitly, consider a reference calculation performed at $\beta_w = 1$ (and thus $v_0 = -x_0^2$), and suppose this calculation produces an eigenvalue ε and normalized wave function $f(\beta)$. Then for a well of the same x_0 but a different width β'_w (and thus $v'_0 = -x_0^2/\beta'^2_w$), the corresponding eigenvalue ε' and normalized wave function $f'(\beta)$ are given by the simple rescalings

$$\begin{aligned} \varepsilon' &= \beta'^{-2}_w \varepsilon \\ f'(\beta) &= \beta'^{-5/2}_w f(\beta/\beta'_w). \end{aligned} \tag{14.13}$$

The scaling properties of matrix elements of the operator β^m, which are encountered in the calculation of electromagnetic transition strengths, are given in Appendix E.

The solution for $x_0 = 10$ is illustrative of the main effects of finite well depth. The level energies and wave functions for this solution are shown in Fig. 14.3. The main consequences of the finite well depth are not unexpected:

> 1. There are only a finite number of bound states. For this example, only members of the lowest few ξ families are bound [Fig. 14.3(a)]. A summary of the number of bound states for other well sizes is given in Table 14.1.

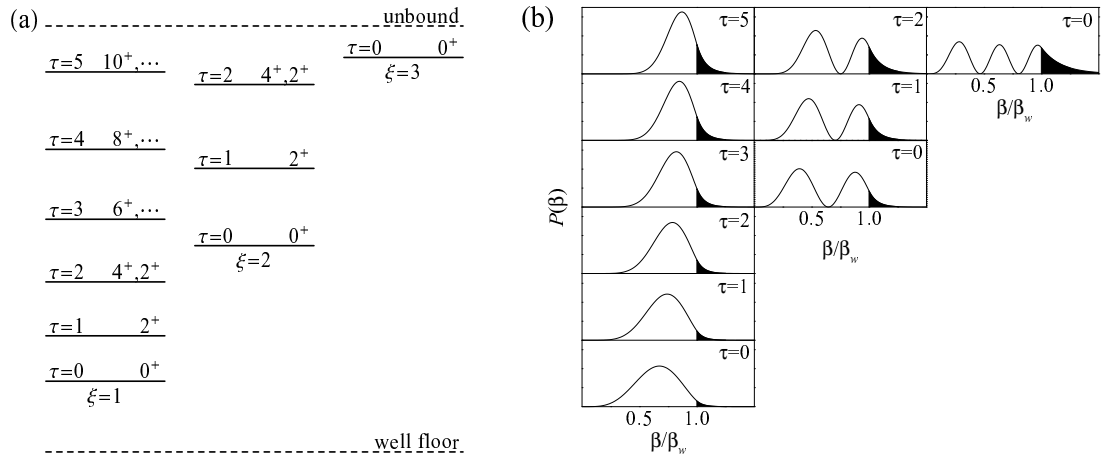

Figure 14.3: Bound states of the $x_0 = 10$ well: (a) excitation energies and (b) probability density functions $P(\beta) \equiv \beta^4 |f(\beta)|^2$. The shaded areas under the probability density functions indicate penetration into classically forbidden β values ($\beta > \beta_w$). (Figure from Ref. [213].)

x_0	$\tau = 0$	$\tau = 1$	$\tau = 2$	$\tau = 3$	$\cdots$
5	1	1			
10	3	2	2	1	$\cdots$
20	6	5	5	4	$\cdots$
50	15	14	14	14	$\cdots$

Table 14.1: Number of bound β solutions, by τ quantum number, for selected x_0.

2. The wave functions penetrate the classically forbidden region $\beta > \beta_w$. For the highest-lying states, a substantial portion of the probability distribution in β lies outside β_w. This is indicated by the shaded areas of Fig. 14.3(b).

3. The eigenvalues are lowered relative to those for the infinite E(5) well of the same β_w [Fig. 14.4(a)]. This is a natural consequence of the finite well depth: the wave functions are given the freedom to spread into the region $\beta > \beta_w$, and this is analogous in effect to a widening of the well, causing the energies to "settle" lower.

Some interesting properties, however, are revealed by an examination of the systematic evolution of the solution with changing well size. A series of calculations ($x_0 = 5, 10, 20$) spanning the physical range of interest in the study of nuclei are presented alongside the E(5) solution in Fig. 14.4. At a fixed width, x_0 is a measure of the depth of the well, and the infinite E(5) well is obtained in the limit $x_0 \to \infty$. Although the energy

eigenvalues do experience a lowering as the well depth decreases [Fig. 14.4(a)], it turns out that the level energies are nearly *uniformly* lowered by the same *factor* for all levels in the well, leaving energy *ratios* virtually unchanged. A plot of excitation energies normalized to the first excited state [Fig. 14.4(b)] reveals these energies to be essentially insensitive to the well depth. Some relevant energy ratios are summarized in Table 14.2.

Electromagnetic transition strengths can be calculated from the matrix elements of the collective multipole operators. Expressed in terms of the intrinsic coordinates β and γ, the $E2$ and $E0$ transition operators are [4]

$$\begin{aligned} \mathfrak{M}(E2;\mu) &\propto \beta\big[D^{2\,*}_{\mu,0}\cos\gamma + \frac{1}{\sqrt{2}}(D^{2\,*}_{\mu,2} + D^{2\,*}_{\mu,-2})\sin\gamma\big] \\ \mathfrak{M}(E0;0) &\propto \beta^2, \end{aligned} \tag{14.14}$$

and the transition strengths are $B(E\lambda; J_i \rightarrow J_f) = \frac{2J_f+1}{2J_i+1}|\,\langle J_f||\mathfrak{M}(E\lambda)||J_i\rangle\,|^2$ (Appendix B). Only integrals of the β-dependent factors with respect to the radial wave functions need be carried out, since the angular integrals of $\mathfrak{M}(E2)$ [218] are common to all γ-soft problems. The evolution of key $E2$ and $E0$ transition strengths is shown in Fig. 14.5 and Fig. 14.6. The absolute transition strengths are larger at finite well depth than for the infinite well, at the same width β_w, but the increase is, again, largely a uniform overall increase, leaving $B(E2)$ or $B(E0)$ *ratios* nearly unchanged from the E(5) limit.

The uniform reduction of all energies and enhancement of all transition matrix elements does not serve as a useful identifying feature of finite well depth, since arbitrary energy and transition strength normalizations can be obtained for the infinite E(5) well simply by varying the parameters β_w and B.

Only the very highest energy levels, just short of being unbound, show appreciable deviations from the E(5) normalized energies and transition strengths. The third 0^+ state at $x_0 = 10$ demonstrates these effects nicely: lowered energy (Fig. 14.4), enhanced $E2$ transitions (Fig. 14.5), and enhanced $E0$ transitions (Fig. 14.6).

The results found for the finite well present a challenge from an experimental viewpoint. There are few clear signatures of finite well depth. Those signature which are present consist of moderate modifications to energies or transition strengths for high-lying levels, but such levels are typically the least accessible experimentally and most subject to contamination from degrees of freedom outside the collective model framework.

The results are, however, reassuring from a theoretical perspective. They suggest that the E(5) description is "robust" in nature. The main features of the E(5) solutions

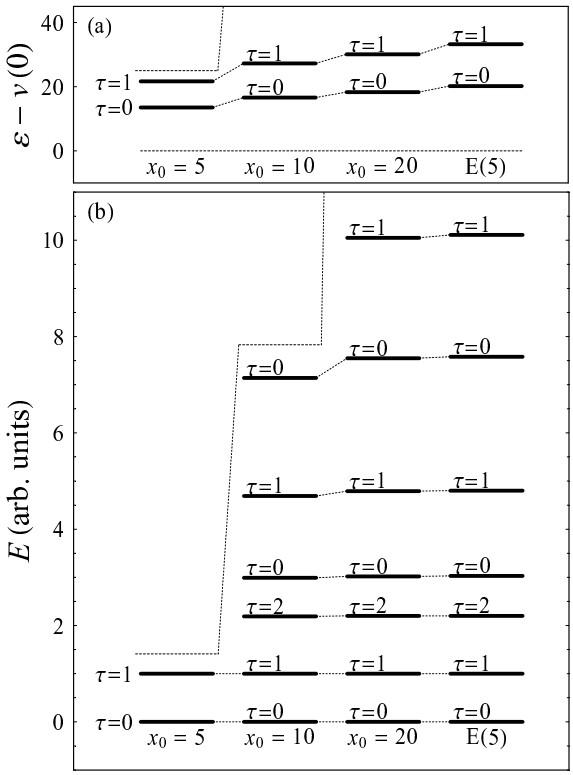

Figure 14.4: Evolution of level excitation energies as a function of well size parameter x_0 for selected low-lying levels. (a) Absolute eigenvalue relative to floor of well $[\varepsilon - v(0)]$. (b) Excitation energy normalized to the first excited state. The upper dashed line indicates the energy at which the system becomes unbound (top of well). (Figure adapted from Ref. [213].)

	$\xi = 1$	$\xi = 2$			$\xi = 3$		
x_0	$R_{4/2}$	$E_{\tau=0}$	$E_{\tau=1}$	$R_{4/2}$	$E_{\tau=0}$	$E_{\tau=1}$	$R_{4/2}$
10	2.19	2.99	4.69	2.09	7.14	—	—
20	2.20	3.02	4.79	2.12	7.55	10.05	2.08
E(5)	2.20	3.03	4.80	2.12	7.58	10.11	2.09

Table 14.2: Excitation energy observables for selected x_0. Excitation energies are normalized to $E_{\xi=1,\tau=1} = 1$. The quantity $R_{4/2}$ is defined for each ξ family as $(E_{\tau=2} - E_{\tau=0})/(E_{\tau=1} - E_{\tau=0})$.

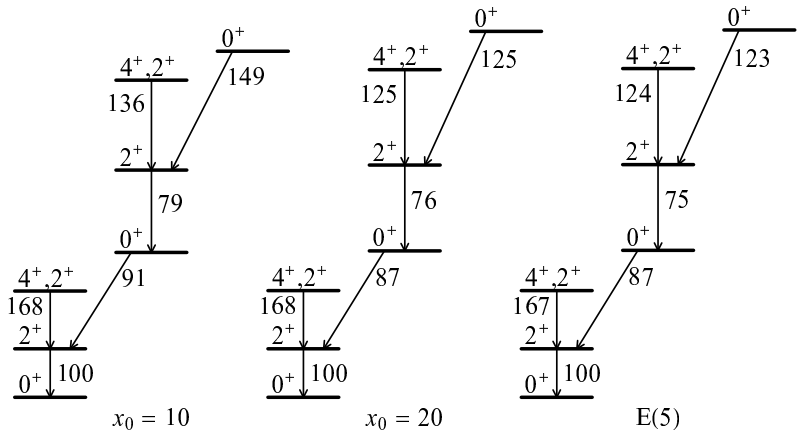

Figure 14.5: Evolution of $B(E2)$ strengths as a function of well parameter x_0. Values are normalized to $B(E2; 2^+_{1,1} \rightarrow 0^+_{1,0}) = 100$. (Figure adapted from Ref. [213].)

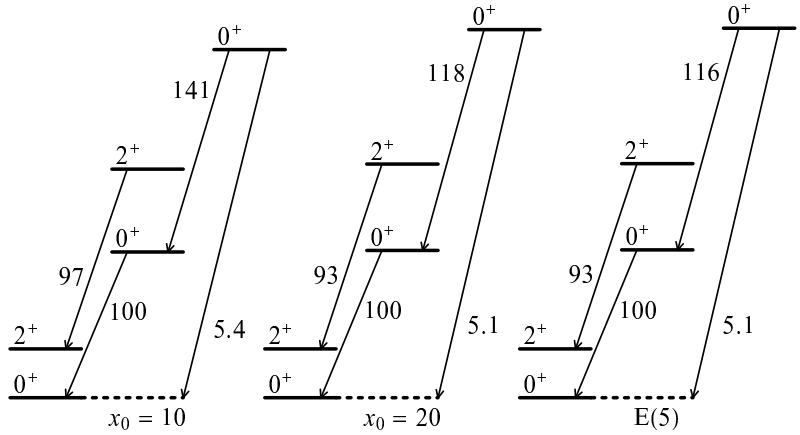

Figure 14.6: Evolution of $B(E0)$ strengths as a function of well parameter x_0. Values are normalized to $B(E0; 0^+_{2,0} \rightarrow 0^+_{1,0}) = 100$. (Figure adapted from Ref. [213].)

remain virtually unchanged under radical modification of the depth of the potential, from the ideal infinite well to the realistic finite well likely to be applicable to actual nuclei.

Chapter 15

Phenomenological interpretation

15.1 The $N\approx$90 transitional nuclei

A rapid change in deformation occurs at $N\approx$90 along the Nd, Sm, Gd, and Dy isotopic chains, as a transition occurs from spherical to axially symmetric deformed structure. Many of the transitional phenomena described in Section 1.3 find some of their best candidates among the N=90 isotopes ^{150}Nd, ^{152}Sm, ^{154}Gd, and ^{156}Dy. The description of these nuclei in the IBM [29, 30, 219] requires parameter values near those of the phase transition in the IBM, and the low-lying level energies of these nuclei place them at or near the phenomenological "critical point" in the evolution of observables (see Section 1.3). These nuclei are thus now of great interest for comparison to the X(5) model predictions, since the first proposed candidates for description by the X(5) model were ^{152}Sm [38] and ^{150}Nd [39], and all four N=90 isotopes have very similar characteristics with respect to the relevant observables. Unusual experimental results have repeatedly drawn attention to the N=90 nuclei. These have included observed (p,t) and (t,p) cross sections and $E0$ strengths suggestive of shape coexistence, as well as spectroscopic results indicating the breakdown of conventional rotational band mixing models, as outlined in Section 6.1.

With both new model descriptions and extensive new sets of spectroscopic and lifetime data available, let us now survey the phenomenology of the N=90 nuclei. It is expecially of interest to consider how the basic observables of low-lying levels in these nuclei compare to the X(5) predictions.

The N=90 Nd–Dy nuclei have yrast band level energies closely matching those of the X(5) model [Fig. 15.1(a)]. The evolution of $R_{4/2}\equiv E(4_1^+)/E(2_1^+)$ along the Nd–Dy isotopic chains is shown in Fig. 15.2(a). It can be seen that the agreement of yrast energies with the X(5) predictions is localized to N=90, as substantial changes occur by N=88 or

N=92.

The situation for the $B(E2)$ strengths within the yrast bands of the N=90 Nd–Dy isotones [Fig. 15.1(b)] is less clear. The spin-dependence of the yrast band $B(E2)$ values is generally intermediate between the ideal vibrator and rotor limits, and the qualitative trend is consistent with the X(5) predictions. However, many of the data points lie somewhat below the X(5) predictions. Some of the experimental $B(E2)$ values shown were deduced using highly reliable techniques, *e.g.*, the differential decay curve method [144] for recoil distance method lifetime measurements. However, for others, reported values differ or the measurements involved experimental ambiguities. The very low value for $B(E2; 6_1^+ \rightarrow 4_1^+)$ in ^{156}Dy [220, 221], which lies below even the rotor model predictions [Fig. 15.1(b)], provides an example of such a case (see Ref. [77] for details). Remeasurement could provide valuable clarification.

The excitation energy of the first excited 0^+ sequence is very similar for all four N=90 Nd–Dy isotones and closely matches the prediction for the first excited $K^\pi = 0^+$ band in the X(5) model [Fig. 15.2(b)]. The observable $E(0_2^+)/E(2_1^+)$ is rapidly changing along the isotopic chains [see also Fig. 1.8(b) on page 11], so the agreement with X(5) is again highly localized to N=90.

In the X(5) predictions, the successive $K^\pi = 0^+$ bands differ from each other in both the energy ratios and energy spacing scale of levels within the band. The dependence of the level energies upon spin becomes successively more linear, or oscillator-like, for more excited $K^\pi = 0^+$ bands. This effect is apparent in the X(5) predictions shown in Fig. 15.3(a) for the first two $K^\pi = 0^+$ bands, where the curve for the $K^\pi = 0_2^+$ band is less sharply upward-curving than is the curve for the yrast band (compare the dashed and dotted lines). The N=90 Nd–Dy nuclei exhibit this behavior; while the yrast band level energies follow the X(5) predictions for the yrast band [Fig. 15.1(a)], the $K^\pi = 0_2^+$ band level energies have a spin dependence which closely matches the X(5) predictions for the $K^\pi = 0_2^+$ band [Fig. 15.3(a)]. For the 2^+ and 4^+ band members specifically, this effect corresponds to a reduction in the ratio of 4^+ state energy to 2^+ state energy (taken relative to the band head) for the higher bands. The values for the N=90 nuclei are summarized in Fig. 15.3(b).

The energy spacing *scale* for the $K^\pi = 0_2^+$ band is predicted in X(5) to be much larger than for the yrast band, with $[E(2_2^+) - E(0_2^+)]/E(2_1^+) \approx 1.81$. Only in ^{150}Nd is the $K^\pi = 0_2^+$ band 2^+-0^+ energy spacing significantly larger than the yrast band

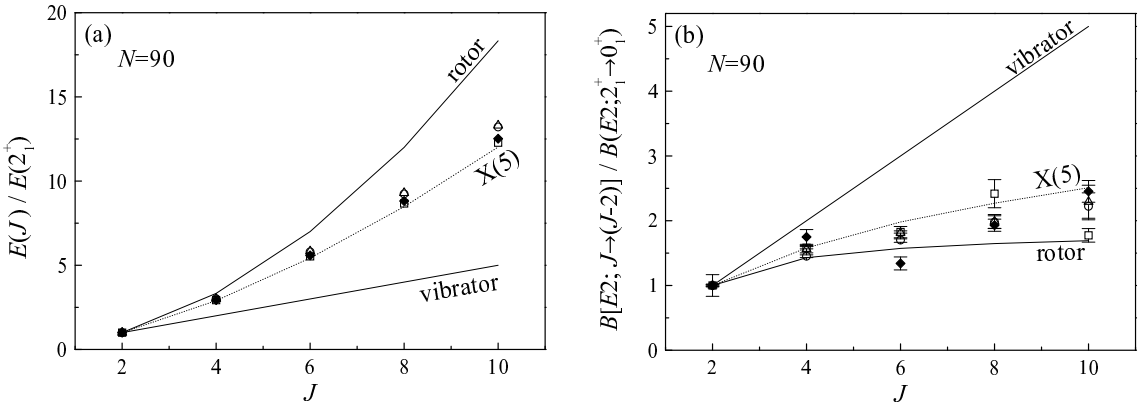

Figure 15.1: Yrast band (a) level energies and (b) $B(E2)$ values, normalized to the those for 2^+ band member, for the N=90 isotones ^{150}Nd (□), ^{152}Sm (○), ^{154}Gd (△), and ^{156}Dy (◆). The rotor, X(5), and harmonic vibrator predictions are shown for comparison. Data are from Refs. [21–24, 39]. (Figure adapted from Ref. [43].)

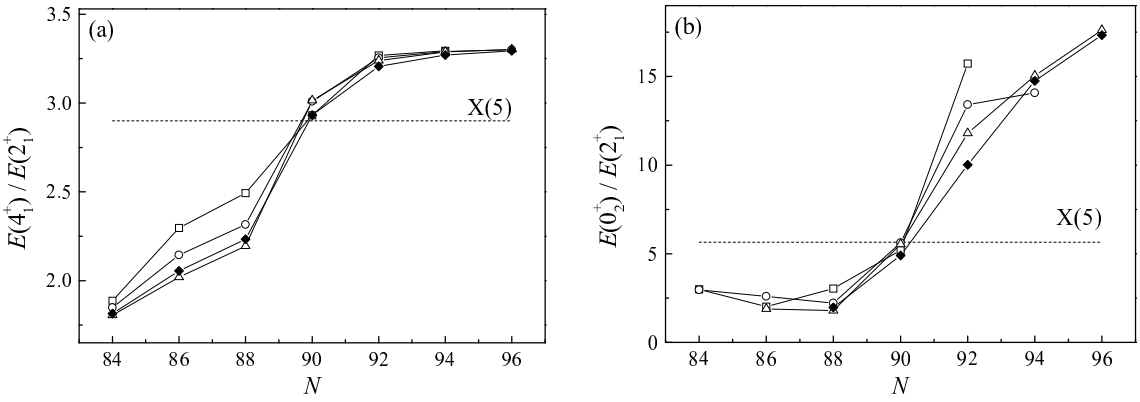

Figure 15.2: Evolution of the (a) 4_1^+ and (b) 0_2^+ energies (normalized to the 2_1^+ energy) across the N=90 transition region, for the Nd (□), Sm (○), Gd (△), and Dy (◆) isotopic chains, compared with the X(5) prediction. (Figure from Ref. [77].)

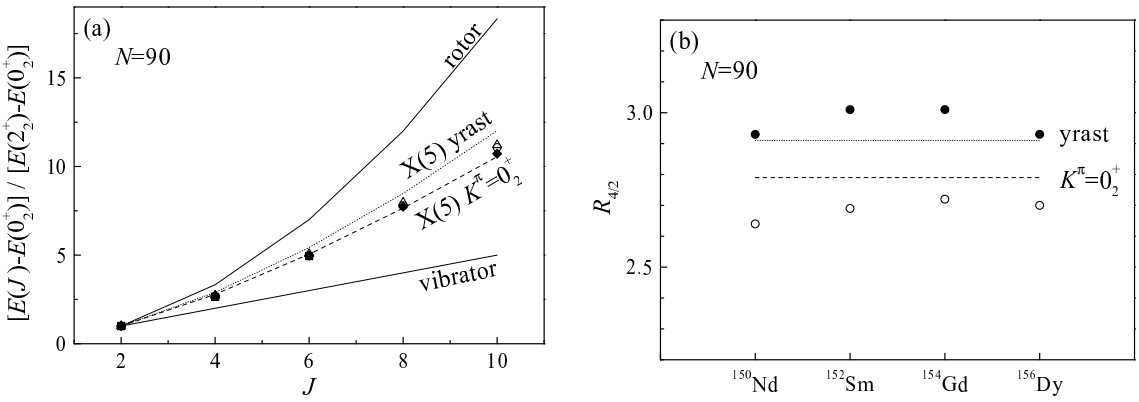

Figure 15.3: $K^\pi = 0_2^+$ band level energies: (a) Energies taken relative to the band head and normalized to the 2^+ band member, for the N=90 isotones ^{150}Nd (□), ^{152}Sm (○), ^{154}Gd (△), and ^{156}Dy (◆). The X(5) predictions both for this band (dashed line) and for the yrast band $[E(J)/E(2_1^+)]$ (dotted line) are shown, illustrating the differing spin dependences discussed in the text. The rotor and harmonic vibrator predictions are also indicated. (b) $R_{4/2}$ values for the yrast (●) and $K^\pi = 0_2^+$ (○) bands in these nuclei, along with the X(5) predictions. [Part (a) from Ref. [77].]

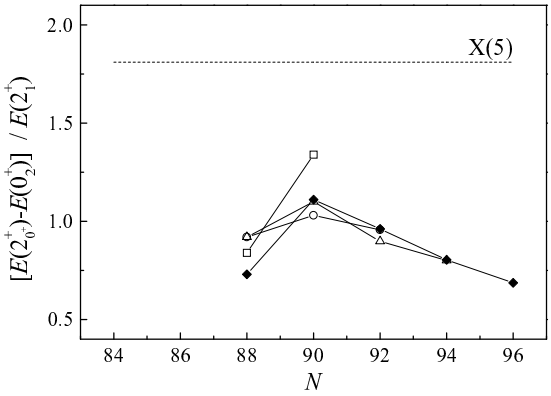

Figure 15.4: Energy spacing scale of the excited 0^+ sequence relative to that of the yrast sequence, for the Nd (□), Sm (○), Gd (△), and Dy (◆) isotopic chains, compared with the X(5) prediction. (Figure from Ref. [77].)

spacing (Fig. 15.4). For the Sm, Gd, and Dy isotopic chains, N=90 is the location of a local maximum $[E(2_2^+) - E(0_2^+)]/E(2_1^+)$ in this ratio (Fig. 15.4), but only relative to neighboring isotopes for which the $K^\pi = 0_2^+$ band spacing is *smaller* than the yrast band spacing. The actual spacing is still much less than predicted by the X(5) model. This substantial discrepancy is also encountered in descriptions of the $N = 90$ nuclei using the IBM [29, 219], truncated GCM (see below), and other collective models [222], which

likewise lead to predictions of a much larger spacing scale for the 0_2^+ sequence.

The new intensity and lifetime results for the N=90 nuclei provide greatly improved information on $B(E2)$ strengths for transitions from the 2^+, 4^+, and 6^+ members of the first excited $K^\pi = 0^+$ band, including both in-band and interband transitions. Absolute $B(E2)$ strengths are known for band members in ^{150}Nd, ^{152}Sm, and ^{154}Gd, while, due to a lack of lifetime data, only relative $B(E2)$ strengths are available for ^{156}Dy (see Refs. [22–24, 39]).

Let us first consider the overall strength scales of the in-band and interband transitions. In ^{150}Nd, ^{152}Sm, and ^{154}Gd, the interband transition strengths from the 0_2^+ and 2_2^+ states to the yrast band are consistently weaker than expected for X(5) by about a factor of two. The pattern of interband transition strengths from the 4_2^+ level is less regular: in ^{150}Nd, the $4_2^+ \rightarrow 6_1^+$ strength is about a factor of two *above* the X(5) prediction, but in ^{152}Sm it is a factor of 10 *below* the X(5) prediction. In ^{156}Dy, the 2_2^+ and 4_2^+ level lifetimes are unknown, so the absolute strengths of the transitions cannot be determined. For the 2^+ band member, not even the relative strengths of the in-band and interband transitions can be compared, since only a limit can be placed on the intensity of the in-band $2_2^+ \rightarrow 0_2^+$ transition (Chapter 7). For the 4_2^+ state in ^{156}Dy, such a comparison of relative strengths can be made (Fig. 15.5), and it is found that the interband transitions are much weaker relative to the in-band transition than would be expected from the X(5) predictions. Thus, the general trend for these nuclei seems to be that the $K^\pi = 0_2^+ \rightarrow K^\pi = 0_1^+$ interband transition strength scale is weaker than predicted in X(5), albeit with some exceptions and some missing data.

The X(5) model predicts a characteristic branching pattern for the decay of members of the first excited band to the yrast band, in which the spin-descending branches are highly suppressed. Fig. 15.6 summarizes the branching properties for the 2^+ state in the first excited 0^+ sequence (denoted by $2_{0^+}^+$) for the N=88, 90, and 92 isotopes of Dy, Gd, and Sm. In going from N=88 to N=92, the $2_{0^+}^+ \rightarrow 0_1^+$ transition evolves from being highly suppressed relative to the $2_{0^+}^+ \rightarrow 4_1^+$ transition [$B(E2; 2_{0^+}^+ \rightarrow 0_1^+)/B(E2; 2_{0^+}^+ \rightarrow 4_1^+) \approx 0.01$ at N=88] to having substantial strength [$B(E2; 2_{0^+}^+ \rightarrow 0_1^+)/B(E2; 2_{0^+}^+ \rightarrow 4_1^+) \approx 0.20$ at N=92]. The suppression for N=88 is reminiscent of the situation in the pure oscillator limit, although clearly these nuclei are far from achieving pure oscillator structure. In this limit, the 2^+ state directly above the 0_2^+ state is the 2_3^+ state, and the only one of the three transitions which is phonon-allowed is the $2_{0^+}^+ \rightarrow 4_1^+$ transition (Fig. 15.6, bottom

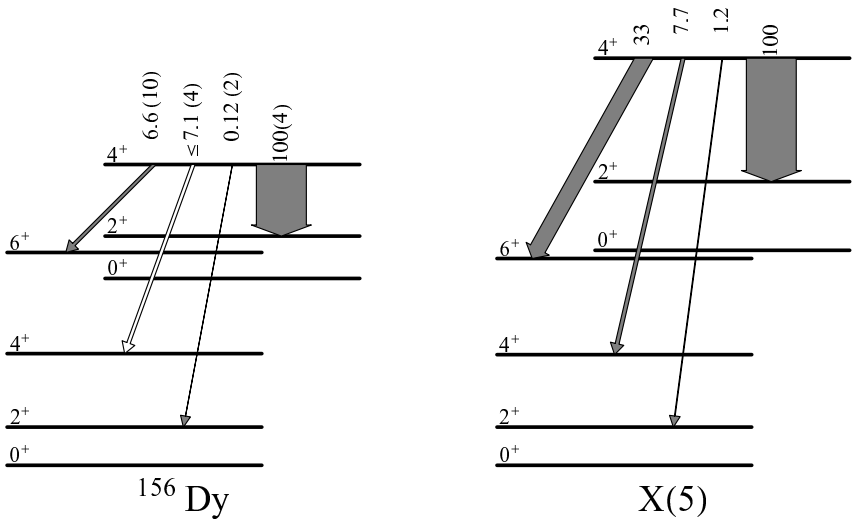

Figure 15.5: Relative $B(E2)$ strengths for transitions from the 4^+ member of the $K^\pi = 0_2^+$ band in ^{156}Dy, based upon data from Chapter 7. The X(5) predictions are shown for comparison. The open arrow for the spin-unchanging transition in ^{156}Dy indicates the possibility of $M1$ contamination. (Figure adapted from Ref. [77].)

left panel). For the N=92 nuclei, the relative $B(E2)$ strengths begin to resemble the Alaga-rule strengths expected for a pure rotor (Fig. 15.6, bottom right panel), though they do not fully match these values. For the N=90 nuclei ^{152}Sm and ^{154}Gd (as well as ^{150}Nd [39], not shown) the agreement with the X(5) predictions (Fig. 15.6, bottom center panel) is quite good. In ^{156}Dy, the $2_2^+ \rightarrow 0_1^+$ transition is extremely weak, with a relative $B(E2)$ strength at least a factor of 3–5 weaker than in the neighboring N=90 isotones or the X(5) predictions.

Of the N=90 isotones, ^{152}Sm is the most useful for comparison to model predictions, due to the availability of a full set of data from complementary types of experiments. Since the other N=90 isotones have similar properties, many aspects of the analysis of ^{152}Sm carry over directly to these nuclei as well. Comparison with the predictions of the X(5) model is straightforward, since the predictions for the yrast and $K^\pi = 0_2^+$ bands have essentially no free parameters (Section A.5). However, comparison with the predictions of the truncated form of the GCM discussed in Chapter 12 first requires a suitable set of parameter values to be identified.

Some of the most basic observables used to characterize the structure of the N=90 nuclei in the preceding discussion were the energy ratio $R_{4/2}$, the 0_2^+ level energy, and the branching ratio $B(E2; 2_2^+ \rightarrow 4_1^+)/B(E2; 2_2^+ \rightarrow 0_1^+)$. The 2_3^+ level energy is strongly

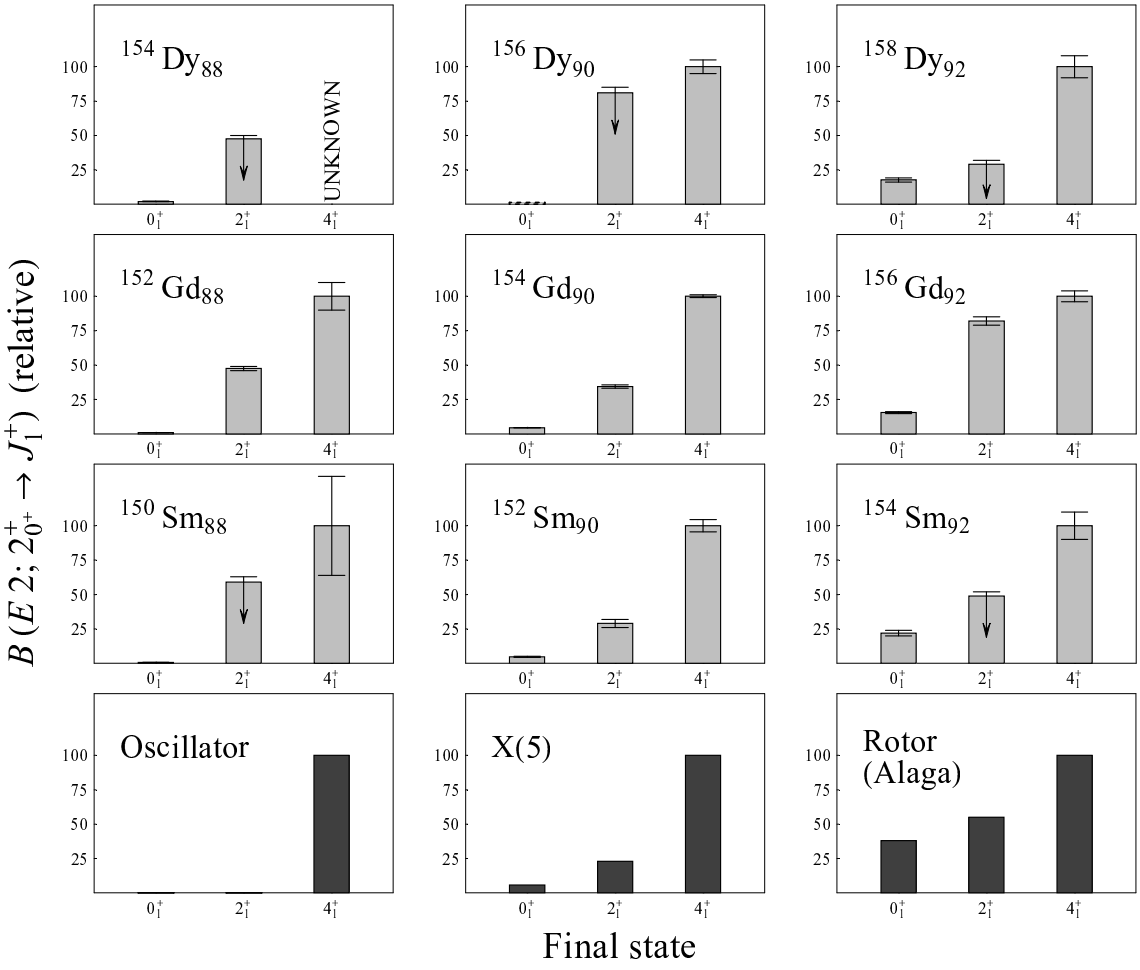

Figure 15.6: Relative $B(E2)$ branching strengths for the "interband" transitions from the 2^+ state built upon the first excited 0^+ state to the yrast 0^+, 2^+, and 4^+ states, shown for the N=88, 90, and 92 isotopes of Dy, Gd, and Sm. The extreme harmonic oscillator limit, X(5), and pure rotor limit predictions are provided for comparison at the bottom. Data are adopted values from Nuclear Data Sheets [21–25] except those for ^{152}Sm (Chapter 6) and ^{156}Dy (Chapter 7). Error bars on the relative $B(E2)$ strengths include contributions from the experimental uncertainties in intensity and $E2/M1$ mixing ratios. In the case of spin-unchanging transitions for which the $E2/M1$ mixing ratio is unknown, the $B(E2)$ strength is deduced assuming pure $E2$ multipolarity, and the possibility of arbitrarily large $M1$ contamination is indicated by a downward arrow. Since the strength of the $2_2^+ \rightarrow 4_1^+$ transition in ^{154}Dy is unknown, the strengths of the $2_2^+ \rightarrow 0_1^+$ and $2_2^+ \rightarrow 2_1^+$ transitions are normalized for comparison purposes by setting the relative $2_2^+ \rightarrow 2_1^+$ strength equal to that in the neighboring isotone ^{152}Gd. (Figure from Ref. [77].)

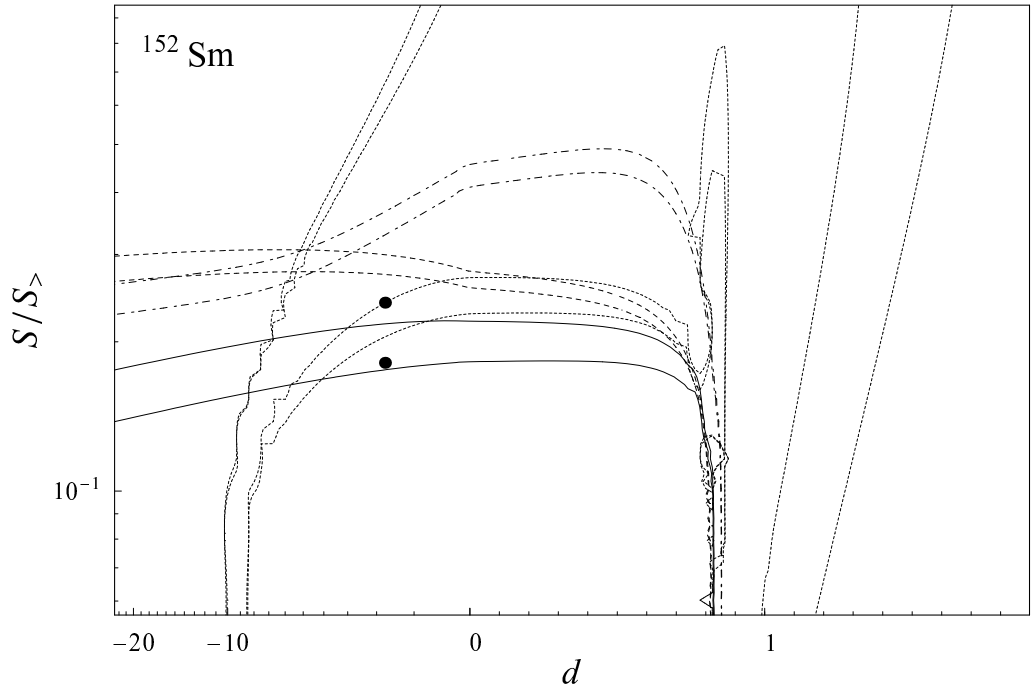

Figure 15.7: Regions in the (d,S) parameter space for which the GCM predictions of selected observables match the values found in ^{152}Sm: $R_{4/2}$=3.02 to within 2% (solid line), $E(0_2^+)/E(2_1^+)$=5.61 to within 5% (dashed line), $E(2_3^+)/E(2_1^+)$=8.90 to within 5% (dashed-dotted line), and $B(E2;2_2^+ \rightarrow 4_1^+)/B(E2;2_2^+ \rightarrow 0_1^+)$=21 to within 25% (dotted line). The solid circles indicate (d=-1.75, S=0.0121$\times 10^{42}$ MeV^{-2}s^{-2}) and (d=-1.75, S=0.018$\times 10^{42}$ MeV^{-2}s^{-2}), the parameter values discussed in the text.

influenced by the γ-dependence of the potential, which is irrelevant in the X(5) description due to a separation of variables but which must be addressed in the GCM description. Fig. 15.7 shows the regions in the (d, S) parameter space for which the GCM predictions of these observables match the values found in ^{152}Sm. No point of simultaneous agreement for all four observables exists, but reasonable compromises may be found. The GCM predictions for d=-1.75 and S=0.0121$\times 10^{42}$ MeV^{-2}s^{-2} were reported in Ref. [223]. The predictions for d=-1.75 and S=0.018$\times 10^{42}$ MeV^{-2}s^{-2}, discussed here, are similar, differing somewhat in the energy scale of the excited 0^+ sequence and in the overall normalization of the interband $B(E2)$ strengths.

The predictions of the GCM for d=-1.75 and S=0.018$\times 10^{42}$ MeV^{-2}s^{-2} are shown in Fig. 15.8(a), together with the observed values in ^{152}Sm and the predictions of the X(5) model. The GCM calculation yields an energy spacing scale for the excited 0^+ sequence which is greatly expanded compared to that of the yrast sequence. This effect is much

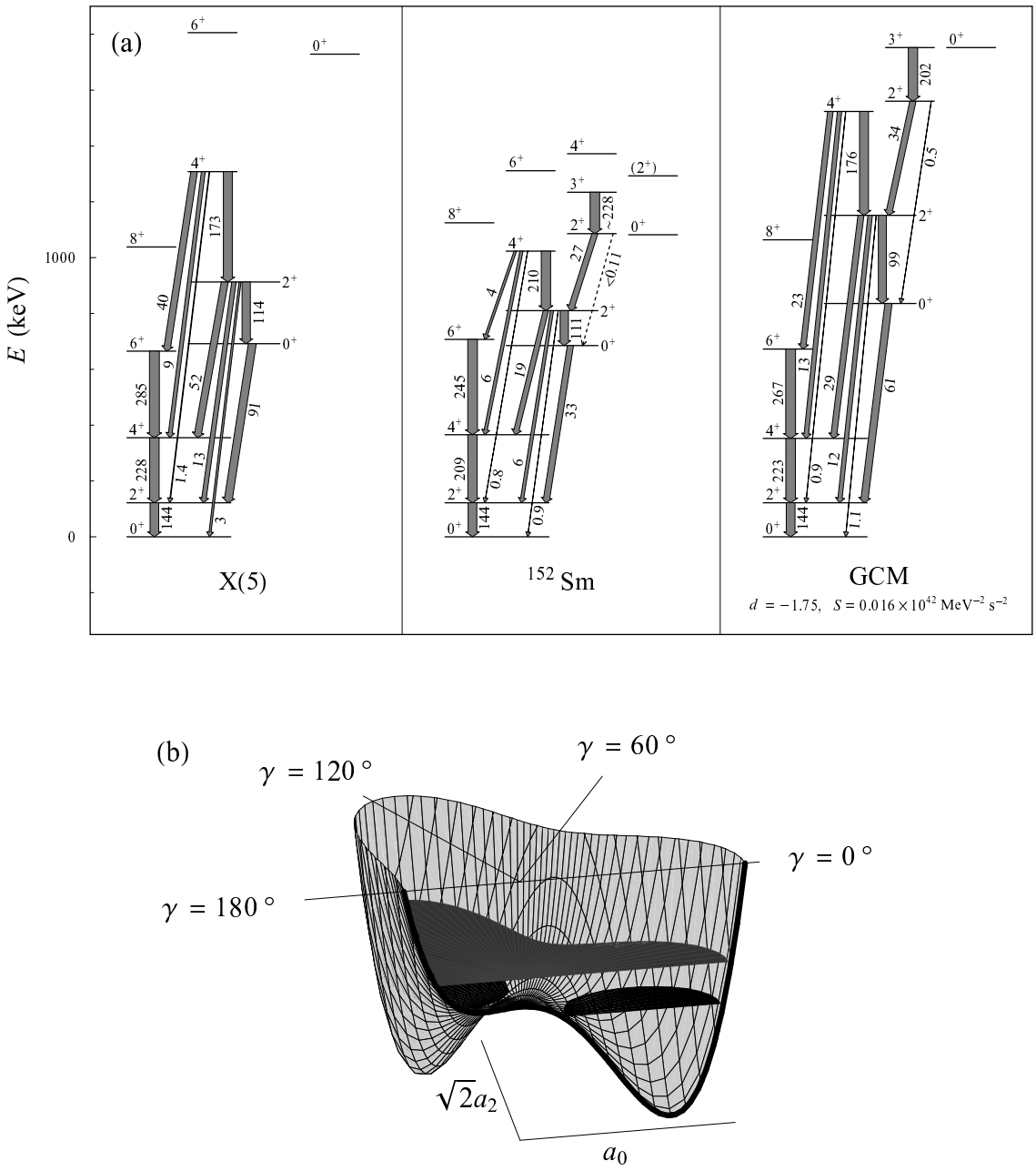

Figure 15.8: Model description of ^{152}Sm: (a) Experimental level scheme and selected $B(E2)$ strengths for ^{152}Sm. The X(5) predictions and the GCM predictions for d=-1.75 and S=0.016×10^{42} MeV^{-2}s^{-2}, normalized to the experimental $E(2_1^+)$ and $B(E2; 2_1^+ \rightarrow 0_1^+)$ values, are shown for comparison. All $B(E2)$ strengths are indicated in W.u., and transition arrow widths are proportional to the logarithm of the $B(E2)$ strength. Experimental values are from data in Refs. [22, 123] and Chapter 6. (See these references for uncertainties.) (b) A plot of the potential for the GCM calculation as a function of the shape coordinates, showing 0_1^+ and 0_2^+ level energies.

more exaggerated than in the X(5) model, as was also found in Section 13.2. The $R_{4/2}$ value for the excited 0^+ band, at 2.18, is much lower than the experimental or X(5) values [Fig. 15.3(b)]. The $B(E2)$ predictions from the GCM calculation are similar to those of X(5), providing comparable or, for several transitions, better agreement with the experimental values. The GCM calculation reproduces the decay properties of the 2_3^+ level to the 0_2^+ sequence, providing a good quantitative prediction for the relatively strong $2_3^+ \rightarrow 2_2^+$ transition and yielding a suppressed $2_3^+ \rightarrow 0_2^+$ transition. (The prediction for the $2_3^+ \rightarrow 0_2^+$ transition's strength varies rapidly in this region of parameter space and is much lower for d=-1.75 and S=0.0121$\times 10^{42}$ MeV^{-2}s^{-2}. See Ref. [223].) The GCM calculation, like the X(5) model, yields a relatively high-lying 0_3^+ state. It is not clear to what extent this state can be structurally identified with the observed 0_3^+ level in ^{152}Sm.

The potential for the GCM calculation at d=-1.75 and S=0.018$\times 10^{42}$ MeV^{-2}s^{-2} is shown in Fig. 15.8(b), together with the 0_1^+ and 0_2^+ level energies relative to this potential. At these energies, the potential is markedly soft in β, and, for the higher-energy of these two levels, $\beta = 0$ is even classically energetically accessible.

It apprears from the phenomenological comparisons that the gross qualitative features of the N=90 nuclei can be explained using a collective model with a β-soft, γ-stabilized deformation potential. Such a potential is a fundamental feature common to the descriptions of the N=90 nuclei provided by the X(5) model and the GCM calculations, as well as by IBM calculations [219]. Description of the N=90 nuclei with a β-soft potential is also consistent with predictions based upon the underlying single-particle structure, in the models of Kumar and Barranger and of Kishimoto and Tamura and in the Nilsson-Strutinsky-BCS model (see Refs. [200, 222, 223]). However, major aspects of the structure and of structural evolution in the region remain to be understood, as evidenced by, for instance, the substantial misprediction by the collective models of the energy scale for the excited sequence and by the erratic variations among the nuclei in the strengths for transitions from the 4_2^+ state.

15.2 ^{102}Pd

The level energies and $B(E2)$ strengths for the nucleus ^{102}Pd qualitatively resemble those predicted by the E(5) model, as discussed in Chapter 10. Let us summarize the comparison between the ^{102}Pd observed properties and the E(5) predictions [Fig. 15.9 (left, middle)] permitted by the new spectroscopic data. In the proposed ξ=1 family, spin multi-

plets following the O(5) structure are present for τ=0, 1, 2, and 3. These occur at energies ($R_{4/2}$, $E_{\tau=3}/E_{\tau=1}$) close to those expected in E(5) (Fig. 15.9), although the splitting of the τ=2 multiplet in ^{102}Pd leaves only the 4^+ member closely matching the predicted $E_{\tau=2}/E_{\tau=1}$ of E(5). A 0^+ member of the τ=3 multiplet must be found for this picture to be complete. The observed strengths for $E2$ transitions which are allowed in an O(5) scheme ($\Delta\tau = \pm 1$) are consistently enhanced over the forbidden transitions ($\Delta\tau = \pm 2$), pending experimental δ values. The lifetime of the 4^+ member of the τ=3 multiplet is known [158], yielding a $B(E2)$ strength to the $2^+_{\tau=2}$ level in agreement with E(5) (Fig. 15.9); lifetimes must be measured for the other multiplet members. With the lowest 0^+ state dismissed as a probable intruder on the basis of its energy evolution along the isotonic chain, the next higher 0^+ state is a good candidate for the ξ=2 family head, showing the $E2$ collectivity required in an O(5) picture and lying close to the energy predicted by E(5).

However, several differences in quantitative detail are present, as can be seen from Fig. 15.9. Some of the main deviations from the E(5) picture are:

1. The 4^+ and 2^+ members of the proposed τ=2 multiplet are split in energy, with the 4^+ level lower.

2. The absolute $B(E2; 2^+_{\tau=2} \rightarrow 2^+_{\tau=1})$ strength is lower than the $B(E2; 4^+_{\tau=2} \rightarrow 2^+_{\tau=1})$ strength.

3. Both the $3^+_{\tau=3}$ and $4^+_{\tau=3}$ states show a strong preference to decay to the $2^+_{\tau=2}$ state rather than to the $4^+_{\tau=2}$ state. Only a slight such preference is expected in E(5). (See also Table 10.1 on page 90.)

These deviations from the E(5) model predictions all are qualitatively consistent with the incipient formation of a γ band. Such structure would be expected if the potential were perturbed from E(5) to impose a slight preference for axial symmetry.

To consider this perturbation quantitatively, let us make use of the truncated GCM. The choice of values for the parameters d and S can be constrained simply by requiring that the low-lying energy observables be reproduced. It is desirable to retain the good agreement with the experimental $4^+_{\tau=2}$ level energy, τ=3 multiplet energy, and first excited 0^+ level energy obtained with the E(5) description while also reproducing the splitting of the $\tau = 2$ multiplet. Contours indicating the regions in GCM (d,S) parameter space for which the predictions match the experimental $R_{4/2}$, $E(2^+_2)/E(2^+_1)$, $E(4^+_2)/E(2^+_1)$, and $E(0^+_2)/E(2^+_1)$ values are shown in Fig. 15.10, leading to parameter values $d\approx$-43 and $S\approx 56\times10^{42}\,\mathrm{MeV}^{-2}\mathrm{s}^{-2}$.

The GCM predictions for d=-43 and $S=56\times10^{42}\,\mathrm{MeV}^{-2}\mathrm{s}^{-2}$ are shown in

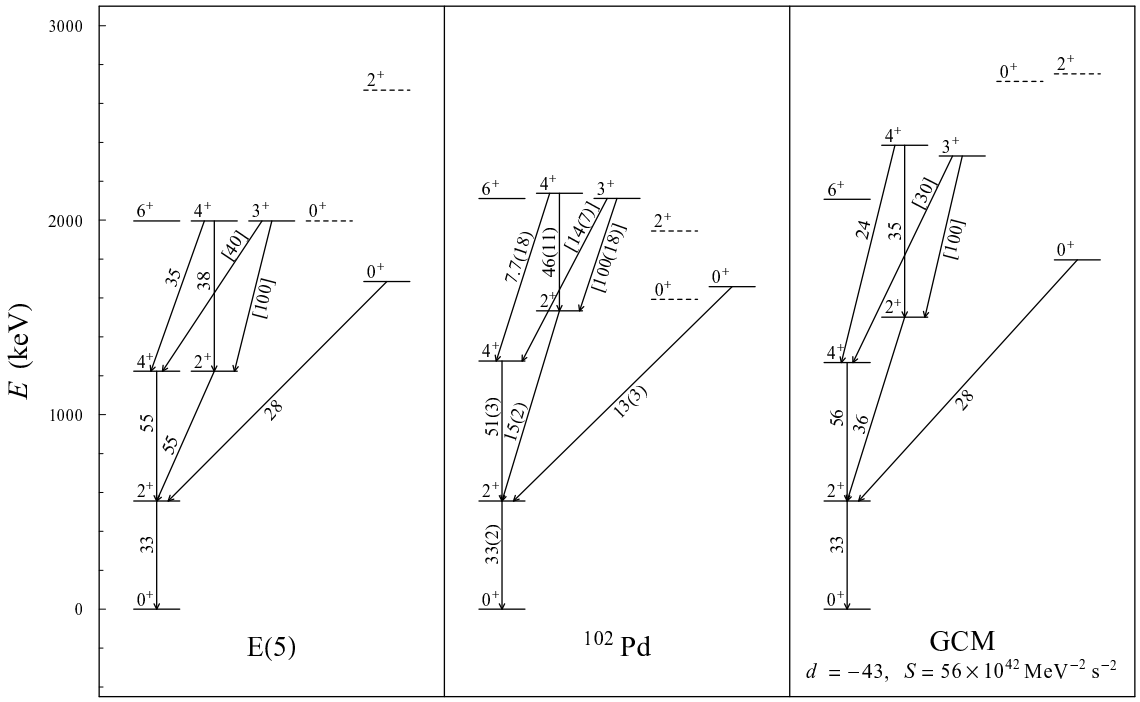

Figure 15.9: Experimental level scheme and $B(E2)$ strengths for ^{102}Pd, alongside the E(5) predictions and the GCM predictions for d=-43 and S=56×10^{42} MeV^{-2}s^{-2}, normalized to the experimental $E(2_1^+)$ and $B(E2; 2_1^+ \rightarrow 0_1^+)$ values. Observed levels with no clear theoretical counterpart or calculated levels with no clear experimental counterpart (see text) are indicated with dashed lines. Experimental $B(E2)$ strengths are from Refs. [153, 158] and Chapter 10, with the assumption of pure $E2$ multipolarity if the multipolarity is not otherwise known (see Table 10.1). $B(E2)$ values in brackets are relative values, while all others are absolute values in W.u.

Fig. 15.9 (right). The 4_1^+-2_2^+ splitting and low-lying level energies are well reproduced, although some splitting is introduced between the 6_1^+, 4_2^+, and 3_1^+ "multiplet" states. The $B(E2)$ strengths for the $2_2^+ \rightarrow 2_1^+$, $4_2^+ \rightarrow 4_1^+$, and $3_1^+ \rightarrow 4_1^+$ transitions are all reduced relative to the E(5) predictions, while the other transition strengths in Fig. 15.9 are relatively unaffected. The change in the predicted $2_2^+ \rightarrow 2_1^+$, $4_2^+ \rightarrow 4_1^+$, and $3_1^+ \rightarrow 4_1^+$ $B(E2)$ strengths is in the correct sense to bring them closer to the experimental values but leaves these strengths still much greater than observed. As noted above, one of the other outstanding issues regarding the interpretation of ^{102}Pd in the context of the E(5) picture is the nonobservation of any 0^+ level degenerate with the proposed τ=3 multiplet. In the GCM calculation, the 0_3^+ level is predicted to be substantially higher in energy than the 6_1^+, 4_2^+, and 3_1^+ states.

The potential for the GCM calculation for ^{102}Pd is plotted in Fig. 15.11, showing

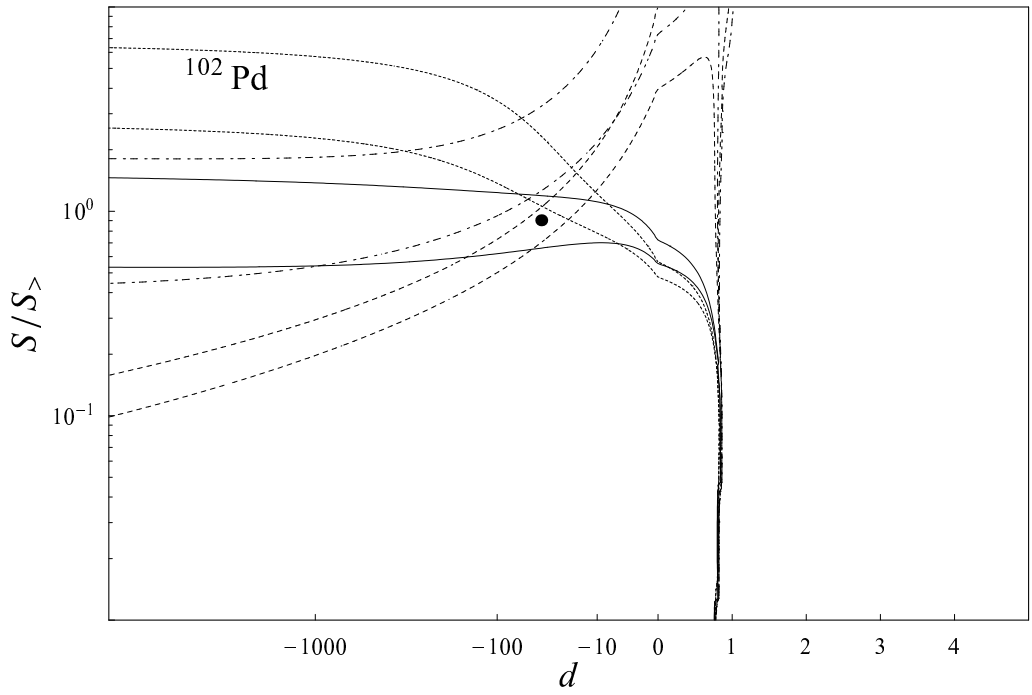

Figure 15.10: Regions in the (d,S) parameter space for which the GCM predictions of selected observables match the values found in ^{102}Pd: $R_{4/2}$=2.29 to within 2% (solid line), $E(2_2^+)/E(2_1^+)$=2.75 to within 5% (dashed line), $E(4_2^+)/E(2_1^+)$=3.84 to within 5% (dashed-dotted line), and $E(0_2^+)/E(2_1^+)$=2.98 to within 5% (dotted line). The solid circle indicates d=-43 and S=56×10^{42} MeV^{-2}s^{-2}, the parameter values discussed in the text.

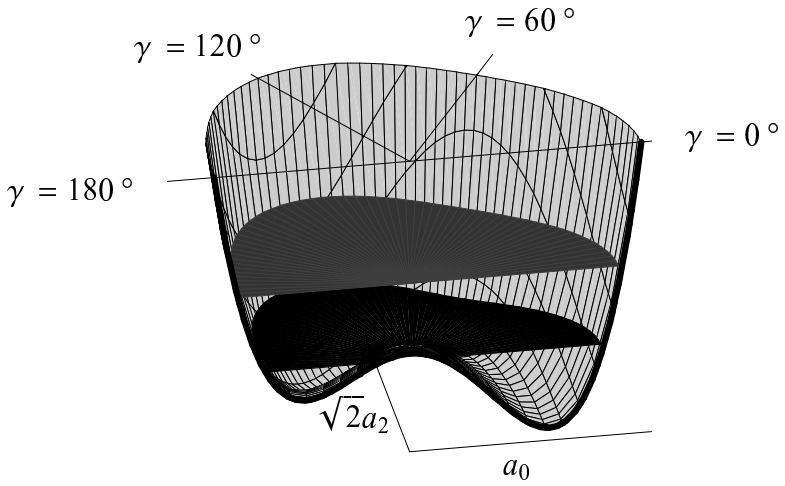

Figure 15.11: Plot of the potential for the GCM calculation for ^{102}Pd (d=-43, S=56×10^{42} MeV^{-2}s^{-2}) as a function of the shape coordinates, showing the 0_1^+ and 0_2^+ level energies.

the extent of the gentle minimum with respect to γ at γ=0°. This potential may be compared with the E(5)-like potential of Fig. 13.4(b) on page 136. In the present calculation, the ground state energy is just below the local maximum at β=0, making zero deformation energetically inaccessible. This does not, however, necessarily imply any major structural change to the states: even for a pure square well, with no maximum in the potential at β=0, the wave functions for low-lying states posess a low probability density at β=0 (see Fig. 14.3 on 146 for an illustration in the case of a finite well).

Part V

Conclusion

Chapter 16

Conclusion

The collective structure and excitation modes of nuclei intermediate between spherical and well-deformed structure present special challenges to categorization and to theoretical understanding. The recently proposed E(5) and X(5) models provide a new perspective on structure near the critical points of shape transitions, suggesting the relevance of an extreme "β-soft" form of structure. Examples of nuclei to which these models are relevant have been identified, including several in the $A\approx100$ and $N\approx90$ ($A\approx150$) regions considered in the present work.

For collective modes in transitional nuclei to be understood, solid experimental information must be obtained, especially for the low-spin, non-yrast states. Detailed and reliable knowledge of level properties is necessary both for an initial characterization of the structure of the nuclear states and for in-depth comparison with model predictions. Acquisition of this information requires varied and complementary experimental techniques, making use of the diverse available population mechanisms and detection resources. Several experimental approaches have been utilized in the present work, all of them involving γ-ray detection, based upon coincidence spectroscopy, electronic timing, and Doppler broadening methods in heavy-ion accelerator, reactor, and radioactive beam environments.

However, the necessary theoretical tools must also be present if an understanding of transitional structure is to be extracted from the experimental data. The E(5) and X(5) models provide benchmarks for structural comparison of transitional nuclei. The present work addressed the robustness of the predictions of the E(5) and X(5) models and identified the extent to which these predictions change under perturbations of the model Hamiltonian. The present work also included the development of an approach simplifying the use of an existing model, the geometric collective model, making this model more

straightforward to apply to transitional and deformed nuclei. This approach facilitates the study of nuclei with structures near, but not necessarily identical to, the E(5) and X(5) descriptions.

The present investigations demonstrate the relevance of β-soft potentials to transitional nuclei. The N=90 isotopes of Nd, Sm, Gd, and Dy all have characteristics reproduced by the X(5) model, with its β-soft, γ-localized potential, and by similar model descriptions. The nucleus ^{162}Er, bordering the $N\approx$90 transition region, appears to support an extremely low-lying β-vibrational excitation, implying a comparatively β-soft rotational structure. And the properties of ^{102}Pd match those of the E(5) model and similar descriptions involving a β-soft, nearly γ-independent potential. Future work must place these β-soft forms of nuclear structure more fully in the context of structural evolution. It must be seen in what form and to what extent these structures occur in other experimentally accessible transition regions.

Appendices

Appendix A

Collective nuclear structure benchmarks

A.1 Preliminary definitions

Several simple analytical models of collective structure are used as benchmarks for comparison throughout the preceding discussions. In this appendix, the basic results of these models are presented for reference. Further details may be found in, *e.g.*, Refs. [4–6] or in the original literature. Detailed level schemes and sets of $B(E2)$ values for the E(5) and X(5) models are also included.

The expansion of the nuclear surface shape in spherical harmonics was introduced in Section 1.2. For quadrupole deformation, the expansion (1.6) reduces to

$$R(\theta,\varphi) = R_0 \left[1 + \sum_{\mu=-2}^{2} \alpha_{2\mu} Y^*_{2\mu}(\theta,\varphi). \right] \tag{A.1}$$

The coefficients $\alpha_{2\mu}$ and the functions $Y^*_{2\mu}(\theta,\varphi)$ are in general both complex valued. For this "radius" $R(\theta,\varphi)$ to be a real number, the constraint $\alpha^*_{2\mu} = (-)^\mu \alpha_{2-\mu}$ must be imposed upon the coefficients.

The "instantaneous principal axis system" is the coordinate system defined by the conditions

$$a_{2-1} = a_{21} = 0 \qquad a_{2-2} = a_{22}, \tag{A.2}$$

so that the coordinate axes are aligned along the quadrupole shape's principal axes. The Euler angles $\underline{\theta}$ describing the rotation which relates this coordinate system ($a_{\lambda\mu}$) to the laboratory coordinate system ($\alpha_{\lambda\mu}$) therefore specify the "orientation" of the nucleus. Two degrees of freedom in the coordinates remain, describing the "shape" of the nucleus. These are the real variables $a_0 \equiv a_{20}$ and $a_2 \equiv a_{22}$, which may be reexpressed in terms of the

"Bohr shape variables" β and γ as

$$a_0 = \beta \cos\gamma \qquad a_2 = \frac{1}{\sqrt{2}}\beta \sin\gamma. \tag{A.3}$$

The coordinate β plays the role of a "radial" variable in the five-dimensional space of the coordinates $\alpha_{2\mu}$, since in general

$$\beta^2 = \sum_{\mu=-2}^{2} \alpha^*_{2\mu}\alpha_{2\mu}. \tag{A.4}$$

The coordinate system defined by (A.2) is ambiguous, in that any of the three coordinate axis may be chosen to lie along any of the three nuclear principal axes. The shapes described by $(\beta,\gamma)=(\beta_0,\gamma_0+2n\pi/3)$ or $(\beta,\gamma)=(\beta_0,-\gamma_0)$ are equivalent to that of $(\beta,\gamma)=(\beta_0,\gamma_0)$, but aligned along a different permutation of the axes. Thus, any function which is to depend upon the nuclear shape only must be invariant under these transformations.

The benchmark models described in the following sections may be defined in terms of a geometric Hamiltonian acting on the deformation coordinates, consisting of a kinetic energy operator and a potential energy operator which is a function of the nuclear shape only. For these models, the "harmonic" kinetic energy operator

$$-\frac{\hbar^2}{2B}\sum_{\mu}\frac{\partial^2}{\partial\alpha_{2\mu}\partial\alpha^*_{2\mu}} \tag{A.5}$$

is used. Several of these models also occur as dynamical symmetries of the IBM (Section 1.2) in the limit of infinite boson number.

A.2 Spherical oscillator

The five-dimensional harmonic oscillator Hamiltonian,

$$H = -\frac{\hbar^2}{2B}\sum_{\mu}\frac{\partial^2}{\partial\alpha_{2\mu}\partial\alpha^*_{2\mu}} + \frac{1}{2}C\beta^2, \tag{A.6}$$

has equally-spaced eigenvalues

$$E = \hbar\omega(N+\frac{5}{2}), \tag{A.7}$$

where $\omega \equiv (C/B)^{1/2}$ and N=0,1,..., analogous to those of the one-dimensional harmonic oscillator.[1] The eigenfunctions are known in closed form [5, 224–227], consisting of a radial

[1] The parameters B and C are related to the GCM parameters B_2 and C_2 (Chapter 12) by $B = (\sqrt{5}/2)B_2$ and $C = (2/\sqrt{5})C_2$.

factor,

$$f(\beta) = A_{n,\tau}\beta^{\tau}e^{-\frac{s^2\beta^2}{2}}L_n^{\tau+\frac{3}{2}}(s^2\beta^2), \tag{A.8}$$

where $A_{n,\tau}$ is a normalization constant, $s \equiv (B_2C_2/\hbar^2)^{1/4}$ is the oscillator "stiffness", $L_n^{\tau+\frac{3}{2}}$ is a Laguerre polynomial, τ is a separation constant, and n is the index for the radial solution, multiplied by a more complicated angular wave function $\Phi(\gamma,\underline{\theta})$. The oscillator eigenstates constitute a convenient basis for the expansion of other states in numerical work, as discussed in Subsection 12.1.2. The harmonic oscillator arises in the IBM as well, as the infinite boson number limit of the U(5) dynamical symmetry [228].

The eigenstates of the harmonic oscillator fall into degenerate multiplets, equally spaced in excitation energy, containing levels of spins 0^+, 2^+, 4^+-2^+-0^+, 6^+-4^+-3^+-2^+-0^+, *etc.*, as illustrated in Fig. 1.3(a) on page 6. For comparison to other models, observe that $R_{4/2}[\equiv E(4_1^+)/E(2_1^+)]$=2.00. The $E2$ transitions between these levels follow a "phonon" creation or destruction selection rule, in which transitions are only possible between states in adjacent multiplets. Specific $B(E2)$ strength predictions exist (*e.g.*, Ref. [228]). Here let us just note that $B(E2;4_1^+ \rightarrow 2_1^+)/B(E2;2_1^+ \rightarrow 0_1^+)$=2.

A.3 Deformed γ-soft structure

If the potential $V(\beta,\gamma)$ is a function of β only, independent of γ, the five-dimensional equivalent of a "central force problem" arises, and the Hamiltonian is invariant under the group O(5) of rotations in five-dimensional space. A separation of variables occurs [229, 230], giving eigenfunctions of the form $f(\beta)\Phi(\gamma,\underline{\theta})$. The solutions for the "angular" $(\gamma,\underline{\theta})$ wave functions [214] are common to all γ-independent ("γ-soft") problems. The equation for $f(\beta)$ is

$$\left[\frac{\hbar^2}{2B}\left(-\frac{1}{\beta^4}\frac{\partial}{\partial\beta}\beta^4\frac{\partial}{\partial\beta}+\frac{\tau(\tau+3)}{\beta^2}\right)+V(\beta)\right]f(\beta) = Ef(\beta), \tag{A.9}$$

where the separation constant τ assumes the values $\tau = 0, 1, \ldots$. Each radial solution gives rise to a degenerate multiplet of states, with each of the angular wave functions obtained for that value of τ. The first few τ multiplets contain members of spins 0^+, 2^+, 4^+-2^+, 6^+-4^+-3^+-0^+, ... For a linear electric quadrupole operator, the $E2$ transitions follow a $\delta\tau=\pm1$ selection rule. Also, since all $E2$ matrix elements between members of two specific multiplets share the same radial matrix element, their relative strengths depend only upon the angular matrix elements, which are universal to all γ-soft problems. Several examples of γ-soft Hamiltonians are encountered in the preceding chapters, including the E(5) finite

well Hamiltonian and the GCM quadratic-quartic Hamiltonian. The harmonic oscillator is a special example, in which extra degeneracies occur.

Wilets and Jean [229] consider the limiting case of near-rigid β deformation, in which harmonic oscillations in β occur, independent of the separation constant τ. This yields an analytic solution for the level excitation energies

$$E = \hbar \left(\frac{B}{C}\right)^{1/2} \left[\frac{\tau(\tau+3)}{2x_0^2} + n_\beta\right] \tag{A.10}$$

where n_β=0,1,..., τ=0,1,..., and the parameters B, C, and $x_0 \gg 1$ arise in the particular parametrization of the potential used [229] to obtain this limiting case. Thus, for each value of n_β, a "family" of τ multiplets arises, as illustrated in Fig. 1.3(c) on page 6, sharing the same radial wave function, and the $B(E2)$ strengths within a family are completely determined [218]. For reference, let us note that $R_{4/2}$=2.50 and $B(E2; 4_1^+ \rightarrow 2_1^+)/B(E2; 2_1^+ \rightarrow 0_1^+)$=10/7. The Wilets-Jean deformed γ-soft structure arises in the IBM as the infinite boson number limit of the O(6) dynamical symmetry [218].

A.4 Deformed axially symmetric rotor

If β is rigidly confined to some nonzero value β_0, and γ is rigidly confined to 0°, the nucleus posesses a fixed axially-symmetric shape, and it can undergo rotations in space. The wave functions for the rotational motion in terms of the Euler angles, $\phi(\underline{\theta})$, have closed-form solutions in terms of the Wigner D functions.

A more general case occurs if the "confinement" in β and γ is not strictly rigid but rather allows small oscillations to occur, decoupled from the overall rotational motion. The relevant modes are illustrated in Fig. 1.4 on page 6. The wave function then may be decomposed as the product of an intrinsic (β, γ) wave function with the rotational wave function (see Ref. [4] for details of symmetrization). The intrinsic wave function describes the state of the system as viewed in the body-fixed principal axis system (Subsection A.1) rotating along with the nucleus. Since the Hamiltonian is invariant under rotations about the symmetry axis, the projection K of angular momentum along this axis must be a good quantum number. The one-phonon excitation for vibrations in the Y_{20}, or β, mode has K=0, while that for the $Y_{2\pm2}$, or γ, mode has K=2. Each intrinsic state gives rise to a sequence, or "band", of rotational states, with spins $J=K, (K+1), \ldots$, except that K=0 yields only even spins J=0,2,.... The excitation energies within a band

depend upon J as $\hbar^2 J(J+1)/(2\mathcal{J})$, where $\mathcal{J}$ is a moment of inertia. A schematic rotational level scheme is shown in Fig. 1.3(b) on page 6. The basic picture of intrinsic vibrational excitations provided here is somewhat schematic, but the topic can be treated quantitatively, in terms of a harmonic oscillator potential at β=β_0, within the rotation vibration model (RVM) [184]. Rotational structure arises in the IBM as the infinite boson number limit of the SU(3) dynamical symmetry [231]. For the rotor, $R_{4/2}$=3.33 and $B(E2;4_1^+ \rightarrow 2_1^+)/B(E2;2_1^+ \rightarrow 0_1^+)$=10/7.

The matrix element of an electromagnetic transition operator between two states is a product of a factor depending upon the intrinsic structure, namely, the matrix element of an "intrinsic frame" multipole operator $\mathfrak{M}'(\sigma\lambda)$ between the respective intrinsic states, and a factor depending upon the rotational wave functions, which depends only upon the J and K quantum numbers involved. For two states, $\alpha_1 K_1 J_1$ and $\alpha_2 K_2 J_2$, $K_1 \leq K_2$, the matrix element of the multipole operator $\mathfrak{M}(\sigma\lambda)$ is

$$\langle \alpha_2 K_2 J_2 || \mathfrak{M}(\sigma\lambda) || \alpha_1 K_1 J_1 \rangle = \frac{(2J_1+1)^{1/2}}{(2J_2+1)^{1/2}} \langle J_1 K_1 \lambda (K_2 - K_1) | J_2 K_2 \rangle \times \langle \alpha_2 K_2 | \mathfrak{M}'(\sigma\lambda; K_2 - K_1) | \alpha_1 K_1 \rangle \begin{cases} \sqrt{2} & K_1 = 0 \text{ and } K_2 \neq 0 \\ 1 & \text{otherwise} \end{cases} , \quad \text{(A.11)}$$

provided that, if K_1 and K_2 are both nonzero, K_1+$K_2 > \lambda$ (otherwise, an extra "signature" cross term is present). Since all states within a band share the same intrinsic state, the intrinsic matrix element is common to all pairs of states chosen from two given bands. This leads to the Alaga strength relations for interband transitions, summarized for selected $E2$ transitions in Table A.1. The Alaga rules are reasonably well reproduced in many rotational nuclei. However, the rotational model is most successful not in its pure form but rather when it incorporates band mixing, according to a mechanism described by Bohr and Mottelson, which can allow large sets of transition strengths to be described with just a single mixing parameter [4]. The specific case of mixing between bands with ΔK=0 is considered in Appendix C.

$K_i \to K_f$	$J_i \to J_f$	$\frac{B(E2;i\to f)}{\langle i\|\mathfrak{M}'(E2)\|f\rangle^2}$	$K_i \to K_f$	$J_i \to J_f$	$\frac{B(E2;i\to f)}{\langle i\|\mathfrak{M}'(E2)\|f\rangle^2}$
$0 \to 0$	$0 \to 2$	1.0000	$2 \to 0$	$2 \to 0$	0.2000×2
	$2 \to 0$	0.2000		2	0.2857×2
	2	0.2857		4	0.0143×2
	4	0.5143		$3 \to 2$	0.3571×2
	$4 \to 2$	0.2857		4	0.1429×2
	4	0.2597		$4 \to 2$	0.1190×2
	6	0.4545		4	0.3506×2
	$6 \to 4$	0.3147		6	0.0303×2
	6	0.2545		$5 \to 4$	0.3182×2
	8	0.4308		6	0.1818×2
	$8 \to 6$	0.3294		$6 \to 4$	0.0979×2
	8	0.2526		6	0.3636×2
	10	0.4180		8	0.0385×2
$0 \to 2$	$0 \to 2$	1.0000×2		$7 \to 6$	0.3000×2
	$2 \to 2$	0.2857×2		8	0.2000×2
	3	0.5000×2		$8 \to 6$	0.0882×2
	4	0.2143×2		8	0.3684×2
	$4 \to 2$	0.0079×2		10	0.0433×2
	3	0.1111×2	$2 \to 2$	$2 \to 2$	0.2857
	4	0.3506×2		3	0.5000
	5	0.3889×2		4	0.2143
	6	0.1414×2		$3 \to 2$	0.3571
	$6 \to 4$	0.0210×2		3	0.0000
	5	0.1538×2		4	0.3429
	6	0.3636×2		5	0.3000
	7	0.3462×2		$4 \to 2$	0.1190
	8	0.1154×2		3	0.2667
	$8 \to 6$	0.0294×2		4	0.0416
	7	0.1765×2		5	0.2333
	8	0.3684×2		6	0.3394
	9	0.3235×2			
	10	0.1022×2			

Table A.1: Ratio of the $B(E2)$ strength to the squared intrinsic matrix element for an ideal rotor, $B(E2;\alpha_i K_i J_i \to \alpha_f K_f J_f)/\langle \alpha_f K_f|\mathfrak{M}'(E2;K_f - K_i)|\alpha_i K_i\rangle^2$, shown for selected K and J values. The values for this ratio yield the Alaga interband strength rules, as well as in-band strength relations. Values are calculated from (A.11) and the definition (B.2) of $B(E2)$.

A.5 Square well potentials: E(5) and X(5)

The E(5) and X(5) models of Iachello [35, 36], introduced in Section 1.3, are both based upon a square well potential in β. For the E(5) model, the potential is γ-independent,

$$V(\beta) = \begin{cases} 0 & \beta \leq \beta_w \\ \infty & \beta > \beta_w, \end{cases} \tag{A.12}$$

and so the separation of variables described in Section A.3 occurs. The radial equation for $\beta<\beta_w$ is equivalent [35] to the Bessel equation of half-integer order $\nu=\tau+3/2$. The solution wave function may be be written in terms of the spherical Bessel function of the first kind, $j_n(x) \equiv \sqrt{\frac{\pi}{2}} x^{-1/2} J_{n+1/2}(x)$, of integer order $n=\tau+1$. In terms of the reduced energy eigenvalue $\varepsilon_{\xi,\tau} \equiv (2B/\hbar^2)E_{\xi,\tau}$, the wave function in β for the ξth solution with separation constant τ is

$$f_{\xi,\tau}(\beta) = \begin{cases} A_{\xi,\tau}\beta^{-1} j_{\tau+1}(\varepsilon_{\xi,\tau}^{1/2}\beta) & \beta \leq \beta_w \\ 0 & \beta > \beta_w, \end{cases} \tag{A.13}$$

where $A_{\xi,\tau}$ is a normalization constant. The wave function must vanish at $\beta = \beta_w$, yielding the eigenvalue condition

$$\varepsilon_{\xi,\tau} = \beta_w^{-2} x_{\tau+3/2,\xi}^2, \tag{A.14}$$

$\xi = 1, 2, \ldots$, where $x_{\nu,i}$ is the ith zero of the ordinary Bessel function $J_\nu(x)$. The value of A is determined by the normalization condition $\int_0^\infty \beta^4 d\beta |f(\beta)|^2 = 1$. The normalization integral can be evaluated analytically [232, (5.54.2)], yielding

$$A = \left[\frac{\beta_w^3}{2} \left[j_n(\varepsilon^{1/2}\beta_w)^2 - j_{n-1}(\varepsilon^{1/2}\beta_w) j_{n+1}(\varepsilon^{1/2}\beta_w) \right] \right]^{-1/2}, \tag{A.15}$$

where $n=\tau+1$.

Electromagnetic transition strengths can be calculated from the matrix elements of the collective multipole operators. In terms of the intrinsic frame coordinates β and γ, the $E2$ transition operator is[2] [4, 5]

$$\mathfrak{M}(E2;\mu) \propto \beta \left[D^{2\,*}_{\mu,0}(\underline{\theta}) \cos\gamma + \frac{1}{\sqrt{2}} \left[D^{2\,*}_{\mu,2}(\underline{\theta}) + D^{2\,*}_{\mu,-2}(\underline{\theta}) \right] \sin\gamma \right], \tag{A.16}$$

[2] The Wigner function $D^j_{mm'}(\underline{\theta})$ used here is that of Rose [233], consistent with Ref. [5], which is related to the "script" $\mathcal{D}^{(j)}_{mm'}(\underline{\theta})$ of both Rose [233] and Edmonds [234] by $D^j_{mm'}(\underline{\theta}) = (-)^{m'-m} \mathcal{D}^{(j)\,*}_{mm'}(\underline{\theta})$ and is related to the $\mathcal{D}^j_{mm'}(\underline{\theta})$ of Bohr and Mottelson [4, 235] by complex conjugation.

and the transition strengths are $B(E2; J_i \rightarrow J_f) = \frac{2J_f+1}{2J_i+1} |\langle J_f || \mathfrak{M}(E2) || J_i \rangle|^2$ (Appendix B). Matrix elements factorize into a radial integral

$$\int_0^\infty \beta^4 d\beta \, f^{\rm I}(\beta) \, \beta \, f^{\rm II}(\beta), \tag{A.17}$$

which may be evaluated using the wave functions (A.13), and an angular integral common to all γ-soft problems, tabulated in, *e.g.*, Ref. [218]. Multiplet energies and $B(E2)$ strengths for the E(5) model are summarized in Fig. A.1.

In the X(5) model, a square well potential in β is combined with a term $V_\gamma(\gamma)$ providing stabilization about γ=0, so

$$V(\beta,\gamma) = \left\{ \begin{array}{ll} 0 & \beta \leq \beta_w \\ \infty & \beta > \beta_w \end{array} \right\} + V_\gamma(\gamma). \tag{A.18}$$

An approximate separation of the wave function into radial, γ, and rotational factors, $f(\beta)\eta(\gamma)\phi(\underline{\theta})$ occurs [36]. The radial equation for $f(\beta)$ is equivalent to the Bessel equation of order

$$\nu = \left(\frac{L(L+1)}{3} + \frac{9}{4} \right)^{1/2}, \tag{A.19}$$

where the separation constant L is the angular momentum quantum number. The radial wave function for the sth radial excitation for separation constant L is

$$f_{s,L}(\beta) = \left\{ \begin{array}{ll} A_{s,L} \beta^{-1} j_{\nu-1/2}(\varepsilon_{s,L}^{1/2} \beta) & \beta \leq \beta_w \\ 0 & \beta > \beta_w, \end{array} \right. \tag{A.20}$$

where $A_{s,L}$ is a normalization constant. The condition that the wave function vanish at $\beta = \beta_w$ yields the eigenvalue condition

$$\varepsilon_{s,L} = \beta_w^{-2} x_{\nu,s}^2, \tag{A.21}$$

$s = 1, 2, \ldots$, and the value of A is again determined from (A.15), but now using n=$\nu - 1/2$ with ν given by (A.19). To the extent that the approximate separation of variables holds, the details of the potential V_γ are irrelevant to the calculation of the properties of states involving only rotational and β excitations. A band structure analogous to that of the rigid rotor arises, with K=0 for all bands involving only radial excitations. However, the energies (A.21) differ substantially from those of a rigidly-deformed rotor, and the intrinsic state (A.20) is different for each member of a band. As in the E(5) calculations, the $E2$ matrix elements factor into a radial part (A.17), involving $f(\beta)$, and an angular part. The angular part in the X(5) case is the same as for the rigid rotor (A.11). Level energies and $B(E2)$ strengths for the X(5) model are summarized in Fig. A.2.

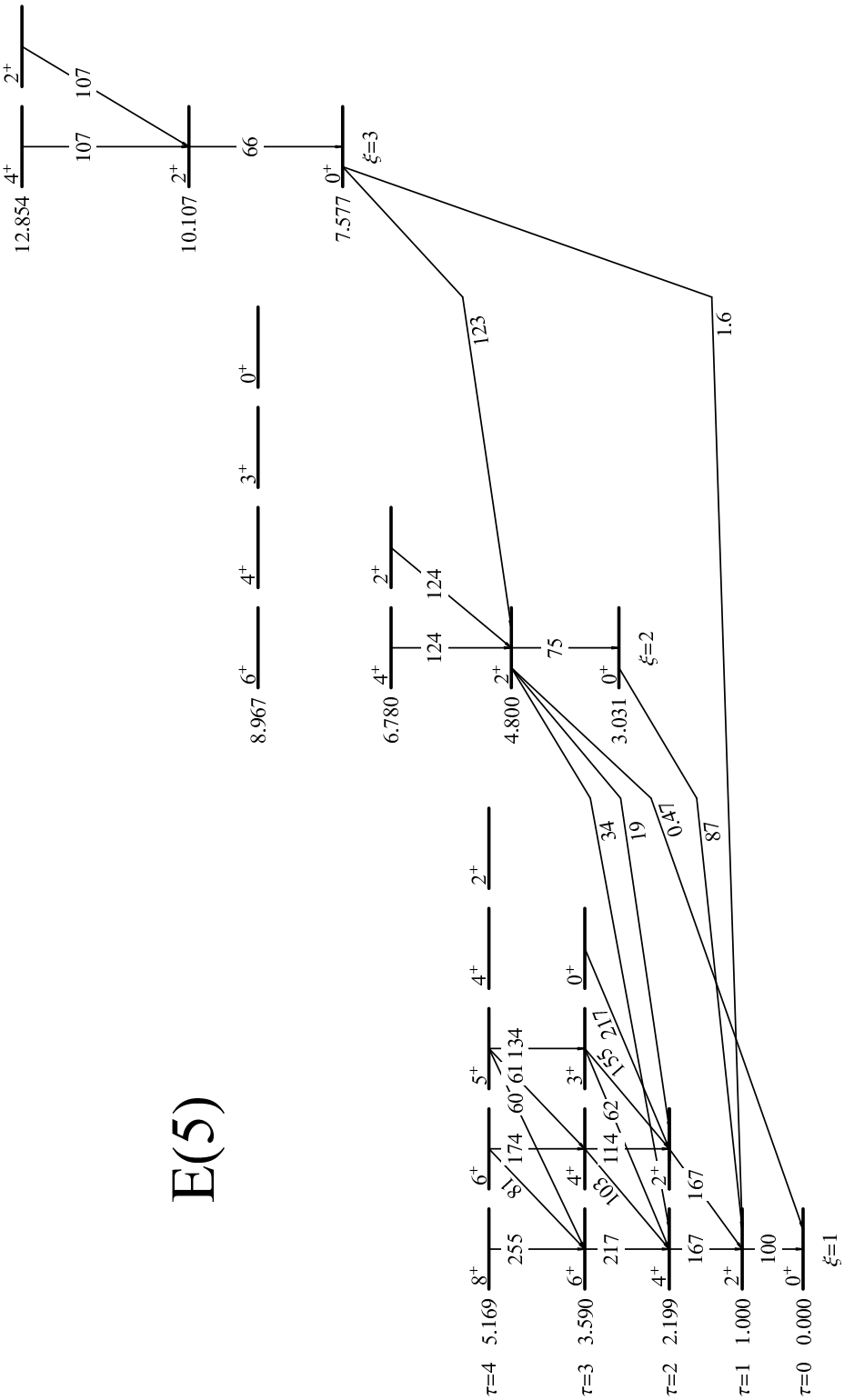

Figure A.1: Level scheme for the E(5) model, showing the lowest τ multiplets of the first three ξ families. Level energies and selected $B(E2)$ strengths are indicated.

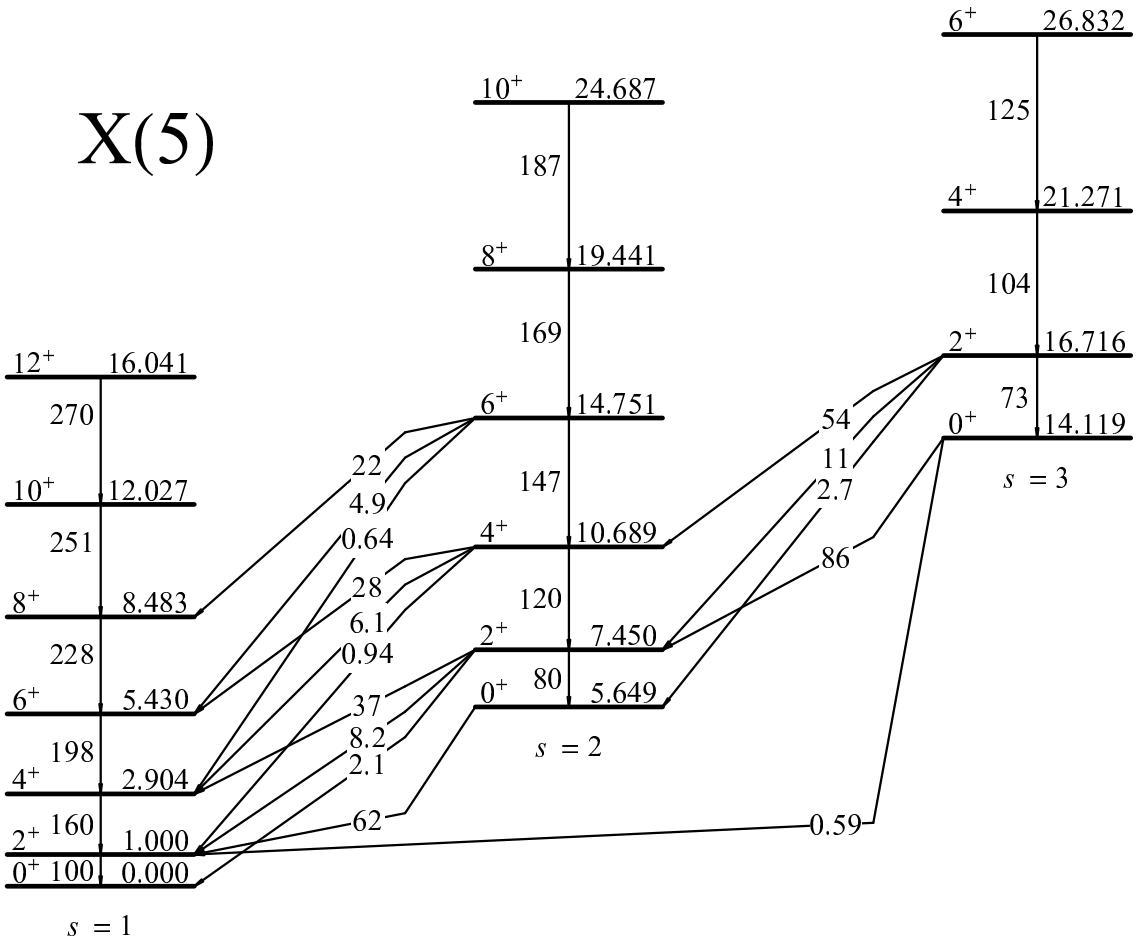

Figure A.2: Level scheme for the X(5) model, showing the lowest members of the first three s bands. Level energies and selected $B(E2)$ strengths are indicated.

Appendix B

Gamma-ray transition rates and matrix elements

Several pieces of spectroscopic and lifetime data must usually be combined to extract an experimental value for single transition matrix element, as discussed in Chapter 2. This appendix provides precise statements of the relations between the multipole matrix elements, transition rates, lifetimes, branching fractions, and mixing ratios used throughout this work, as well as a definition for the "Weisskopf unit" used for reporting $B(\sigma\lambda)$ strengths. These relations are also restated in forms more directly useful in practical spectroscopic data analysis.

For a γ-ray transition of multipolarity $\sigma\lambda$ between two levels, the transition probability per unit time is, in first order perturbation theory (*e.g.*, Refs. [4, 53, 54]),

$$T(\sigma\lambda; i \to f) = \frac{8\pi(\lambda+1)}{\lambda[(2\lambda+1)!!]^2}\frac{1}{\hbar}\left(\frac{E_\gamma}{\hbar c}\right)^{2\lambda+1} B(\sigma\lambda; i \to f), \tag{B.1}$$

where E_γ is the transition energy and $B(\sigma\lambda; i \to f)$ is the squared matrix element of the multipole operator $\mathfrak{M}(\sigma\lambda)$, averaged over initial and summed over final spin projection substates,

$$\begin{aligned} B(\sigma\lambda; i \to f) &\equiv \frac{1}{2J_i+1}\sum_{m_i,\mu,m_f} |\langle f J_f m_f|\mathfrak{M}(\sigma\lambda;\mu)|i J_i m_i\rangle|^2 \\ &= \frac{2J_f+1}{2J_i+1}\,|\langle f||\mathfrak{M}(\sigma\lambda)||i\rangle|^2 . \end{aligned} \tag{B.2}$$

Specifically, for $E2$ and $M1$ transitions, the decay rates obtained are

$$\begin{aligned} T(E2) &\approx (1.225\times 10^{-2}/\mathrm{s})\left(\frac{E_\gamma}{\mathrm{keV}}\right)^5 \left[\frac{B(E2)}{e^2\mathrm{b}^2}\right] \\ T(M1) &\approx (1.758\times 10^{4}/\mathrm{s})\left(\frac{E_\gamma}{\mathrm{keV}}\right)^3 \left[\frac{B(M1)}{\mu_N^2}\right], \end{aligned} \tag{B.3}$$

making use of the relations $e^2{=}\alpha\hbar c$ and $\mu_N = e\hbar/(2m_p c)$ in Gaussian units.

Weisskopf [4, 236] introduced estimates $B_W(\sigma\lambda)$ for the transition strength induced by a single proton moving in a schematic orbit,

$$\begin{aligned} B_W(E\lambda) &\equiv \frac{(0.12)^{2\lambda}}{4\pi}\left(\frac{3}{\lambda+3}\right)^2 A^{2\lambda/3}\, e^2 \mathrm{b}^\lambda \\ B_W(M\lambda) &\equiv \frac{10}{\pi}(0.12)^{2(\lambda-1)}\left(\frac{3}{\lambda+3}\right)^2 A^{2(\lambda-1)/3}\, \mu_N^2 \mathrm{b}^{(\lambda-1)}, \end{aligned} \tag{B.4}$$

and it is common to use these estimates as units ("W.u.") for reporting $B(\sigma\lambda)$ strengths. To provide a concrete example, a 1 MeV $E2$ γ-ray of 1 W.u. strength in a mass 100 nucleus produces a transition rate of $3.4{\times}10^{10}$/s; a level decaying only by this transition would have a lifetime of 30 ps. If the same transition were an $M1$ transition of 1 W.u. strength, the lifetime would be 32 fs.

The partial transition probabilities for the branches combine to produce an aggregate decay rate

$$T = \sum_i T_i^\gamma + \sum_i T_i^{\text{c.e.}}, \tag{B.5}$$

and hence lifetime $\tau = T^{-1}$, for the level. The total time-integrated probability B_a that the level will decay by any one particular branch a is simply the ratio of the partial transition rate for that branch to the total rate, so

$$B_a = \frac{T_a}{T}. \tag{B.6}$$

Each individual γ-ray transition can in general proceed by multiple radiation multipolarities simultaneously, subject to angular momentum and parity selection rules. However, as a consequence of the finite size of the nucleus, each successively higher multipole of γ radiation is suppressed by a factor of $\sim k_\gamma R_{\text{nucl}}$ (typically ∼10–100), where k_γ is the photon wave number and R_{nucl} is the approximate nuclear radius. Therefore, in practice, γ radiation is usually encountered either with pure multipolarity or in an admixture of two successive multipolarities — specifically, if the lowest multipolarity capable of connecting the initial and final states is magnetic in nature ($M\lambda$), the next higher electric multipole [$E(\lambda+1)$] often contributes substantially. The "amplitude mixing ratio" is $\delta \equiv \langle f||E(\lambda+1)||i\rangle \;/\; \langle f||M\lambda||i\rangle$, where the "multipole operators" used here are the $\mathfrak{M}(\sigma\lambda)$ renormalized to give the transition rates (B.1) directly. Phase conventions for δ are discussed further in Appendix D. The relative contribution of the two multipolarities to the transition rate, or the "multipole radiation intensity ratio", is then $\delta^2 = T[E(\lambda+1); i\to f]/T(M\lambda; i\to f)$. Some experimental methods for determining δ are described in Section 4.2.

Let us now combinine the information presented so far into expressions of direct use to the spectroscopist: for a mixed $E2/M1$ transition a from level i to level f, the $B(M1)$ and $B(E2)$ transition strengths in W.u. are related to experimentally accessible quantities as

$$\begin{aligned} B(E2; i \to f) &\approx \frac{(1.374 \times 10^7 \text{ W.u.})}{A^{4/3}} \left(\frac{E_a}{\text{keV}}\right)^{-5} \left(\frac{\tau_i}{\text{s}}\right)^{-1} B_a \frac{\delta_a^2}{1+\delta_a^2} \\ B(M1; i \to f) &\approx (3.176 \times 10^{-5} \text{ W.u.}) \left(\frac{E_a}{\text{keV}}\right)^{-3} \left(\frac{\tau_i}{\text{s}}\right)^{-1} B_a \frac{1}{1+\delta_a^2}, \end{aligned} \tag{B.7}$$

where A is the atomic mass, E_a is the transition energy, τ_i is the initial level lifetime, B_a is the γ-ray branching fraction, and δ_a is the mixing ratio.

Appendix C

Rotational $\Delta K = 0$ mixing relations

Relations describing the mixing of two rotational bands of the same K quantum number (ΔK=0 mixing) are needed for the interpretation of the ^{162}Er data in Section 11.4. The purpose of this appendix is to collect and summarize the relevant relations from Ref. [4] and to present additional specialized results needed for Section 11.4.

Bohr and Mottelson [4] deduce a mixing operator

$$H_c = h_0(\mathbf{J}^2 - J_3^2) \tag{C.1}$$

between the same-spin levels of two bands related by ΔK=0. Here h_0 is an "intrinsic" operator (*i.e.*, the matrix element of h_0 between two levels depends only upon their intrinsic states), and J_3 is the projection of angular momentum on the nuclear symmetry axis. If the bands have the same moment of inertia, the energy difference $E(\alpha_2 KJ) - E(\alpha_1 KJ)$ between same-spin levels is independent of J, and the mixing "energy denominator" for the perturbation calculation can be absorbed into a redefined operator

$$\varepsilon_0 \equiv \frac{h_0}{E(\alpha_2 K) - E(\alpha_1 K)}, \tag{C.2}$$

where band 2 is the *higher* energy band. The states in the mixed bands still have good quantum number K, but there is no longer a single intrinsic state common to all members of the band. The mixed states, as a function of spin, are

$$\begin{aligned} |\hat{\alpha}_1 KJ\rangle &= |\alpha_1 KJ\rangle \; - \; \langle \alpha_2 K|\varepsilon_0|\alpha_1 K\rangle \, J(J+1) \, |\alpha_2 KJ\rangle \\ |\hat{\alpha}_2 KJ\rangle &= |\alpha_1 KJ\rangle \; + \; \langle \alpha_2 K|\varepsilon_0|\alpha_1 K\rangle \, J(J+1) \, |\alpha_2 KJ\rangle \end{aligned} \tag{C.3}$$

in the limit of small mixing.

The interband $E2$ matrix elements between members of mixed band 2 and mem-

bers of mixed band 1 are

$$\langle \alpha_2 K J_2 || \mathfrak{M}(E2) || \alpha_1 K J_1 \rangle$$
$$= (2J_1+1)^{1/2} \langle J_1 K 20 | J_2 K \rangle \left[M_1 + M_2 \left[J_2(J_2+1) - J_1(J_1+1) \right] \right], \quad \text{(C.4)}$$

where

$$\begin{aligned} M_1 &\equiv \langle \alpha_2 K | \mathfrak{M}'(E2;0) | \alpha_1 K \rangle \\ M_2 &\equiv \langle \alpha K | \mathfrak{M}'(E2;0) | \alpha K \rangle \langle \alpha_2 K | \varepsilon_0 | \alpha_1 K \rangle, \end{aligned} \quad \text{(C.5)}$$

provided both of the original bands have the same intraband matrix element $\langle \alpha K | \mathfrak{M}'(E2;0) | \alpha K \rangle$. Experimental papers often report the ratio

$$a_0 \equiv \frac{M_2}{M_1}. \quad \text{(C.6)}$$

In practice, (C.4) is rewritten as

$$\frac{\langle \alpha_2 K J_2 || \mathfrak{M}(E2) || \alpha_1 K J_1 \rangle}{(2J_1+1)^{1/2} \langle J_1 K 20 | J_2 K \rangle} = M_1 \ + \ M_2 \ \left[J_2(J_2+1) - J_1(J_1+1) \right], \quad \text{(C.7)}$$

casting M_1 and M_2 as the slope and intercept parameters for a linear relation between a spin-corrected matrix element (LHS) and a quadratic expression in terms of spins (on the RHS). These quantities are used as variables for plotting the entire set of data on interband transitions for a band ("Mikhailov plot"), and M_1 and M_2 are obtained by a linear fit (see Ref. [4] for examples). If *relative* transition strengths are known experimentally (*e.g.*, from a branching ratio measurement) but absolute strengths are not, only the ratio $a_0 = M_2/M_1$ can be obtained. Even if absolute strengths are known, but with less precision than the relative strengths, it can still be beneficial to perform such an analysis to extract M_2/M_1 with higher accuracy.

The value of the unmixed intraband matrix element $\langle \alpha K | \mathfrak{M}'(E2;0) | \alpha K \rangle$ is only needed for the analysis if the mixing strength $\langle \alpha_2 K | \varepsilon_0 | \alpha_1 K \rangle$ is to be extracted explicitly. This matrix element is usually expressed in terms of the "intrinsic quadrupole moment" Q_0, where

$$eQ_0 \equiv \left(\frac{5}{16\pi} \right)^{1/2} \langle \alpha K | \mathfrak{M}'(E2;0) | \alpha K \rangle. \quad \text{(C.8)}$$

For the ground state band ($K^\pi = 0^+$), the magnitude of the intrinsic quadrupole moment is deduced most simply from the experimental $2_g^+ \rightarrow 0_g^+$ transition strength. Since $\langle \alpha 02 || \mathfrak{M}(E2) || \alpha 00 \rangle = \langle \alpha 0 | \mathfrak{M}'(E2;0) | \alpha 0 \rangle$ by (A.11) and $B(E2; \alpha 02^+ \rightarrow \alpha 00^+) = (1/5) \langle \alpha 02 || \mathfrak{M}(E2) || \alpha 00 \rangle^2$ by (B.2),

$$B(E2; \alpha 02^+ \rightarrow \alpha 00^+) = \frac{1}{16\pi} |eQ_0|^2. \quad \text{(C.9)}$$

In Section 11.4, an experimental value for a_0 is deduced from the $B(E2; 2^+_{K=0_2} \to 4^+_g)/B(E2; 2^+_{K=0_2} \to 0^+_g)$ branching ratio. Specializing (C.4) to the cases $\langle 2^+_{K=0_2}||\mathfrak{M}(E2)||4^+_g\rangle$ and $\langle 2^+_{K=0_2}||\mathfrak{M}(E2)||4^+_g\rangle$, and solving the resulting system of two equations for a_0, yields the value and uncertainty

$$a_0 = \frac{1-x}{14+6x} \qquad \sigma_{a_0} = \frac{20}{(14+6x)^2}\sigma_x \tag{C.10}$$

in terms of the matrix element ratio $x \equiv (7/18)^{1/2}\langle 2^+_{K=0_2}||\mathfrak{M}(E2)||4^+_g\rangle/\langle 2^+_{K=0_2}||\mathfrak{M}(E2)||0^+_g\rangle$ and its uncertainty σ_x.

Appendix D

Calculation of angular correlation and polarization functions

The purpose of this appendix is to condense the results directly needed for the interpretation of γ-γ angular correlation and polarimetry measurements following β decay, as well as to summarize the necessary steps to be taken for the derivation of related results.

An extensive formalism [78] exists for the prediction of the angular correlations between sucessive radiations emitted in nuclear decay. Quite general results can be deduced for correlations between different types of emitted particle (α, β, γ, e^-), in various cascades, with specific properties (*e.g.*, propagation direction, spin polarization) detected for each particle. The main constraint to this formalism is that initial, final, and intervening states all be states of good spin and parity and that the initial and final states be unoriented, so this formalism applies to essentially all decay experiments but not to in-beam experiments. The angular correlation functions $W(\theta)$ or direction-polarization correlation functions $W(\theta, \gamma)$ (Section 4.2) for the various special cases are very similar in form.

The results may be summarized most compactly if the correlation function for the "simplest" case, that of two consecutive γ-ray transitions of pure multipolarity with only their propagation directions measured, is stated explicitly. Then all the correlation functions for more complicated cases are obtained from this simple function by straightforward "prescriptions". For the $J_1 \xrightarrow{L_1} J \xrightarrow{L_2} J_2$ cascade,

$$W(\theta) = \sum_{\nu} F_\nu(L_1 L_1 J_1 J) F_\nu(L_2 L_2 J_2 J) P_\nu(\cos\theta), \tag{D.1}$$

where the sum is over ν=0,2,... The F_ν coefficients are given by simple expressions in terms of Clebsch-Gordan and Racah coefficients; the zeroth order coefficients are $F_0(LL'J_xJ) = \delta_{LL'}$, and the higher orders coefficients are widely available in tabulated form [237, 238]. The highest nonvanishing term is of order $\nu_{\max}$=min$(2L_1, 2J, 2L_2)$. It is apparent from this expression that the angular correlation functions are the same for the cascade $J_1 \xrightarrow{L_1}$

$J \xrightarrow{L_2} J_2$ and the reversed cascade $J_2 \xrightarrow{L_2} J \xrightarrow{L_1} J_1$. It can also be shown [239] that the correlation patterns for all "stretched" cascades $(J_0 + L_1 + L_2) \xrightarrow{L_2} (J_0 + L_1) \xrightarrow{L_1} J_0$ are also identical, independent of the base spin J_0.

Let us now summarize the prescriptions for modifying (D.1) to cover more general cases:

- If one or more of the radiations involved is not a γ ray, corresponding "particle factors" b_ν must be included (see Ref. [78]).

- If unobserved intervening radiations are present in the cascade, this is accomodated by insertion of a factor U_ν for each such radiation (see Refs. [79, 240]).

- If one of the observed transitions i is of mixed multipolarity, the corresponding factor $F_\nu(L_iL_iJ_iJ)$ is replaced by

$$\frac{1}{1+\delta_i^2}\left[F_\nu(L_iL_iJ_iJ) \pm 2\delta_i F_\nu(L_iL_i'J_iJ) + \delta_i^2 F_\nu(L_i'L_i'J_iJ)\right], \tag{D.2}$$

  where δ_i is the admixture of multipolarity L_i', as defined in Appendix B. Since δ_i is a ratio of multipole operator matrix elements, the sign to be used on the interference term in (D.2) depends upon the sign conventions involved in the definition of these operators. The convention of Krane and Steffen [241] dictates that, for mixing of two consecutive multipoles, the $(-)$ sign be chosen when the mixed radiation is the first radiation in the cascade and that the $(+)$ sign be chosen when the mixed radiation is the final radiation. A variety of alternate conventions are also in use, and these are not necessarily even self-consistent between when the same radiation is considered as the first or second radiation in a cascade (*e.g.*, Ref. [78]); care must therefore be taken to explicitly specify the sign convention adopted when quoting a value of δ_i extracted from angular correlation data.

- If the polarization of one of the γ-ray transitions, i, possibly a mixed-multipolarity transition, is observed, then, in each term involving the multipolarities L_iL_i', $F_\nu(L_iL_i'J_iJ)P_\nu(\cos\theta)$ must be replaced with

$$F_\nu(L_iL_i'J_iJ)P_\nu(\cos\theta) + F_\nu(L_iL_i'J_iJ)P_\nu(\cos\theta)\kappa(L_iL_i')(\pm)_{\sigma_i'}P_\nu^{(2)}(\cos\theta)\cos 2\gamma, \tag{D.3}$$

  where $\kappa(L_iL_i')$ is a simple ratio of Clebsch-Gordon coefficients (tabulated in Ref. [79]), $(\pm)_{\sigma_i'}$ is $(+)$ for electric and $(-)$ for magnetic radiation, and the angle γ is the polarization angle relative to the coincidence plane (Section 4.2). $P_\nu^{(2)}$ is the associated

Legendre polynomial of order 2, which is undefined for ν=0. Note that L_i and L'_i are used as dummy variables in (D.3): when mixed radiation is involved, either one may correpond to either L_i or L'_i of (D.2) on a term-by-term basis. (Note also that the sign on the polarization term is indicated as the opposite by authors who define γ as the complementary angle.)

Two especially common cases of the direction-polarization correlation function, needed for Section 4.2 and Section 6.3, are presented here for reference. For a γ-ray cascade $J_1 \xrightarrow[\text{POL}]{L_1,L'_1} J \xrightarrow{L_2} J_2$ ($L'_1 = L_1 + 1$), *i.e.*, where the first radiation is a mixture of consecutive multipoles and the polarization of the first transition is measured,

$$\begin{aligned} W(\theta,\gamma) = \frac{1}{1+\delta_1^2}\Bigg[\sum_\nu \Big(F_\nu(L_1L_1J_1J) - 2\delta_1 F_\nu(L_1L'_1J_1J) \\ + \delta_1^2 F_\nu(L'_1L'_1J_1J)\Big)F_\nu(L_2L_2J_2J)P_\nu(\cos\theta)\Bigg] \\ + \frac{1}{1+\delta_1^2}(\pm)_{\sigma_1}\Bigg[\sum_\nu \Big(\kappa(L_1L_1)F_\nu(L_1L_1J_1J) + 2\delta_1\kappa(L_1L'_1)F_\nu(L_1L'_1J_1J) \\ - \delta_1^2\kappa(L'_1L'_1)F_\nu(L'_1L'_1J_1J)\Big)F_\nu(L_2L_2J_2J)P_\nu^{(2)}(\cos\theta)\Bigg]\cos 2\gamma. \end{aligned} \tag{D.4}$$

For a γ-ray cascade $J_1 \xrightarrow{L_1,L'_1} J \xrightarrow[\text{POL}]{L_2} J_2$ ($L'_1 = L_1 + 1$), *i.e.*, where the first radiation is a mixture of consecutive multipoles and the polarization of the second transition is measured,

$$\begin{aligned} W(\theta,\gamma) = \frac{1}{1+\delta_1^2}\Bigg[\sum_\nu \Big(F_\nu(L_1L_1J_1J) - 2\delta_1 F_\nu(L_1L'_1J_1J) \\ + \delta_1^2 F_\nu(L'_1L'_1J_1J)\Big)F_\nu(L_2L_2J_2J)P_\nu(\cos\theta)\Bigg] \\ + \frac{1}{1+\delta_1^2}(\pm)_{\sigma_2}\Bigg[\sum_\nu \Big(F_\nu(L_1L_1J_1J) - 2\delta_1 F_\nu(L_1L'_1J_1J) \\ + \delta_1^2 F_\nu(L'_1L'_1J_1J)\Big)\kappa(L_2L_2)F_\nu(L_2L_2J_2J)P_\nu^{(2)}(\cos\theta)\Bigg]\cos 2\gamma. \end{aligned} \tag{D.5}$$

Appendix E

Scaling relation for the n-dimensional Schrödinger equation

For the Schrödinger equation in n dimensions, "deepening" and "narrowing" a potential in the correct proportion simply multiplies all eigenvalues by an overall factor and dilates all eigenfunctions. In this appendix, a simple proof of the scaling relation is given. The behavior of the matrix elements of certain operators under this transformation and the adaptations necessary for application to the special case of the GCM Hamiltonian are also discussed. These results serve as the foundation for the approach to using the GCM developed in Chapters 12–13. They are also applied in the treatment of the finite square well potential in Chapter 14.*

Consider the Schrödinger equation in the n Cartesian coordinates $x_1, \ldots, x_n$, with a kinetic energy operator having the standard Cartesian form and a potential energy operator which depends only upon the coordinates,

$$\left[\sum_{i=1}^{n}\left(-\frac{\hbar^2}{2m_i}\frac{\partial^2}{\partial x_i^2}\right) + V(x_1,\ldots,x_n) - E\right]\Psi(x_1,\ldots,x_n) = 0, \tag{E.1}$$

where the m_i are constants, V is the potential energy operator, and E is the energy eigenvalue for wave function Ψ. Suppose that this equation is satisfied by a particular function Ψ, with eigenvalue of E, for a specific potential V. Now consider the related expression obtained by substituting the quantities

$$\begin{aligned} V'(x_1,\ldots,x_n) &= a^2 V(ax_1,\ldots,ax_n) \\ \Psi'(x_1,\ldots,x_n) &= \sqrt{a^n}\Psi(ax_1,\ldots,ax_n) \\ E' &= a^2 E \end{aligned} \tag{E.2}$$

*The results of this appendix were subsequently reported in M. A. Caprio, Phys. Rev. C **68**, 054303 (2003).

for the corresponding quantities on the left hand side of (E.1). This yields

$$\left[\sum_{i=1}^{n}\left(-\frac{\hbar^2}{2m_i}\frac{\partial^2}{\partial x_i^2}\right)+a^2V(ax_1,\ldots,ax_n)-a^2E\right]\sqrt{a^n}\Psi(ax_1,\ldots,ax_n) \tag{E.3}$$

which, with the substitution $u_i = ax_i$, becomes

$$\begin{aligned}
&= \left[\sum_{i=1}^{n}\left(-\frac{\hbar^2}{2m_i}a^2\frac{\partial^2}{\partial u_i^2}\right)+a^2V(u_1,\ldots,u_n)-a^2E\right]\sqrt{a^n}\Psi(u_1,\ldots,u_n)\\
&= a^2\sqrt{a^n}\left[\sum_{i=1}^{n}\left(-\frac{\hbar^2}{2m_i}\frac{\partial^2}{\partial u_i^2}\right)+V(u_1,\ldots,u_n)-E\right]\Psi(u_1,\ldots,u_n)\\
&= 0 \qquad\qquad \text{for all values of } (u_1,\ldots,u_n), \text{ by (E.1).}
\end{aligned}$$

Thus, the dilated wave function Ψ' satisfies the Schrödinger equation with the same kinetic energy operator as in (E.1) but with the modified potential V', and Ψ' has eigenvalue E'. The factor $\sqrt{a^n}$ included in the definition of Ψ' in (E.2) serves to preserve normalization with respect to the volume element $dx_1\cdots dx_n$.

It is often convenient to use n-dimensional spherical coordinates (r,Ω), where $r = (x_1^2+\cdots+x_n^2)^{1/2}$ and Ω represents the angular coordinates. (This corresponds to polar or spherical coordinates in the specific cases n=2 or n=3, respectively.) In these coordinates, the transformation is $V'(r,\Omega) = a^2V(ar,\Omega)$ and $\Psi'(r,\Omega) = \sqrt{a^n}\Psi(ar,\Omega)$, which preserves normalization with respect to the volume element $r^{n-1}drd\Omega$.

The matrix elements of the operator r^q between two eigenfunctions are frequently encountered, *e.g.*, in the determination of transition strengths, so it is useful to derive their properties under dilation. Consider the radial integral

$$I^{AB} = \int_0^\infty r^{n-1}dr\,[\Psi^A(r)]^*\,r^q\,[\Psi^B(r)], \tag{E.4}$$

where the angular variables have been suppressed for simplicity. Then the radial integral for the corresponding transformed eigenfunctions,

$$I^{AB'} = \int_0^\infty r^{n-1}dr\,[\sqrt{a^n}\Psi^A(ar)]^*\,r^q\,[\sqrt{a^n}\Psi^B(ar)], \tag{E.5}$$

is related to the original integral by

$$I^{AB'} = a^{-q}I^{AB}, \tag{E.6}$$

as can be shown by means of a simple change of variable $u = ar$.

The harmonic kinetic energy term (12.2) for the GCM,

$$-\frac{\hbar^2}{\sqrt{5}B_2}\sum_{\mu}\frac{\partial^2}{\partial\alpha_{2\mu}\partial\alpha^*_{2\mu}}, \tag{E.7}$$

is not manifestly Cartesian in form, due to the presence of mixed partial derivatives. However, the preceding proof can readily be adapted to apply in these coordinates. Alternatively, a change of variables [5]

$$\begin{aligned}
x_0 &= \alpha_{20} &&= \mathrm{Re}\,\alpha_{20}\\
x_1 &= \frac{1}{\sqrt{2}}(\alpha_{21}-\alpha_{2-1}) &&= \sqrt{2}\,\mathrm{Re}\,\alpha_{21}\\
x_{-1} &= \frac{1}{i\sqrt{2}}(\alpha_{21}+\alpha_{2-1}) &&= \sqrt{2}\,\mathrm{Im}\,\alpha_{21}\\
x_2 &= \frac{1}{\sqrt{2}}(\alpha_{22}+\alpha_{2-2}) &&= \sqrt{2}\,\mathrm{Re}\,\alpha_{22}\\
x_{-2} &= \frac{1}{i\sqrt{2}}(\alpha_{22}-\alpha_{2-2}) &&= \sqrt{2}\,\mathrm{Im}\,\alpha_{22},
\end{aligned} \tag{E.8}$$

replaces the five complex coordinates $\alpha_{2\mu}$, subject to the five constraints $\alpha^*_{2\mu} = (-)^\mu\alpha_{2-\mu}$, with five real coordinates x_i and explicitly recasts the kinetic energy operator in the Cartesian form

$$-\frac{\hbar^2}{\sqrt{5}B_2}\sum_{i=-2}^{2}\frac{\partial^2}{\partial x_i^2}. \tag{E.9}$$

The "radial" coordinate to which the scaling property applies is β.

Appendix F

Moving tape collector cycle optimization

Optimization of the tape advance cycle for moving tape collector experiments of the type discussed in Chapter 3 is summarized in this appendix. Experiments in which spectroscopy is performed on the daughter or granddaughter of the deposited parent nucleus are considered.

The "life" of a spot of activity deposited on the tape consists of four stages (Fig. F.1):

1. Activity is deposited on the tape in the target box or other deposition location (Chapter 3), usually at a constant rate R, for the time period T_s that the tape is stationary. The activity immediately begins to suffer losses due to decay in the deposition location.

2. The tape is advanced, requiring a time T_m in which the tape is in motion. Activity is lost due to decay *en route*. For the experiments discussed in the present work, T_m is $\lesssim$1 s while T_s is several minutes, so this loss is negligible, but the loss can be significant in experiments involving short half lives.

3. The decay radiations from the activity are observed in the detector area, for a time T_s.

4. The activity is transported to a storage area.

The number of radioactive nuclei present at a given time, $N(t)$, is governed by

$$\frac{d}{dt}N(t) = Q(t) - \lambda N(t), \tag{F.1}$$

where $Q(t)$ is the rate at which new nuclei are being added and λ is the decay probability per unit time, related to the mean and half lives by $\lambda{=}1/\tau{=}\ln 2/T_{1/2}$. This is an inhomogeneous first-order differential equation, and can thus be solved in closed form (*e.g.*,

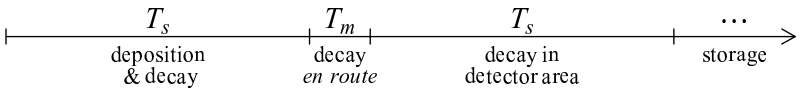

Figure F.1: Time line for a moving tape collector activity spot.

Ref. [242]), yielding

$$N(t) = \underbrace{N(0)}_{\substack{\text{original}\\ \text{activity}}} \quad \underbrace{e^{-\lambda t}}_{\substack{\text{decay of}\\ \text{original}\\ \text{activity}}} + \int_0^t \underbrace{dt'\,Q(t')}_{\substack{\text{activity}\\ \text{deposited}\\ \text{at time } t'}} \quad \underbrace{e^{-\lambda(t-t')}}_{\substack{\text{decay of}\\ \text{activity}\\ \text{deposited}\\ \text{at time } t'}} . \tag{F.2}$$

For the nuclide deposited on the tape, denoted here as the first member of the decay chain by a subscript 1, the rate $Q_1(t)$ at which activity is added is R for $0 \le t < T_s$ and zero after. Consequently,

$$N_1(t) = \begin{cases} R\frac{1}{\lambda_1}(1 - e^{-\lambda_1 t}) & 0 \le t < T_s \\ R\frac{1}{\lambda_1}(1 - e^{-\lambda_1 T_s})e^{-\lambda_1 (t-T_s)} & t > T_s. \end{cases} \tag{F.3}$$

The number of decays occurring in the detector area during the observation time is

$$\begin{aligned} D_1 &= \int_{T_s+T_m}^{T_s+T_m+T_s} dt\,\lambda_1 N_1(t) \\ &= R\frac{1}{\lambda_1}\left[1 - e^{-\lambda_1 T_s}\right]^2 e^{-\lambda_1 T_m}. \end{aligned} \tag{F.4}$$

As longer tape cycle times are chosen, more decays will occur in each individual cycle, but fewer cycles will fit into an experiment of fixed length. We are interested in maximizing the number of decays in the detector area during the *experiment*, not during one particular tape cycle. The maximum yield per experiment time is obtained by maximizing $D_1/(T_s + T_m)$. This quantity is plotted in Fig. F.2 as a function of T_s, for the case in which T_m is negligible. The maximum occurs for a tape cycle duration of $T_s \approx 1.81 T_{1/2}$, for which about 41% of deposited nuclei decay in the detector area.

For the daughter nuclide, denoted here by a subscript 2, the activity as a function of time is again dictated by (F.1). In this case the source of new nuclei is the decay of

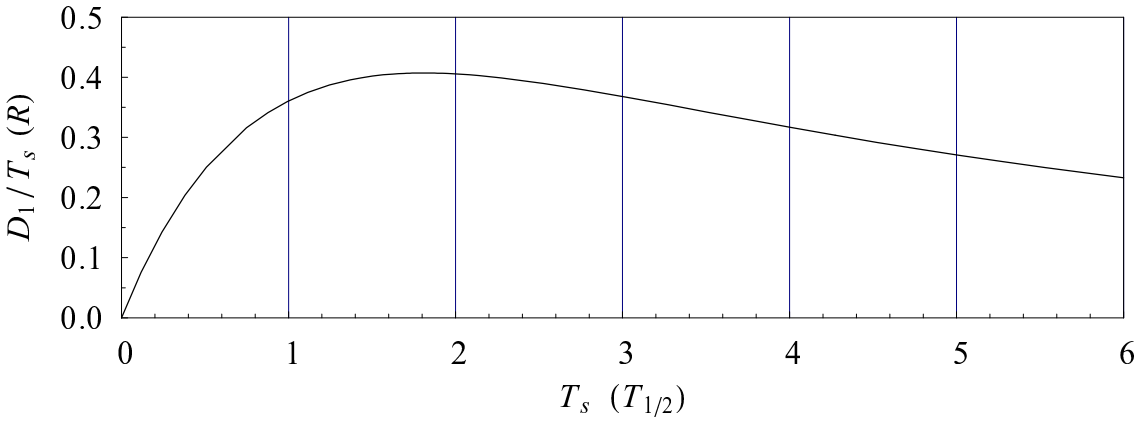

Figure F.2: Number of decays in the detector area per experiment time, D_1/T_s, as a fraction of the initial deposition rate R, plotted as a function of the tape cycle T_s, for T_m=0. This graph applies to decay of the original deposited parent (nucleus 1), populating its daughter (nucleus 2).

nuclide 1, so $Q_2(t)=\lambda_1 N_1(t)$, with $N_1(t)$ given by (F.3). The resulting function $N_2(t)$ is

$$N_2(t) = \begin{cases} R\left[\frac{1}{\lambda_2} - \frac{1}{\lambda_2-\lambda_1}e^{-\lambda_1 t} + \frac{\lambda_1}{\lambda_2(\lambda_2-\lambda_1)}e^{-\lambda_2 t}\right] & 0 \le t < T_s \\ R\left[\left(\frac{1}{\lambda_2} - \frac{1}{\lambda_2-\lambda_1}e^{-\lambda_1 T_s} + \frac{\lambda_1}{\lambda_2(\lambda_2-\lambda_1)}e^{-\lambda_2 T_s}\right)e^{-\lambda_2(t-T_s)}\right. & \\ \left. \quad + \frac{1}{\lambda_2-\lambda_1}\left(e^{\lambda_1 T_s}-1\right)\left[e^{-\lambda_1 t} - e^{-\lambda_2 t}e^{(\lambda_2-\lambda_1)T_s}\right]\right] & t > T_s. \end{cases} \tag{F.5}$$

The number of decays of the daughter in the detector area during one tape cycle is

$$D_2 = R\frac{1}{\lambda_1-\lambda_2}\left[-\frac{\lambda_1}{\lambda_2}\left(1-e^{-\lambda_2 T_s}\right)^2 e^{-\lambda_2 T_m} + \frac{\lambda_2}{\lambda_1}\left(1-e^{-\lambda_1 T_s}\right)^2 e^{-\lambda_2 T_m}\right]. \tag{F.6}$$

In order to optimize the observation of daughter decays populating the granddaughter, for spectroscopy experiments making use of two-step β decay, the quantity $D_2/(T_s+T_m)$ must be maximized.

Appendix G

Data acquisition and the `cscan` sorting package

Within the timespan covered by the work described here, the facilities available for nuclear structure experiments at WNSL expanded considerably, in both the detection resources available and variety of experiment types possible. The demands upon the acquisition electronics and flexibility required of the data analysis software have increased correspondingly. At the time of YRAST Ball's early runs [61], the detection array consisted of a relatively homogeneous set of Ge elements for γ-ray coincidence spectroscopy, and analysis required only the construction of basic 1-, 2-, and 3-dimensional γ-ray energy histograms. Recent combined FEST and spectroscopy experiments at the Yale MTC entail the simultaneous analysis of clover, LEPS, BaF_2, plastic scintillator, and fast-timing TAC signals, with wall-time clock time stamps for γ-ray multiscaling. Similarly, a typical current experiment using the SASSYER recoil separator [243] involves approximately 40 channels of clover and LEPS data from a target-position array, several additional Ge channels from an isomer array, and implantation and α-decay tagging signals from highly-pixelated particle detectors at the focal plane. The addition of time-of-flight detectors is planned. A correspondingly diverse range of diagnostic and analysis histograms must be constructed by the sorting software.

This appendix summarizes the acquisition and sorting software suite [244, 245] developed, as part of the present work, for WNSL nuclear structure experiments. This suite consists of three main elements: the `cscan` sorting package, an acquisition readout code with event builder, and specialized data sorting routines. Portions of this software have also been used in β-decay experiments at the TRIUMF ISAC and ORNL HRIBF radioactive beam facilities.

The `cscan` sorting package is a generic framework for online and offline sorting. This portion of the software suite is not specialized to the specifics of the present WNSL

acquisition environment but rather is a control program, which calls external routines for the site-specific tasks. This same program, used with different site-specific routines, provided the online and offline sorting capability for TRIUMF E801 (Chapter 11) and offline sorting for HRIBF RIB-095 [246]. The spirit of this package is similar to that of earlier packages (*e.g.*, Ref. [247]), used for tape-based sorting in nuclear spectroscopy, in which the control and site-specific functions are separated. The main differences lie in the provisions for communication with the acquisition code in an online environment and for the flexible input and output of file-based data formats. For online use, the `cscan` control code calls a site-specific routine at startup to establish a data connection to the acquisition code. This connection can be, *e.g.*, via a first-in-first-out (FIFO) pipe on the local host (as at WNSL) or via a remote procedure call (RPC) server to receive data from an acquisition computer located elsewhere on the network (as at TRIUMF). For offline use, the `cscan` control program calls site-specific routines to handle all data file input tasks, and thus does not impose any specific limitations on the data format, such as the requirements of fixed-size block structure or event separator codes typical of tape-based systems. The site-specific input routines are free to support variable-length events, whether or not they are stored in fixed-sized blocks, and can also provide on-the-fly decompression of data files during the sorting process. The `cscan` package outputs histograms in the RadWare [248, 249] spectrum, matrix, and cube formats.

The expanded acquisition hardware needs for WNSL spectroscopy experiments were addressed by the installation of a current-generation acquisition system, based on 32-channel VME analog to digital converter (ADC), time to digital converter (TDC), and scaler modules with internal multievent storage buffers [250], read out via a fiber-optic link [251] by an Intel/Linux workstation. The task of the acquisition code, which runs on the Linux workstation, is to read data from the VME acquisition modules [250], construct events from this data, and save these events to disk and/or transmit them to the `cscan` online sorting code. The VME modules each store data from several successive events in an internal multievent buffer. The acquisition code then periodically reads out all data from all modules, and an event builder routine cross-correlates data items from the different modules to reassemble the contents of individual events. Although the modules tag each data item with an internally-generated event serial number, the event builder must carry out validation to robustly handle the drifts between counters which occur at the level of $\sim$1 per 10^3–10^4 events. The ADC, TDC, and scaler data are stripped of hardware-specific

encoding information, and the events are written in a header-plus-data format, along with run marker and diagnostic error message pseudo-events sharing the same header format. These events may be sorted by `cscan`, in conjunction with WNSL site-specific routines, or by the custom sorting codes of outside research groups [252].

The sorting routine used with `cscan` for analyzing data from WNSL spectroscopy experiments is based upon an approach which greatly simplifies the processing of data from an inhomogeneous assortment of detectors. Commonly, sorting routines intended for use with only a few types of detectors contain separate segments of code to perform the basic processing for each detector type and use separate sets of variables to store the data from each detector type. As more detector types are defined, this approach leads to a cumbersome and highly redundant code structure. Maintenance or improvement of the code is impractical and error prone, since even minor changes must be manually duplicated for each detector type, and the implementation of new sorting tasks which encompass whole classes of detector types, *e.g.*, all Ge detectors, requires separate code to be written for each detector type in the class.

The `cscan` WNSL sorting routine instead uses one compact segment of code to process all detector types. The code can accommodate an arbitrary number of detectors of an arbitrary number of types with no modification. At the beginning of a sorting run, a list of detector definitions is read from an input file provided by the user, specifying the type, ADC channel (if applicable), TDC channel (if applicable), and such auxiliary information as array angle or pixel grid position for each detector. Separately, a list of corrections, such as gain matching or Doppler correction, to be applied to all detectors of a given type is constructed from information provided by the user. Then, the code processes the list of ADC data and TDC data for each event in three steps, as summarized in Fig. G.1. The ADC and TDC data are scanned to identify "hits" in any of the detectors in the detector definition list. If a hit occurs, the corrections list is consulted, and the corrections appropriate to this particular detector type are applied to the ADC and TDC data. A record of the hit, containing the energy and timing information together with the detector ID and all auxiliary information included in the detector definition, is added to a common list of hits shared by all detector types. After all hits of single-element detectors are identified from the ADC and TDC data, a second pass is made through these hits to construct hits in composite detectors built from these individual array elements (*e.g.*, clover detectors built from clover leaves), and the resulting hit records are appended to the

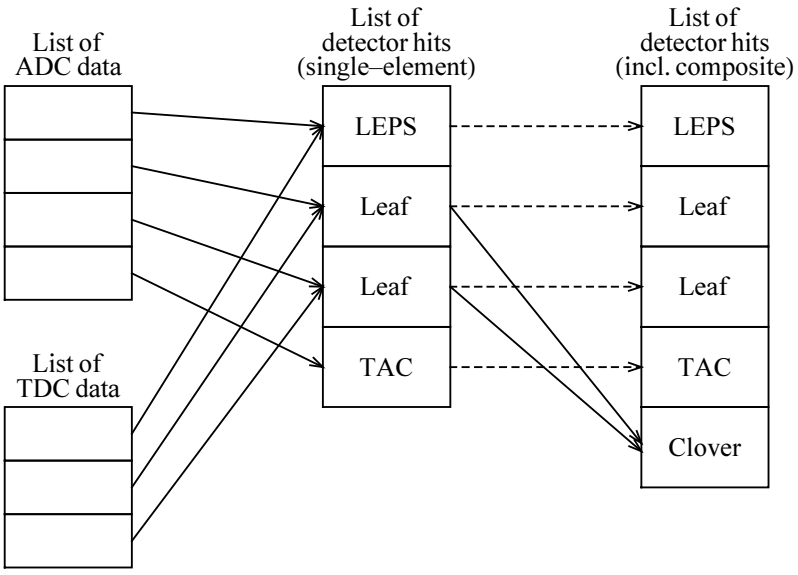

Figure G.1: Event processing scheme for the `cscan` WNSL site-specific sorting routine, in which "hits" for all detector types are processed using the same code and stored in one common list. ADC and TDC data are first scanned to construct hits of single-element detectors, and these are in turn used to construct hits of composite detectors.

common list of detector hits. All sorting tasks are then carried out using the common list of hits, typically looping over the hits and selecting data from those for which the detector type and data values match certain criteria.

Appendix H

Gamma-ray coincidence intensity spectroscopy

H.1 Coincidence techniques

The advent of compact, high-efficiency arrays of large-volume Ge detectors makes possible a new generation of γ-ray spectroscopy β-decay experiments, in which high-statistics γ-ray coincidence data are available. In order to obtain γ-ray intensity measurements comparatively free of the contamination endemic to singles data, the present work relies upon coincidence data for the determination of intensities (Section 4.1). In this appendix, a "formalism" for the extraction of intensities from coincidence data is presented, and basic examples of its application are given. The properties and calibration of the coincidence efficiency for a multi-detector array are also discussed.

The methods used in the present work to accurately extract the intensities of specific, often weak, transitions differ greatly from the global least-squares intensity fitting techniques commonly applied in high-spin studies with large multi-detector arrays [248]. The methods for extracting intensities from coincidence data are somewhat more involved than those for the simple conversion of a singles spectrum peak area to an intensity. However, the application of a few basic principles makes reliable analysis of intensities from coincidence data a straightforward process.

As discussed in Section 4.1, in a spectroscopy experiment, a set of *decays* in an ensemble of nuclei results in a set of *events* observed in the detector array, in a way which depends upon the instrument response. Let us establish the relevant quantities describing the ensemble of decays and set of events. Let N be the total number of decays in the ensemble. For a γ-ray transition x, we are interested in the fraction I_x of decays which involve the emission of radiation x, that is, the "intensity" of x. For two γ-ray transitions, x and y, we can consider the fraction $I_{x:y}$ of decays which involve emission of both transitions x and y in coincidence, and so on for higher numbers of coincident radiations. In the

observed data, there are analogous quantities: the number S_x of observed singles counts of x and the number $G_{x:y}$ of detected coincidences between x and y, usually extracted by observing the peak area for y in a spectrum gated on x.

The observed quantities are related to the physical quantities by the array efficiencies, technical aspects of which are discussed in the following section. In general, the efficiency for detecting a specific radiation or coincident set of radiations depends upon many parameters (relative directions of emission, isomeric delays between emission, other correlated radiations which may block their detection, *etc.*), but, under most routine circumstances, the efficiencies depend, to a good approximation, upon just the energies of the radiations involved. Thus,

$$S_x = N I_x \varepsilon(E_x) \tag{H.1}$$

and

$$G_{x:y} = N I_{x:y} \varepsilon(E_x, E_y). \tag{H.2}$$

Note that $I_{x:y} = I_{y:x}$ by definition. If symmetric gating is performed, *i.e.*, the set of detectors used for gating is the same as that included in the gated spectra, then also $G_{x:y} = G_{y:x}$ and $\varepsilon(E_x, E_y) = \varepsilon(E_y, E_x)$. Coincidences between distinct detector sets, *e.g.*, LEPS detectors and clover detectors, may also be considered, in which case such symmetry is not present in G and ε.

Two simple situations in which intensities may be extracted from coincidence data were introduced in Section 4.1. If a transition x directly feeds a level which decays by a transition b [Fig. H.1(a)], then the probability of emission of x followed by emission of b is $I_{x:b}$=$I_x B_b$, where B_b is the branching probability for the level to decay by b. Thus, (4.1) follows as a special case of (H.2). As noted in Section 4.1, B_b is in practice calculated from $B_b = I_b/(\sum_i I_i + \sum_i I_i^{\mathrm{ce}})$, where the sums are over all γ-ray and conversion electron transitions i depopulating the level. Similarly, when a transition a directly feeds a level which decays by two transitions x and y [Fig. H.1(b)], we have

$$\frac{I_{a:x}}{I_{a:y}} = \frac{I_a B_x}{I_a B_y} = \frac{I_x}{I_y}, \tag{H.3}$$

so (4.2) also follows as a special case of (H.2).

However, much more complicated situations may be reliably addressed by the methodical use of the present formalism. Let us conclude this section with three representative examples.

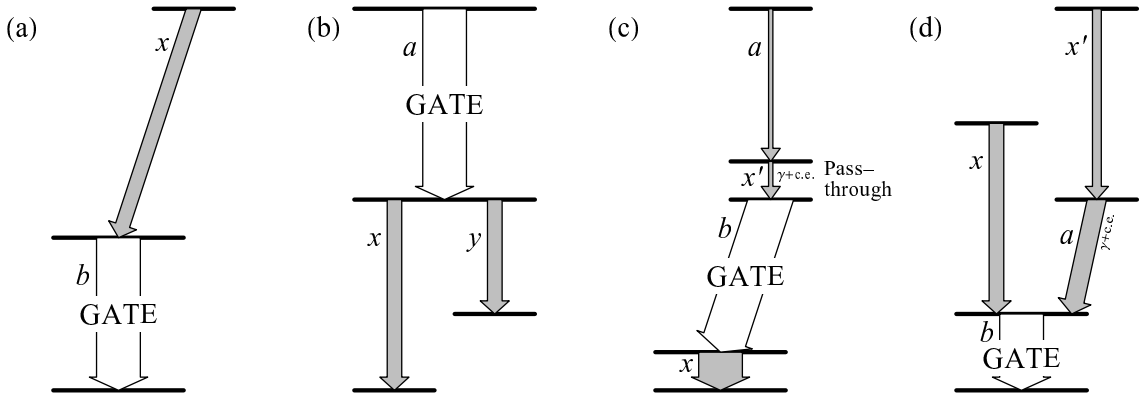

Figure H.1: Examples of the use of the formalism for extraction of intensities from coincidence data: (a) a simple gate below, (b) a simple gate above, (c) a pass-through measurement to find the intensity of an otherwise "hidden" transition x', and (d) a gate below in which the contribution of the contaminant x' must be subtracted to obtain the intensity of x. The observed transitions (gray) are drawn with widths indicating their intensity *coincident* with the gating transition (white).

Consider the decay scheme of Fig. H.1(c), in which the transition of interest, x', is degenerate in energy with a low-lying and much more strongly populated transition x. Such doublet pairs are inevitable in "good" rotor nuclei with the same moment of inertia for different bands. The transition x' is completely obscured by x in spectra gated on a or b, and so its intensity cannot be measured directly. However, the transitions a and b can only be coincident with each other if "pass-though" via the transition x', or its associated conversion electrons, occurs. Quantitatively, $I_{a:b} = I_a(B_{x'} + B^{\rm ce}_{x'})B_b$, so, if the intensities of I_a and B_b are known, $B_{x'} + B^{\rm ce}_{x'}$ can be deduced from $G_{a:b}$.

The decay scheme of Fig. H.1(d) illustrates a situation in which the intensity of a transition x cannot be deduced trivially from its coincidences with a gating transition b below, because of contamination from a coincident doublet transition x'. The measured combined area is $G_{b:x}+G_{b:x'}=N(I_{b:x}+I_{b:x'})\varepsilon(E_b, E_x)$. However, since $I_{b:x'} = I_{x'}(B_a+B^{\rm ce}_a)B_b$, if $I_{x'}$ can be determined independently, and the combined γ and conversion electron branching strength of a is known, then the contribution of x' to the gate can be subtracted. Thus, I_x can be recovered. Such a situation occurs for the 950.5 keV $4^+_{1088} \rightarrow 2^+_{138}$ transition in ^{156}Dy (see Fig. 7.4 on page 70), which is unresolved, in the spectrum gated on the 138 keV $2^+_{138} \rightarrow 0^+_0$ transition, from the higher-lying 949.6 keV $(?)_{1840} \rightarrow 2^+_{890}$ transition.

As a final example, and cautionary note, consider the case in which the transitions b and x of Fig. H.1(a) are degenerate to within the detector resolution. Such is the case for

the 79.6 keV and 81.0 keV transitions in ^{133}Ba source decay, or for the 1030.7 keV $4^+_{1088} \rightarrow 2^+_{138}$ and 1031.8 keV $(?)_{2200} \rightarrow 4^+_{1088}$ transitions in ^{156}Dy (Table I.1). A naive application of (4.1) yields an intensity I_x which is a factor of two too high. Any gate on b is also a gate on x, so the observed counts are actually $G_{b:x} + G_{x:b}{=}I_{b:x}\varepsilon(E_b, E_x) + I_{x:b}\varepsilon(E_x, E_b)$, but this is just $2I_{b:x}\varepsilon(E_b, E_b)$. Since both lines contribute an exactly equal number of counts to the gated peak, the peak centroid energy is the arithmetic mean of the individual energies ($E_{\rm cent}{=}(E_x + E_b)/2$). Thus, if E_b is measured independently, E_x can be recovered from the observed peak centroid.

H.2 Array coincidence efficiency

The probability for two γ-rays emitted simultaneously to both be detected in a detector array, and registered as coincident, is *approximately* just the probability that each will be detected individually in distinct array elements. Thus, the coincidence efficiency of an array of detectors is approximately the sum of the pairwise products of efficiencies of the individual array elements:

$$\varepsilon(E_x, E_y) = \sum_{i,j\,(i\neq j)} \varepsilon_i(E_x)\varepsilon_j(E_y), \tag{H.4}$$

where the sum is over individual detectors i and j, $i{\neq}j$. For an array of n identical detectors of efficiency $\varepsilon_0(E)$, this reduces to $\varepsilon(E_x, E_y) = n(n-1)\varepsilon_0(E_x)\varepsilon_0(E_y)$. For asymmetric gating, in which a gate condition is placed on detectors in class A, and the resulting counts in detectors in class B are measured, the sum runs over $i{\in}A$ and $j{\in}B$.

However, deviations from this ideal product efficiency occur. At low γ-ray energies, electronic timing jitter and walk can cause the signals from two coincident γ rays to fall outside the acquisition system's timing acceptance. In this case, the expression (H.4) serves as a useful baseline for the calculation of $\varepsilon(E_x, E_y)$, valid at high γ-ray energies, but the attenuation of efficiency due to such time "windowing" effects at low energies must be calibrated against known coincidences, yielding a correction factor $w(E_x, E_y){\equiv}\varepsilon(E_x, E_y)/\sum\varepsilon_i(E_x)\varepsilon_j(E_y)$. Time windowing attenuation introduces not only a loss of statistics but also analysis uncertainties resulting from the correction factor $w(E_x, E_y)$, and thus it is undesirable in the γ-ray energy range of interest. The attenuation can be avoided if it is possible to set constant fraction discriminator thresholds sufficiently below the energies of interest to prevent leading-edge walk effects [253] from

occuring and if generous timing acceptances are allowed in the hardware trigger, time to digital converters, and offline analysis cuts.

Deviations from the product form (H.4) also occur if additional correlations are present between the emitted γ rays. Angular correlation effects depend upon the array geometry and are usually most important for 0^+–2^+–0^+ cascades (see Section 7.2). Additional γ-rays emitted in the same decay suppress detection of coincidences of the γ-rays of interest, since they may directly interact with the same detector as one of the γ-rays of interest (conventional "summing") or scatter into the Compton suppression shield of that detector. This effect is most important for high-multiplicity decays and for arrays in which individual detector elements have efficiencies of $\gtrsim$1%.

For (H.4) to be applied, the single-detector efficiency functions $\varepsilon_i(E)$ must first be determined. A parametrized form which reproduces the efficiency characteristics of both the LEPS and clover detectors used at the Yale MTC (Fig. H.2) is

$$\varepsilon(E) = AE^{p_1}\left[1 - u_{a,d}(E)\right] + BE^{-p_2}u_{a,d}(E), \tag{H.5}$$

where

$$u_{a,d}(E) \equiv 1 - \frac{1 + e^{-a/d}}{1 + e^{(E-a)/d}}. \tag{H.6}$$

This function has of a power law dependence at low energies and a power law dependence at high energies, joined smoothly by a "softened" step function $u_{a,d}(E)$ constructed from the Woods-Saxon potential function.

No single γ-ray calibration standard (*e.g.*, Ref. [95]) covers the full energy range of interest ($\sim$100 keV–2500 keV) in the experiments in the present work, so multiple sources (^{60}Co, ^{133}Ba, ^{152}Eu, ^{226}Ra), covering different portions of the energy range, are used to calibrate $\varepsilon_i(E)$ in a piecewise fashion. The absolute activities of calibration sources are usually only known to within $\sim$5–10%, with possible further uncertainties arising from the acquisition dead time determination in calibrations using strong sources, so these calibrations generally do not match in normalization at the points of overlap and provide only a moderately accurate overall efficiency normalization. To address these considerations, a special approach has been used in the present work. The singles data from the sources are used only to determine the *shape* of the efficiency curve. The relative strengths of the sources are matched by allowing the normalizations of the calibration points from different data sets to vary as a power law function is locally fit through them in their region of overlap. The renormalized calibration points then yield a *relative* efficiency function $f_i(E)$,

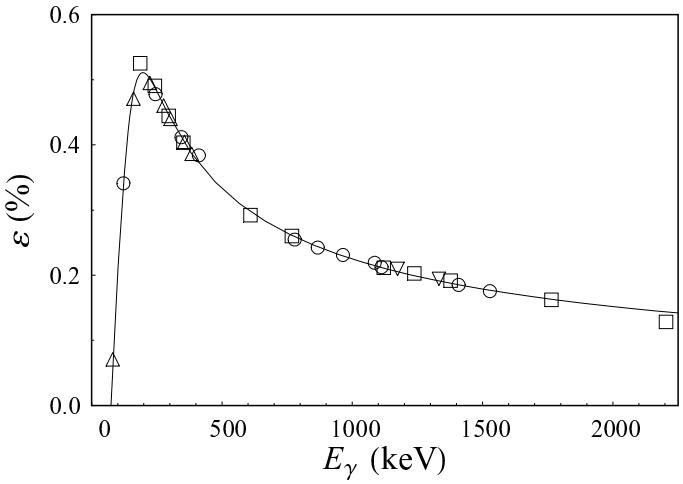

Figure H.2: Efficiency curve for a clover detector at the Yale MTC, at a face distance of 13 cm from the source position, without add-back, fitted using the parametrization (H.5). Calibration points from ^{60}Co (▽), ^{133}Ba (△), ^{152}Eu (○), and ^{226}Ra (□) are matched in normalization as described in the text, and the overall normalization is deduced by the coincidence method.

related to the true efficiency by $\varepsilon_i(E) = K f_i(E)$, where the factor K is common to all detectors in the array if the same source strength renormalization factors are consistently used for all.

The normalization factor K is then determined by a natural extension of the standard "coincidence method" (*e.g.*, Ref. [95]) for calibrating two-detector systems. The coincidence efficiency (H.4) contains products involving two factors of K, while singles efficiency, $\varepsilon(E)=\sum_i K f_i(E)$, contains only one. Thus, K can be determined by considering the ratio of any gated coincident area and any singles area, eliminating any need for reference to the poorly-known integrated source activity N:

$$\frac{G_{x:y}}{S_z} = \frac{I_{x:y}}{I_z} \frac{K \sum_{i,j\,(i\neq j)} f_i(E_x) f_j(E_y)}{\sum_i f_i(E_z)}. \tag{H.7}$$

Known coincidences in several common calibration sources, deduced from γ-ray intensity and γ-ray and conversion electron branching information in Refs. [22, 254–256], are summarized in Table H.1. If intense transitions from strong sources are used, the calibration gate will contain a substantial time randoms contribution, which must be subtracted either by the standard relations for time randoms [95] or through graphical subtraction of a singles spectrum from the gated spectrum, weighted so that false coincidences exactly disappear.

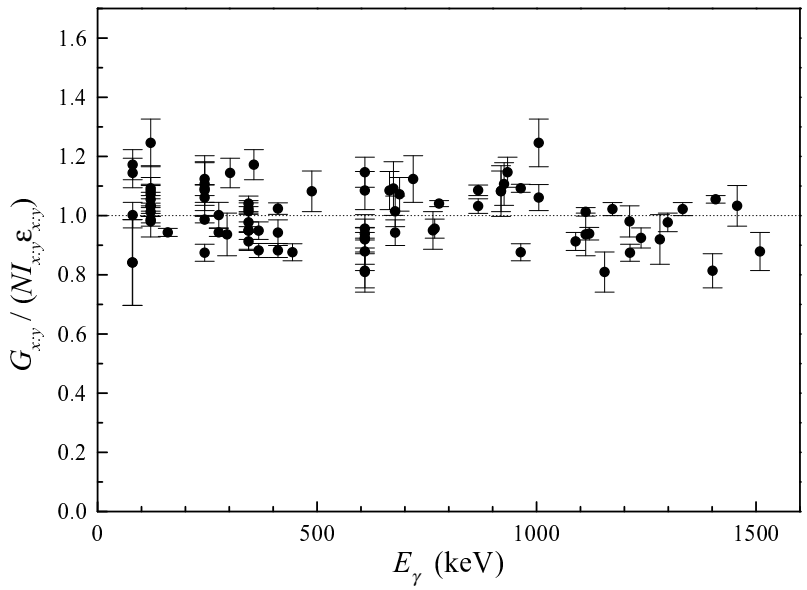

Figure H.3: Ratio of the observed coincident counts to the number expected from the known decay scheme and the assumed product form (H.4) for the array coincidence efficiency. Data are shown for 43 pairs of coincident γ-ray transitions in ^{60}Co, ^{133}Ba, ^{152}Eu, and ^{226}Ra source decay (Table H.1), detected in the array of three clover detectors used for the experiment of Section 11.3. The ratio for each coincidence is plotted both for the lower γ-ray energy and higher γ-ray energy.

Actual calibrations data, showing the ratio of the measured $G_{x:y}$ to that expected from the known $I_{x:y}$ and assumed array efficiency (H.4), are plotted in Fig. H.3. The values are for 43 calibrator coincidences in ^{60}Co, ^{133}Ba, ^{152}Eu, and ^{226}Ra source decay (Table H.1), detected in an array of three clover detectors at the Yale MTC. Such a calibration serves as a test for energy-dependent attenuation effects. These are not significantly present for the setup of Fig. H.3, *i.e.*, $w \approx 1$ throughout the energy range calibrated. The narrow spread of values indicates the reliability of intensities extracted using the form (H.4) for the coincidence efficiency.

Table H.1: Coincident intensities of pairs of transitions in ^{60}Co, ^{133}Ba, ^{152}Eu, and ^{226}Ra source decay deduced from the decay schemes of Refs. [22, 254–256], for use in calibration of coincidence efficiencies. All intensities are per parent decay.

E_x (keV)	I_x (%)	E_y (keV)	I_y (%)	$I_{x:y}$ (%)	E_x (keV)	I_x (%)	E_y (keV)	I_y (%)	$I_{x:y}$ (%)
^{152}Eu source decay[a]					411	2.232(4)	368	0.860(5)	0.840
							679	0.471(4)	0.460
122	28.58(9)	245	7.58(3)	3.49	586	0.459(5)[b]	503	0.148(8)	0.155
		689	0.857(8)	0.395					
		867	4.25(2)	1.96					
		919	0.427(6)	0.196	^{60}Co source decay[c]				
		964	14.60(4)	6.73					
		1005	0.646(5)	0.298	1332	99.9826(6)	1173	99.85(3)	99.8
		1112	13.64(4)	6.29					
		1213	1.422(6)	0.656					
		1408	21.00(6)	9.68	^{133}Ba source decay[d]				
		1458	0.502(5)	0.231					
		1528	0.281(5)	0.130	81.0	34.1(3)[e]	79.6	2.62(6)[f]	0.964[g]
245	7.58(3)	656	0.1448(19)	0.131[h]			276	7.16(2)	2.63[i]
		675	0.172(5)	0.155			303	18.33(6)	6.75
		867	4.25(2)	3.83			356	62.05(19)	22.8
		719.4	0.278(8)[j]	0.251[k]	161	0.645(8)	276	7.16(2)	0.544
		926	0.278(5)	0.251	303	18.33(6)	53	2.20(2)	1.40
		1005	0.646(5)	0.583	384	8.94(3)	53	2.20(2)	0.684
		1213	1.422(6)	1.28					
919	0.427(6)	489	0.419(3)	0.298					
675	0.172(4)	489	0.419(3)	0.121	^{226}Ra source decay[l]				
964.1	14.58(2)[m]	444	2.82(2)[n]	1.64					
		564	0.489(6)[o]	0.284[p]	609	46.1(5)	665	1.46(3)	1.43
1112	13.64(2)	296	0.447(5)	0.340			768	4.94(6)	4.84
		416	0.110(2)	0.083			806	1.22(2)	1.20[q]
867	4.246(19)	296	0.447(5)	0.106			934	3.03(4)	2.97
344	26.5(3)	271	0.073(3)	0.070[q]			1120	15.1(2)	14.8
		368	0.860(5)	0.827			1155	1.63(2)	1.60
		411	2.232(4)	2.15			1238	5.79(8)	5.67
		586	0.459(5)	0.442[b]			1281	1.43(2)	1.30
		679	0.471(4)	0.453			1402	1.27(2)	1.24
		765	0.21(2)	0.202			1408	2.15(5)	2.11[q]
		779	12.93(2)	12.4			1509	2.11(4)	2.07
		1090	1.726(6)	1.66			1583	0.690(15)	0.68
		1299	1.622(8)	1.56					

[a] Radiations are from ^{152}Eu(β^+/ε)^{152}Sm and ^{152}Eu(β^-)^{152}Gd.
[b] Area measurements for S_{586} and $G_{344:586}$ are impeded by the Compton edge of the 778 keV line.
[c] Radiations are from ^{60}Co(β^-)^{60}Ni.
[d] Radiations are from ^{133}Ba(β^+/ε)^{133}Cs.
[e] If 79.6 keV/81.0 keV transitions are not resolved, the measured $S_{81.0}$ must be multiplied by 0.929.
[f] If 79.6 keV/81.0 keV transitions are not resolved, the measured $S_{79.6}$ must be multiplied by 0.0714.
[g] If 79.6 keV/81.0 keV transitions are not resolved, the measured $G_{81.0:79.6}$ must by multiplied by 1/2.
[h] Insufficiently well resolved in a typical gated spectrum to be of use as a calibrator.
[i] If 79.6 keV/81.0 keV transitions are not resolved, the measured $G_{81.0:276}$ must by multiplied by 0.507.

[j]The measured $S_{719.4}$ must be multiplied by 0.825 to eliminate the 719.3 keV contribution.
[k]The measured $G_{245:719.4}$ must be multiplied by 0.96(4) to eliminate the 719.3 keV contribution.
[l]Radiations are from ^{214}Bi(β^-)^{214}Po.
[m]The measured $S_{964.1}$ must be multiplied by 0.991 to eliminate the 963.4 keV contribution.
[n]The measured S_{444} must be multiplied by 0.896 to eliminate the doublet contribution.
[o]The 564.0 keV line is only partially resolved from the 566.4 keV line in singles, rendering intensity measurement difficult.
[p]The measured $G_{964.1:564}$ should not be used for calibration, since there is partially-resolved contamination from the 963.4 keV and 566 keV coincident pair of transitions.
[q]The coincidence is a 0^+–2^+–0^+ cascade, so strong angular correlation effects are present.

Appendix I

Spectroscopic data for ^{156}Dy

The γ-ray intensity data obtained in the experiment of Chapter 7 are summarized in Tables I.1 and I.2.

Table I.1: Observed γ-ray transitions in ^{156}Dy, arranged in order of increasing transition energy. Intensities, normalized to $I_{137} \equiv 100$, and coincidence relations[a] are given.

E_γ (keV)	E_i (keV)	E_f (keV)	I	Coincidences[a]
137.80(10)	137.80	0.00	100(7)	266, 366, 684, 691, 764, 884
259.59(15)[b]	1088.28	828.66	1.46(13)	138, 349, 424, 589, 691, 855, 1156, 1002, 1730
266.38(10)	404.18	137.80	127(6)	138, 366, 684, 764, 931, 1122, 1223
277.96(18)	1168.4	890.50	0.71(7)	138, 753, 890, 1174, 1650
304.6(7)[c,d]	2408.7	2103.3	0.10(3)	1081
313.4(2)	1335.51	1022.10	0.66(5)	138, 618, 884, 1483
317.9(2)	1088.28	770.40	0.27(4)	266, 366
348.96(14)	1437.28	1088.28	1.41(7)	138, 266, 260, 684, 951, 1381
356.5(3)[b]	1525.3	1168.4	0.53(5)[e]	764, 1031
360.7(12)[c,d]	1382.3	1022.10	0.11(4)	884
366.22(12)	770.40	404.18	27.9(16)	138, 266, 565, 667, 755, 1087, 1128, 2053
393.2(6)[b]	1728.7	1335.51	0.09(4)	931
397.9(2)[b]	1168.4	770.40	0.21(5)	266, 366
424.5(2)	828.66	404.18	1.12(6)	138, 260, 266, 796, 1174, 1416
437.6(6)[c,d]	1526.0	1088.28	0.08(6)[e]	684
445.23(17)[b]	1215.6	770.40	0.37(3)	138, 266, 366, 595, 1572
456.2(8)[d]	1624.6	1168.4	0.09(3)	138, 266, 764, 1031
458.9(4)[d]	1627.5	1168.4	0.20(6)	138, 266, 764, 1031
486.4(3)	890.50	404.18	0.50(8)	138, 266, 1416
491.6(3)[d]	1382.3	890.50	0.23(6)	138, 753, 890
537.8(2)	675.6	137.80	0.86(12)	138, 707, 839
553.7(2)[d]	1382.3	828.66	0.28(3)	138, 691
562.6(5)[d]	1898.5	1335.51	0.12(5)	931
565.07(17)	1335.51	770.40	1.15(6)	138, 266, 366, 768, 858, 1483
585.6(2)[d]	1476.10	890.50	0.35(7)	138, 753, 890
588.88(14)[d]	1677.2	1088.28	0.52(4)	138, 260, 266, 684, 691
594.9(6)[b]	1809.8	1215.6	0.047(13)	445
605.5(3)	1627.5	1022.10	0.36(7)	138, 618, 884
617.88(12)	1022.10	404.18	3.6(4)	138, 266, 655, 818, 1081, 1277, 1301, 1386
620.1(8)[d]	2244.7	1624.6	0.10(3)	796
624.4(3)[d]	1515.0	890.50	0.11(5)	753, 890

E_γ (keV)	E_i (keV)	E_f (keV)	I	Coincidences[a]
654.9(4)[d]	1677.2	1022.10	0.33(9)	138, 266, 618, 884
666.88(15)	1437.28	770.40	1.92(10)	138, 266, 366, 1381
671.2(2)[d]	1840.1	1168.4	0.18(4)	138, 266, 764, 1031
684.10(10)	1088.28	404.18	13.3(9)	138, 266, 349, 589, 855, 1002, 1156, 1219, 1235, 1730
688.9(5)[c,d]	1857.82	1168.4	0.15(9)	764, 1031
690.86(13)	828.66	137.80	10.4(5)	138, 260, 349, 554, 796, 1174, 1416, 1479, 1494, 1825
706.74(16)[d]	1382.3	675.6	0.14(2)	138, 538
722.3(7)[d]	2058.6	1335.51	0.13(4)	931
723.5(4)[d]	2199.7	1476.10	0.14(4)	138, 1338
752.67(15)	890.50	137.80	3.3(3)	138, 278, 492, 586, 950, 1417, 1433, 1519
754.9(2)[b]	1525.3	770.40	1.75(11)[e]	138, 266, 366
764.12(13)	1168.4	404.18	9.0(5)	138, 266, 356, 1076, 1139, 1155, 1174, 1650
767.8(4)[d]	2103.3	1335.51	0.16(4)	565, 931
786.1(5)[c,d]	1677.2	890.50	0.10(3)	890
796.03(15)[d]	1624.6	828.66	0.98(6)	138, 424, 620, 691
818.1(2)[d]	1840.1	1022.10	0.26(6)	138, 884
818.7(4)[c,d]	2445.2	1627.5	0.19(5)	1223
820.9(6)[c,d]	2445.2	1624.6	0.08(2)	796
829.4(7)			0.13(4)[f]	1122
839.3(2)[d]	1515.0	675.6	0.20(2)	138, 538
845.3(3)[d]	1933.6	1088.28	0.11(2)	684
848.2(5)[d]	1677.2	828.66	0.12(5)	138, 691
851.0(12)[c,d]	1679.9	828.66	0.07(4)	138, 691
854.6(3)[d]	1942.9	1088.28	0.34(5)	138, 260, 266, 684
858.0(3)[d]	2193.5	1335.51	0.34(5)	138, 266, 931
863.3(10)[d]	2199.7	1335.51	0.10(4)	931
871.6(5)[d]	2207.4	1335.51	0.18(5)	931
884.30(10)	1022.10	137.80	16.4(16)	138, 313, 655, 819, 1081, 1278, 1301, 1386
884.3(8)[d]	2818.4	1933.6	0.11(5)	1529
890.2(4)[d]	2058.6	1168.4	0.27(10)	138, 266, 764, 1031
890.44(12)	890.50	0.00	5.9(9)	277, 492, 586, 950, 1417, 1433, 1519
907.2(4)[d]	1677.2	770.40	0.14(5)	138, 266, 366
908.0(10)[c,d]	2433.8	1526.0	0.19(6)	1122
911.5(6)[d]	1933.6	1022.10	0.15(4)	138, 884
914.6(3)[d]	2003.0	1088.28	0.14(5)	138, 266, 684
919.7(15)[d]	2818.4	1898.5	0.13(5)	366, 1128
921.2(3)	2089.9	1168.4	0.26(6)	138, 266, 764, 1031
931.35(16)	1335.51	404.18	7.2(4)	138, 266, 768, 858, 872, 1111, 1483
935.0(4)[d]	2103.3	1168.4	0.19(6)	764, 1031
939.2(11)[d]	2307.4	1368.53	0.17(6)	964, 1231
944.3(4)[d]	2572.0	1627.5	0.15(3)	266, 1223
949.60(16)[d]	1840.1	890.50	0.71(5)	138, 753, 890
950.5(2)	1088.28	137.80	1.2(2)	138, 349, 1730
955.4(4)[d]	2323.6	1368.53	0.19(4)	964, 1231
958.3(8)[b]	1728.7	770.40	0.22(7)[g]	366
960.6(3)[d]	2818.4	1857.82	0.69(7)	266, 366, 1087, 1454
964.36(18)	1368.53	404.18	1.51(12)	138, 266, 939
965.3(8)[d]	2823.3	1857.82	0.10(5)	1454
970.4(18)[c,d]	2058.6	1088.28	0.06(4)	684
988.7(5)[c,d]	1878.8	890.50	0.14(3)	890
996.1(4)[d]	2331.7	1335.51	0.14(5)	266, 931
1001.7(3)[d]	2089.9	1088.28	0.43(6)	138, 260, 266, 684
1011.7(2)[d]	1840.1	828.66	0.10(3)	138, 691

E_γ (keV)	E_i (keV)	E_f (keV)	I	Coincidences[a]
1024.6(6)[d]	1794.6	770.40	0.12(5)	138, 266, 366
1030.7(2)	1168.4	137.80	7.7(4)	138, 356, 1076, 1139, 1155, 1174, 1650
1031.8(8)[d]	2199.7	1168.4	0.11(3)[g]	1031
1033.2(3)[b]	1437.28	404.18	0.65(13)	266, 1381
1036.4(2)[d]	2058.6	1022.10	0.32(6)	138, 618, 884
1038.6(8)			0.12(4)[f]	931
1039.3(2)[b]	1809.8	770.40	0.33(5)	138, 266, 366
1040.0(7)[d]	2408.7	1368.53	0.11(4)	1231
1049.6(15)[c,d]	1878.8	828.66	0.12(5)	691
1050.0(5)[d]	2385.6	1335.51	0.11(3)	931
1050.3(7)			0.07(3)[f]	1223
1076.2(5)[d]	2244.7	1168.4	0.42(8)	764, 1031
1081.2(4)[d]	2103.3	1022.10	0.64(5)	138, 266, 618, 884
1087.40(16)[d]	1857.82	770.40	0.62(4)	138, 266, 366, 961
1094.8(10)[c,d]	2264.1	1168.4	0.15(5)	764, 1031
1095.9(5)[c,d]	2183.8	1088.28	0.10(6)	684
1110.7(7)[d,h]	2445.2	1335.51	0.29(6)	931
1111.2(6)[d]	1515.0	404.18	0.53(13)[g]	138, 266
1121.8(2)	1526.0	404.18	8.2(8)[e]	138, 266
1128.07(15)[b]	1898.5	770.40	0.89(5)	138, 266, 366, 920
1137.0(5)			0.21(7)[f]	890
1139.0(6)[d]	2307.4	1168.4	0.32(9)	266, 764, 1031
1154.4(8)[c,d]	2489.5	1335.51	0.14(6)	931
1155.3(2)[d]	2323.6	1168.4	1.26(9)	764, 1031
1156.4(3)[d]	2244.7	1088.28	0.32(7)	260, 684
1163.1(6)[c,d]	2331.7	1168.4	0.10(5)	764, 1031
1172.5(16)[c,d]	1942.9	770.40	0.20(6)	138, 266, 366
1174.2(2)[d]	2342.6	1168.4	0.42(7)	764, 1031
1174.5(8)[d]	2003.0	828.66	0.22(8)	138, 691
1176.8(8)			0.10(4)[f]	1231
1177.6(2)[d]	2199.7	1022.10	0.29(5)	138, 618, 884
1179.4(8)			0.27(8)[f]	931
1185.6(5)[d]	2207.4	1022.10	0.22(4)	884
1191.1(5)	2818.4	1627.5	0.43(6)	138, 266, 1223
1199.0(3)			0.20(5)[f,i]	931, (1231)
1205.2(2)	1609.4	404.18	1.27(11)	138, 266
1217.2(3)[d]	2385.6	1168.4	0.25(7)	138, 266, 764, 1031
1218.9(5)[d]	2307.4	1088.28	0.39(10)	266, 684
1222.8(3)[d]	2244.7	1022.10	0.37(8)	618, 884
1223.36(18)	1627.5	404.18	5.6(4)	138, 266, 944, 1191
1230.72(14)	1368.53	137.80	5.3(5)	138, 939, 955, 1450
1235.3(2)[d]	2323.6	1088.28	0.43(9)	138, 266, 260, 684, 951
1241.2(6)[c,d]	2264.1	1022.10	0.15(6)	884
1241.3(12)[c,d]	2408.7	1168.4	0.14(6)	764, 1031
1245.7(8)			0.13(5)[f]	1122
1259.1(7)[d]	2594.3	1335.51	0.19(8)	931
1272.8(3)[d]	1677.2	404.18	0.32(8)	138, 266
1276.8(5)			0.12(4)[f]	266, 366
1278.0(3)[d]	2300.1	1022.10	0.52(14)	138, 618, 884
1285.4(4)[d]	2307.4	1022.10	0.18(7)	884
1289.1(8)			0.16(6)[f]	884
1292.3(3)[d]	2818.4	1526.0	0.87(11)	1122
1293.0(5)[c,d]	2183.8	890.50	0.14(8)	890

E_γ (keV)	E_i (keV)	E_f (keV)	I	Coincidences[a]
1293.4(15)[d]	2818.4	1525.3	0.27(4)	356, 366, 755
1297.3(2)[d]	2823.3	1526.0	0.33(8)	1122
1301.5(4)[d]	2323.6	1022.10	2.58(14)	138, 266, 618, 884
1309.7(4)[d]	2331.7	1022.10	0.37(8)	618, 884
1314.7(2)[d]	2085.1	770.40	0.52(5)	138, 266, 366
1320.3(15)	2408.7	1088.28	0.12(5)	138, 266, 684
1323.2(4)[d]	2492.0	1168.4	0.17(5)	138, 266, 764, 1031
1338.31(17)[d]	1476.10	137.80	1.11(11)	138, 723
1345.6(3)[d]	2433.8	1088.28	0.19(5)	138, 266, 684
1348.9(5)	2516.6	1168.4	0.19(5)	764, 1031
1351.3(6)[c,d]	2439.2	1088.28	0.10(4)	684
1354.1(2)[d]	2244.7	890.50	0.41(5)	138, 753, 890
1355.1(4)[d]	2183.8	828.66	0.21(5)	691
1363.4(7)[c,d]	2385.6	1022.10	0.08(3)	884
1380.9(2)[d]	2818.4	1437.28	0.65(6)	138, 266, 349, 366, 667, 684, 1033
1386.3(2)	2408.7	1022.10	0.67(6)	138, 266, 618, 884
1390.33(17)[d]	1794.6	404.18	2.07(12)	138, 266
1393(2)			0.13(5)[f,i]	684, 753, 890
1393.9(7)[c,d]	2164.3	770.40	0.09(4)	366
1415.9(2)[d]	2244.7	828.66	1.50(9)	138, 266, 424, 691
1416.8(2)	2307.4	890.50	0.92(10)	138, 486, 753, 890
1421.2(6)			0.12(4)[f]	366
1423.0(2)[d]	2445.2	1022.10	0.68(9)	138, 618, 884
1423.3(6)[d]	2193.5	770.40	0.16(6)	366
1425.9(4)[d]	2594.3	1168.4	0.20(5)	764, 1031
1432.8(2)[d]	2323.6	890.50	1.00(10)	138, 486, 753, 890
1435.7(5)[d]	1840.1	404.18	0.47(9)	138, 266
1450.0(3)[d]	2220.4	770.40	0.22(6)[g]	138, 266, 366
1450.0(8)[c,d]	2818.4	1368.53	0.15(6)	1231
1453.65(15)[d]	1857.82	404.18	2.5(3)	138, 266, 961
1460.5(3)[d]	2230.9	770.40	0.22(4)	366
1467.1(8)[d]	2489.5	1022.10	0.10(5)	138, 884
1469.9(5)[d]	2492.0	1022.10	0.19(6)	138, 884
1471.5(2)	1609.4	137.80	2.5(3)[g]	138
1471.9(6)			0.22(13)[f]	266
1474.2(4)[d]	1878.8	404.18	0.56(14)	138, 266
1478.7(2)	2307.4	828.66	0.28(3)	138, 424, 691
1480.6(7)			0.11(3)[f]	1231
1482.7(2)[d]	2818.4	1335.51	0.30(5)	138, 266, 931
1486.4(7)[d]	1624.6	137.80	0.54(16)	138
1493.8(10)	2516.6	1022.10	0.20(5)	884
1494.5(5)[d]	2323.6	828.66	0.29(7)	138, 691
1499.6(3)[d]	2270.0	770.40	0.62(9)	138, 266, 366
1518.3(7)			0.38(12)[f,g]	138
1518.7(3)[d]	2408.7	890.50	0.25(7)	753, 890
1523.0(3)[d]	2293.4	770.40	0.38(6)	138, 266, 366
1526.1(6)[d]	1930.0	404.18	0.64(16)	138, 266
1529.4(2)[d]	1933.6	404.18	1.52(13)	138, 266, 884
1536.0(4)	2307.4	770.40	0.49(8)	138, 266, 366
1538.0(12)[c,d]	1942.9	404.18	0.41(13)	138, 266
1542.1(8)[d]	1679.9	137.80	0.80(16)[h]	138
1545.8(2)[d]	1950.0	404.18	1.44(8)	138, 266
1572.0(5)[d]	2594.3	1022.10	0.13(5)	884

E_γ (keV)	E_i (keV)	E_f (keV)	I	Coincidences[a]
1572.5(8)[d]	2788.1	1215.6	0.08(2)	366, 445
1580.3(4)[d]	2408.7	828.66	0.11(3)	138, 691
1598.7(5)[d]	2003.0	404.18	0.25(7)	138, 266
1626.8(6)[c]	2516.6	890.50	0.16(6)	890
1633.5(10)			0.18(5)[f]	366
1634.6(10)[d]	1772.4	137.80	1.1(3)[g]	138
1642.0(10)			0.36(17)[f]	138, 266
1648.1(7)[c,d]	2418.9	770.40	0.19(6)	366
1649.7(2)	2818.4	1168.4	1.37(11)	138, 266, 278, 764, 1031
1653.4(13)			0.13(4)[f]	691
1654.0(11)[c,d]	2823.3	1168.4	0.14(6)	764, 1031
1654(2)			0.13(5)[f]	366
1658(2)			0.13(5)[f]	366
1663.3(2)[d]	2433.8	770.40	0.52(10)	138, 266, 366
1668.7(2)[d]	2439.2	770.40	0.32(7)	138, 266, 366
1688.2(15)[c]	2516.6	828.66	0.07(5)	691
1704(2)			0.09(3)[f]	366
1730.1(2)	2818.4	1088.28	0.57(6)	138, 260, 266, 684, 951
1733.4(7)			0.22(5)[f]	366
1734.3(5)			0.7(2)[f,g]	138, 266
1735.7(5)[d]	2757.8	1022.10	0.18(5)	884
1741.5(7)[d]	1878.8	137.80	0.36(9)	138
1757.8(4)			0.37(9)[f,i]	138, 266, (366)
1760.1(4)[d]	2164.3	404.18	0.31(9)	138, 266
1791.9(9)[d]	1930.0	137.80	0.50(18)	138
1795.6(5)[d]	2199.7	404.18	0.42(15)	266
1824.7(5)[d]	2228.9	404.18	0.63(9)	138, 266
1824.7(6)[d]	2653.4	828.66	0.20(5)	424, 691
1840.5(8)[c,d]	2244.7	404.18	0.22(9)	138, 266
1843.6(7)			0.07(3)[f]	884
1860.1(5)[d]	2264.1	404.18	0.81(13)	138, 266
1867.6(5)			0.30(8)[f]	138, 266
1872.9(4)[d]	2894.9	1022.10	0.21(5)	138, 618, 884
1888.8(15)[c,d]	2293.4	404.18	0.27(10)	266
1898.8(8)			0.32(8)[f]	138, 266
1902.5(5)	2307.4	404.18	0.42(10)	138, 266
1919.8(4)[d]	2323.6	404.18	0.61(13)	138, 266
1952.3(9)[c]	2089.9	137.80	0.24(10)	138
1959.1(9)			0.09(4)[f]	366
1959.7(6)			0.25(8)[f,g]	266
1961.8(15)			0.05(3)[f]	366
1967.9(3)[d]	2372.1	404.18	0.59(16)	138, 266
1989.2(12)			0.39(16)[f,i]	266, (366)
2003.7(7)[c]	2408.7	404.18	0.34(10)	138, 266
2004.2(9)[c,d]	2894.9	890.50	0.10(4)	753, 890
2008.9(5)			0.26(8)[f]	138, 266
2014.9(6)[d]	2418.9	404.18	0.42(10)	138, 266
2029.70(18)[d]	2433.8	404.18	2.17(16)	138, 266
2035.0(2)[d]	2439.2	404.18	1.7(2)	138, 266
2039.9(10)[c,d]	2810.4	770.40	0.11(4)	266, 366
2041.1(10)			0.32(10)[f]	138
2048.0(2)[d]	2818.4	770.40	0.19(6)	266, 366
2052.8(2)[d]	2823.3	770.40	0.69(11)	266, 366

E_γ (keV)	E_i (keV)	E_f (keV)	I	Coincidences[a]
2063.2(4)[d]	2833.6	770.40	0.23(4)	266, 366
2064.6(8)			0.13(8)[f]	138
2085.4(5)[d]	2489.5	404.18	0.49(10)	138, 266
2088.2(6)[d]	2492.0	404.18	0.37(15)	138, 266
2134.1(5)			0.09(3)[f]	691
2135.6(15)[h]			0.45(12)[f]	266
2168.9(7)[c,d]	2572.0	404.18	0.23(8)	266
2185.6(6)[d]	2323.6	137.80	0.31(10)	138
2234.2(4)[d]	2372.1	137.80	1.7(4)	138
2238.3(2)[d]	2642.5	404.18	0.77(13)	138, 266
2249(2)[c,d]	2653.4	404.18	0.32(15)	138, 266
2271.0(2)[d]	2408.7	137.80	0.88(13)	138
2277.4(4)			0.42(13)[f]	138
2286.3(10)			0.26(9)[f]	266
2303.9(6)			0.22(8)[f]	138
2306.7(15)			0.33(11)[f]	266
2307.4(8)[d]	2445.2	137.80	0.27(11)	138
2339.2(9)			0.18(7)[f]	266
2354.1(2)[d]	2492.0	137.80	0.90(8)	138
2406.2(7)[d]	2810.4	404.18	0.38(11)	266
2414.2(2)[d]	2818.4	404.18	1.60(18)	138, 266
2419.2(2)	2823.3	404.18	3.3(3)	138, 266
2429.5(7)[d]	2833.6	404.18	0.63(9)	138, 266
2481.4(6)			0.18(5)[f]	266
2490.7(6)[d]	2894.9	404.18	0.21(7)	138, 266
2577.3(13)[d]	2981.5	404.18	0.33(7)	138, 266
2579.8(10)			0.08(3)[f]	366
2590.8(7)			0.06(2)[f]	366
2613.4(9)			0.09(2)[f]	366

[a]In the entries for many of the less intense higher-lying transitions, coincidences with the low-lying 138 keV and 266 keV transitions are not explicitly listed. This indicates that the corresponding region of the spectrum gated on the 138 keV or 226 keV transition is sufficiently complicated — either dominated by a more intense close doublet transition or obscured by multiple smaller background peaks — that coincidence with 138 keV or 226 keV transition cannot be unambiguously confirmed and therefore does not provide useful additional placement or intensity information. This should *not* be construed as indicating *noncoincidence*. Also, to make efficient use of space, coincidences with weaker feeding transitions are omitted in the entries for low-lying transitions coincident with a large number of feeding transitions and are included only in the entries for these weaker feeding transitions.
[b]Transition was previously reported, but not in β decay.
[c]Identification of transition is tentative.
[d]Gamma-ray line was not previously reported or was not reported in this placement.
[e]Transitions from the closely-spaced pair of levels at 1525.3(2) and 1526.0(2) keV are all potentially doublets. Each transition is assigned a primary placement as depopulating one of these levels on the basis of transition energy as measured in gated spectra but may contain a significant unresolved contribution depopulating the other member of the pair. (See text.)
[f]Transition was observed in a gated spectrum, but its placement is unknown, and its absolute intensity cannot therefore be uniquely determined from the data. The intensity value reported here is an estimate, calculated from the intensity of coincidences between this transition and the other coincident transition, corrected for the branching fraction of the coincident transition.
[g]Energy and intensity are deduced from gated spectrum after subtraction of contribution(s) from other placement(s). (See also Table I.1.)
[h]Peak in gated spectrum has abnormally large width.

[i]Multiple gamma-ray transitions may be present on the basis of the coincidences observed or their relative intensities, but the transitions have been consolidated into one entry. Any coincidence significantly weaker than the others is enclosed in parentheses.

Table I.2: Branching properties of levels populated in ^{156}Dy. Both absolute (in β decay) and relative intensities are given for γ-ray transitions depopulating the levels, and these intensities are compared with literature values [24] where available. Intensity limits are given for many unobserved transitions, in which case the approximate transition energy expected from the level energy difference is shown in brackets. (Transitions on which limits were placed include spin-allowed but unobserved transitions between low-lying levels relevant to the structural interpretation of the nucleus and presently-unobserved transitions which were reported to have been observed in the prior literature.)

Transition				Experiment			Literature	
J_i^π [a]	E_i (keV)	J_f^π	E_f (keV)	E_γ (keV)	I	$I^{\rm rel}$	I [b]	$I^{\rm rel}$ [c]
2^+	137.80(10)	0^+	0.00	137.80(10)	100(7)	100(7)	100	100
4^+	404.18(14)	2^+	137.80	266.38(10)	127(6)	100(5)	107.1(11)	100
0^+	675.6(2)	2^+	137.80	537.8(2)	0.86(12)	100(15)	0.53(7)	100
6^+	770.40(17)	4^+	404.18	366.22(12)	27.9(16)	100(6)	21.0(2)	100
2^+	828.66(15)	0^+	0.00	[829]	<0.4	<4		16(18), not obs.
		2^+	137.80	690.86(13)	10.4(5)	100(5)	8.46(13)	100(2)
		4^+	404.18	424.5(2)	1.12(6)	10.8(5)	0.77(13)	9(2)
		0^+	675.6	[153]	<0.07	<0.7	0.19[d]	36(7), 1.9[d,e]
2^+	890.50(11)	0^+	0.00	890.44(12)	5.9(9)	100(6)	5.21(8)	100(2)
		2^+	137.80	752.67(15)	3.3(3)	56(5)	3.05(18)	59(3)
		4^+	404.18	486.4(3)	0.50(8)	8.5(10)	0.31(12)	6.0(23)
		0^+	675.6	[214]	<0.05	<0.8		
		2^+	828.66	[62]	<0.06	<1.0	0.05[d]	0.9[d]
3^+	1022.10(14)	2^+	137.80	884.30(10)	16.4(16)	100(7)	13.86(11)	100.0(8)
		4^+	404.18	617.88(12)	3.6(4)	22(2)	2.68(5)	19.3(4)
		2^+	828.66	[193]	<0.07	<0.4		
		2^+	890.50	[131]	<0.08	<0.5	0.48[d]	3.5[d,f]
4^+	1088.28(14)	2^+	137.80	950.5(2)	1.2(2)	9.0(15)	1.39(6)	13.2(6)
		4^+	404.18	684.10(10)	13.3(9)	100(7)	10.54(14)	100.0(13)
		6^+	770.40	317.9(2)	0.27(4)	2.0(3)	0.33(13)	3.1(12)
		2^+	828.66	259.59(15)[g]	1.46(13)	11.0(10)		45(14),[h] 11(2),[h] not obs.
		2^+	890.50	[197]	<0.19	<1.4		
		3^+	1022.10	[66]	<0.3	<2		
4^+	1168.4(2)	2^+	137.80	1030.7(2)	7.7(4)	86(4)	6.19(9)	89.1(13)
		4^+	404.18	764.12(13)	9.0(5)	100(6)	6.91(7)	100.0(10)
		6^+	770.40	397.9(2)[g]	0.21(5)	2.3(6)		557(90),[i] not obs.
		2^+	828.66	[340]	<0.17	<1.9		
		2^+	890.50	277.96(18)	0.71(7)	7.9(8)	0.87(9)	12.5(13)
		3^+	1022.10	[146]	<0.2	<3	0.11[d]	530(60),[j] 1.7[d]
		4^+	1088.28	[80]	<0.3	<3	[0.6][k]	[9][k]
8^+	1215.6(2)[l]	6^+	770.40	445.23(17)[g]	0.37(3)	100(8)		100
5^+	1335.51(18)	4^+	404.18	931.35(16)	7.2(4)	100(6)	5.83(6)	100.0(10)
		6^+	770.40	565.07(17)	1.15(6)	16.0(8)	1.25(5)	21.4(9)
		3^+	1022.10	313.4(2)	0.66(5)	9.2(7)	0.68(13)	11.7(22)
		4^+	1088.28	[247]	<0.2	<3		
		4^+	1168.4	[167]	<0.3	<4	0.66[d]	11[d]
3^-	1368.53(18)	2^+	137.80	1230.72(14)	5.3(5)	100(10)	4.20(13)	100(3)
		4^+	404.18	964.36(18)	1.51(12)	29(2)	1.22(8)	29(2)
		2^+	828.66	[540]	<0.12	<2		
		2^+	890.50	[478]	<0.13	<3		

Transition				Experiment			Literature	
J_i^π [a]	E_i (keV)	J_f^π	E_f (keV)	E_γ (keV)	I	$I^{\rm rel}$	I [b]	$I^{\rm rel}$ [c]
		3^+	1022.10	[346]	<0.10	<1.9		
		4^+	1088.28	[280]	<0.19	<4		
		4^+	1168.4	[200]	<0.2	<4		
$(2^+)^m$	1382.3(2)[l,n]	0^+	0.00	[1382]	<0.6	<207		
		2^+	137.80	[1245]	<0.9	<314		
		4^+	404.18	[978]	<0.4	<150		
		0^+	675.6	706.74(16)[o]	0.14(2)	50(7)		
		2^+	828.66	553.7(2)[o]	0.28(3)	100(11)		
		2^+	890.50	491.6(3)[o]	0.23(6)	82(21)		
		3^+	1022.10	360.7(12)[o,p]	0.11(4)	39(14)		
		4^+	1088.28	[294]	<0.11	<39		
		4^+	1168.4	[214]	<0.2	<71		
6^+	1437.28(17)	4^+	404.18	1033.2(3)[g]	0.65(13)	34(7)		16(8)
		6^+	770.40	666.88(15)	1.92(10)	100(5)	2.07(9)	100(4)
		4^+	1088.28	348.96(14)	1.41(7)	73(4)	1.46(8)	71(5)
		4^+	1168.4	[268]	<0.4	<20		
		8^+	1215.6	[222]	<0.11	<6		
		5^+	1335.51	[101]	<0.7	<37		
(?)	1476.10(16)[q]	2^+	137.80	1338.31(17)[o]	1.11(11)	100(10)		
		2^+	890.50	585.6(2)[o]	0.35(7)	32(6)		
$(2^+)^m$	1515.0(2)[q]	4^+	404.18	1111.2(6)[o]	0.53(13)[r]	100(25)		
		0^+	675.6	839.3(2)[o]	0.20(2)	37(4)		
		2^+	890.50	624.4(3)[o]	0.11(5)	21(9)		
6^+	1525.3(2)[l,s]	4^+	404.18	[1121]	<3[t]	<149[t]		≤52
		6^+	770.40	754.9(2)[g]	1.75(11)[t]	100(6)[t]		27(14)
		4^+	1088.28	[437]	<0.13[t]	<7[t]		
		4^+	1168.4	356.5(3)[g]	0.53(5)[t]	30(3)[t]		43(9)
		5^+	1335.51	[190]	<0.2	<13		100(5)[u]
(5^-)	1526.0(2)	4^+	404.18	1121.8(2)	8.2(8)[t]	100(10)[t]	6.54(11)	100.0(17)
		6^+	770.40	[755]	<0.6[t]	<7[t]	1.39(11)	21.2(17)
		4^+	1088.28	437.6(6)[o,p]	0.08(6)[t]	1.0(7)[t]		
		4^+	1168.4	[357]	<0.2[t]	<3[t]	0.42(8)	6.4(12)
$(3)^-$	1609.4(2)	0^+	0.00	[1609]	<1.3	<52	0.14(3)	6.5(14)
		2^+	137.80	1471.5(2)	2.5(3)[r]	100(12)	2.17(8)	100(4)
		4^+	404.18	1205.2(2)	1.27(11)	51(4)	0.97(9)	45(4)
(?)	1624.6(2)[q]	2^+	137.80	1486.4(7)[o]	0.54(16)	55(16)		
		2^+	828.66	796.03(15)[o]	0.98(6)	100(6)		
		4^+	1168.4	456.2(8)[o]	0.09(3)	9(3)		
$(4)^+$	1627.5(2)	4^+	404.18	1223.36(18)	5.6(4)	100(7)	4.75(13)	100(3)
		3^+	1022.10	605.5(3)	0.36(7)	6.4(13)	0.47(9)	10(2)
		4^+	1168.4	458.9(4)[o]	0.20(6)	3.6(11)		
				[178][v]	<0.07[w]	<1.2		≤133(43)[x]
$(4^+)^m$	1677.2(2)[q]	4^+	404.18	1272.8(3)[o]	0.32(8)	62(15)		
		6^+	770.40	907.2(4)[o]	0.14(5)	29(4)		
		2^+	828.66	848.2(5)[o]	0.12(5)	23(10)		
		2^+	890.50	786.1(5)[o,p]	0.10(3)	19(6)		
		3^+	1022.10	654.9(4)[o]	0.33(9)	63(17)		
		4^+	1088.28	588.88(14)[o]	0.52(4)	100(8)		
(?)	1679.9(8)[q]	2^+	137.80	1542.1(8)[o]	0.80(16)[y]	100(20)		
		2^+	828.66	851.0(12)[o,p]	0.07(4)	9(5)		
7^+	1728.7(5)[l]	6^+	770.40	958.3(8)[g]	0.22(7)[r]	100(32)		100(10)
		5^+	1335.51	393.2(6)[g]	0.09(4)	41(18)		52(8)
(?)	1772.4(10)[q]	2^+	137.80	1634.6(10)[o]	1.1(3)[r]	100(27)		
(?)	1794.6(2)[q]	4^+	404.18	1390.33(17)[o]	2.07(12)	100(6)		
		6^+	770.40	1024.6(6)[o]	0.12(5)	6(2)		
7^-	1809.8(3)[l]	6^+	770.40	1039.3(2)[g]	0.33(5)	100(15)		observed[z]
		8^+	1215.6	594.9(6)[g]	0.047(13)	14(4)		observed[z]
(?)	1840.1(2)[q]	4^+	404.18	1435.7(5)[o]	0.47(9)	66(23)		

Transition				Experiment			Literature	
J_i^π [a]	E_i (keV)	J_f^π	E_f (keV)	E_γ (keV)	I	$I^{\rm rel}$	I [b]	$I^{\rm rel}$ [c]
		2^+	828.66	1011.7(2)[o]	0.10(3)	14(4)		
		2^+	890.50	949.60(16)[o]	0.71(5)	100(7)		
		3^+	1022.10	818.1(2)[o]	0.26(6)	37(8)		
		4^+	1168.4	671.2(2)[o]	0.18(4)	25(6)		
(?)	1857.82(17)[q]	4^+	404.18	1453.65(15)[o]	2.5(3)	100(12)		
		6^+	770.40	1087.40(16)[o]	0.62(4)	24.8(16)		
		4^+	1168.4	688.9(5)[o,p]	0.15(9)	6(4)		
(?)	1878.8(6)[q]	2^+	137.80	1741.5(7)[o]	0.36(9)	64(16)		
		4^+	404.18	1474.2(4)[o]	0.56(14)	100(25)		
		2^+	828.66	1049.6(15)[o,p]	0.12(5)	21(9)		
		2^+	890.50	988.7(5)[o,p]	0.14(3)	25(5)		
(6)	1898.5(2)[l,aa]	6^+	770.40	1128.07(15)[g]	0.89(5)	100(6)		100(5)
		5^+	1335.51	562.6(5)[o]	0.12(5)	13(6)		
		$(4)^+$	1627.5	[271]	<0.16	<18		≤88
(?)	1930.0(5)[q]	2^+	137.80	1791.9(9)[o]	0.50(18)	78(28)		
		4^+	404.18	1526.1(6)[o]	0.64(16)	100(25)		
(?)	1933.6(2)[q]	4^+	404.18	1529.4(2)[o]	1.52(13)	100(9)		
		3^+	1022.10	911.5(6)[o]	0.15(4)	10(3)		
		4^+	1088.28	845.3(3)[o]	0.11(2)	7.2(13)		
(?)	1942.9(3)[q]	4^+	404.18	1538.0(12)[o,p]	0.41(13)	121(38)		
		6^+	770.40	1172.5(16)[o,p]	0.20(6)	59(19)		
		4^+	1088.28	854.6(3)[o]	0.34(5)	100(15)		
(?)	1950.0(2)[q]	4^+	404.18	1545.8(2)[o]	1.44(8)	100(6)		
(?)	2003.0(3)[q]	4^+	404.18	1598.7(5)[o]	0.25(7)	100(28)		
		2^+	828.66	1174.5(8)[o]	0.22(8)	88(32)		
		4^+	1088.28	914.6(3)[o]	0.14(5)	56(20)		
(?)	2058.6(2)[q]	3^+	1022.10	1036.4(2)[o]	0.32(6)	100(19)		
		4^+	1088.28	970.4(18)[o,p]	0.06(4)	19(13)		
		4^+	1168.4	890.2(4)[o]	0.27(10)	84(31)		
		5^+	1335.51	722.3(7)[o]	0.13(4)	41(13)		
(?)	2085.1(3)[q]	6^+	770.40	1314.7(2)[o]	0.52(5)	100(10)		
2^+	2089.9(3)	0^+	0.00	[2089]	<0.6	<144	0.31(13)	27(12)
		2^+	137.80	1952.3(9)[p]	0.24(10)	56(23)	0.29(4)	26(4)
		4^+	1088.28	1001.7(3)[o]	0.43(6)	100(14)		
		4^+	1168.4	921.2(3)	0.26(6)	60(14)	0.14(6)	12(5)
				[796][v]			1.13(4)	100(4)
(?)	2103.3(3)[q]	3^+	1022.10	1081.2(4)[o]	0.64(5)	100(8)		
		4^+	1168.4	935.0(4)[o]	0.19(6)	30(9)		
		5^+	1335.51	767.8(4)[o]	0.16(4)	25(6)		
(?)	2164.3(4)[q]	4^+	404.18	1760.1(4)[o]	0.31(9)	100(29)		
		6^+	770.40	1393.9(7)[o,p]	0.09(4)	29(12)		
(?)	2183.8(4)[q]	2^+	828.66	1355.1(4)[o]	0.21(5)	100(23)		
		2^+	890.50	1293.0(5)[o,p]	0.14(8)	67(38)		
		4^+	1088.28	1095.9(5)[o,p]	0.10(6)	48(29)		
(?)	2193.5(3)[q]	6^+	770.40	1423.3(6)[o]	0.16(6)	47(18)		
		5^+	1335.51	858.0(3)[o]	0.34(5)	100(15)		
(?)	2199.7(3)[q]	4^+	404.18	1795.6(5)[o]	0.42(15)	100(36)		
		3^+	1022.10	1177.6(2)[o]	0.29(5)	69(12)		
		4^+	1168.4	1031.8(8)[o]	0.11(3)[r]	26(7)		
		5^+	1335.51	863.3(10)[o]	0.10(4)	24(10)		
		(?)	1476.10	723.5(4)[o]	0.14(4)	33(10)		
(?)	2207.4(5)[q]	3^+	1022.10	1185.6(5)[o]	0.22(4)	100(18)		
		5^+	1335.51	871.6(5)[o]	0.18(5)	82(23)		
(?)	2220.4(4)[q]	6^+	770.40	1450.0(3)[o]	0.22(6)[r]	100(27)		
(?)	2228.9(5)[q]	4^+	404.18	1824.7(5)[o]	0.63(9)	100(14)		
(?)	2230.9(4)[q]	6^+	770.40	1460.5(3)[o]	0.22(4)	100(18)		
(?)	2244.7(3)[q]	4^+	404.18	1840.5(8)[o,p]	0.22(9)	15(6)		
		2^+	828.66	1415.9(2)[o]	1.50(9)	100(6)		

Transition				Experiment			Literature	
J_i^π [a]	E_i (keV)	J_f^π	E_f (keV)	E_γ (keV)	I	$I^{\rm rel}$	I [b]	$I^{\rm rel}$ [c]
		2^+	890.50	1354.1(2)[o]	0.41(5)	27(3)		
		3^+	1022.10	1222.8(3)[o]	0.37(8)	25(5)		
		4^+	1088.28	1156.4(3)[o]	0.32(7)	21(5)		
		4^+	1168.4	1076.2(5)[o]	0.42(8)	28(5)		
		(?)	1624.6	620.1(8)[o]	0.10(3)	7(2)		
(?)	2264.1(6)[q]	4^+	404.18	1860.1(5)[o]	0.81(13)	100(16)		
		3^+	1022.10	1241.2(6)[o,p]	0.15(6)	19(7)		
		4^+	1168.4	1094.8(10)[o,p]	0.15(5)	19(6)		
(?)	2270.0(4)[q]	6^+	770.40	1499.6(3)[o]	0.62(9)	100(15)		
(?)	2293.4(4)[q]	4^+	404.18	1888.8(15)[o,p]	0.27(10)	71(26)		
		6^+	770.40	1523.0(3)[o]	0.38(6)	100(16)		
(?)	2300.1(4)[q]	3^+	1022.10	1278.0(3)[o]	0.52(14)	100(27)		
4^+	2307.4(3)	2^+	137.80	[2169]	<0.4	<39	0.31(4)	14(2)
		4^+	404.18	1902.5(5)	0.42(10)	46(11)	0.48(6)	22(3)
		6^+	770.40	1536.0(4)	0.49(8)	53(9)	0.57(8)	26(4)
		2^+	828.66	1478.7(2)	0.28(3)	30(3)	0.66(8)	40(4)
		2^+	890.50	1416.8(2)	0.92(10)	100(11)	2.21(4)	100(2)
		3^+	1022.10	1285.4(4)[o]	0.18(7)	20(8)		
		4^+	1088.28	1218.9(5)[o]	0.39(10)	42(10)		
		4^+	1168.4	1139.0(6)[o]	0.32(9)	35(10)		
		3^-	1368.53	939.2(11)[o]	0.17(6)	18(7)		
		$(4)^+$	1627.5	[680]	<0.10	<11	0.48(10)	22(5)
(?)	2323.6(2)[q]	2^+	137.80	2185.6(6)[o]	0.31(10)	12(4)		
		4^+	404.18	1919.8(4)[o]	0.61(13)	24(5)		
		2^+	828.66	1494.5(5)[o]	0.29(7)	11(3)		
		2^+	890.50	1432.8(2)[o]	1.00(10)	39(4)		
		3^+	1022.10	1301.5(4)[o]	2.58(14)	100(5)		
		4^+	1088.28	1235.3(2)[o]	0.43(9)	17(3)		
		4^+	1168.4	1155.3(2)[o]	1.26(9)	49(3)		
		3^-	1368.53	955.4(4)[o]	0.19(4)	7.4(16)		
(?)	2331.7(3)[q]	3^+	1022.10	1309.7(4)[o]	0.37(8)	100(22)		
		4^+	1168.4	1163.1(6)[o,p]	0.10(5)	27(14)		
		5^+	1335.51	996.1(4)[o]	0.14(5)	37(14)		
(?)	2342.6(3)[q]	4^+	1168.4	1174.2(2)[o]	0.42(7)	100(17)		
(?)	2372.1(3)[q]	2^+	137.80	2234.2(4)[o]	1.7(4)	100(23)		
		4^+	404.18	1967.9(3)[o]	0.59(16)	35(9)		
(?)	2385.6(3)[q]	3^+	1022.10	1363.4(7)[o,p]	0.08(3)	32(12)		
		4^+	1168.4	1217.2(3)[o]	0.25(7)	100(28)		
		5^+	1335.51	1050.0(5)[o]	0.11(3)	44(12)		
(?)	2408.7(4)[bb]	2^+	137.80	2271.0(2)[o]	0.88(13)	100(15)		
		4^+	404.18	2003.7(7)[p]	0.34(10)	39(11)	0.24(5)	36(7)
		2^+	828.66	1580.3(4)[o]	0.11(3)	13(3)		
		2^+	890.50	1518.7(3)[o]	0.25(7)	28(8)		
		3^+	1022.10	1386.3(2)	0.67(6)	76(7)	0.67(8)	100(12)
		4^+	1088.28	1320.3(15)	0.12(5)	14(6)	0.31(5)	46(7)
		4^+	1168.4	1241.3(12)[o,p]	0.14(6)	16(7)		
		3^-	1368.53	1040.0(7)[o]	0.11(4)	13(5)		
				[880][v]			0.66(8)	99(12)
		(?)	2103.3	304.6(7)[o,p]	0.10(3)	11(3)		
(?)	2418.9(6)[q]	4^+	404.18	2014.9(6)[o]	0.42(10)	100(24)		
		6^+	770.40	1648.1(7)[o,p]	0.19(6)	45(14)		
(?)	2433.8(2)[q]	4^+	404.18	2029.70(18)[o]	2.17(16)	100(7)		
		6^+	770.40	1663.3(2)[o]	0.52(10)	24(5)		
		4^+	1088.28	1345.6(3)[o]	0.19(5)	9(2)		
		(5^-)	1526.0	908.0(10)[o,p]	0.19(6)	9(3)		
(?)	2439.2(2)[q]	4^+	404.18	2035.0(2)[o]	1.7(2)	100(12)		
		6^+	770.40	1668.7(2)[o]	0.32(7)	19(4)		
		4^+	1088.28	1351.3(6)[o,p]	0.10(4)	6(2)		

Transition				Experiment			Literature	
J_i^π [a]	E_i (keV)	J_f^π	E_f (keV)	E_γ (keV)	I	$I^{\rm rel}$	I [b]	$I^{\rm rel}$ [c]
(?)	2445.2(3)[q]	2^+	137.80	2307.4(8)[o]	0.27(11)	40(16)		
		3^+	1022.10	1423.0(2)[o]	0.68(9)	100(13)		
		5^+	1335.51	1110.7(7)[o,y]	0.29(6)	43(9)		
		(?)	1624.6	820.9(6)[o,p]	0.08(2)	12(3)		
		$(4)^+$	1627.5	818.7(4)[o,p]	0.19(5)	28(7)		
(?)	2489.5(5)[q]	4^+	404.18	2085.4(5)[o]	0.49(10)	100(20)		
		3^+	1022.10	1467.1(8)[o]	0.10(5)	20(10)		
		5^+	1335.51	1154.4(8)[o,p]	0.14(6)	29(12)		
(?)	2492.0(3)[q]	2^+	137.80	2354.1(2)[o]	0.90(8)	100(9)		
		4^+	404.18	2088.2(6)[o]	0.37(15)	41(17)		
		3^+	1022.10	1469.9(5)[o]	0.19(6)	21(7)		
		4^+	1168.4	1323.2(4)[o]	0.17(5)	19(6)		
(?)	2516.6(7)[cc]	0^+	675.6	[1841]	<0.03	<17	0.14(3)	19(4)
		2^+	828.66	1688.2(15)[p]	0.07(5)	32(25)	0.15(7)	20(9)
		2^+	890.50	1626.8(6)[p]	0.16(6)	80(30)	0.18(3)	24(4)
		3^+	1022.10	1493.8(10)	0.20(5)	100(25)	0.74(7)	99(9)
		4^+	1168.4	1348.9(5)	0.19(5)	95(25)	0.10(8)	13(11)
				[1297][v]			0.75(5)	100(7)
		3^-	1368.53	[1148]	<0.15	<75	0.12(5)	16(7)
		$(3)^-$	1609.4	[907]	<0.10	<50	0.29(5)	39(7)
(?)	2572.0(5)[q]	4^+	404.18	2168.9(7)[o,p]	0.23(8)	100(35)		
		$(4)^+$	1627.5	944.3(4)[o]	0.15(3)	65(13)		
(?)	2594.3(4)[q]	3^+	1022.10	1572.0(5)[o]	0.13(5)	62(25)		
		4^+	1168.4	1425.9(4)[o]	0.20(5)	100(25)		
		5^+	1335.51	1259.1(7)[o]	0.19(8)	95(40)		
(?)	2642.5(3)[q]	4^+	404.18	2238.3(2)[o]	0.77(13)	100(17)		
(?)	2653.4(6)[q]	4^+	404.18	2249(2)[o,p]	0.32(15)	100(47)		
		2^+	828.66	1824.7(6)[o]	0.20(5)	63(16)		
(?)	2757.8(6)[q]	3^+	1022.10	1735.7(5)[o]	0.18(5)	100(28)		
(?)	2788.1(9)[q]	8^+	1215.6	1572.5(8)[o]	0.08(2)	100(25)		
(?)	2810.4(6)[q]	4^+	404.18	2406.2(7)[o]	0.38(11)	100(29)		
		6^+	770.40	2039.9(10)[o,p]	0.11(4)	29(11)		
(?)	2818.4(2)	4^+	404.18	2414.2(2)[o]	1.60(18)	100(11)		
		6^+	770.40	2048.0(2)[o]	0.19(6)	12(4)		
		2^+	828.66	[1990]	<0.07	<4	0.21(9)	11(5)
		3^+	1022.10	[1796]	<0.13	<8	0.46(4)	25.0(22)
		4^+	1088.28	1730.1(2)	0.57(6)	36(4)	0.49(9)	27(5)
		4^+	1168.4	1649.7(2)	1.37(11)	86(7)	1.84(4)	100.0(22)
				[1525][v]			0.68(7)	37(4)
		5^+	1335.51	1482.7(2)[o]	0.30(5)	19(3)		
		3^-	1368.53	1450.0(8)[o,p]	0.15(6)	9(4)		
		6^+	1437.28	1380.9(2)[o]	0.65(6)	41(4)		
		6^+	1525.3	1293.4(15)[o]	0.27(4)	17(3)		
		(5^-)	1526.0	1292.3(3)[o]	0.87(11)	54(7)		
		$(4)^+$	1627.5	1191.1(5)	0.43(6)	27(4)	0.20(7)	11(4)
		(?)	1857.82	960.6(3)[o]	0.69(7)	43(4)		
		(6)	1898.5	919.7(15)[o]	0.13(5)	8(3)		
		(?)	1933.6	884.3(8)[o]	0.11(5)	7(3)		
(?)	2823.3(2)[dd]	4^+	404.18	2419.2(2)	3.3(3)	100(9)	2.93(6)	100.0(20)
		6^+	770.40	2052.8(2)[o]	0.69(11)	21(3)		
		2^+	828.66	[1994]	<0.07	<2	0.13(9)	4(3)
		2^+	890.50	[1932]	<0.11	<3	0.26(4)	8.9(14)
		4^+	1168.4	1654.0(11)[o,p]	0.14(6)	4.2(18)		
		(5^-)	1526.0	1297.3(2)[o]	0.33(8)	10(2)		
		(?)	1857.82	965.3(8)[o]	0.10(5)	3.0(15)		
(?)	2833.6(4)[q]	4^+	404.18	2429.5(7)[o]	0.63(9)	100(14)		
		6^+	770.40	2063.2(4)[o]	0.23(4)	37(6)		
(?)	2894.9(4)[q]	4^+	404.18	2490.7(6)[o]	0.21(7)	100(33)		

Transition				Experiment			Literature	
J_i^π [a]	E_i (keV)	J_f^π	E_f (keV)	E_γ (keV)	I	$I^{\rm rel}$	I [b]	$I^{\rm rel}$ [c]
		2^+	890.50	2004.2(9)[o,p]	0.10(4)	48(19)		
		3^+	1022.10	1872.9(4)[o]	0.21(5)	100(24)		
(?)	2981.5(13)[q]	4^+	404.18	2577.3(13)[o]	0.33(7)	100(21)		

[a] Level spin assignments are nominal assignments from the evaluation [24], except as noted.
[b] Literature values for absolute intensities are from the evaluated ^{156}Ho EC decay data of Ref. [24], which is based primarily upon Ref. [133], except as noted.
[c] Literature values for relative intensities are from the adopted γ radiations of the evaluation [24], except as noted. Where the evaluation [24] gives more than one possible adopted value, all are listed here.
[d] The literature γ-ray intensity is deduced from conversion electron data only, using an assumed conversion coefficient from Ref. [133].
[e] Listed in the evaluation [24] as 5.9, but the intensity and conversion coefficient given in the original literature [133] actually yield 1.9.
[f] Listed in the evaluation [24] as 7.2, but the intensity and conversion coefficient given in the original literature [133] actually yield 3.5. The evaluation also notes larger but ambiguous intensities reported in $(\alpha, 4n)$ [131].
[g] Transition was previously reported, but not in β decay.
[h] Relative intensity from $(\alpha, 4n)$ is listed in the evaluation [24] as 57, but the intensities given in the original literature [131] actually yield 45(14). The uncertainties from the original $(p, 4n)$ literature [132] are used here to obtain the value 11(2).
[i] Relative intensity from $(\alpha, 4n)$ is listed in the evaluation [24] as 370, but the intensities given in the original literature [131] actually yield 557(90).
[j] Relative intensity from $(\alpha, 4n)$ is listed in the evaluation [24] as 515. The uncertainties, and unrounded intensities, from the original literature [131] are used here to obtain 530(60).
[k] This is a literature $I^{\rm ce}$ value from conversion electron data from Ref. [133]. Ref. [133] makes no prediction for the corresponding γ-ray intensity since an unknown portion of the electron intensity may result from an $E0$ contribution.
[l] Level was previously reported, but not in β decay [24].
[m] Probable spin assignment for newly-identified level is given on the basis of observed transitions to levels of known spin.
[n] The level at 1382.3(2) keV may be identified with the adopted (3^-) level at 1385(5) keV [24] reported in (p, t) scattering [134].
[o] Gamma-ray line was not previously reported or was not reported in this placement.
[p] Identification of transition is tentative.
[q] Level was not previously reported.
[r] Energy and intensity are deduced from gated spectrum after subtraction of contribution(s) from other placement(s). (See also Table I.1.)
[s] Level is not identified as having been populated in β decay in the published literature [133] but is quoted as having been populated in an unpublished β-decay study [135].
[t] Transitions from the closely-spaced pair of levels at 1525.3(2) and 1526.0(2) keV are all potentially doublets. Each transition is assigned a primary placement as depopulating one of these levels on the basis of transition energy as measured in gated spectra but may contain a significant unresolved contribution depopulating the other member of the pair. (See text.)
[u] The placement here, reported in $(\alpha, 4n)$ [131], is noted by the evaluation [24] to be uncertain.
[v] A literature transition was reported to a level the existence of which is not supported by the present data. (See text.)
[w] Limit obtained on any possible absolute intensity coincident with the alleged 1310 keV transition from Ref. [131], which is claimed as the only branch from the literature $(2^+)_{1447}$ level. (See text.)
[x] The intensity for the adopted 178.93(20) keV branch is omitted in the evaluation [24], with an indication that the placement of the transition in the level scheme is uncertain. The relative intensity for this branch deduced from the original literature [131] is 133(43).
[y] Peak in gated spectrum has abnormally large width.
[z] The evaluation [24] does not deduce relative intensities for the 1039 and 594 keV branches. The 1039 keV branch was reported in (HI, xn), $(\alpha, 4n)$, and $(p, 4n)$ [131, 132, 136]. The 594 keV branch was only

reported in $(\alpha, 4n)$ and $(p, 4n)$ [131], and the line was noted by the authors to contain ^{127}I contamination.
[aa]The nominal spin assignment for the adopted level at 1898.64(10) keV [24] is $(6, 7^-)$. (See text.)
[bb]The level at 2408.7(4) keV may be identified with the adopted (2^-) level at 2409.64(20) keV [24] reported in β decay [133]. (See text.)
[cc]The level at 2516.6(7) keV may be identified with the adopted $(1)^-$ level at 2517.55(16) keV [24] reported in β decay [133]. (See text.)
[dd]The level at 2823.3(2) keV may be identified with the adopted level at 2822.2(4) keV [24] reported in β decay [133].

Bibliography

[1] P. A. M. Dirac, *The Principles of Quantum Mechanics*, No. 27 in *The International Series of Monographs on Physics* (Clarendon Press, Oxford, 1967), 4th (revised) ed.

[2] A. Messiah, *Quantum Mechanics* (Dover, Mineola, New York, 1999).

[3] K. L. G. Heyde, *The Nuclear Shell Model* (Springer-Verlag, Berlin, 1990).

[4] A. Bohr and B. R. Mottelson, *Nuclear Deformations*, Vol. 2 of *Nuclear Structure* (World Scientific, Singapore, 1998).

[5] J. M. Eisenberg and W. Greiner, *Nuclear Models: Collective and Single-Particle Phenomena*, Vol. 1 of *Nuclear Theory* (North-Holland, Amsterdam, 1987), 3rd ed.

[6] R. F. Casten, *Nuclear Structure from a Simple Perspective*, No. 23 in *Oxford Studies in Nuclear Phsics* (Oxford University Press, Oxford, 2000), 2nd ed.

[7] F. Iachello and A. Arima, *The Interacting Boson Model* (Cambridge University Press, Cambridge, 1987).

[8] D. D. Warner and R. F. Casten, Phys. Rev. C **28**, 1798 (1983).

[9] P. O. Lipas, P. Toivonen, and D. D. Warner, Phys. Lett. B **155**, 295 (1985).

[10] R. F. Casten and J. A. Cizewski, Nucl. Phys. A **309**, 477 (1978).

[11] J. N. Ginocchio and M. W. Kirson, Phys. Rev. Lett. **44**, 1744 (1980).

[12] A. E. L. Dieperink, O. Scholten, and F. Iachello, Phys. Rev. Lett. **44**, 1747 (1980).

[13] R. F. Casten, Nucl. Phys. A **443**, 1 (1985).

[14] R. F. Casten and N. V. Zamfir, J. Phys. G **22**, 1521 (1996).

[15] P. Federman and S. Pittel, Phys. Lett. B **69**, 385 (1977).

[16] P. Federman and S. Pittel, Phys. Lett. B **77**, 29 (1978).

[17] A. Wolf and R. F. Casten, Phys. Rev. C **36**, 851 (1987).

[18] J. K. Tuli, Nucl. Data Sheets **56**, 607 (1989).

[19] L. K. Peker and J. K. Tuli, Nucl. Data Sheets **82**, 187 (1997).

[20] M. R. Bhat, Nucl. Data Sheets **89**, 797 (2000).

[21] E. der Mateosian and J. K. Tuli, Nucl. Data Sheets **75**, 827 (1995).

[22] A. Artna-Cohen, Nucl. Data Sheets **79**, 1 (1996).

[23] C. W. Reich and R. G. Helmer, Nucl. Data Sheets **85**, 171 (1998).

[24] R. G. Helmer, Nucl. Data Sheets **49**, 383 (1986); **65**, 65 (1992).

[25] R. G. Helmer, Nucl. Data Sheets **77**, 471 (1996).

[26] C. W. Reich, Nucl. Data Sheets **78**, 547 (1996).

[27] R. G. Helmer and C. W. Reich, Nucl. Data Sheets **87**, 317 (1999).

[28] R. F. Casten, M. Wilhelm, E. Radermacher, N. V. Zamfir, and P. von Brentano, Phys. Rev. C **57**, R1553 (1998).

[29] N. V. Zamfir, R. F. Casten, M. A. Caprio, C. W. Beausang, R. Krücken, J. R. Novak, J. R. Cooper, G. Cata-Danil, and C. J. Barton, Phys. Rev. C **60**, 054312 (1999).

[30] F. Iachello, N. V. Zamfir, and R. F. Casten, Phys. Rev. Lett. **81**, 1191 (1998).

[31] J. Jolie, P. Cejnar, and J. Dobeš, Phys. Rev. C **60**, 061303(R) (1999).

[32] R. F. Casten, N. V. Zamfir, and D. S. Brenner, Phys. Rev. Lett. **71**, 227 (1993).

[33] A. Wolf, R. F. Casten, N. V. Zamfir, and D. S. Brenner, Phys. Rev. C **49**, 802 (1994).

[34] N. V. Zamfir, P. von Brentano, R. F. Casten, and J. Jolie, Phys. Rev. C **66**, 021304(R) (2002).

[35] F. Iachello, Phys. Rev. Lett. **85**, 3580 (2000).

[36] F. Iachello, Phys. Rev. Lett. **87**, 052502 (2001).

[37] R. F. Casten and N. V. Zamfir, Phys. Rev. Lett. **85**, 3584 (2000).

[38] R. F. Casten and N. V. Zamfir, Phys. Rev. Lett. **87**, 052503 (2001).

[39] R. Krücken, B. Albanna, C. Bialik, R. F. Casten, J. R. Cooper, A. Dewald, N. V. Zamfir, C. J. Barton, C. W. Beausang, M. A. Caprio, A. A. Hecht, T. Klug, J. R. Novak, N. Pietralla, and P. von Brentano, Phys. Rev. Lett. **88**, 232501 (2002).

[40] J. M. Arias, Phys. Rev. C **63**, 034308 (2001).

[41] A. Frank, C. E. Alonso, and J. M. Arias, Phys. Rev. C **65**, 014301 (2001).

[42] F. Iachello, in *Testimonios por Marcos Moshinsky*, edited by A. Frank and K. B. Wolf (Edicion UNAM, Mexico, 2001), p. 107.

[43] M. A. Caprio, in Ref. [257], p. 17.

[44] H. R. McK. Hyder, J. McKay, P. D. Parker, and D. A. Bromley, Nucl. Instrum. Methods A **268**, 285 (1988).

[45] J. Ashenfelter, Pramana J. Phys. **59**, 713 (2002).

[46] P. W. Schmor, in *Proceedings of the 1999 Particle Accelerator Conference*, edited by A. Luccio and W. MacKay (IEEE, Piscataway, NJ, 1999), p. 508.

[47] J. O. Newton, in Ref. [258], p. 185.

[48] R. S. Hager and E. C. Seltzer, Nucl. Data A **4**, 1 (1968).

[49] F. K. McGowan and P. H. Stelson, in Ref. [258], p. 4.

[50] D. Cline, Annu. Rev. Nucl. Part. Sci. **36**, 683 (1986).

[51] P. J. Nolan and J. Sharpey-Schafer, Rep. Prog. Phys. **42**, 1 (1979).

[52] K. Heyde, *Basic Ideas and Concepts in Nuclear Physics* (Institute of Physics Publishing, Bristol, 1994).

[53] J. M. Eisenberg and W. Greiner, *Excitation Mechanisms of the Nucleus*, Vol. 2 of *Nuclear Theory* (North-Holland, Amsterdam, 1988), 3rd, revised ed.

[54] S. A. Moskowski, in Ref. [259], p. 863.

[55] P. F. Zweifel, Phys. Rev. **96**, 1572 (1954); **107**, 329(E) (1957).

[56] A. Gavron, Phys. Rev. C **21**, 230 (1980).

[57] A. Gavron, computer code `PACE` (unpublished).

[58] N. V. Zamfir and R. F. Casten, J. Res. Natl. Inst. Stand. Technol. **105**, 147 (2000).

[59] M. A. Caprio, N. V. Zamfir, R. F. Casten, C. J. Barton, C. W. Beausang, J. R. Cooper, A. A. Hecht, R. Krücken, H. Newman, J. R. Novak, N. Pietralla, A. Wolf, and K. E. Zyromski, Rom. J. Phys. **46**, 41 (2001).

[60] G. Duchêne, F. A. Beck, P. Twin, G. de France, D. Curien, L. Han, C. W. Beausang, M. A. Bentley, P. J. Nolan, and J. Simpson, Nucl. Instrum. Methods A **432**, 90 (1999).

[61] C. W. Beausang, C. J. Barton, M. A. Caprio, R. F. Casten, J. R. Cooper, R. Krücken, B. Liu, J. R. Novak, Z. Wang, M. Wilhelm, A. N. Wilson, N. V. Zamfir, and A. Zilges, Nucl. Instrum. Methods A **452**, 431 (2000).

[62] B. E. Tomlin, C. J. Barton, N. V. Zamfir, M. A. Caprio, R. L. Gill, R. Krücken, J. R. Novak, J. R. Cooper, K. E. Zyromski, G. Cata-Danil, C. W. Beausang, A. Wolf, N. A. Pietralla, H. Newman, J. Cederkäll, B. Liu, Z. Wang, R. F. Casten, and D. S. Brenner, Phys. Rev. C **63**, 034314 (2001).

[63] D. S. Brenner, C. J. Barton, N. V. Zamfir, M. A. Caprio, A. Aprahamian, C. W. Beausang, Z. Berant, R. F. Casten, J. R. Cooper, R. L. Gill, R. Krücken, J. R. Novak, N. Pietralla, M. Shawcross, A. Teymurazyan, A. Wolf, and M. Wiescher, in *Proceedings of the Eleventh International Symposium on Capture Gamma-Ray Spectroscopy and Related Topics* (World Scientific, in press).

[64] A. Wolf, N. V. Zamfir, M. A. Caprio, Z. Berant, D. S. Brenner, N. Pietralla, R. L. Gill, R. F. Casten, C. W. Beausang, R. Krücken, K. E. Zyromski, C. J. Barton, J. R. Cooper, A. A. Hecht, H. Newman, J. R. Novak, and J. Cederkäll, Phys. Rev. C **66**, 024323 (2002).

[65] N. Pietralla *et al.* (unpublished).

[66] J. M. D'Auria, Nucl. Instrum. Methods B **99**, 330 (1995).

[67] D. Habs, O. Kester, K. Rudolph, P. Thirolf, G. Hinderer, E. Nolte, G. Bollen, H. Raimbault-Hartmann, H. Ravn, F. Ames, L. Liljeby, K. G. Rensfelt, D. Schwalm, R. von Hahn, R. Repnow, A. Schempp, U. Ratzinger, P. V. Duppen, M. Huyse, and G. Walter, Nucl. Instrum. Methods B **126**, 218 (1997).

[68] G. D. Alton and J. R. Beene, J. Phys. G **24**, 1347 (1998).

[69] E. Hagberg, T. K. Alexander, I. Neeson, V. T. Koslowsky, G. C. Ball, G. R. Dyck, J. S. Forster, J. C. Hardy, J. R. Leslie, H.-B. Mak, H. Schmeing, and I. S. Towner, Nucl. Phys. A **571**, 555 (1994).

[70] G. C. Ball, S. Bishop, J. A. Behr, G. C. Boisvert, P. Bricault, J. Cerny, J. M. D'Auria, M. Dombsky, J. C. Hardy, V. Iacob, J. R. Leslie, T. Lindner, J. A. MacDonald, H.-B. Mak, D. M. Moltz, J. Powell, G. Savard, and I. S. Towner, Phys. Rev. Lett. **86**, 1454 (2001).

[71] M. Dombsky, D. Bishop, P. Bricault, D. Dale, A. Hurst, K. Jayamanna, R. Keitel, M. Olivo, P. Schmor, and G. Stanford, Rev. Sci. Instrum. **71**, 978 (2000).

[72] S. Ritt and P.-A. Amaudruz, *The Midas DAQ system: A versatile and compact data acquisition system* (unpublished).

[73] D. Shapira, T. A. Lewis, and L. D. Hulett, Nucl. Instrum. Methods A **454**, 409 (2000).

[74] C. J. Gross, T. N. Ginter, D. Shapira, W. Milner, J. W. McConnell, A. N. James, J. Johnson, J. Mas, P. F. Mantica, R. L. Auble, J. J. Das, J. L. Blankenship, J. H. Hamilton, R. L. Robinson, Y. A. Akovali, C. Baktash, J. C. Batchelder, C. R. Bingham, M. J. Brinkman, H. K. Carter, R. A. Cunningham, T. Davinson, J. D. Fox, A. Galindo-Uribarri, R. Grzywacz, J. F. Liang, B. D. MacDonald, J. MacKenzie, S. D. Paul, A. Piechaczek, D. C. Radford, A. V. Ramayya, W. Reviol, D. Rudolph, K. Rykaczewski, K. S. Toth, W. Weintraub, C. Williams, P. J. Woods, C.-H. Yu, and E. F. Zganjar, Nucl. Instrum. Methods A **450**, 12 (2000).

[75] D. Habs, D. Rudolph, P. Thirolf, C. Fischbeck, C. Gund, D. Schwalm, J. Eberth, E. Grosse, H. Prade, H. Emling, J. Gerl, R. M. Lieder, P. V. Duppen, C. Rossi-Alvarez, and M. Pignanelli, Prog. Part. Nucl. Phys. **38**, 111 (1997).

[76] F. W. N. de Boer, P. F. A. Goudsmit, B. J. Meijer, P. Koldewijn, J. Konijn, and R. Beetz, Nucl. Phys. A **236**, 349 (1974).

[77] M. A. Caprio, N. V. Zamfir, R. F. Casten, C. J. Barton, C. W. Beausang, J. R. Cooper, A. A. Hecht, R. Krücken, H. Newman, J. R. Novak, N. Pietralla, A. Wolf, and K. E. Zyromski, Phys. Rev. C **66**, 054310 (2002).

[78] L. C. Biedenharn and M. E. Rose, Rev. Mod. Phys. **25**, 729 (1953).

[79] L. W. Fagg and S. S. Hanna, Rev. Mod. Phys. **31**, 711 (1959).

[80] H. Frauenfelder, R. M. Steffen, S. R. de Groot, H. A. Tolhoek, and W. J. Huiskamp, in Ref. [259], p. 997.

[81] R. Stump, Phys. Rev. **86**, 249 (1952).

[82] D. R. Hamilton, A. Lemonick, and F. M. Pipkin, Phys. Rev. **92**, 1191 (1953).

[83] M. Asai, K. Kawade, M. Shibata, Y. Kojima, A. Osa, M. Koizumi, and T. Sekine, Nucl. Instrum. Methods A **463**, 205 (2002).

[84] S. Frankel, Phys. Rev. **83**, 673 (1951).

[85] M. E. Rose, Phys. Rev. **91**, 610 (1953), but see Ref. [86] for correct expression for $x(\beta)$.

[86] M. J. L. Yates, in Ref. [259], p. 1691.

[87] A. M. Feingold and S. Frankel, Phys. Rev. **97**, 1025 (1955).

[88] P. M. Jones, L. Wei, F. A. Beck, P. A. Butler, T. Byrski, G. Duchêne, G. de France, F. Hannachi, G. D. Jones, and B. Kharraja, Nucl. Instrum. Methods A **362**, 556 (1995).

[89] L. M. Garcia-Raffi, J. L. Taín, J. Bea, A. Gadea, J. Rico, and B. Rubio, Nucl. Instrum. Methods A **391**, 461 (1997).

[90] P. A. Butler, P. E. Carr, L. L. Gadeken, A. N. James, P. J. Nolan, J. F. Sharpey-Schafer, P. J. Twin, and D. A. Viggars, Nucl. Instrum. Methods **108**, 497 (1973).

[91] H. Mach, R. L. Gill, and M. Moszyński, Nucl. Instrum. Methods A **280**, 49 (1989).

[92] M. Moszyński and H. Mach, Nucl. Instrum. Methods A **277**, 407 (1989).

[93] H. Mach, F. K. Wohn, G. Molnár, K. Sistemich, J. C. Hill, M. Moszyński, R. L. Gill, W. Krips, and D. S. Brenner, Nucl. Phys. A **523**, 197 (1991).

[94] G. Knop and W. Paul, in Ref. [260], p. 1.

[95] G. F. Knoll, *Radiation Detection and Measurement* (John Wiley & Sons, New York, 1989), 2nd ed.

[96] B. Bengtson and M. Moszyński, Nucl. Instrum. Methods **117**, 227 (1974).

[97] M. Laval, M. Moszyński, R. Allemand, E. Cormoreche, P. Guinet, R. Odru, and J. Vacher, Nucl. Instrum. Methods **206**, 169 (1983).

[98] J. D. McGervey, J. Vogel, P. Sen, and C. Knox, Nucl. Instrum. Methods **143**, 435 (1977).

[99] B. Bengtson and M. Moszynski, Nucl. Instrum. Methods **204**, 129 (1982).

[100] T. Morikawa, M. Oshima, T. Sekine, Y. Hatsukawa, S. Ichikawa, H. Iimura, A. Osa, M. Shibata, and A. Taniguchi, Phys. Rev. C **46**, R6 (1992).

[101] P. F. Mantica and W. B. Walters, Phys. Rev. C **53**, R2586 (1996).

[102] H. Mach and B. Fogelberg, in *Proceedings of the International Workshop on Research with Fission Fragments*, edited by T. von Egidy, D. Habs, F. J. Hartmann, K. E. G. Löbner, and H. Nifenecker (World Scientific, Singapore, 1997), p. 211.

[103] M. Eldrup, J. Phys. IV (Paris) **5**(C1), 93 (1995).

[104] P. K. Joshi, P. F. Mantica, S. J. Robinson, R. L. Gill, and E. F. Zganjar, Nucl. Instrum. Methods A **335**, 461 (1993).

[105] W. Klamra, T. Lindblad, M. Moszyński, and L. O. Norlin, Nucl. Instrum. Methods A **254**, 85 (1987).

[106] GE Silicones, Viscasil 100M, polydimethylsiloxane fluid.

[107] 3M Corporation, Product Number 3075, 51 μm polypropylene film.

[108] L. Boström, B. Olsen, W. Schneider, and E. Matthias, Nucl. Instrum. Methods **44**, 61 (1966).

[109] B. Olsen and L. Boström, Nucl. Instrum. Methods **44**, 65 (1966).

[110] H. Motz and G. Bäckström, in Ref. [260], p. 769.

[111] D. Breitig, R. F. Casten, and G. W. Cole, Phys. Rev. C **9**, 366 (1974); **9**, 2088(E) (1974).

[112] J. W. Knowles, in Ref. [260], p. 203.

[113] G. L. Greene, E. G. Kessler, Jr., R. D. Deslattes, and H. Börner, Phys. Rev. Lett. **56**, 819 (1986).

[114] M. S. Dewey, E. G. Kessler, Jr., G. L. Greene, R. D. Deslattes, H. Börner, and J. Jolie, Nucl. Instrum. Methods A **284**, 151 (1989).

[115] H. G. Börner and J. Jolie, J. Phys. G **19**, 217 (1993).

[116] H. G. Börner, M. Jentschel, N. V. Zamfir, R. F. Casten, M. Krticka, and W. Andrejtscheff, Phys. Rev. C **59**, 2432 (1999).

[117] L. L. Riedinger, N. R. Johnson, and J. H. Hamilton, Phys. Rev. **179**, 1214 (1969).

[118] J. H. Bjerregaard, O. Hansen, O. Nathan, and S. Hinds, Nucl. Phys. **86**, 145 (1966).

[119] W. McLatchie, W. Darcey, and J. E. Kitching, Nucl. Phys. A **159**, 615 (1970).

[120] P. Debenham and N. M. Hintz, Nucl. Phys. A **195**, 385 (1972).

[121] J. L. Wood, E. F. Zganjar, C. de Coster, and K. Heyde, Nucl. Phys. A **651**, 323 (1999).

[122] N. V. Zamfir, H. G. Börner, N. Pietralla, R. F. Casten, Z. Berant, C. J. Barton, C. W. Beausang, D. S. Brenner, M. A. Caprio, J. R. Cooper, A. A. Hecht, M. Krtička, R. Krücken, P. Mutti, J. R. Novak, and A. Wolf, Phys. Rev. C **65**, 067305 (2002).

[123] T. Klug, A. Dewald, V. Werner, P. von Brentano, and R. F. Casten, Phys. Lett. B **495**, 55 (2000).

[124] R. A. Meyer, Fizika (Zagreb) **22**, 153 (1990).

[125] N. M. Stewart, E. Eid, M. S. S. El-Daghmah, and J. K. Jabber, Z. Phys. A **335**, 13 (1990).

[126] I. A. Fraser, J. S. Greenberg, S. H. Sie, R. G. Stokstad, G. A. Burginyon, and D. A. Bromley, Phys. Rev. Lett. **23**, 1047 (1969).

[127] J. Goswamy, B. Chand, D. Mehta, N. Singh, and P. N. Trehan, Appl. Radiat. Isot. **42**, 1025 (1991).

[128] R. Krücken, in *Proceedings of the Sixteenth International Conference on Applications of Accelerators in Research and Industry*, edited by J. L. Duggan and I. L. Moran, AIP Conf. Proc. **576** (AIP, Melville, NY, 2001), p. 319.

[129] T. Seo, Nucl. Instrum. Methods A **325**, 176 (1993).

[130] F. Iachello (in preparation).

[131] F. W. N. de Boer, P. Koldewijn, R. Beetz, J. L. Maarleveld, J. Konij, R. Janssens, and J. Vervier, Nucl. Phys. A **290**, 173 (1977).

[132] Y. El Masri, J. M. Ferté, R. Janssens, C. Michel, P. Monseu, J. Steyaert, and J. Vervier, Nucl. Phys. **271**, 133 (1976).

[133] K. Y. Gromov, Z. T. Zhelev, K. Zuber, Y. Zuber, T. A. Islamov, V. V. Kuznetsov, H.-G. Ortlepp, and A. V. Potempa, Acta Phys. Pol. B **7**, 507 (1976).

[134] J. J. Kolata and M. Oothoudt, Phys. Rev. C **15**, 1947 (1977).

[135] P. Koldewijn, F. W. N. de Boer, B. J. Meijer, and J. Konijn, as quoted in Ref. [131].

[136] M. A. Riley, J. Simpson, J. F. Sharpey-Schafer, J. R. Cresswell, H. W. Cranmer-Gordon, P. D. Forsyth, D. Howe, A. H. Nelson, P. J. Nolan, P. J. Smith, N. J. Ward, J. C. Lisle, E. Paul, and P. M. Walker, Nucl. Phys. A **486**, 456 (1988).

[137] T. Grotdal, K. Nybø, T. Thorsteinsen, and B. Elbek, Nucl. Phys. A **110**, 385 (1968).

[138] J. Blachot and G. Marguier, Nucl. Data Sheets **73**, 81 (1994).

[139] E. A. McCutchan *et al.* (in preparation).

[140] M. A. Caprio, N. V. Zamfir, E. A. McCutchan, R. F. Casten, Z. Berant, H. Amro, C. J. Barton, C. W. Beausang, D. S. Brenner, J. R. Cooper, R. L. Gill, G. Gürdal, A. A. Hecht, C. Hutter, R. Krücken, D. A. Meyer, J. R. Novak, N. Pietralla, P. H. Regan, and J. J. Ressler, Eur. Phys. J. A **16**, 177 (2003).

[141] H. Backe, L. Richter, R. Willwater, E. Kankeleit, E. Kuphal, Y. Nakayama, and B. Martin, Z. Phys. A **285**, 159 (1978).

[142] F. K. McGowan, N. R. Johnson, C. Baktash, I. Y. Lee, Y. Schutz, J. C. Wells, and A. Larabee, Nucl. Phys. A **539**, 276 (1992).

[143] B. Bochev, S. A. Karamian, R. Kutsarova, E. Nadjakov, and Y. T. Oganessian, Nucl. Phys. A **267**, 344 (1976).

[144] G. Böhm, A. Dewald, P. Petkov, and P. von Brentano, Nucl. Instrum. Methods A **329**, 248 (1993).

[145] D. R. Zolnowski, M. B. Hughes, J. Hunt, and T. T. Sugihara, Phys. Rev. C **21**, 2556 (1980).

[146] J. Stachel, P. Van Isacker, and K. Heyde, Phys. Rev. C **25**, 650 (1982).

[147] D. Bucurescu, G. Căta, D. Cutoiu, G. Constantinescu, M. Ivaşcu, and N. V. Zamfir, Z. Phys. A **324**, 387 (1986); **327**, 241(E) (1987).

[148] Feng Pan and J. P. Draayer, Nucl. Phys. A **636**, 156 (1998).

[149] P. Van Isacker and G. Puddu, Nucl. Phys. A **348**, 125 (1980).

[150] K. Kim, A. Gelberg, T. Mizusaki, T. Otsuka, and P. von Brentano, Nucl. Phys. A **604**, 163 (1996).

[151] A. Giannatiempo, A. Nannini, and P. Sona, Phys. Rev. C **58**, 3316 (1998).

[152] O. K. Vorov and V. G. Zelevinsky, Nucl. Phys. A **439**, 207 (1985).

[153] D. de Frenne and E. Jacobs, Nucl. Data Sheets **83**, 535 (1998).

[154] N. V. Zamfir, M. A. Caprio, R. F. Casten, C. J. Barton, C. W. Beausang, Z. Berant, D. S. Brenner, W. T. Chou, J. R. Cooper, A. A. Hecht, R. Krücken, H. Newman, J. R. Novak, N. Pietralla, A. Wolf, and K. E. Zyromski, Phys. Rev. C **65**, 044325 (2002).

[155] J. Wouters, D. Vandeplassche, E. van Walle, N. Severijns, and L. Vanneste, Nucl. Instrum. Methods B **26**, 463 (1987).

[156] J. A. Grau, L. E. Samuelson, F. A. Rickey, P. C. Simms, and G. J. Smith, Phys. Rev. C **14**, 2297 (1976).

[157] J. Lange, A. T. Kandil, J. Neuber, C. D. Uhlhorn, H. von Buttlar, and A. Bockisch, Nucl. Phys. A **292**, 301 (1977).

[158] M. Luontama, R. Julin, J. Kantele, A. Passoja, W. Trzaska, A. Bäcklin, N.-G. Jonsson, and L. Westerberg, Z. Phys. A **324**, 317 (1986).

[159] K. Cornelis, G. Lhersonneau, M. Huyse, D. Vandeplassche, and J. Verplancke, Z. Phys. A **292**, 403 (1979).

[160] K. Cornelis, E. Coenen, M. Huyse, G. Lhersonneau, and J. Verplancke, in *Proceedings of the 4th International Conference on Nuclei Far From Stability*, edited by L. O. Skolen, CERN Proc. **81-09** (CERN, Geneva, 1981).

[161] K. Farzin, J. Lange, M. L. Narasimha Raju, and H. von Buttlar, in *Structure of Medium-Heavy Nuclei*, edited by G. S. Anagnostatos *et al.*, IOP Conf. Series **49** (IOP, Bristol, 1980), p. 259.

[162] K. Farzin, H. Hardenberg, H. Möllman, K. Uebelgünn, and H. v. Buttlar, Z. Phys. A **326**, 401 (1987).

[163] J. L. Wood, K. Heyde, W. Nazarewicz, M. Huyse, and P. van Duppen, Phys. Rep. **215**, 101 (1992).

[164] P. E. Garrett, J. Phys. G **27**, R1 (2001).

[165] R. F. Casten, P. von Brentano, and N. V. Zamfir, Phys. Rev. C **49**, 1940 (1994).

[166] R. F. Casten and P. von Brentano, Phys. Rev. C **50**, R1280 (1994).

[167] A. Aprahamian, R. C. de Haan, H. G. Börner, H. Lehmann, C. Doll, M. Jentschel, A. M. Bruce, and R. Piepenbring, Phys. Rev. C **65**, 031301(R) (2002).

[168] P. E. Garrett, M. Kadi, C. A. McGrath, V. Sorokin, Min Li, Minfang Yeh, and S. W. Yates, Phys. Lett. B **400**, 250 (1997).

[169] R. M. Ronningen, R. S. Grantham, J. H. Hamilton, R. B. Piercey, A. V. Ramayya, B. van Nooijen, H. Kawakami, W. Lourens, R. S. Lee, W. K. Dagenhart, and L. L. Riedinger, Phys. Rev. C **26**, 97 (1982).

[170] R. F. Casten, D. S. Brenner, N. V. Zamfir, R. L. Gill, B. Liu, C. Barton, and G. Cata-Danil, *Studies of multi-phonon states via β-decay*, TRIUMF research proposal, 1997 (unpublished).

[171] P. E. Garrett, M. Kadi, Min Li, C. A. McGrath, V. Sorokin, Minfang Yeh, and S. W. Yates, Phys. Rev. Lett. **78**, 4545 (1997).

[172] W. F. Davidson, D. D. Warner, R. F. Casten, K. Schreckenbach, H. G. Börner, J. Simić, M. Stojanović, M. Bogdanović, S. Koički, W. Gelletly, G. B. Orr, and M. L. Stelts, J. Phys. G **7**, 455 (1981); **7**, 843(E) (1981).

[173] H. Börner, J. Jolie, S. J. Robinson, B. Krusche, R. Piepenbring, R. F. Casten, A. Aprahamian, and J. P. Draayer, Phys. Rev. Lett. **66**, 691 (1991); **66**, 2837(E) (1991).

[174] H. Lehmann, J. Jolie, F. Corminboeuf, H. G. Börner, C. Doll, M. Jentschel, R. F. Casten, and N. V. Zamfir, Phys. Rev. C **57**, 569 (1998).

[175] M. A. Caprio, N. V. Zamfir, R. F. Casten, G. C. Ball, K. P. Jackson, P.-A. Amaudruz, and J.-C. Thomas, Phys. Rev. C **66**, 014307 (2002).

[176] P. D. Cottle and N. V. Zamfir, Phys. Rev. C **54**, 176 (1996).

[177] H. Strusny, H. Tyroff, E. Herrmann, G. Musiol, F. Molnar, A. A. Abdurazakov, G. Beyer, K. Y. Gromov, T. A. Islamov, M. Jachim, H.-U. Siebert, and S. A. Usmanova, Czech. J. Phys. B **25**, 626 (1975).

[178] V. A. Morozov, T. M. Muminov, and A. B. Khalikulov, JINR P6-5201, 1970 (unpublished).

[179] R. M. Ronningen, R. B. Piercey, J. H. Hamilton, C. F. Maguire, A. V. Ramayya, H. Kawakami, B. van Nooijen, R. S. Grantham, W. K. Dagenhart, and L. L. Riedinger, Phys. Rev. C **16**, 2218 (1979).

[180] Z. Berant *et al.* (private communication).

[181] K. Alder, A. Bohr, T. Huus, B. Mottelson, and A. Winther, Rev. Mod. Phys. **28**, 432 (1956).

[182] K. Alder and A. Winther, *Electromagnetic Excitation* (North-Holland, Amsterdam, 1975).

[183] D. A. Bell, C. E. Aveledo, M. G. Davidson, and J. P. Davidson, Can. J. Phys. **48**, 2542 (1970).

[184] A. Faessler, W. Greiner, and R. K. Sheline, Nucl. Phys. **70**, 33 (1965).

[185] P. O. Lipas, Nucl. Phys. **39**, 468 (1962).

[186] D. D. Warner, R. F. Casten, and W. F. Davidson, Phys. Rev. C **24**, 1713 (1981).

[187] W.-T. Chou, N. V. Zamfir, and R. F. Casten, Phys. Rev. C **56**, 829 (1997).

[188] P. O. Tjøm and B. Elbek, Nucl. Phys. A **107**, 385 (1968).

[189] F. W. N. de Boer *et al.*, Nucl. Phys. A **169**, 577 (1971).

[190] G. Gneuss, U. Mosel, and W. Greiner, Phys. Lett. B **30**, 397 (1969).

[191] G. Gneuss, U. Mosel, and W. Greiner, Phys. Lett. B **31**, 269 (1970).

[192] G. Gneuss and W. Greiner, Nucl. Phys. A **171**, 449 (1971).

[193] A. Bohr, Mat. Fys. Medd. Dan. Vid. Selsk. **26**(14) (1952).

[194] P. O. Hess, J. Maruhn, and W. Greiner, J. Phys. G **7**, 737 (1981).

[195] K. Kumar and M. Baranger, Nucl. Phys. A **92**, 608 (1967).

[196] D. Troltenier, P. O. Hess, and J. A. Maruhn, in *Computational Nuclear Physics 1: Nuclear Structure*, edited by K. Langanke, J. A. Maruhn, and S. E. Koonin (Springer-Verlag, Berlin, 1991), p. 105.

[197] P. O. Hess, M. Seiwert, J. Maruhn, and W. Greiner, Z. Phys. A **296**, 147 (1980).

[198] F. J. Margetan and S. A. Williams, Phys. Rev. C **25**, 1602 (1982).

[199] U. Mosel and W. Greiner, Z. Phys. **217**, 256 (1968).

[200] K. Kumar, Nucl. Phys. A **231**, 189 (1974).

[201] J. M. Eisenberg and W. Greiner, *Microscopic Theory of the Nucleus*, Vol. 3 of *Nuclear Theory* (North-Holland, Amsterdam, 1976), 2nd ed.

[202] L. von Bernus, A. Kappatsch, V. Rezwani, W. Scheid, U. Schneider, M. Sedlmayr, and R. Sedlmayr, in *Heavy-Ion, High-Spin States and Nuclear Structure* (IAEA, Vienna, 1975), Vol. 2, p. 3.

[203] Jing-ye Zhang, R. F. Casten, and N. V. Zamfir, Phys. Lett. B **407**, 201 (1997).

[204] D. Troltenier, J. P. Draayer, B. R. S. Babu, J. H. Hamilton, A. V. Ramayya, and V. E. Oberacker, Nucl. Phys. A **601**, 56 (1996).

[205] K. Starosta *et al.* (in preparation).

[206] P. Petkov, A. Dewald, and W. Andrejtscheff, Phys. Rev. C **51**, 2511 (1995).

[207] L. von Bernus, diploma thesis, Univ. Frankfurt am Main (1971), as quoted in Ref. [208].

[208] D. Habs, H. Klewe-Nebenius, K. Wisshak, R. Löhken, G. Nowicki, and H. Rebel, Z. Phys. **267**, 149 (1974).

[209] W. Greiner, Z. Phys. **172**, 386 (1963).

[210] H. L. Acker, dissertation, Phys. Inst. Univ. Freiburg/Breisgau (1965), as quoted in Ref. [5].

[211] M. A. Caprio, R. F. Casten, and J. Jolie, Phys. Rev. C **65**, 034304 (2002).

[212] Jing-Ye Zhang, N. V. Zamfir, R. F. Casten, and M. A. Caprio, Phys. Rev. C **64**, 017302 (2001).

[213] M. A. Caprio, Phys. Rev. C **65**, 031304(R) (2002).

[214] D. R. Bès, Nucl. Phys. **10**, 373 (1959).

[215] S. Flügge, *Practical Quantum Mechanics I*, Vol. 177 of *Grundlehren der mathematischen Wissenschaften* (Springer-Verlag, Berlin, 1971).

[216] G. B. Arfken and H. J. Weber, *Mathematical Methods for Physicists* (Academic Press, San Diego, 1995), 4th ed.

[217] M. Abramowitz and I. A. Stegun, *Handbook of Mathematical Functions* (Dover, New York, 1965).

[218] A. Arima and F. Iachello, Ann. Phys. (N.Y.) **123**, 468 (1979).

[219] O. Scholten, F. Iachello, and A. Arima, Ann. Phys. (N.Y.) **115**, 325 (1978).

[220] D. Ward, H. R. Andrews, O. Häusser, Y. El Masri, M. M. Aléonard, I. Yang-Lee, R. M. Diamond, F. S. Stephens, and P. A. Butler, Nucl. Phys. A **332**, 433 (1979).

[221] H. Emling, E. Grosse, R. Kulessa, D. Schwalm, and H. J. Wollersheim, Nucl. Phys. A **419**, 187 (1984).

[222] T. Kishimoto and T. Tamura, Nucl. Phys. A **270**, 317 (1976).

[223] Jing-Ye Zhang, M. A. Caprio, N. V. Zamfir, and R. F. Casten, Phys. Rev. C **60**, 061304(R) (1999).

[224] E. Chacón, M. Moshinsky, and R. T. Sharp, J. Math. Phys. **17**, 668 (1976).

[225] E. Chacón and M. Moshinsky, J. Math. Phys. **18**, 870 (1977).

[226] T. M. Corrigan, F. J. Margetan, and S. A. Williams, Phys. Rev. C **14**, 2279 (1976).

[227] A. Gheorghe, A. A. Răduţă, and V. Ceauşescu, Nucl. Phys. A **296**, 228 (1978).

[228] A. Arima and F. Iachello, Ann. Phys. (N.Y.) **99**, 253 (1976).

[229] L. Wilets and M. Jean, Phys. Rev. **102**, 788 (1956).

[230] G. Rakavy, Nucl. Phys. **4**, 289 (1957).

[231] A. Arima and F. Iachello, Ann. Phys. (N.Y.) **111**, 201 (1978).

[232] I. S. Gradshteyn and I. M. Ryzhik, *Table of Integrals, Series, and Products* (Academic Press, Boston, 1994), 5th ed.

[233] M. E. Rose, *Elementary Theory of Angular Momentum* (John Wiley & Sons, New York, 1957).

[234] A. R. Edmonds, *Angular Momentum in Quantum Mechanics* (Princeton University Press, Princeton, New Jersey, 1960), 2nd ed.

[235] A. Bohr and B. R. Mottelson, *Single-Particle Motion*, Vol. 1 of *Nuclear Structure* (World Scientific, Singapore, 1998).

[236] V. F. Weisskopf, Phys. Rev. **83**, 1073 (1951).

[237] H. A. Wapstra, G. J. Nijgh, and R. van Leishout, *Nuclear Spectroscopy Tables* (North-Holland, Amsterdam, 1959).

[238] M. Ferentz and N. Rosenzweig, in Ref. [259], p. 1687.

[239] J. Weneser and D. R. Hamilton, Phys. Rev. **92**, 321 (1953).

[240] G. R. Satchler, Phys. Rev. **94**, 1304 (1954).

[241] K. S. Krane and R. M. Steffen, Phys. Rev. C **2**, 724 (1970).

[242] M. R. Spiegel, *Mathematical Handbook of Formulas and Tables* (McGraw Hill, New York, 1968).

[243] J. J. Ressler, R. Krücken, C. W. Beausang, J. M. D'Auria, H. Amro, R. F. Casten, M. A. Caprio, G. Gürdal, Z. Harris, C. Hutter, A. A. Hecht, D. Meyer, M. Sciaccitano, and N. V. Zamfir, in Ref. [257], p. 125.

[244] M. A. Caprio and J. J. Ressler, `cscan` sorting package and site-specific routines (unpublished).

[245] M. A. Caprio and J. M. Baris, `VMEacquire` acquisition code and event builder (unpublished).

[246] N. V. Zamfir *et al.* (in preparation).

[247] H. Jin, `TSCAN` sorting package (unpublished).

[248] D. C. Radford, Nucl. Instrum. Methods A **361**, 297 (1995).

[249] D. C. Radford, RadWare analysis package (unpublished).

[250] Construzioni Apparecchiature Elettroniche Nucleari, S.p.A., Model V775 32-channel multievent TDC, Model V785 32-channel multievent ADC, and Model V830 32-channel multievent latching scaler.

[251] SBS Technologies, Inc., Model 618, PCI to VMEbus adapter.

[252] G. Kumbartzki (unpublished).

[253] *Principles and Applications of Timing Spectroscopy*, Application Note AN 42 (EG&G Ortec, Oak Ridge, TN, 1982).

[254] M. M. King, Nucl. Data Sheets **69**, 1 (1993).

[255] S. Rab, Nucl. Data Sheets **75**, 491 (1995).

[256] Y. A. Akovali, Nucl. Data Sheets **75**, 127 (1995).

[257] A. Aprahamian, J. A. Cizewski, S. Pittel, and N. V. Zamfir, eds., *Mapping the Triangle*, AIP Conf. Proc. **638** (AIP, Melville, NY, 2002).

[258] J. Cerny, ed., *Nuclear Spectroscopy and Reactions*, Part C, Vol. 40-C of *Pure and Applied Physics* (Academic Press, New York, 1974).

[259] K. Siegbahn, ed., *Alpha-, Beta-, and Gamma-Ray Spectroscopy*, Vol. 2 (North-Holland, Amsterdam, 1965).

[260] K. Siegbahn, ed., *Alpha-, Beta-, and Gamma-Ray Spectroscopy*, Vol. 1 (North-Holland, Amsterdam, 1965).